

Shale Gas Potential of the Major Marine Shale Formations in the Upper Yangtze Platform, South China

vorgelegt von
M. Sc. Geologe
Jingqiang Tan
aus Hunan, China

Von der Fakultät VI - Planen Bauen Umwelt
der Technischen Universität Berlin
zur Erlangung des akademischen Grades eines
Doktor der Naturwissenschaften
Dr. rer. nat.

genehmigte Dissertation

Promotionsausschuss:

Vorsitzender: Prof. Dr. Wilhelm Dominik

Berichter: Prof. Dr. Ralf Littke

Berichter: Prof. Dr. Brian Horsfield

Tag der wissenschaftlichen Aussprache: 27.05.2014

Berlin 2014

D83

Dedicated to my grandmother and my parents

Statement of Original Authorship

I, Jingqiang Tan, hereby state that the work contained in this thesis or any parts thereof has not previously been submitted to the Fakultät VI - Planen, Bauen, Umwelt at the Technical University of Berlin or any other institution except where explicitly acknowledged.

To the best of my knowledge and belief, the thesis does not contain any previously published material or any material which has been written by another person except where due reference is made.

Hiermit erkläre ich, Jingqiang Tan, dass diese Arbeit bisher von mir weder an der Fakultät VI -Planen, Bauen, Umwelt der Technischen Universität Berlin noch einer anderen wissenschaftlichen Einrichtung zum Zwecke der Promotion eingereicht wurde. Ferner erkläre ich, dass ich diese Arbeit selbständig verfasst und keine weiteren als die darin angegebenen Quellen und Hilfsmittel benutzt habe.

Jingqiang Tan

14-02-2014

Acknowledgements

This PhD dissertation represents unforgettable experience of my study in unconventional natural gas over the last three and a half years. The work presented in the dissertation would not have been possible without the help, support, and encouragement from many people.

First and foremost, I want to thank my supervisor Prof. Brian Horsfield for leading me into the shale gas world and for the valuable advice and guidance through my PhD study. He has been motivating and inspiring me since I started work in the section of organic geochemistry at GFZ-Potsdam. With his unreserved support and intelligent ideas, I had this wonderful opportunity to conduct comprehensive investigation on the shale samples from south China. In addition, I greatly appreciate Dr. Nicolaj Mahlstedt for his time on numerous discussions, which deeply improved my understanding of organic geochemistry and shale gas reservoir.

My special words of thanks should also go to Prof. Ralf Littke (RWTH Aachen) and Prof. Wilhelm Dominik (TU-Berlin) for reviewing the thesis and attending dissertation defense.

I gratefully acknowledge the funding received towards my PhD from Statoil. My heartfelt thanks go to Ger van Graas (Statoil) for this wonderful opportunity.

I am very grateful to Prof. Jinchuan Zhang (China University of Geosciences (Beijing)) for his kind support, samples, and cooperation. I also would like to thank Dr. Christopher J. Boreham (Geoscience Australia) and Dr. Dorothee Hippler (TU-Berlin) for providing samples, data, and collaboration on publications.

My heartfelt gratitude goes to Hans-Martin Schulz, Rolando di Primio, Ferdinand Perssen, Rudolf Naumann, Helga Kemnitz, Richard Wirth, Erik Rybacki, and Andreas Reinicke (GFZ-Potsdam), and Bernhard Krooss, Philipp Weniger, Alexej Merkel, Reinhard Fink, Amin Ghanizadeh, Matus Gasparik, and Yves Gensterblum (RWTH Aachen), for the valuable discussion, professional guidance, and collaboration on publications.

I would like to acknowledge Claudia Engelhardt, and former office mates, Ilya Ostanin, Enmanuel Rodrigues Duran, and Alexander Hartwig, for their help and the time spent together. Sascha Kuske is acknowledged for translating the abstract to German.

The Chinese students in our section, Yuanjia Han, Yaling Zhu, Nana Mu, Shengyu Yang, and Shuangbiao Han, and in other sections in GFZ-Potsdam, Ming Shangguan, Zhiguo Deng, et al, are sincerely appreciated for sharing the ups and downs of my life in Germany.

My special thanks go to my former supervisor, Prof. Yiwen Ju, and his group in Chinese Academy of Sciences, for their endless support and encouragement.

My sincere thanks also go to my cousin's family, Chengzhong Tan, Fan Li, Ailun Tan, and Mengna Tan, for their help, support, as well as many dinner invitations. I am so lucky having them around during my study in Germany. I also would like to thank Matthias Duebgen and Yaxin Xu for their generous help in my beginning time in Germany.

I deeply thank my mom and dad. My great parents have been providing unconditional love and care for decades. I would not have the opportunity to complete a PhD abroad without them. I sincerely thank my sister for all her support and understanding during my long-term study. I also extend my sincere word of thanks to my mom- and dad-in-law for their understanding in the special time. The deepest appreciation and thanks go to my wife, Yue Yin, for all her help and support through all the years. I am very grateful to all my family members for showing faith in me and giving me liberty to choose what I desired.

Jingqiang Tan

14-02-2014

List of Publications

Articles in peer-reviewed journals

- 1) **Tan, J.**, Horsfield, B., Mahlstedt, N., Zhang, J., Boreham, C.J., Hippler, D., van Graas, G. and Tocher, B.A., 2014. Shale Gas Potential of the Major Marine Shale Formations in the Upper Yangtze Platform, South China, Part I: Geological and Geochemical Characterization. In submission.
- 2) **Tan, J.**, Weniger, P., Krooss, B., Merkel, A., Horsfield, B., Zhang, J., Boreham, C. J., van Graas, G. and Tocher, B.A., 2014. Shale Gas Potential of the Major Marine Shale Formations in the Upper Yangtze Platform, South China, Part II: Methane Sorption Capacity. *Fuel*, 129:204-218.
- 3) **Tan, J.**, Horsfield, B., Fink, R., Krooss, B., Schulz, H.-M., Rybacki, E., Zhang, J., Boreham, C.J., van Graas, G. and Tocher, B.A., 2014. Shale Gas Potential of the Major Marine Shale Formations in the Upper Yangtze Platform, South China, Part III: Mineralogical, Lithofacial, Petrophysical, and Rock Mechanical Properties. *Energy & Fuels*, 28:2322-2342.
- 4) **Tan, J.**, Horsfield, B., Mahlstedt, N., Zhang, J., di Primio, R., Vu, T.A.T., Boreham, C.J., van Graas, G. and Tocher, B.A., 2013. Physical properties of petroleum formed during maturation of Lower Cambrian shale in the upper Yangtze Platform, South China, as inferred from PhaseKinetics modelling. *Marine and Petroleum Geology*, 48: 47-56.
- 5) **Tan, J.**, Ju, Y., Yuan, W., Hou, Q., Pan, J. and Fan. J., 2011. Thermochronological structural evolution of the Huaibei coalfield in eastern China: constrains from zircon fission-track data. *Radiation Measurements*, 46, 183-189.

Presentations at international symposia

- 1) **Jingqiang Tan.** PhaseKinetics and Phase Behavior Evolution Process of the Petroleum Generated from the Lower Cambrian Shale in the Upper Yangtze Platform, South China. Unconventional Resource Conference. Beijing, China, 2013 (Oral).

- 2) Christopher J. Boreham, Dianne S. Edwards, Lisa Hall, Thomas Bernecker, Lidena K. Carr, Junhong Chen, Tegan E. Smith, John Laurie, Andrew Stacey, **Jingqiang Tan**, and Brian Horsfield. Unconventional Middle Cambrian Petroleum Systems in the Georgina Basin, Australia. AAPG Hedberg Conference, Beijing, China, 2013 (Oral)
- 3) **Jingqiang Tan**, Brian Horsfield, Nicolaj Mahlstedt, et al. Predicting unconventional shale resources potential of the lower Cambrian shale in the Upper Yangtze Platform, South China. International Symposium on Shale Oil Resources and Exploitation Technology. Wuxi, China, 2012 (Oral).
- 4) **Jingqiang Tan**, Dorothee Hippler, Jinchuan Zhang, et al. Preliminary investigations into Gas-In-Place and fraccability of shales from the Sichuan Basin, China. 25th International Meeting on Organic Geochemistry, Interlaken, Switherland, 2011, p 371 (Poster).

Presentations at internal seminar and project workshop

- 1) **Jingqiang Tan** & Brian Horsfield. Shale gas potential of the Ediacaran, Lower Cambrian, and Lower Silurian Black shales in the Upper Yangtze Platform, South China. Statoil, Oslo, Norway, 2014 (Project workshop).
- 2) **Jingqiang Tan**. Petrophysics, rock mechanics, and methane sorption isotherms of Lower Paleozoic black shales from the Upper Yangtze Platform, South China. GFZ-Potsdam, Germany, 2013 (Section seminar).
- 3) **Jingqiang Tan** & Brian Horsfield. Shale gas in the Sichuan Basin, South China. Statoil, Oslo, Norway, 2011 (Project workshop).
- 4) **Jingqiang Tan**. Shale gas in the Sichuan Basin, South China - the preliminary results. GFZ-Potsdam, Germany, 2011 (Section seminar).

Contribution of Collaborators

Project funding and execution

This project, sponsored by Statoil ASA, was an Industry Partnership Project of the Organic Geochemistry Section of the Helmholtz Centre Potsdam - GFZ German Research Centre for Geosciences (GFZ-Potsdam).

Samples

Jingqiang Tan, Brian Horsfield (GFZ-Potsdam), and Jinchuan Zhang (China University of Geosciences) collected the Lower Silurian and Lower Cambrian outcrop samples in south China in April, 2011.

Dorothee Hippler provided the Lower Cambrian samples from the Heishapo profile and Ediacaran outcrop samples.

Core samples from south China were provided by China University of Geosciences (Beijing) (Jinchuan Zhang), and that from north Australia were provided by Geoscience Australia (Christopher J. Boreham).

Experiments and data in chapter 3

Rock-Eval Pyrolysis and TOC measurements were performed by Applied Petroleum Technology (APT) in Kjeller, Norway.

Volker Lüders (GFZ-Potsdam) measured the carbon isotope ratio of methane inclusions and provided guidance with interpretation.

Dorothee Hippler (TU-Berlin) provided the Rock-Eval and TOC data of Cambrian samples from the Heishapo profile and Ediacaran samples from the Maoshi and Lijiatio profiles.

Experiments and data in chapter 4

Ferdinand Perssen and Nicolaj Mahlstedt (GFZ-Potsdam) performed the bulk kinetics analysis and provided guidance with interpretation, respectively.

Rolando di Primio (GFZ-Potsdam) conducted the analysis of compositional kinetics and provided guidance with interpretation.

The open py-GC, Rock-Eval, and TOC data of the Cambrian shale sample from Australia were provided by Christopher J. Boreham (Geoscience Australia).

Experiments and data in chapter 5

Rudolf Naumann, Helga Kemnitz, Richard Wirth, and Andreas Reinicke (GFZ-Potsdam) guided the measurements of XRD, SEM, TEM, and rock mechanical measurements.

Bernhard Krooss, Reinhard Fink, and Amin Ghanizadeh (RWTH Aachen) helped with the petrophysical measurement and sample preparation.

A part of the rock mechanical and petrophysical data were measured by Geomecon.

Experiments and data in chapter 6

Bernhard Krooss, Philipp Weniger, and Alexej Merkel (RWTH Aachen) helped with the measurement of high-pressure methane sorption isotherms and provided guidance with interpretation.

Abstract

The Ediacaran (Upper Sinian), Lower Cambrian, and Lower Silurian shale formations on the Upper Yangtze Platform (UYP), south China are characterized to a large extent, by their great thickness, and variable burial depth ranging from surface exposure to more than 5000 m. They are the principal source rocks of conventional petroleum fields in the UYP, and have been recently regarded as the most promising shale gas plays of China. The work presented in this dissertation aims to evaluate the gas-in-place and fraccability of these shale formations. Beginning with a detailed investigation on the geological setting and sedimentary history, a comprehensive study was then conducted focusing on the organic geochemical characteristics, petroleum physical properties, methane sorptive capacity, mineralogical constituents, lithofacies, petrophysical features, and rock mechanical properties of the shales.

Measured total organic carbon (TOC) is mainly higher than 2%, and averages 5%. The kerogen has evolved into the metagenesis stage, which was demonstrated by the abundant pyrobitumen on microphotographs, the high vitrinite reflectance ($R_o=3.0\%$) calculated via bitumen reflectance (R_b), as well as the $\delta^{13}C$ of gas (methane) inclusions. Pyrolysates from open system pyrolysis gas chromatography are therefore quantitatively low and qualitatively dominated by light hydrocarbons. The original organic matter is presumably dominated by hydrogen-rich kerogen deposited under marine conditions via selective accumulation of algal material, based on the analysis of $\delta^{13}C$ of methane, kerogen, and chloroform bitumen, as well as its close similarity in aromaticity evolution with those of available time equivalents of lower maturity from Australia. Because this correlation suggests the presence of a Type I kerogen the implication is that the UYP shales were highly prolific sources of liquid and gaseous hydrocarbons.

The onset (transformation ratio TR=10%) and end (TR=90%) of bulk hydrocarbon generation was calculated to take place at 120°C and 165°C respectively for an assumed average geological heating rate of 1.5°C/Ma. Based on the thermal history of a local “model”-well, this onset temperature was not reached until the Middle Triassic (241 Ma) when sediments were buried to more than 2000 m and basalt eruptions caused enhanced heat flows. The main generation stage of primary petroleum took place during the Middle-Late Triassic and ended in the Early Jurassic (187 Ma) for burial depths exceeding 4000m (TR 90%; 165°C). Temperatures increased to more than 200°C in the Middle-Late Jurassic leading to secondary cracking of primary products. The shale reservoir position within the sedimentary

basin indicates that the bubble point pressure was always below the reservoir pressure, and fluids in the shale reservoir occurred only as a single, undersaturated phase throughout maturation history. Black oil and volatile oil phases dominated during the primary cracking period, whereas wet gas and dry gas phases dominated during the secondary cracking period.

Results of the high pressure (up to 25 MPa) methane sorption isotherms indicate that the maximum methane excess sorption of the Lower Silurian samples is between 0.045 and 0.064 mmol/g rock, and that of the Lower Cambrian samples is between 0.036 and 0.210 mmol/g rock. The Langmuir sorption capacity of the Lower Silurian samples ranges from 0.096 to 0.115 mmol/g rock, while that of the Lower Cambrian shale ranges from 0.077 to 0.310 mmol/g rock. They are close to the sorption capacities of the Barnett (U.S.), Devonian-Mississippian (Western Canada), and Alum (Southern Scandinavia) shale samples. The shape of sorption isotherms and thus methane sorption capacity vary from sample to sample, which can be affected by the TOC content, thermal maturity, clay mineral, moisture content, pore properties, particle size, as well as the applied temperature and pressure.

The bulk mineralogy of all three formations is dominated by a high proportion of quartz, low content of clay, and rare or non-existent content of carbonates. The Ediacaran and Lower Cambrian shales deposited in deep water marine platform to marine basin environments with limited circulation are characterized by a higher content of quartz and lower content of clay than the Lower Silurian shales which were deposited in a more restricted marine basin environment. The carbonate content varies from 0 to over 50%, with the higher values measured on the Lower Silurian samples. These stratigraphic units were rarely influenced by bioturbation. Lithologically, laminated and non-laminated siliceous mudstones predominate, with minor contributions of other lithotypes. Pores generally have diameters in the nanometer to micrometer range, and abundant pores are found within organic matter. Most of the measured samples have porosities less than 4%, although a few samples show porosity in excess of 10%. Pores with radii less than 50 nm contribute significantly to total pore volume and total porosity. Permeability is extremely low, and helium permeability coefficients (Klinkenberg corrected permeability coefficient) are less than 20.2 nD (nano-Darcy, $\sim 2 \times 10^{-20} \text{ m}^2$). The rock mechanical properties of the samples are characterized by a highly brittle behaviour, which coincides with their high compressive and tensile strengths and elastic properties. The Lower Cambrian shale is generally more brittle than the Lower Silurian shales. The rock mechanical properties of the measured samples, however, depend on the overall mineral compositions and physical properties.

Zusammenfassung

Die Schieferformationen des Ediacarium (Oberes Sinian), Unterkambrium und Untersilur der Oberen Yangtze Plattform (OYP) im Süden Chinas sind zum größten Teil durch ihre große Mächtigkeiten und ihre variablen Tiefenbereiche (von oberflächlichen Aufschlüssen bis 5000m Tiefe) gekennzeichnet. Sie sind wichtige Muttergesteine konventioneller Petroleumfelder innerhalb der OYP, und wurden unlängst als die vielversprechendsten Schiefergasvorkommen Chinas betitelt worden. Die hier vorgelegte Arbeit, in Form einer Dissertation, beabsichtigt es den Gasvorrat und die sogenannte frackability dieser Schieferformationen zu evaluieren. Angefangen mit einer detaillierten Untersuchung der geologischen Gegebenheiten und dem Sedimentationsverlauf, wurde eine umfassende Studie mit Fokus auf organochemische, Petroleum-physikalische, petrophysikalische und felsmechanische Attribute, Methan-Sorptionsvermögen, mineralogische Komponenten und Lithofazies der Schiefer durchgeführt.

Der gemessene gesamtorganische Kohlenstoff (TOC) betrug meistens über 2%, durchschnittlich 5%. Anhand von reichlich vorhandenem Pyrobitumen auf Mikrofotogrammen, einem hohen Vitrinitreflektionswert ($R_o=3.0\%$), welcher mittels Bitumenreflektion (R_b) bestimmt wurde und durch $\delta^{13}C$ -Werte von eingeschlossenem Gas (Methan) konnte ermittelt werden, dass das Kerogen die Metagenese-Phase bereits erreicht hat. Die Quantität der Pyrolysate aus der offenen Pyrolyse-Gas-Chromatographie sind dementsprechend niedrig. Qualitativ konnten nur leichte Kohlenwasserstoffe erkannt werden. Vermutlich besteht das ursprüngliche organische Material überdurchschnittlich aus wasserstoffreichem Kerogen und wurde unter marinen Bedingungen mit selektiver Ansammlung von Algen abgelagert. Diese Vermutungen sind gestützt durch $\delta^{13}C$ -Analysen des Methans, Kerogens und Chloroformbitumen, sowie einer großen Ähnlichkeit der Aromatizitätsentwicklung mit zeitlich äquivalenten Ablagerungen, mit geringer Maturität, in Australien. Diese Korrelation lässt den Schluss zu, dass es sich bei diesen Ablagerungen ursprünglich um Kerogen Typ I handelte, was wiederum impliziert, dass die OYP-Schiefer einmal exzellente Quellen flüssiger und gasförmiger Kohlenwasserstoffe waren.

Berechnungen ergaben, dass der Beginn (Umwandlungsrate $TR=10\%$) und das Ende ($TR=90\%$) der Gesamtkohlenwasserstoffgenese jeweils bei $120^\circ C$ und $165^\circ C$ bei einer geologischen Heizrate von $1.5^\circ C/Ma$ stattfanden. Der Temperaturverlauf einer „Modell“-Bohrung ergab, dass diese Anfangstemperatur nicht vor der Mitteltrias (241 Ma) erreicht

wurde. Zu diesem Zeitpunkt waren die Sedimente 2000m tief begraben und Basalteruptionen erhöhten den Wärmefluss. Die Hauptgenese primären Petroleums erfolgte in der Mittleren und Späten Trias und endete in der Frühen Jura (187 Ma) in Tiefen größer als 4000m (TR=90%; 165°C). Im der Mittleren und Späten Jura führten Temperaturen von über 200°C zu sekundärem Cracken von Primärprodukten. Die Position des Schieferreservoirs innerhalb des Sedimentbeckens weist darauf hin, dass der Sättigungsdruck stets unterhalb des Reservoirdrucks war und dass Fluide im Schieferreservoir nur als einzelne, untersättigte Phase während der gesamten Maturitätsentwicklung existierten. Schwarzöl- und Leichtölphasen dominierten während des primären Crackens, wohingegen Nassgas- und Trockengasphasen während der Zeit des sekundären Crackens überwogen.

Ergebnisse von Hochdruck- (bis zu 25 MPa) Methan-Sorptions-Isothermen deuten darauf hin, dass die maximale Methan-Überschuss-Sorption der Proben aus dem Unteren Silur zwischen 0.045 und 0.064 mmol/g Gestein und die der unterkambrischen Proben zwischen 0.036 und 0.210 mmol/g Gestein schwankt. Die Lanmuir-Sorptionskapazität der Proben aus dem Unteren Silur reicht von 0.096 bis 0.115 mmol/g Gestein und bei den Proben aus dem Unteren Kambrium von 0.077 bis 0.310 mmol/g Gestein. Diese Ergebnisse ähneln der Sorptionskapazität von Proben aus den Barnett- (U.S.), Devon- Mississippium- (Westkanada), und Alumschiefer (Südkandinavien). Die Form der Sorptionsisothermen und damit auch die Methansorptionskapazität variieren von Probe zu Probe. Dies könnte durch TOC-Gehalt, thermische Reife, Tonminerale, Feuchtegehalt, Poreneigenschaften, Partikelgröße, sowie angewandte Temperaturen und Drücke beeinflusst worden sein.

Die Gesamtmineralogie aller drei Formationen ist gekennzeichnet durch einen hohen Quarz-, niedrigen Ton- und sehr niedrigen bis nichtvorhandenen Karbonatgehalt. Die Schiefer des Ediacariums und des Unteren Kambriums wurden in Ablagerungsmilieus tief mariner Plattformen bis marinen Becken abgelagert, die eine beschränkte Zirkulation aufwiesen. Des Weiteren zeichnen sie sich durch einen höheren Quarz- und Tongehalt aus als die Schiefer des Unteren Silurs, welche in noch eingeschränkteren, marinen Becken abgelagert wurden. Der Karbonatgehalt liegt zwischen 0 bis über 50%, wobei hier höhere Gehalte in den Proben des Unteren Silurs gemessen wurden. Diese stratigraphischen Einheiten wurden nur selten durch Bioturbation beeinflusst. Lithologisch gesehen dominieren laminierte und nicht-laminierte kieselige Mudstones mit eher geringererfrequenteren Zuschaltungen anderer Lithotypen. Poren weisen generell Nanometer- bis Mikrometer-Größen auf, wobei das organische Material reichlich Porenräume aufweist. Die meisten der gemessenen Proben haben Porositäten von

weniger als 4%. Trotzdem gibt es einige Proben mit Porositäten über 10%. Poren, die einen Radius von weniger als 50nm aufweisen, tragen signifikant zum absoluten Porenvolumen bei. Die Permeabilität ist extrem niedrig und Helium-Permeabilitätskoeffizienten (Klinkenberg korrigierter Permeabilitätskoeffizient) sind kleiner als 20.2 nD (nano-Darcy, $\sim 2 \times 10^{-20} \text{ m}^2$). Die felsmechanischen Eigenschaften der Proben sind gekennzeichnet durch hoch-brüchiges Verhalten. Dies geht mit hohen Druck- und Zugfestigkeiten, sowie elastischen Merkmalen einher. Der Unterkambrische Schiefer ist im Allgemeinen brüchiger als der untersilurische Schiefer. Dennoch hängen die felsmechanischen Eigenschaften der gemessenen Proben insgesamt von der Mineralzusammensetzung und von physikalischen Merkmalen ab.

Table of Contents

Acknowledgements	I
List of Publications.....	IV
Abstract	VII
Zusammenfassung.....	X
Table of Contents	XIV
List of Figures	XIII
List of Tables.....	XXI
List of Abbreviations.....	XXIII
Chapter 1 Introduction	1
1.1. Overview	1
1.1.1. Global Shale Gas Resource.....	1
1.1.2. Chinese Shale Gas Resource.....	3
1.1.3. Black Shales in the Upper Yangtze Platform.....	4
1.2. Resource Evaluation and Reservoir Characterisation	7
1.2.1. Shale Gas Geology.....	8
1.2.2. Organic Geochemistry	10
1.2.3. Mineralogy.....	15
1.2.4. Petrophysics	16
1.2.5. Rock Mechanics.....	17
1.2.6. Gas Storage Mechanism	18
1.3. Research Objectives	19
1.4. Structure of Dissertation.....	20
Chapter 2 Samples and Methods.....	24
2.1. Samples.....	24
2.1.1. UYP - Lower Silurian Shale	24
2.1.2. UYP - Lower Cambrian Shale	28
2.1.3. UYP - Ediacaran Shale	28
2.1.4. AU - Cambrian Shale.....	28
2.2. Sample Preparation.....	28
2.3. Methodology.....	29
2.3.1. Organic Geochemical Measurements	29

2.3.2. Microstructural and Mineralogical Examinations.....	32
2.3.3. Petrophysical Experiments.....	33
2.3.4. Rock Mechanical Tests	35
2.3.5. Methane Sorption Isotherms	35
Chapter 3 Geological and Geochemical Characterisation.....	39
3.1. Abstract.....	39
3.2. Introduction	40
3.3. Geological Setting	42
3.3.1. Tectonic and Sedimentary History.....	42
3.3.2. Petroleum Systems of the UYP.....	43
3.4. Black Shale Intervals under Investigation	44
3.5. Applied Methods	47
3.6. Results and Discussions.....	52
3.6.1. Organic Matter Richness.....	52
3.6.2. Thermal History and Maturity	54
3.6.3. Sorbed Hydrocarbon Composition as Revealed by T _{vap} -GC	57
3.6.4. Remaining Hydrocarbon Generative Potential as Revealed by open py-GC	58
3.6.5. Evolution of Kerogen Structure and Hydrocarbon Generation Properties	62
3.6.6. Kerogen Typing	66
3.6.7. Reconstruction of Original Hydrocarbon Generative Potential.....	69
3.7. Conclusions	72
3.8. Acknowledgements	73
Chapter 4 Petroleum Physical Properties	75
4.1. Abstract.....	75
4.2. Introduction	76
4.3. Selection of Cambrian Geological Analogue	78
4.3.1. Cambrian Geology - UYP.....	78
4.3.2. Cambrian Geology - Georgina Basin.....	80
4.4. Selection of Shale Samples.....	80
4.4.1. Lower Cambrian Shale Samples from the UYP	80
4.4.2. Cambrian Shale Sample from the Georgina Basin, north Australia	81
4.5. Analytical and Modelling Methods	81
4.5.1. Open-system Pyrolysis Gas Chromatography (open-Py)	81
4.5.2. Bulk Kinetics	82

4.5.3. Closed-system Pyrolysis Gas Chromatography (MSSV-Py).....	82
4.5.4. Compositional Kinetic Modelling.....	83
4.5.5. 1-D Petroleum System Modelling	83
4.6. Results and Discussions.....	84
4.6.1. Petroleum Type Organofacies.....	84
4.6.2. Bulk Maturation Characteristics	87
4.6.3. Compositional Kinetics.....	88
4.6.4. Petroleum Phase Behaviour Prediction in the UYP.....	90
4.7. Conclusions	93
4.8. Acknowledgements	94
Chapter 5 Methane Sorption Capacity	96
5.1. Abstract.....	96
5.2. Introduction	97
5.3. Samples and Methods.....	99
5.3.1. Sample Characterisation	99
5.3.2. Sample Preparation	101
5.3.3. Experimental Setup and Procedure	102
5.3.3. Experimental Setup and Procedure.....	102
5.3.4. Results Calculation and Parameterisation.....	103
5.3.5. Equation of State (EOS).....	104
5.3.6. Thermovaporisation Gas Chromatography (Tvap-GC).....	104
5.4. Results	105
5.4.1. Methane Sorption Isotherm Results.....	105
5.4.2. Tvap-GC Results.....	106
5.5. Discussions	108
5.5.1. Effect of Organic Matter Richness	108
5.5.2. Effect of Thermal Maturity	109
5.5.3. Effect of Mineral Content	112
5.5.4. Effect of Moisture Content	113
5.5.5. Effect of Pressure and Temperature.....	114
5.5.6. Effect of Pores and Particle Size.....	116
5.5.7. Tvap-GC Measured Gas	119
5.5.8. Data Comparison	119
5.6. Conclusions	122

5.7. Acknowledgements	123
Chapter 6 Mineralogy, Lithofacies, Petrophysics, and Rock Mechanics.....	125
6.1. Abstract.....	125
6.2. Introduction	126
6.3. Experimental Details	127
6.3.1. Analyzed Samples.....	127
6.3.2. Sample Preparation	128
6.3.3. Methodology	128
6.4. Results	133
6.4.1. Mineralogy.....	133
6.4.2. Lithofacies.....	134
6.4.3. Petrophysics	142
6.4.4. Rock Mechanics.....	148
6.5. Discussions	152
6.5.1. Mineralogy and Lithofacies: Implications for Sedimentary Environments.....	152
6.5.2. Porosity and Permeability of the Shale Reservoir	155
6.5.3. Physical Properties of the Shale Reservoir	156
6.6. Conclusions	159
6.7. Acknowledgements	160
Chapter 7 Summary and Outlook.....	162
7.1. Summary.....	162
7.1.1. Geological Characterisation.....	162
7.1.2. Organic Geochemical Properties	163
7.1.3. Petroleum Physical Properties in the Shale Reservoir	163
7.1.4. Methane Sorption Capacity.....	164
7.1.5. Mineralogy and Lithofacies	165
7.1.6. Petrophysical and Rock Mechanical Properties.....	166
7.2. Outlook	166
References	169
Appendix	181

List of Figures

Figure 1.1 Global distribution of shale resources (EIA, 2013b).

Figure 1.2 Distribution map of black shale (A-C), modified after (Zhang et al., 2009; Zou et al., 2010), and tectonic framework of China and locations of the Upper Yangtze Platform and the Sichuan Basin (D), modified after (Zhang et al., 2011). TR-P: Tarim Platform, YZ-P: Yangtze Platform, NC-P: North China Platform, JG-F: Junggar fold system, TS-F: Tianshan fold system, EK-F: East Kunlun fold system, QI-F: Qilian fold system, SG-F: Songpan-Ganzi fold system, GN-F: Gangdise-Nyainqentanglha fold system, SJ-F: Sanjiang fold system, HY-F: Himalayan fold system, MD-F: Mongolia-Daxinganlin fold system, JH-F: Ji-He fold system, ND-F: Nadezhda fold system, QL-F: Qinling fold system, SC-F: south China fold system, SE-F: Southeast China fold system, Upper YP: Upper Yangtze Platform, Middle YP: Middle Yangtze Platform, and Lower YP: Lower Yangtze Platform.

Figure 1.3 Distribution of shale gas resources in China (Zhang et al., 2012a).

Figure 1.4 Generalised stratigraphic column in the Sichuan Basin, UYP, modified after (Editorial Committee of the Sichuan Oil & Gas field, 1989; Zou et al., 2010).

Figure 2.1 Overview maps of the Yangtze Platform, south China (A), and the Georgina Basin, north Australia (B). Numbers show the investigated profiles and wells, and names are listed in Table 2.1.

Figure 3.1 Generalized stratigraphic column and petroleum system event chart of the Sichuan Basin, UYP, modified after (Editorial Committee of the Sichuan Oil & Gas field, 1989).

Figure 3.2 Isopach maps of the Lower Silurian (upper) and Lower Cambrian (lower) shale formations in the Yangtze Platform, modified after (Liang et al., 2008; Zou et al., 2011), and the locations of investigated profiles and wells. Sampled Lower Silurian profiles or wells are 1-YY1# well, 2-Guankou, and 3-Lujiao. Sampled Lower Cambrian profiles are 4-Jinggang, 5-Rongxi, 6-Cenggong, and 7-Heishapo. Data compiled Lower Silurian profiles or wells are 10-Zhenba-Guanyin, 11-Shizhu-Qiliao, 12-Shizhu-Dafengao, 13-Dingshan 1# well, 14-Xishui-liangchun 5# well, and 15-Changxin 1# well. Data compiled Lower Cambrian profiles or wells are 16-Nanjiang-Shatang, 17-Guangyuan, 18-Gaoke 1# well, 19-Wei 001-2# well, 20-Fanshen 1# well, and 21-Majiang-Yangtiao. In addition, two sampled Ediacaran profiles denoted in the bottom plot are 8-Maoshi and 9-Lijiatuo.

Figure 3.3 Outcrop photographs and selected hand specimens. A-Lower Cambrian shale in the Cenggong profile, Guizhou province; B-Lower Silurian shale in the Guankou profile, Chongqing area; C-Lower Cambrian black (bottom) and silicious (upper) shale in the Jinggang profile, Chongqing area; D-Silicious shale in the Cenggong profile, Guizhou province; E-Lower Silurian calcareous shale sample

from the Lujiao profile, Chongqing area; F-Lower Silurian fossiliferous (graptolite) shale sample from the Guankou profile, Chongqing area; G-Lower Silurian mudstone with big pyrite accumulation or segregation, sample from the YY1 well; H-Fractured Lower Silurian mudstone filled with quartz, sampled from the YY1 well; K-Lower Cambrian carbonaceous shale sample from the Cenggong profile, Guizhou area; L-Distinct horizontal laminations in the Lower Cambrian shale, sampled from the Rongxi profile, Chongqing area; M-Ediacaran black shale from the Lijiatuo profile, Hunan province; N-Ediacaran phosphatic shale sample from the Maoshi profile, Guizhou province.

Figure 3.4 Organic matter in section photomicrographs of selected and representative shale samples. 2-Organic matter (pyrobitumen) and pyrite framboids (polished section with reflected light). 20-Disseminated pyrobitumen in shale matrix, with light reflectance of the bitumen is over 4.0 % (polished section, reflected light). 6- Unlaminated siliceous shale showing organic matter (black), platy clay or mica minerals and subrounded to angular detrital quartz grains (white) (thin section, plane polarized light). G011315-Siliceous shale showing graded bedding with crinkle to wavy laminated organic matter in the bottom and lower organic content in the more granular top (thin section, plane polarized light).

Figure 3.5 Histograms of TOC content in relation to stratigraphic age. The TOC content almost positively correlates with increasing geological age. Sample IDs are denoted Table 3.1.

Figure 3.6 TOC content versus stratigraphic depth for 8 sections studied on the UYP. A-H: data compiled profiles from (Liang et al., 2008), 10-13 are the Lower Silurian profiles/wells. 14-17 are the Lower Cambrian profiles/wells. The locations are denoted in Figure 3.2.

Figure 3.7 Compilation of $\delta^{13}C$ of methane ($\delta^{13}C_1$) versus vitrinite reflectance R_o . Carbon isotopic composition of methane and vitrinite reflectance are positively correlated for both marine source rocks as well as terrestrial coal samples, with both arrays being considerably offset. This is reflected in $\delta^{13}C_1$ -values from marine source rocks being more fractionated than $\delta^{13}C_1$ -values from terrestrial coal. Values for UYP samples are in agreement with values measured for the Barnett shale (Stahl & Carey, 1975) plotting on the extrapolation towards higher $\delta^{13}C_1$ and higher vitrinite reflectance, respectively.

Figure 3.8 $HI-T_{max}$ plot of different source rocks, comprising the UYP shale, Barnett shale (Jarvie, 2008), Bakken shale (Kuhn et al., 2010), Posidonia shale (Schenk and Horsfield, 1998), German coal (Schenk and Horsfield, 1998), and New Zealand coal (Vu, 2008).

Figure 3.9 The dominant open py-GC pyrolysates of the Lower Silurian, Lower Cambrian and Ediacaran shale sample. Considerable differences in open py-GC pyrolysate composition are found for the respective units. The Lower Silurian sample show relatively stronger yields than that of the Lower Cambrian sample which in turn has higher yields than that of the Ediacaran sample.

Figure 3.10 Open py-GC products of selected samples. A-Total amount of open py-GC products of per gram rock; B-Total amount of open py-GC products, values were normalized to TOC weight; C-The amount of the identified light hydrocarbons in per gram rock; D-The amount of the identified light

hydrocarbons, values were normalized to TOC; E-Light hydrocarbons vs. depth of the core samples; and F-The correlations between C5 and TOC.

Figure 3.11 X-Y plot of open-py-GC products and temperature illustrating the remaining hydrocarbon generative potential of artificially matured residues.

Figure 3.12 Variation gas wetness (A), GOR (B) and aromatics (C and D) of artificially matured residues, as a function of temperature.

Figure 3.13 Hydrocarbon generation properties with Tmax increase in natural samples. The UYP shales show possible correlations with the AU shales.

Figure 3.14 Aromatics generation properties with Tmax increase in natural samples. The UYP shales show possible correlations with the AU shales.

Figure 3.15 $\delta^{13}\text{C}$ of kerogen and extracted bitumen (left) and the histogram of $\delta^{13}\text{C}$ of kerogen (right) in the Palaeozoic source rocks, UYP (Liang et al., 2009b). The $\delta^{13}\text{C}$ of both kerogen and chloroform bitumen increases with decreasing geological age, and different source rocks show variations in $\delta^{13}\text{C}$ values.

Figure 4.1 Lower Cambrian shale distributions in the Yangtze Platform, modified after (Liang et al., 2008; Zou et al., 2011).

Figure 4.2 Palecontinents in the Cambrian: red points indicate locations of south China and north Australia, modified after (Scotese and McKerrow, 1990).

Figure 4.3 1D results in central-south Sichuan Basin, UYP. Reservoir conditions of the Lower Cambrian shale represented by red points are respectively: A – 2000m, 241 ma, and 120°C; B – 2800m, 216 ma, and 130°C; C – 3100m, 209 ma, and 137°C; D – 3300 m, 203 ma, and 145°C; E – 3500m, 200 ma, and 152°C; F – 4000 m, 187 ma, and 165°C; G – 5200 m, 162 ma, and 200°C; H – 6000m, 143 ma, and 223°C; I – 5500 m, 93 ma, and 200°C.

Figure 4.4 OI versus HI.

Figure 4.5 Pyrolysis gas chromatogram of the sample from Georgina Basin.

Figure 4.6 Petroleum type organofacies.

Figure 4.7 Activation energy distribution populated by MSSV data.

Figure 4.8 Predicted TR evolution with a function of temperature for a heating rate of 1.5 °C/ ma.

Figure 4.9 Calculated GOR, P_{sat} , B_o evolution with a function of TR.

Figure 4.10 Predicted GOR evolution with a function of temperature for a heating rate of 1.5 °C/ ma.

Figure 4.11 Predicted P_{sat} and B_o for a heating rate of 1.5 °C/ ma. Ellipses are the ranges of natural oils from the Central Graben) (di Primio and Neumann, 2008), Viking Graben(Bhullar et al., 2003) and Tampen Spur (di Primio et al., 1998) in the Northern Sea, Norway, from the top down. Curves are the predicted ranges of natural oils in the Central Graben, Lower Cambrian shale in the UYP, natural oils in the Tampen Spur (di Primio and Skeie, 2004) and Bakken shale (Kuhn et al., 2010), from the top down.

Figure 4.12 Phase behavior evolution with burial depth and temperature increasing of Lower Cambrian shale in the UYP. Diagonals are the temperature-pressure gradients in reservoir conditions; Points on the diagonal are the reservoir conditions in given times; Curves are the phase envelopes; Points on the envelope are bubble points; Plots A-H are corresponding to the six reservoir positions in Figure 4.3.

Figure 5.1 Locations of the sampled profiles and wells in the Upper Yangtze Platform, south China (A) and Georgina Basin, north Australia (B). Profiles and wells in the Chongqing area are the 1-Lujiao profile, 2-Datianba profile, 3-Rongxi profile, 4-Jinggang profile, and 5-Yuke1 well; however, the 6-Songqian1 well and 7-Cenggong profile are located in the Guizhou Province. The AU Middle Cambrian shale samples are from the BMR Mt Isa 1 well in the Georgina Basin.

Figure 5.2 Methane excess sorption isotherms at 46°C measured on the received samples. The plots on the left are in mmol/g rock and on the right were normalized to TOC in mmol/g TOC.

Figure 5.3 Measured maximum excess sorption capacity (n_{excess}) and Langmuir sorption capacity (n_L) as a function of TOC. Plot A contains all the measured samples, plot B contains all the UYP samples, and plot C contains samples that have similar thermal maturity, clay, and moisture content.

Figure 5.4 Effect of thermal maturity on the maximum excess sorption (A) and its corresponding pressure (B) and on the maximum Langmuir sorption capacity (C) and the Langmuir pressure (D). The sorption capacities are TOC-normalized. The R_o of the Lower Silurian shale was presented by 2.8%, whereas that of the Lower Cambrian shale was represented by 3.3%.

Figure 5.5 Effects of clay on the maximum excess sorption capacity (A and C) and Langmuir sorption capacity (B and D). TOC-normalized and rock-normalized values are presented.

Figure 5.6 The effect of moisture content on the maximum excess sorption (A and C) and Langmuir sorption capacity (B and D). TOC-normalized and rock-normalized values are presented.

Figure 5.7 Methane excess sorption isotherms at 60°C measured on dry samples (Wang et al., 2013a). QT-2, QT-4, QT-5, and MB-1 are the sample IDs of Lower Silurian samples, and ST-1 and LT-1 are the sample IDs of Lower Cambrian samples.

Figure 5.8 Pore size distributions of selected samples measured by mercury inject porosimetry.

Figure 5.9 Effect of particle size on the excess sorption.

Figure 5.11 Effect of clay on T_{vap}-GC measured gas hydrocarbon.

Figure 5.12 Comparison of methane sorption capacity of shale samples from China, Canada, Europe, and U.S.

Plot A: Data in this research vs. published data of dry samples. Plot B: Data in this research vs. published data of moist samples. The sorption capacities of the samples from the Sichuan and Lower Cretaceous samples from the Western Canadian Basin have values of 10 and 6 MPa, respectively, whereas other samples show theoretical sorption capacities. Published results are from (Chalmers and Bustin, 2008; Ross and Bustin, 2009; Gasparik et al., 2013; Wang et al., 2013a).

Figure 6.1 Overview maps of the Yangtze Platform, south China (A), and the Georgina Basin, north Australia (B). Numbers show the investigated profiles and wells, and names are listed in Table 6.1.

Figure 6.2 Mineralogical compositions according to XRD results. A: All measured samples and compiled data; B: Lower Silurian samples; C: Lower Cambrian samples. Basically, “quartz group minerals” include quartz, feldspar, apatite, and pyrite; “clay group minerals” comprise clay and mica; and carbonates consist of calcite, dolomite, ankerite, and siderite. Plot A and C contains 14 AU Cambrian samples.

Figure 6.3 Microphotographs of laminated siliceous mudstone and siliceous calcareous mudstone. 56 (sample ID)-Ediacaran siliceous mudstone: Quartz and mica concentrate in the white laminae, while clay and organic matter concentrate in the black laminae in microphotograph; 44-Lower Cambrian siliceous mudstone: Discontinuous laminae can be seen in microphotograph; 48- Lower Cambrian siliceous mudstone: Faint laminae are shown by the orientation of quartz (66.4%, wt) and organic matter (13.2% TOC); 39-Lower Cambrian siliceous mudstone: It shows similar texture as the sample 48, but has obviously high content of pyrite (11.2%), concentrating to form thin laminae; 4-Lower Silurian siliceous calcareous mudstone: Faintly rhythmic lamination texture is illustrated by the alternating clay-rich (dark) and ankerite-rich (bright) laminae; 43-Lower Cambrian siliceous mudstone (reflected light): Organic matter (grey part) occupies significant area in the texture, and concentrates to form thin laminae; and 48 (bottom)-Lower Cambrian siliceous mudstone (reflected light): Organic matter (grey part) occupies significant area in the texture, but scatters in the matrix. The pyrite could occur either as framboids (yellow arrows in 43 and 48), or single crystals (blue arrows in 43 and 48). Samples for these microphotographs were cut perpendicular to bedding planes.

Figure 6.4 Sample slabs and microphotographs of non-laminated siliceous mudstones and phosphatic concretion.

5 (Sample ID)-Lower Silurian non-laminated siliceous mudstone: Graptolite fossils randomly distribute in hand specimen (left), while the microphotograph exhibits homogeneous matrix comprising subangular quartz grains, clay, mica, and organic matter (right); 55-Ediacaran non-laminated siliceous calcareous mudstone: Core photograph shows a dark and massive texture (left), and fine-grained dolomite minerals scatter in a dark (TOC=14.5%) and clayey matrix (right); 16- Lower Silurian non-laminated calcareous mudstone: Microphotograph shows calcite matrix and mineral veins (sealed fractures); 30-Lower Cambrian phosphatic concretion: Appearance of phosphatic pellets in microphotograph. Excluding the photograph of 5-left, samples were cut perpendicular to bedding planes.

Figure 6.5 Fracture photographs. 50 (sample ID): Stylolites (white arrows) in a chert matrix, with mineral veins and pellets (red arrows) (upper left); Microphotographs of the same sample shows load casts (upper right), and exhibits dark elliptic pellets (red arrows) in a chert matrix (middle left). 22- Crossed fracture system cuts through pellets (red arrows). 40: Mineral veins (sealed fractures) show in a siliceous mudstone sample. 10 and 43: Vertical sealed fractures occur frequently in the Lower Silurian shales (e.g., 10) or in the Lower Cambrian shales (e.g., 43).

Figure 6.6 Pores in the mineral matrix. 31 (sample ID) - Micrometer scale matrix pores (white arrows, SEM); 59-Intraparticle pores (white arrows) in a quartz grain (SEM); 7-Organic matter, angular-subangular pores (white arrows), fractures (artificial or natural?), and fluid inclusions in the matrix (FIB-TEM); 9- Elongate pores (black arrows) distribute between clay flakes (FIB-TEM).

Figure 6.7 Pore in the organic matter. A and B-Nanometer to micrometer scale pores are abundant in the organic matter, and rarely occur in the mineral matrix, FE-SEM image of a Lower Silurian shale sample (courtesy of Tian, and from Tian, et al (2013)); C and D-Nanometer scale pores are abundant in the pyrobitumen between silt minerals, or in the pyrobitumen that is located between pyrite and clay flakes of a Lower Cambrian shale sample (courtesy of Zou, and from Zou, et al (Zou et al., 2010)).

Figure 6.8 Porosity and bulk density, and their correlations with TOC. A: Hg-porosity versus TOC; B: Correlations between bulk density (ρ_b) and TOC; C: Hg-porosity versus He-porosity.

Figure 6.9 Pore size distributions and cumulative pore volume of the selected Lower Silurian (upper) and Lower Cambrian (lower) shale sample.

Figure 6.10 K_{gas} vs. $1/P_{mean}$ (Klinkenberg-plot) for sample 25, 29, 43 and 58. The intercepts between the linear regressions and the y-axis are the Klinkenberg corrected permeability coefficients k_{∞} . For sample 58 it was not possible to calculate k_{∞} , because at lower P_{mean} could not detect a pressure decline/incline at the upstream/downstream reservoirs.

Figure 6.11 Stress (δ)-strain curves (ϵ) of selected samples. A-Lower Silurian shale, and B-Cambrian shale.

Figure 6.12 Uniaxial compression strength (UCS) and Young's modulus (E) and their correlations with mineral content and porosity.

Figure 6.13 Confining pressure (S_3) vs. maximum stress (S_1) of triaxial compression test with multiple failure. A-UYP outcrops, B-AU Cambrian cores.

Figure 6.14 Mineral influences on the triaxial compression strength (TCS, A-C) and the internal friction coefficient (μ , D).

Figure 6.15 Correlations between Young's modulus and compression strength (A), Young's modulus and P-wave velocity perpendicular to bedding (V_p) (B), tensile strength and uniaxial compressive strength (C), and tensile strength and Young's modulus (D). E12 and CS12 mean Young's modulus and compression strength measured at 12 MPa confinements.

Figure 6.16 Tensile strength (St) and model I fracture toughness (K_{IC}), and their correlations with minerals.

Figure 6.17 Thickness and sedimentary environments of the Lower Cambrian shale (A and B) and the Lower Silurian shale (C and D), modified after (Editorial Committee of the Sichuan Oil & Gas field, 1989).

Figure 6.18 Depositional models of the lower Cambrian shale (upper) and the lower Silurian shale (lower), profiles and sampled places are denoted in Figure 6.17.

Figure 6.19 Measured rock mechanical parameters vs. minerals. In contrast to Figure 13 and 15, no correlations can be observed in these plots because a different mineral grouping method, e.g., clay, mica, and organic matter represent weak constituents; quartz, feldspar, and pyrite represent strong constituents; and carbonates are in between the weak and strong constituents.

List of Tables

Table 2.1 Analyzed samples and applied methods.

Table 3.1 Sample information, TOC and Rock-Eval data.

Table 3.2 T_{vap}-GC products in ug/g TOC.

Table 3.3 Open py-GC products in ug /g TOC.

Table 3.4 Properties of artificially matured samples.

Table 3.5 Open-GC products of the original samples and artificially matured residues.

Table 3.6 Mass balance calculations using the different approaches.

Table 4.1 Bulk kinetics parameters of total hydrocarbon potential (%), frequency factor $A=8.429E+14$ (1/s).

Table 5.1 Samples measured for the methane sorption isotherms.

Table 5.2 Maxima in excess sorption isotherms (46°C) and Langmuir fitting parameters by the fit of three parameters.

Table 5.3 T_{vap}-GC and XRD results of selected samples.

Table 5.4 Pore structural properties of the selected samples, as determined by mercury injection porosimetry and helium pycnometry.

Table 5.5 Properties and experimental conditions of the compared samples in Figure 5.12.

Table 6.1 Investigated samples and applied measurements.

Table 6.2 Results of TOC (wt %) and XRD mineralogy (wt %).

Table 6.3 Lithofacies statistics.

List of Abbreviations

1D	One-dimensional
A	Frequency factor
AU	Australia
BD	Brazilian disk
B ₀	Formation volume factor
cm	Centimeter
DC	Dead carbon
E	Young's modulus
E _a	Activation energy
EOS	Equation of state
FE-SEM	Field emission-scanning electron microscope
FIB	Focused ion beam
FID	Flame Ionization Detector
GC	Gas chromatography
GIP	Gas-in-place
GOR	Gas to oil ratio
GP	Gas (helium) permeability
HC	Hydrocarbon
Hg	Mercury
He	Helium
HI	Hydrogen index
HI ₀	Original hydrogen index
HP	Helium pycnometry
k _{gas}	Apparent gas permeability coefficient
K _{IC}	Mode I fracture toughness
k _∞	Klinkenberg-corrected gas permeability coefficient
LM	Light microscope
Ma	Million years
MCM	Million cubic meters
m _{excess}	Amount of adsorbed gas
min.	Minute

MIP	Mercury intrusion porosimetry
mm	Millimeter
MSSV	Micro-scale-sealed-vessel
n_{excess}	Maximum excess sorption
n_L	Langmuir sorption capacity
nm	Nanometer
OI	Oxygen index
Open py	Open-system pyrolysis
P	Pressure
P_b	Bubble point pressure
$P_{\text{conf.}}$	Confining pressure
PEE/ExEf	Petroleum expulsion efficiency
P_{excess}	The pressures at which the excess sorption maxima occur
PGI	Petroleum generation index
PI	Production index
PIo	Original production index
P_L	Langmuir pressure
P_{mean}	Mean pressure
P_r	Reservoir pressure
P_{sat}	Saturation pressure
Py	Pyrolysis
S1	Amount of volatized hydrocarbons at Rock Eval
S1EX	Amount of expelled petroleum
S2	Amount of generated hydrocarbons during pyrolysis at Rock Eval
S1o+S2o	Original petroleum potential
SEM	Scanning electron microscopy
SRA	Source rock analyzer
Tcf	Trillion cubic feet
TCM	Trillion cubic meters
TCT	Triaxial compressive test
TCT-MF	Triaxial compression test with multiple failures
TCS	Triaxial compressive strength
TEM	Transmission electron microscopy
Tmax	Temperature of maximum pyrolysis yield

TOC	Total organic carbon
TOCo	Total original organic carbon
TR	Transformation ratio
TS	Tensile strength
Tvap	Thermovaporisation gas chromatography
Ro	Vitrinite reflectance - oil emulsion
UCS	Uniaxial compressive strength
UCT	Uniaxial compressive test
UYP	Upper Yangtze Platform in south China
Vp	P-wave velocity
UV	Ultrasonic velocity
V _{void}	Void volume
wt. %	Weight-%
XRD	X-ray powder diffraction
ρ_{ads}	Density of adsorbed gas phase
ρ_{gas}	Gas density
ρ_{sample}	Density of rock samples
μm	Micrometer
μ	Coefficient of internal friction
ΔP	Pressure difference between the upstream and downstream reservoirs

Chapter 1 Introduction

1.1. Overview

1.1.1. Global Shale Gas Resource

Organic rich shale is widely distributed in many places worldwide and traditionally regarded as an important source rock of conventional petroleum reservoirs. In recent years, however, natural gas production from organic rich shale formations has become one of the most rapidly expanding trends in global onshore petroleum exploration and development. The latest estimate of technically recoverable shale gas resource in 42 evaluated countries is 7795 trillion cubic feet (TCF), whereas more than 60% of the assessed shale gas resource is in the Asian-Pacific region, e.g., China and Australia, and in the Americas, e.g., the United States, Canada, Mexico, and Argentina (EIA, 2011a; EIA, 2013b) (Figure 1.1). To put this shale gas resource estimate in context, the total global amount of technically recoverable natural gas resources can be increased by approximately 47% (EIA, 2013b). Although such estimates could change over time as more information becomes available, this increase in shale gas resources has been considered significant. Exploration activities have been underway in many countries. Nevertheless, currently, the United States and Canada are the only major producers of commercially viable natural gas from black shale formations in the world.

In the United States, fine-grained and organic rich shale plays are widespread in many regions of the Lower 48 states, particularly in the northeast and southwest-Gulf Coast regions (Figure 1.1). This country is the largest holder of the recoverable shale gas resources, totalling 1161 TCF. Shale gas production has grown dramatically over the past few years, accounting for 10-39% of annual natural gas production during the period 2008-2012. This proportion has been expected to reach 50% by 2040 (EIA, 2013a). Currently, shale gas is primarily produced from the Barnett, Marcellus, Haynesville, and Fayetteville Shales and the Eagle Ford Group. The Mississippian Barnett Shale has been one of the successful shale gas plays for more than a decade, and key technologies, e.g., hydraulic fracturing and horizontal drilling, were successively developed to promote gas production from shale intervals (Martineau, 2007). These technical breakthroughs were then rapidly applied to produce natural gas from other shale formations. The largest shale gas play in the United States is the Devonian

Chapter 1 Introduction

Marcellus Shale, which accounts for over 50% of total technically recoverable shale gas in that country (EIA, 2011a). Commercial shale gas production from the Marcellus Shale play began in 2004, and shale gas production from this unit has increased remarkably since 2011(Carter et al., 2011).

In Canada, a series of thick, organic rich shales have been found in British Columbia and Alberta (Figure 1.1). Canada has 573 TCF of shale gas that is technically recoverable, and it is the fifth country in global rank in this regard. A dramatic increase in shale gas production in this country began in 2011, and 15% of annual natural gas production consisted of shale gas by 2012. Shale gas is primarily produced from the Muskwa-Otter Park Shale, which is widespread below the Horn River Basin, northern British Columbia, and in the Montney Basin in British Columbia and Alberta. Significant exploration activities are underway in other shale formations. In addition, the shale gas reserves of Canada might be much higher than the reported value because many shale formations have not been considered due to either limited information, e.g., the Frederick Brook Shale in New Brunswick, or are primarily categorised as tight sand and siltstone reservoirs, e.g., the Montney and Doig resource plays in western Canada (EIA, 2013b).

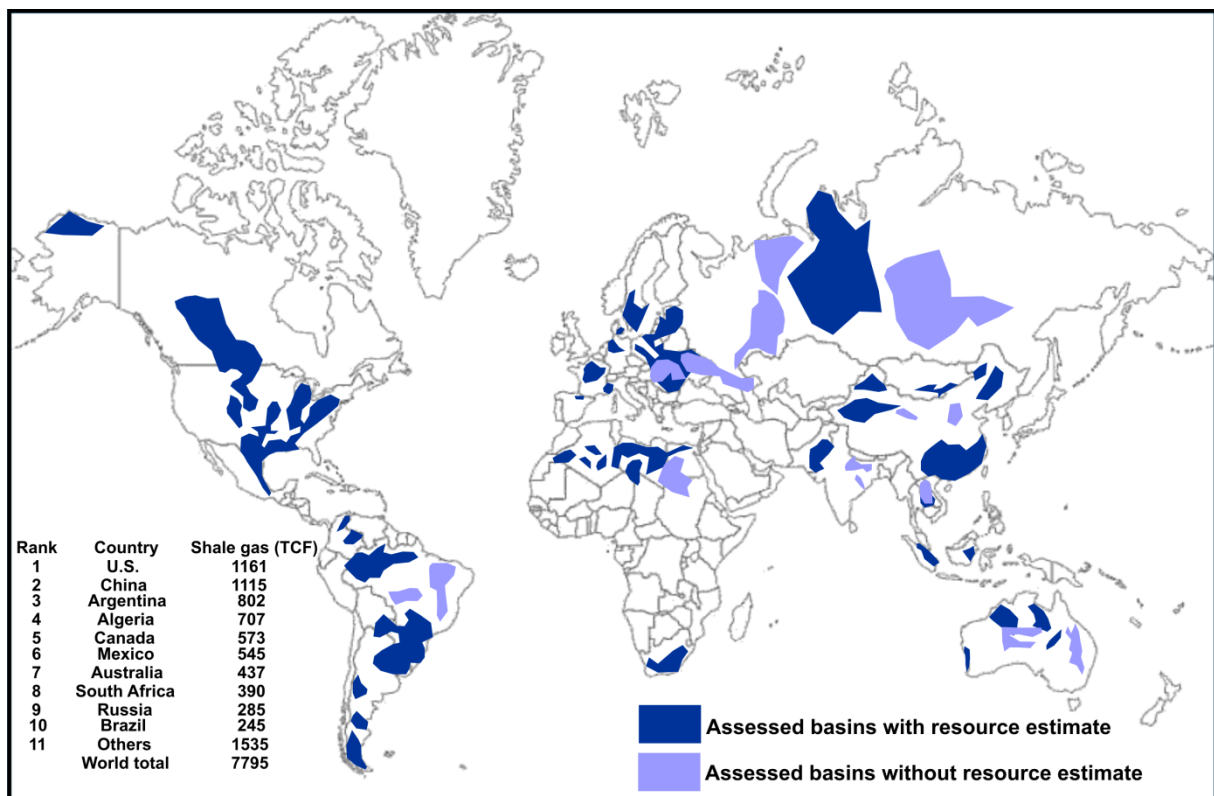


Figure 1.1 Global distribution of shale resources (EIA, 2013b).

1.1.2. Chinese Shale Gas Resource

In China, organic rich shales deposited in marine, transitional (marine to lacustrine) and lacustrine environments are present in many regions (Figure 1.2 A-C). The marine organic rich shales were deposited during the Neo-proterozoic to Early Palaeozoic, are generally thick, and are widespread below the Yangtze, north China, and Tarim Platforms. The transitional shales primarily formed during the Carboniferous and Permian. Many Carboniferous and Permian coal measure with interbedded black shale formations can be found throughout the Junggar, Tarim, Ordos, and Sichuan Basins. The lacustrine shales were deposited during the Mesozoic and Cenozoic. Thick Triassic and Jurassic organic rich shales are present in the Sichuan, Ordos, Junggar, Tuha, and Tarim Basins, whereas Cretaceous and Cenozoic shales extend below the Songliao, Bahai Bay, and Qaidam Basins (Zou et al., 2010). Unlike black shale in the United States, where most formations are at depths of less than 3000 m, with the exception of the Haynesville Shale (Curtis, 2002; Hammes et al., 2011), many black shale formations in China have been impacted by multiple tectonic movements during geological history, and thus, their depths can exceed 5000 m in certain depressions. As a result, successful development models from the United States cannot be simply applied to the development of shale gas in China, and the complex geological conditions (Figure 1.2 D) there must be taken into account when creating an effective developing strategy.

China has been ranked as the second largest holder of shale gas resources among the 42 countries assessed for technically recoverable shale gas resource in the study released by EIA, possessing recoverable reserves of 1115 TCF (2013b). The Chinese government, specifically the Research Centre of Oil and Gas Resources (RCOGR) of the Ministry of Land and Resources, estimated a domestic technically recoverable shale gas resource of 25 trillion cubic metres (TCM) (885.7 TCF) (National Energy Administration, 2011), a lower figure than that of the EIA (2013b). Figure 1.3 illustrates the distribution of shale gas in China, and roughly four shale gas zones were delineated in RCOGR's research. The recoverable shale gas reserves in the Middle-Lower Yangtze Platform and northwest zones are less than 5 TCM, accounting for less than 20% of the total, whereas nearly 16.6 TCM and 66% of total reserves are in the north-northeast and Upper Yangtze Platform-southwest regions.

The promising shale gas potential and development success in the United States have put shale gas in the spotlight in China. Clear targets have been set for shale gas development, and the government aims to complete an investigation of shale gas reserves and their national distribution by 2015. According to the Shale Gas Development Plan issued by the National Development and Reform Commission (National Energy Administration, 2011), China

Chapter 1 Introduction

expects to develop 6.5 billion cubic metres of shale gas by 2015. Significant geological survey and exploration activities are already underway across China, particularly in the Yangtze Platform, south China, and in the Ordos Basin, north China. Currently, China is the only nation outside of North America that has commercially produced shale gas. This shale gas production reached 25 and 200 million cubic metres (MCM) in 2012 and 2013, respectively.

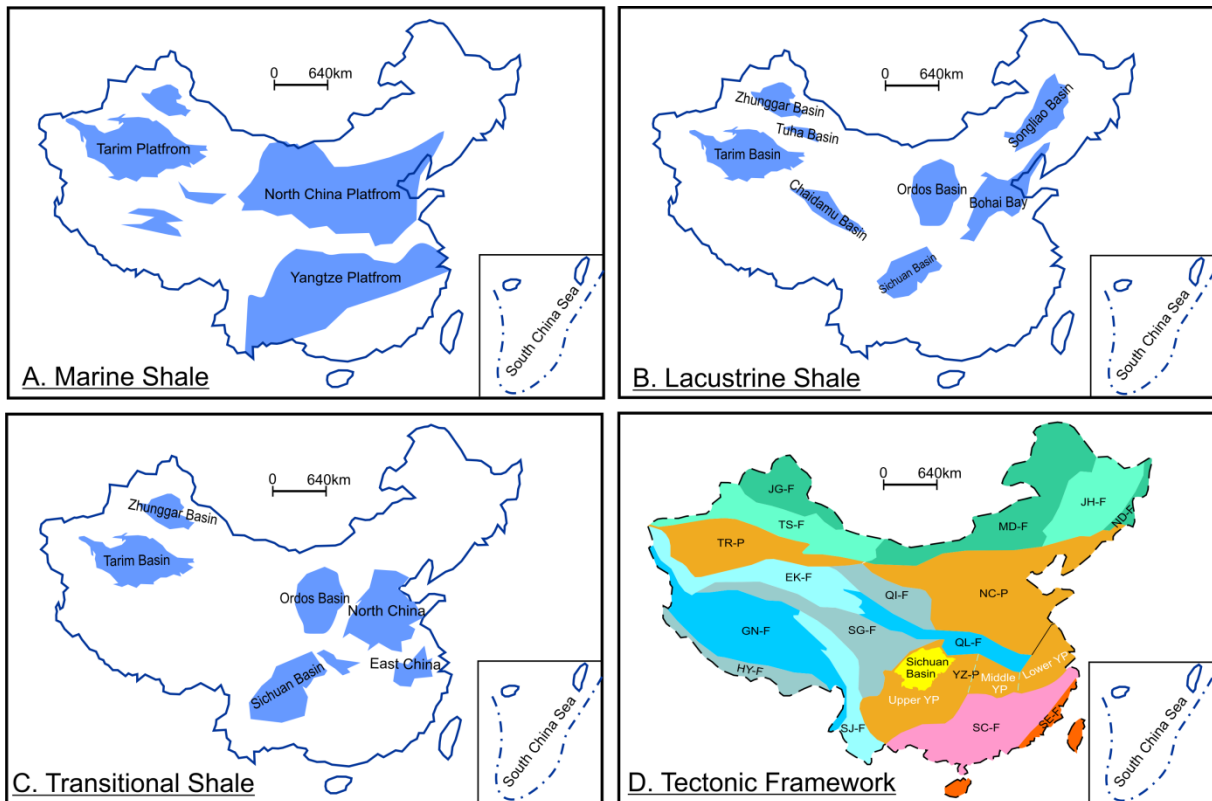


Figure 1.2 Distribution map of black shale (A-C), modified after (Zhang et al., 2009; Zou et al., 2010), and tectonic framework of China and locations of the Upper Yangtze Platform and the Sichuan Basin (D), modified after (Zhang et al., 2011). TR-P: Tarim Platform, YZ-P: Yangtze Platform, NC-P: North China Platform, JG-F: Junggar fold system, TS-F: Tianshan fold system, EK-F: East Kunlun fold system, QI-F: Qilian fold system, SG-F: Songpan-Ganzi fold system, GN-F: Gangdise-Nyainqentanglha fold system, SJ-F: Sanjiang fold system, HY-F: Himalayan fold system, MD-F: Mongolia-Daxinganlin fold system, JH-F: Ji-He fold system, ND-F: Nandanhada fold system, QL-F: Qinling fold system, SC-F: south China fold system, SE-F: Southeast China fold system, Upper YP: Upper Yangtze Platform, Middle YP: Middle Yangtze Platform, and Lower YP: Lower Yangtze Platform.

1.1.3. Black Shales in the Upper Yangtze Platform

The Upper Yangtze Platform (UYP) and southwest regions of China, corresponding to the Sichuan, Yunnan, Guizhou, and Chongqing areas, has nearly 10 TCM of technically

Chapter 1 Introduction

recoverable shale gas resources, which equates to 40% of the total national reserves (Figure 1.3). This region is the most favourable location for shale gas development, and it is the first place in China where commercial viable shale gas was produced. By 2013, most of the produced shale gas was from the Sichuan Basin and the Chongqing-GuiZhou area in the UYP. In addition, shale gas test wells were drilled in adjacent regions, for example, western Hunan and Hubei provinces.

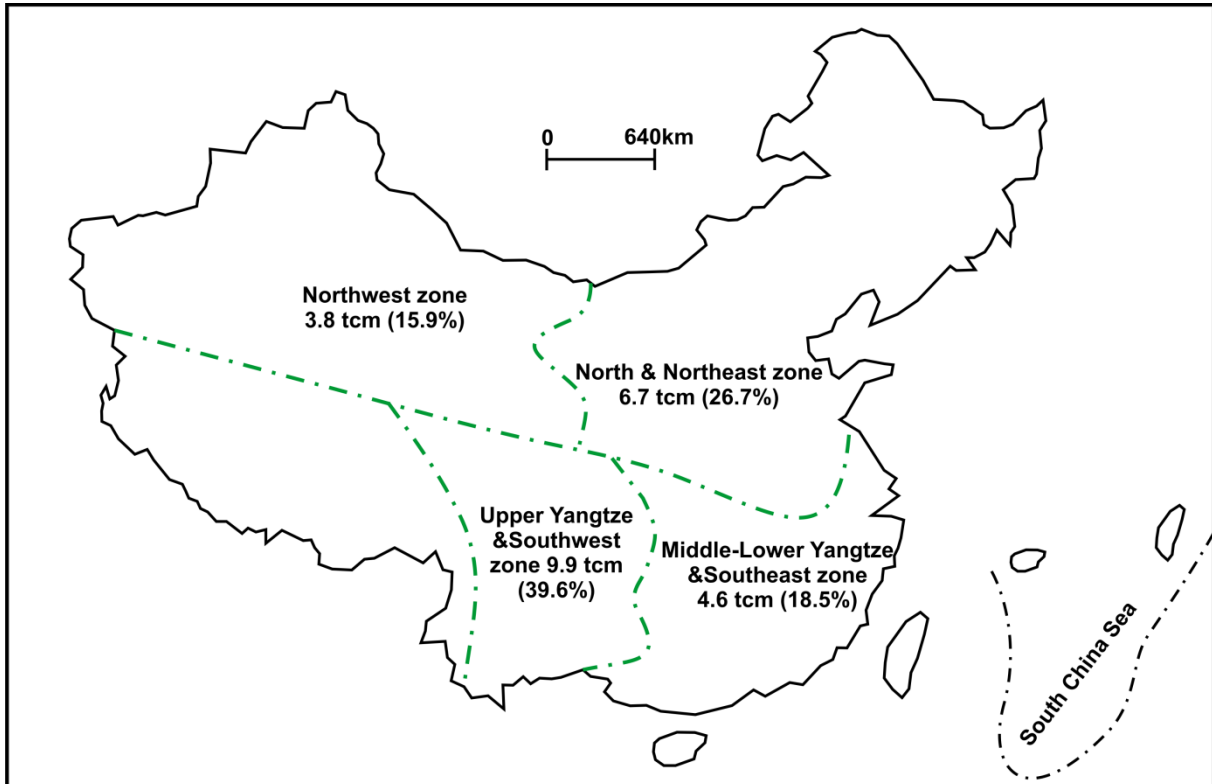


Figure 1.3 Distribution of shale gas resources in China (Zhang et al., 2012a).

Shale in the UYP is of three types, i.e., marine, transitional (marine to lacustrine), and lacustrine shales, and nearly ten black shale intervals can be identified (Editorial Committee of the Sichuan Oil & Gas field, 1989; Zou et al., 2010) (Figure 1.4). They are the principal source rocks of conventional petroleum reservoirs in the UYP, and recently they have been regarded as favourable shale gas plays. The marine black shale intervals deposited during the Precambrian to Carboniferous primarily consist of the Ediacaran (Upper Sinian) Doushantuo Formation, Lower Cambrian Qiongzusi/Niutitang Formation, Ordovician Dachengsi Formation, Lower Silurian Longmaxi Formation, Devonian Luofu Formation, and Carboniferous Dewu-Datang Formation. At present, the shale gas in the UYP has been primarily produced from the Lower Silurian and Lower Cambrian black shale intervals. These

Chapter 1 Introduction

two intervals were deposited in anoxic marine shelf environments and are characterised by a high total organic content (TOC) and vitrinite reflectance ($R_o > 2.0\%$). They are thick and laterally extensive in the southeast Sichuan Basin, Chongqing area, north Guizhou, and west Hunan province. Their distribution has been significantly affected by prolonged tectonic movements. As a result, these rocks crop out in many places in Chongqing, Guizhou, and western Hunan, while their burial depth can exceed 5000 m in certain depressions.

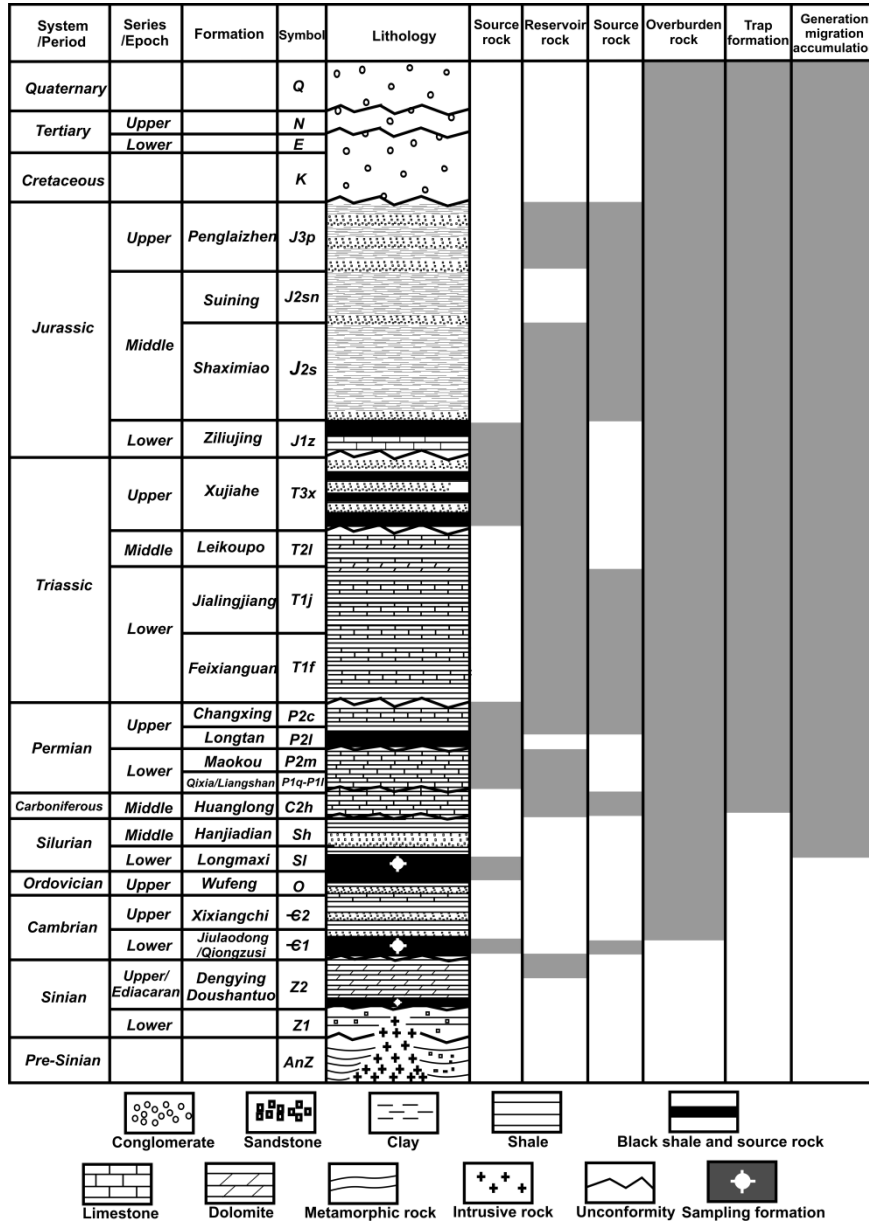


Figure 1.4 Generalised stratigraphic column in the Sichuan Basin, UYP, modified after (Editorial Committee of the Sichuan Oil & Gas field, 1989; Zou et al., 2010).

Transitional shale formations in the UYP primarily consist of the Upper Permian and Upper Triassic formations. The Upper Permian Longtan black shale formation in the Sichuan

Basin is between 10 and 125 m thick and is characterised by thickening in the southern regions and thinning in the northern and boundary regions. In northern Yunnan and Guizhou provinces, this interval is generally between 20 and 60 m thick. In contrast, the Upper Triassic Xujiahe black shale interval is thick in the central and western Sichuan Basin and northern Yunnan province and relatively thin in other regions. Both the Upper Permian and Upper Triassic black shale intervals interbedded with thick coal measures are the primary regional source rocks. Compared to the Lower Palaeozoic black shales, these two formations are dominated by type II and III organic matter, and relatively low maturity, with values of R_o commonly less than 2.0%.

Typical lacustrine shales consisting of several intervals are part of the Lower Jurassic series. In most parts of the UYP, the thickness exceeds 100 m, with thickening toward north-eastern Sichuan and Chongqing. These shales were deposited in deep to semi-deep lacustrine environments with high amounts of typical type III kerogen. The thermal maturity varies significantly, e.g., less than 1% where the rock is shallow and exceeding 1.5% at substantial depths in certain depressions. In contrast to the marine and transitional formations that produce only gas, most oil production of the UYP is from the lacustrine formations. However, the highly mature Lower Jurassic black shale interval is currently the exploration target for shale gas.

1.2. Resource Evaluation and Reservoir Characterisation

Shales are generally characterised by a tight matrix, which causes them to be relatively impermeable with respect to gas flow unless natural or artificial fractures occur (EIA, 2011a). Shale gas systems are unique in that organic rich shales are both the source of and the reservoir for natural gas. Thermogenic or biogenic natural gas may thus be stored in organic rich shale in a free, adsorbed, or dissolved state. In contrast to conventional petroleum systems, shale gas systems thus possess unique trapping and storing mechanisms (Martini et al., 1998; Curtis, 2002). As a result, specific evaluation, exploration, and development techniques are required for successful shale gas exploitation. No two shale gas systems are exactly alike, and thus, strategies differ from one system to the next. Nevertheless, prolific shale plays are normally recognised using certain minimal technical thresholds that need to be met. These thresholds include but are not limited to aspects of the geological architecture,

sedimentary framework, geochemical properties, mineralogical composition, petrophysical character, rock mechanical behaviour, and amount of gas-in-place (Curtis, 2002; Bowker, 2007; Jarvie et al., 2007; Strapoć et al., 2010; Miceli Romero and Philp, 2012).

1.2.1. Shale Gas Geology

Case studies of successful shale gas plays in the United States clearly indicate that the geological characterisation of shale gas reservoirs basically consists of the investigation of the shale extent, burial depth, thickness, depositional environment, and sedimentary framework, similar to the evaluation of conventional petroleum reservoirs.

As illustrated in Figure 1.1, shale gas plays in North America are extensively distributed in the Lower 48 states of the United States and in western Canada. The Mississippian Barnett Shale, with an extent of 38100 km², underlies 38 counties of the Fort Worth Basin in north-central Texas. The Barnett Shale interval is thin but highly petroliferous along the Llano uplift and in the southern Fort Worth Basin, where the thickness is generally less than 15 m. This formation thickens progressively northward, reaching a thickness of more than 120 m in the Newark East field and more than 300 m near the Muenster arch in the northern Fort Worth Basin. The depth of the Barnett Shale is generally between 2000 and 2600 m (Montgomery et al., 2005; Pollastro et al., 2007). The Devonian Marcellus Shale, with an areal extent of 500000 km², underlies most of the Appalachian Basin (Wang and Carr, 2013). This formation can be subdivided into three sub-intervals based on the sequence stratigraphy of logging data. The total thickness is generally less than 100 m but increases from northwest to southeast. Consequently, the gross thickness of the Marcellus Shale in north-eastern Pennsylvania, south-eastern New York, and north-eastern West Virginia can be as much as 300 m (Lash and Engelder, 2011). The unit is present at shallow depths along the margins of the Appalachian Basin, although it may be as deep as 2000 m within the basin (Wang and Carr, 2013). The Haynesville Shale, however, lies much deeper than the Barnett Shale and Marcellus Shale, i.e., at depths ranging from 3000 to 4700 m, and is on average approximately 70-100 m thick. The Haynesville Shale, with an area exceeding 23000 km², underlies more than 16 counties in large parts of south-western Arkansas, northwest Louisiana, and east Texas (Hammes et al., 2011).

These successful shale gas plays were all deposited in marine environments, in relatively deep water with anoxic bottom-water conditions. Their lithofacies are predominantly siliceous mudstone or siliceous shale but vary significantly. The stratigraphy and lithology of

Chapter 1 Introduction

the Barnett Shale vary across the Fort Worth Basin, although three general lithofacies can be recognised on the basis of the mineralogy, fabric, biota, and texture. These lithofacies are laminated siliceous mudstone, laminated argillaceous lime mudstone, and skeletal argillaceous lime packstone. These sediments were deposited at water depths between 120 and 215 m in a foreland basin that had poor connection/circulation with the open ocean. During deposition, the bottom waters were euxinic, i.e., preserving of organic matter, thus creating an organic rich source rock containing abundant framboidal pyrite (Loucks and Ruppel, 2007). Lithologically, the Marcellus Shale is dominated by black shale but contains lighter coloured shales and interbedded limestone layers due to sea level variations during the Devonian Period. Wang and Carr (2013) identified seven lithofacies in the Marcellus Shale, i.e., organic siliceous shale, organic mixed shale, organic mudstone, grey siliceous shale, grey mixed shale, grey mudstone, and carbonate. The dark shale facies of the Marcellus play corresponds to flysch, a fine mud deposited in deep water, which covered the underlying limestone beds as the deepening sea cut off the supply of carbonates that formed the limestone (Werne et al., 2002). The Haynesville Shale consists of a variety of facies, including bioturbated calcareous mudstone, laminated calcareous mudstone, silty peloidal siliceous mudstone, and unlaminated siliceous organic rich mudstone. Framboidal to colloidal pyrites are present as concretion laminae and individual frambooids and replace calcite cement and mollusc shells. This organic- and carbonate-rich mudrock was deposited in a deep, partly euxinic and anoxic basin during the Kimmeridgian to the early Tithonian as a result of a second-order transgression that caused worldwide deposition of organic rich black shales (Hammes et al., 2011).

In terms of these geologic features, the Ediacaran, Lower Cambrian, and Lower Silurian black shale intervals in the UYP are comparable to these energy-producing shale formations in North America. The gross thickness of these three formations is generally less than 10 m along the western and southern margins of the UYP, but it exceeds 100 m in most parts of the UYP (Liang et al., 2008; Zou et al., 2010). These formations may be at or near the surface, e.g., in or near outcrops along the margins of the Sichuan Basin and in the south-eastern UYP, or at depths exceeding 5000 m in certain depressions. These three organic rich shale formations were deposited during three major marine transgressions of the Neo-proterozoic and Early Palaeozoic. Deposition of the shales occurred in anoxic, deep-marine and marine shelf environments, and thus, their constituent organic matter was well preserved (Editorial Committee of the Sichuan Oil & Gas field, 1989; Liang et al., 2009a).

1.2.2. Organic Geochemistry

The shale is both the source of and reservoir for the target gas. Thus, geochemical evaluation of the shale gas plays includes the characterisation of the source rock and reservoir rock. This general evaluation includes assessment of the organic matter richness, kerogen type, thermal maturity, and gas geochemical properties.

Organic Matter Richness

Geochemical and geological studies of petroleum-bearing rocks over the past decades have clearly demonstrated that the bulk of the world's petroleum originated from the decomposition of organic matter deposited in sedimentary basins. Although a minor fraction of the hydrocarbons in the crust might be of inorganic origin, such quantities are negligible compared with those from organic sources (Hunt, 1995). Given this context, the amount of organic matter in a petroleum system determines how much hydrocarbon could be generated from a source rock, which ultimately affects the production potential of hydrocarbon reservoirs.

The organic matter content of a petroleum system is generally represented by the total organic carbon (TOC) content. The amounts of TOC in shale gas systems vary significantly among shale plays. For example, the TOC ranges from 0.3% to over 20% (wt.%) in the Antrim and New Albany Shale and is generally less than 5% in the Ohio and Lewis Shale (Curtis, 2002). The TOC content of the Barnett Shale varies with the lithology, being the highest in clay-rich intervals, and differs significantly between mature core samples in the northern Fort Worth Basin and immature outcrop samples in the southern Fort Worth Basin (Montgomery et al., 2005). The present-day average TOC from 290 high-thermal-maturity core samples from six wells in the Newark Field of the Barnett Shale is 4.5%, whereas immature outcrop samples taken from the southern margins of the basin in Lampasas County exhibit TOC values that range up to 11-13% (Montgomery et al., 2005; Jarvie et al., 2007).

The measured TOC content represents the organic carbon in the retained hydrocarbon, i.e., the organic carbon that was converted to hydrocarbon, and organic carbon that cannot yield any hydrocarbon (Jarvie et al., 2007). In overmature samples, however, the residual organic carbon may have been progressively enhanced during the maturation process due to aromatisation and condensation reactions involving aromatic structures and possibly cross-linked moieties, which have been observed in both natural and closed system simulations (Muscio and Horsfield, 1996). The reconstruction of the original TOC in mature or overmature source rocks is thus critical to the understanding of the extent of petroleum

Chapter 1 Introduction

generation and expulsion. Algebraic procedures in mass balance models for calculating the original TOC, original petroleum potential, petroleum generation index, and petroleum expulsion efficiency have been developed and described in detail (Pelet, 1985; Cooles et al., 1986; Santamaria and Horsfield, 2004; Peters et al., 2005). These mass balance calculations can be used to constrain the quantity and quality of organic matter in the source rock before maturation.

Kerogen Type

Dispersed organic material in sedimentary rocks can be separated into insoluble and soluble portions using organic solvents. The insoluble portion is referred to as kerogen, whereas the soluble portion is referred to as bitumen. Kerogen consists of very large molecules and is a type of polymer. When kerogen has been exposed to certain high temperatures for a sufficient time, these large molecules will crack into hydrocarbon molecules. The major components of kerogen are carbon, hydrogen, and oxygen, with nitrogen and sulphur in lesser amounts. Three kerogen types can be identified, based on their composition and evolution path in a Krevelen diagram (H/C vs. O/C) (van Krevelen, 1961). The general properties of these three kerogen types have been summarised by Tissot and Welte (1984), and all of these kerogen types play different roles in the formation of hydrocarbon.

Type I kerogen is characterised by a high initial H/C atomic ratio, ≥ 1.5 , and a low O/C atomic ratio, <0.1 . This type of kerogen is composed mostly of lipid material, particularly material abundant in aliphatic chains. The numbers of polyaromatic nuclei and heteroatomic bonds are low, and oxygen is present mostly in the ester bonds. When pyrolysed, volatile and extractable compounds are produced. The high proportion of lipids may result either from a selective accumulation of algal material or from a severe biodegradation of the organic matter during deposition. Type II kerogen has a relatively high initial H/C atomic ratio (1-1.5) and a low atomic O/C ratio. Polyaromatic molecule cores, heteroatomic groups of ketones, and carboxylic acids are of greater importance than in type I kerogen. The bitumen associated with this kerogen includes many cyclic structures, and its sulphur content is higher than in the other component parts. Type II kerogen is usually associated with marine sediments deposited in a reducing environment. Type III kerogen has a relatively low H/C atomic ratio, <1 , and a high O/C atomic ratio (0.2–0.3). This type of kerogen contains substantial polyaromatic cores, heteroatomic ketone, and carboxylic groups but contains no ester groups. Type III kerogen is derived from continental plants and contains much identifiable vegetal debris.

Chapter 1 Introduction

In exploration for shale gas, the current targets are heavily dominated by type II kerogen, for example the aforementioned Barnett, Marcellus, and Haynesville shale plays in the United States and shale gas formations in the Western Canadian Basin. Nevertheless, the thick, widespread, gas-saturated, fine-grained, organic rich units containing other types of kerogen, which were subjected to extensive biogenic decomposition in the thermally immature stage or significant thermal degradation in the thermally mature and overmature stages, can also serve as potential exploration targets (Martini et al., 2003; Hamblin, 2006). In China, the targeted Ediacaran and Lower Palaeozoic shale formations in the Yangtze Platform have been thought to be dominated by type I original kerogen, although more detailed investigation is necessary. In addition, terrigenous source rocks in the Sichuan Basin (He and Zhu, 2012; Zheng et al., 2013) and Ordos Basin (Wang et al., 2011; Jian et al., 2013) have been regarded as favourable exploration targets for shale gas.

Thermal Maturity

The organic theory of petroleum generation is based on the formation of hydrocarbons by the heating of biological organic matter. As sedimentation and subsidence continue, the temperature and pressure increase. As a result, the lipids, proteins, and carbohydrates in biological material are converted into the kerogen of sedimentary rocks. When the kerogen is buried deeper at higher temperatures, it cracks to form bitumen, which breaks down further to form petroleum. Certain hydrocarbons also form directly from kerogen. If the petroleum is buried deeper at higher temperatures, it is converted along two pathways, one leading to increasingly small hydrogen-rich molecules and the other leading to larger, hydrogen-deficient molecules. The end products are methane and graphite (Tissot and Welte, 1984; Hunt, 1995).

Inasmuch as vitrinite alterations are irreversible and its reflectance is preserved after a subsequent temperature drop, the vitrinite reflectance (R_o) is considered the parameter most suitable for determining the thermal maturity. As the thermal maturity increases during burial of sediments, three evolutionary stages i.e., diagenesis, catagenesis, and metagenesis, can be identified on the basis of the progressive evolution of organic matter (Tissot and Welte, 1984). Diagenesis corresponds to the stage associated with a R_o of less than 0.5%, and thus, the kerogen is immature. During diagenesis, sediments tend to approach equilibrium under shallow burial conditions and become consolidated. Microbial activity is one of the primary agents of transformation. Chemical rearrangements, i.e., polycondensation and insolubilisation, occur at shallow depths. At the end of diagenesis, the organic matter consists

Chapter 1 Introduction

primarily of kerogen. In this stage, only a minor amount of hydrocarbon might be generated from organic matter, whereas large quantities of carbon dioxide, water, and a few heavy heteroatomic compounds may be produced. Catagenesis refers to the evolutionary stage associated with a R_o between 0.5% and 2.0%, which results from a considerable increase in temperature during burial in sedimentary basins. During this stage, a significant amount of hydrocarbon is generated from the organic matter. Through this progressive evolution, the kerogen first produces liquid petroleum and then wet gas and condensate. Both liquid oil and condensate are accompanied by remarkable amounts of methane. Metagenesis is the evolutionary stage of organic matter corresponding to a R_o between 2% and 4%, which begins earlier than metamorphism of the mineral phases. At this stage, the organic matter is composed only of methane and carbon residue, and a minor amount of crystalline reordering begins to develop. Thus, metagenesis in its entirety occurs within the dry gas zone.

In unconventional shale plays, the level of thermal maturity is fundamental in reservoir characterisation and guiding exploration strategies. Generally, a thermogenic gas play is expected to be most productive in the deeper sections of a basin where the organic material is mature or overmature. However, in an unconventional shale play, wherein the gas is mostly microbial, the margins of the basin where the organic matter is less mature or immature and hydrologic flow systems are active are the target of exploration (Martini et al., 2003; Martini et al., 2008). Hence, natural gas may be produced from shale plays with a wide range of maturity. The Barnett Shale has been buried to a sufficient depth and has thus reached stages of oil or gas generation in most parts of the Fort Worth Basin. In areas where the Barnett Shale reaches a R_o higher than 1.1%, there are large amount of commercial gas resources, and the unit is highly productive. Areas where the Barnett Shale has values of R_o lower than 1% are generally characterised by lower gas flow rates and are less productive than areas of high thermal maturity (Montgomery et al., 2005; Jarvie et al., 2007). In the Antrim shale of the Michigan Basin, commercial shale gas is predominantly microbial, and the productive wells are located near the basin margins where the shale has a relatively low thermal maturity and fresh water infiltrates the permeable fracture network, whereas both microbial and thermogenic gases are produced from various thermally mature parts of the New Albany Shale in the Illinois Basin (Martini et al., 2003; Martini et al., 2008).

Gas Geochemical Properties

Analysis of the geochemical properties of natural gas relies on the characterisation of its molecular and isotopic composition, which is critical to predicting the gas origin, source rock

Chapter 1 Introduction

maturity, and exploration potential. Natural gases are a naturally occurring mixture of hydrocarbon and non-hydrocarbon gases. The most common chemical compounds of natural gas in a reservoir are light paraffinic hydrocarbons, such as methane, ethane, propane, butane, and pentane. Commercially valuable petroleum gas is predominantly composed of methane with decreasing quantities of ethane, propane, and other heavier hydrocarbon components. The ratio of the amount of methane to the total amount of other gas hydrocarbons can be used to determine the gas's origin and conditions of formation. Dry gas, i.e., methane with a very low content of higher hydrocarbons ($C_1/\sum C_n > 0.97$), may be generated either during diagenesis as a result of microbial activity at low temperatures or during metagenesis as a result of thermal degradation of overmature kerogen or the secondary cracking of heavy oil hydrocarbons at high temperatures ($>150^\circ\text{C}$). In contrast, wet gas ($C_1/\sum C_n < 0.98$) is generally formed during the catagenesis stage (Tissot and Welte, 1984).

The carbon isotope ratio ($\delta^{13}\text{C}$) in the C_1 - C_5 hydrocarbons may be used to evaluate the nature and thermal maturity of potential source rocks, the gas migration pathways, the presence of mixed-source gases, and even the reservoir accumulation and loss history (Tang et al., 2000). The $\delta^{13}\text{C}$ of biogenic methane ranges from -90‰ to -55‰, and that of catagenic methane ranges between -55‰ and -30‰, whereas that of metagenic methane is higher, i.e., between -40‰ and -20‰ (Stahl, 1974; Schoell, 1980; Rice and Claypool, 1981). The isotopic composition of light hydrocarbon gases is controlled kinetically because the ^{12}C - ^{13}C bond strength is more stable than the ^{12}C - ^{12}C bond. During the thermal degradation process, hydrocarbon gases that are generated thus show progressive depletion in ^{13}C from butane to propane, to ethane, and to methane. Likewise, thermal maturation results in the loss of ^{12}C -enriched methane and the concentration of ^{13}C in the residual kerogen (James, 1983; Schoell, 1983; Chung et al., 1988; Clayton, 1991).

Nevertheless, isotopically reversed gases, i.e., $\delta^{13}\text{C}$ methane $>$ $\delta^{13}\text{C}$ ethane $>$ $\delta^{13}\text{C}$ propane, may be present in a reservoir with mixed thermogenic gases. This mixture of gases may be the result of gases that formed at various stages of thermal maturity (Jenden et al., 1993; Seewald and Whelan, 2005), were generated from various types of kerogen (Dai et al., 2004), and formed with various cracking mechanisms (primary and secondary cracking) (Tilley et al., 2011). In addition, it has been proposed that isotopically reversed gases can also be created in closed organic rich shale systems as a result of an accumulation of gases generated at various stages during ongoing maturation of organic matter in a single source without migration (Tilley et al., 2011). Isotopically reversed gases have been found in natural gases from many mature shale plays, e.g., the Barnett, Haynesville, Faynesville, Woodford,

Marcellus, and Horn River shales, and have been associated with the most productive wells in these shale plays (Ferworn et al., 2008; Zumberge et al., 2009). Hence, an understanding of the isotopic reversals in thermal gases may be significant for the exploration and development of mature shale gas plays (Tilley et al., 2011).

1.2.3. Mineralogy

Organic shales are fine-grained sedimentary rocks with complex mineralogy. The mineral constituents are typically composed of intrabasinal and extrabasinal sources of siliciclastic and/or carbonate debris and most likely have been affected by diagenetic processes. There is generally a significant correlation between the mineralogy and well completion quality in most shale plays in the United States. Specifically, the minimum closure stress, Thomsen's gamma, and brittle mineral index appear to be controlled by the mineralogy. Moreover, the shale reservoir quality appears to be a function of both the compositional and textural components of the organic shales (Diaz et al., 2012; Diaz et al., 2013). Thus, the mineralogy affects both the reservoir quality and well completion quality, and detailed characterisation of the mineralogy is critical to the identification of exploration target zones. In addition, a mineralogy-based classification may yield a better understanding of the depositional conditions and correlations between reservoirs of various formations and basins (Schlumberger, 2012).

Although large amounts of gas hydrocarbons may be present in a shale system, the flow of gas is generally limited if reservoir compartments cannot be well connected via stimulation. Highly productive shale plays generally are those that exhibit favourable brittleness and good response to stimulation, which are intrinsically related to the mineralogy. Thus, the mineralogy is a crucial factor in gas production from the Barnett, Marcellus, and other shale systems requiring stimulation. The amounts of clay, quartz, and carbonate in the Barnett Shale are highly variable, which in turn results in variable degrees of brittleness in various intervals. In general, productive intervals in the Barnett Shale are characterised by relative high amounts of quartz and relative low amounts of clay, whereas the amounts of carbonate vary significantly (Jarvie et al., 2007; Loucks and Ruppel, 2007; Rickman et al., 2008). Specifically, high productive shale gas wells in North America generally have clay fractions less than 40% (wt.%) and quartz fractions exceeding 40% (Britt and Schoeffler, 2009). Core analysis based on X-ray diffraction (XRD) data and mineralogical data from pulsed neutron spectroscopy logging revealed that samples of the Marcellus Shale generally have quartz

fractions of 40-80% and clay fractions of 20-60%. The fractions of carbonates are variable, but intervals with a high TOC content are generally associated with carbonate fractions less than 20% (Wang and Carr, 2013). In contrast, the quartz fractions are between 30 and 60%, whereas the clay fractions are between 40 and 70% in the Haynesville Shale. The clay fractions in the Bossier shale are even higher than those in the Haynesville Shale (Passey et al., 2010; Hammes et al., 2011).

1.2.4. Petrophysics

When discussing shale gas, the term “shale” is generally used to refer to a geological gas reservoir rather than a homogeneous lithology. Shale gas reservoirs are actually composed of a variety of rock types that could include shale, mudstone, marlstone, sandstone, and carbonate. The fabric and texture of these shale gas reservoirs may be homogeneous on a very small scale but are generally heterogeneous, particularly in the vertical direction and on a reservoir scale. Despite the considerable effort expended on estimating the resource potential of shale gas plays, these complex heterogeneous reservoirs require innovative exploration and well completion strategies to produce natural gas economically. Two issues that are critical to successful shale gas exploration and development are (1) the location of the stored gas in the rock and (2) the pathways that the gas follows from the matrix to induced fractures that allow it to flow into the well bore (Loucks et al., 2009). Most of the challenges in shale gas production are related to the fact that the matrix porosity and permeability of shale are generally very low, and thus, reservoir stimulation and an artificial fracture system are commonly required.

Pore networks in the shale system are predominantly composed of pores of nanometre (nm) to micrometre (μm) size, and thus, pore throat connectivity is relatively ineffective. The matrix permeability is extremely low, in the micro-Darcy (μD) or nano-Darcy (nD) range. Interparticle and intraparticle pores may be present between or within mineral crystals and organic particles, respectively (Loucks et al., 2012). In certain overmature organic shales, as much as 50% of the volume of the original organic matter may consist of organic pores (Passey et al., 2010; Curtis et al., 2012). Thus, the pore volume within the organic matter may constitute a substantial fraction of the total porosity of certain shale gas systems (Loucks et al., 2009; Slatt and O'Brien, 2011; Chalmers et al., 2012; Milliken et al., 2013). During shale gas production, these nm- and μm -scale pores and natural fractures form a network of pathways that allows a flow of gas from the shale to the induced fractures. In general, interparticle

mineral pores are likely to be part of an effective pore network than are intraparticle mineral pores, as the former have a higher probability of being interconnected. Nevertheless, intraparticle pores within the organic matter are also likely to be part of an interconnected network because of the interconnectivity of organic matter particles (Loucks et al., 2012). Gas conductivity in shales is thus attributed to both the pore networks in the shale matrix and the fracture systems. If unsealed fractures are present, they may serve as the primary pathways of gas flow in the shale because the permeability of the pore networks is generally much lower than that of the fracture system. Nevertheless, even in the presence of fractures, the fluid transport in the matrix determines the long-term gas production in shale gas plays.

The determination of the porosity and permeability of shale rocks is challenging due to the very small particles and pores in the matrix. In clay-rich shale rocks, the measurement of porosity is even more complex, due to the high surface area of the clay minerals and the presence of water in very small matrix pores. In addition, the pores within the organic matter may exhibit entirely different wettability behaviour than that of the pores in the mineral matrix (Passey et al., 2010). The porosity and permeability measured in the core can be correlated with the log response. However, several studies have shown that the results obtained from different core analysis laboratories can vary significantly (Passey et al., 2010; Glorioso and Rattia, 2012). Due to the difficulty of measuring the low to extremely low permeability of shale rocks, there have been very few investigations of the fluid flow mechanisms in the matrices of organic rich shales. Consequently, the fluid flow mechanisms and processes within shale systems are still poorly understood (Amann-Hildenbrand et al., 2012; Ghanizadeh et al., 2013a; Ghanizadeh et al., 2013b).

1.2.5. Rock Mechanics

The economic recovery of gas from shale reservoirs requires optimal multistage hydraulic stimulation via horizontal wells. To optimise the effectiveness of hydraulic fracturing, the most favourable intervals in which to initiate fractures must be identified. The rock's mechanical properties and mineralogy composition are critical parameters in determining the zone with the best potential for effective fracturing (Buller et al., 2010). However, identifying effective intervals for productive shale is generally difficult because most logging techniques and interpretation methods have been developed in conventional formations and are calibrated for specific rock types, e.g., carbonates and sandstones. As mentioned earlier, the lithological facies of shale formations are very complex and vary

significantly on a reservoir scale, which tends to result in significant variations in the mechanical properties.

The Young's modulus and Poisson's ratio are important parameters in determining the brittle or ductile behaviour of shale samples. Prospective shale plays are generally characterised by a high Young's modulus and low Poisson's ratio. In contrast, shales with a low Young's modulus and high Poisson's ratio are generally too ductile to be prospective producers of gas (Rickman et al., 2008; Britt and Schoeffler, 2009). Based on this high dependence on rock mechanical properties and mineralogy, Britt and Schoeffler (2009) concluded that brittle shale intervals generally contain clay fractions less than 40% and quartz fractions greater than 40%. The primary static rock mechanical properties, e.g., compressive strength, elastic properties, and tensile strength, can be determined via uni- and triaxial compression tests and the Brazilian test on standardised core plugs in the laboratory (Bieniawski and Hawkes, 1978; Guo et al., 1993; Ulusay and Hudson, 2007). The dynamic mechanical properties, including the Young's Modulus and Poisson's ratio, can be estimated using cross dipole acoustics and density log inputs (Abousleiman et al., 2007; Grieser and Bray, 2007; Buller et al., 2010). The characterisation of magnitudes and orientations of the in-situ stress is also necessary to design effective hydraulic fracturing and horizontal well orientation strategies, which can be generally derived from examination of the borehole stress environment from image logs and interpretation of the acoustic anisotropy (Bratovich and Sommer, 2009). In addition, those studying shale gas reservoirs have suggested that the Poisson's ratio and Young's modulus are a function of the mineralogy and fabric (Slatt and Abousleiman, 2011; Sondergeld and Rai, 2011), which in turn are functions of the sedimentology, provenance, diagenesis, and tectonic regime (Bustin et al., 2009; Clarkson et al., 2011).

1.2.6. Gas Storage Mechanism

Natural gas in shale reservoirs is primarily composed of free and adsorbed gas, with a minor amount of dissolved gas (Schettler and Parmoly, 1990; Martini et al., 1998; Curtis, 2002). Free gas is stored in the pore space of the shale and behaves in the same way as does the gas in conventional reservoirs when the pressure decreases. Adsorbed gas is the accumulation of gas hydrocarbons on the surface of organic matter and minerals and is gradually released to the wellbore as the pressure decreases. Both types of gas will be produced over time but at different rates. Thus, it is desirable to distinguish between adsorbed

Chapter 1 Introduction

and free gas if possible. The proportion of sorbed methane in a shale reservoir may be considerable. In the Antrim, Ohio, New Albany, Barnett, and Lewis shale gas plays, the adsorbed gas accounts for 20-85% of the total gas (Curtis, 2002), whereas the adsorbed gas accounts for more than 50% of the total gas in the Devonian shale of the Appalachian Basin (Lu et al., 1995).

Because of the high sorption energy and large internal surface area of micropores, the methane sorption capacity in shale samples positively correlates with factors that have or could create more micropores, whereas this capacity negatively correlates with factors that could reduce or block the micropores. The organic matter properties, e.g., organic richness, thermal maturity, and organic type, significantly affect the methane sorption capacity of shale samples (Chalmers and Bustin, 2007b; Chalmers and Bustin, 2008; Ross and Bustin, 2009; Zhang et al., 2012b; Gasparik et al., 2013). A large number of micropores may be present within the organic matter, whereas many micropores may be created in the organic matter during the processes of organic matter degradation, hydrocarbon generation, and expulsion as the maturity increases (Gan et al., 1972; Prinz et al., 2004; Prinz and Littke, 2005; Ross and Bustin, 2009). Thus, the overmature and high-TOC samples generally display significantly higher sorption capacities than do the low-maturity and low-TOC samples (Chalmers and Bustin, 2008; Ross and Bustin, 2009; Gasparik et al., 2013). The clay content is another significant factor affecting the methane sorption capacity of shale due to clay's crystal layers and pore structures, which cause the clay minerals to provide more adsorption sites and larger surface areas than other minerals (Aringhieri, 2004; Cheng and Huang, 2004; Wang et al., 2004). Nevertheless, the sorption capacity of clay may be reduced significantly when water is present in the sample. Generally, the presence of water may result in swelling of clay mineral, take-up of sorption sites, and blockage of the pore system and thus negatively affect the methane sorption capacity (Krooss et al., 2002). Above a certain moisture concentration, however, the methane adsorption capacity does not decrease any further because all possible adsorption sites for water are occupied, and hence, the amount of water present in excess of the adsorbed water has no effect on the methane sorption (Joubert et al., 1974; Levy et al., 1997; Bustin and Clarkson, 1998).

1.3. Research Objectives

The Ediacaran (Upper Sinian), Lower Cambrian, and Lower Silurian shale formations deposited in marine environments are widespread in many regions on the UYP. They are

Chapter 1 Introduction

regional source rocks of conventional petroleum fields in south China, and have been recently regarded as prolific shale gas plays. The objectives of this thesis are to 1) evaluate the Gas-In-Place (GIP) and 2) assess the fraccability of these marine shale formations.

First of all, the geological evaluation, sedimentary history, and current geological distribution were investigated in detail, and then used as fundamental material for further research.

In order to evaluate the GIP, we investigated:

- 1) Organic matter richness, thermal maturity, and kerogen properties;
- 2) Original TOC content and hydrocarbon potential;
- 3) Retained hydrocarbon components in the sample and remained hydrocarbon generative potential of the organic matter within the sample;
- 4) Physical properties of hydrocarbon formed during maturation; and
- 5) Methane sorption capacity.

Focusing on the fraccability, we investigated:

- 1) Macro-, micro-, and nano-scale texture;
- 2) Mineralogical constituents and lithofacies;
- 3) Porosity and permeability, and
- 4) Static rock mechanical properties.

1.4. Structure of Dissertation

Chapter 2 describes the investigated samples and applied methods. There are 4 sets of sample investigated, including the Ediacaran, Lower Cambrian, and Lower Silurian shale samples from the UYP, south China, and Cambrian shale samples from the Georgina Basin, north Australia. The applied methods for GIP evaluation include the TOC measurement, Rock-Eval, pyrolysis gas chromatography, thermovaporisation gas chromatography, carbon isotope analysis, organic petrology, phase kinetics approach, and high pressure methane sorption. The methods for fraccability assessment comprise the light microscopy, scanning electron microscopy, focused ion beam-transmission electron microscopy, X-ray powder diffraction, mercury intrusion porosimetry, helium pycnometry, helium permeability, uniaxial compression test, triaxial compression test, Brazilian disk tensile test, and ultrasonic velocity.

Chapter 3 is geological and geochemical characterization. This part of the work was started by the investigation of geological setting, sedimentary environment, and geological

Chapter 1 Introduction

distribution of these shale formations in the UYP. The present organic geochemical properties were revealed in detail using the measured data and compiled data. Followed on, the origin and evolution of kerogen, and thus the evolution of hydrocarbon generation during maturation were investigated, using open py-GC results of both naturally and artificially matured samples. Finally, original organic abundance and hydrocarbon generative potential were reconstructed using the mass balance models developed by Cooles et al. (1986) and Claypool (in Peters et al., 2005).

Chapter 4 discusses the physical properties of the petroleum formed during maturation in the Lower Cambrian shale. In this part of the work, hydrocarbon generation kinetics and petroleum physical properties were investigated using the PhaseKinetics approach and a Cambrian shale sample from the Georgina Basin, North Territory Australia (NTA), as similar paleogeological and sedimentary environments in Cambrian are found for the UYP and NTA. The onset (transformation ratio TR=10%) and end (TR=90%) of bulk hydrocarbon generation was calculated for an assumed average geological heating rate of 1.5°C/Ma. Based on the thermal history of a local “model”-well, the geological conditions (burial depth, temperature, and time) of the onset, main stage, and end of bulk hydrocarbon generation were calculated. Assuming zero expulsion, the shale reservoir position within the sedimentary basin indicated that the bubble point pressure was always below the reservoir pressure, and fluids in the shale reservoir occurred only as a single, undersaturated phase throughout maturation history.

Chapter 5 reports on the methane sorption capacity of thermally overmature samples from the Lower Silurian and Lower Cambrian shale formations. Two immature shale samples from the Middle Cambrian formation in the Georgina Basin, north Australia were also tested to investigate the effect of thermal maturity on sorption isotherms. Excess sorption isotherms were performed over a pressure range of 0-25 MPa at 46°C. The effects of TOC content, thermal maturity, clay minerals, moisture content, pore properties, particle size, temperature, and pressure on methane sorption capacity were analysed. In addition, T_{vap}-GC was used to measure the residual gas that is stored in the samples under atmospheric pressure and temperature conditions.

Chapter 6 focuses on the mineralogical, lithofacial, petrophysical, and rock mechanical properties. Samples collected from 15 profiles/wells in the core area of the UYP were examined from the centimeter scale (cm, hand specimen and light microscopy) down to the nm scale (Transmission Electron Microscope). The results were correlated with the data of mineralogical composition, porosity and permeability and the elastic properties and mechanical strengths gained by a series of rock mechanical experiments. Additionally,

Chapter 1 Introduction

published data, including the XRD results of nearly 700 samples from more than 20 profiles/wells scattered on the UYP, were compiled with the purpose of characterizing mineralogical properties.

Chapter 7 is the summary of the obtained results and outlook of the future work.

Chapter 2 Samples and Methods

2.1. Samples

The analyzed samples comprise shales from the UYP, south China (UYP samples) and from the Georgina Basin, north Australia (AU samples) (Figure 2.1 and Table 2.1).

The UYP samples are marine black shales collected from the Lower Silurian, Lower Cambrian and Ediacaran formations. A total of 68 UYP samples from 15 profiles and wells were investigated. The sampling region is located in the central area of the UYP, where the succession of marine black shale is generally more than a hundred meters thick (Liang et al., 2008; Cheng et al., 2009; Wang et al., 2009b; Zou et al., 2011). The Ediacaran outcrop samples were provided by the Technical University of Berlin, while core samples were provided by the China University of Geosciences.

The AU samples are marine black shales recovered from the Cambrian Arthur Creek Formation, which hosts one of the major regional source rocks for conventional petroleum (Ambrose et al., 2001; Ambrose and Putnam, 2007; Boreham and Ambrose, 2007), and has been regarded as a major unconventional petroleum target (Bennett et al., 2010; Boreham et al., 2013) in the southern Georgina Basin, north Australia (Figure 2.1). All AU samples are cores, provided by Geoscience Australia.

2.1.1. UYP - Lower Silurian Shale

A total of 23 Lower Silurian shale samples from 4 profiles in the Chongqing area and Hunan province and 1 well in the Chongqing area were investigated. Core samples were taken from a depth between 136 and 321m (Figure 2.1 and Table 2.1). All Lower Silurian samples were conducted TOC and Rock-Eval Pyrolysis, and most samples were measured XRD, light microscope, and scanning electron microscope (SEM). Samples from the Lujiao profile and YY1 well were performed open system pyrolysis gas chromatography (open py-GC), thermovaporisation gas chromatography (Tvap-GC), as well as petrophysical and rock mechanical measurements. In addition, high-pressure methane (up to 25 MPa) was measured on 3 samples from the Lower Silurian shale interval.

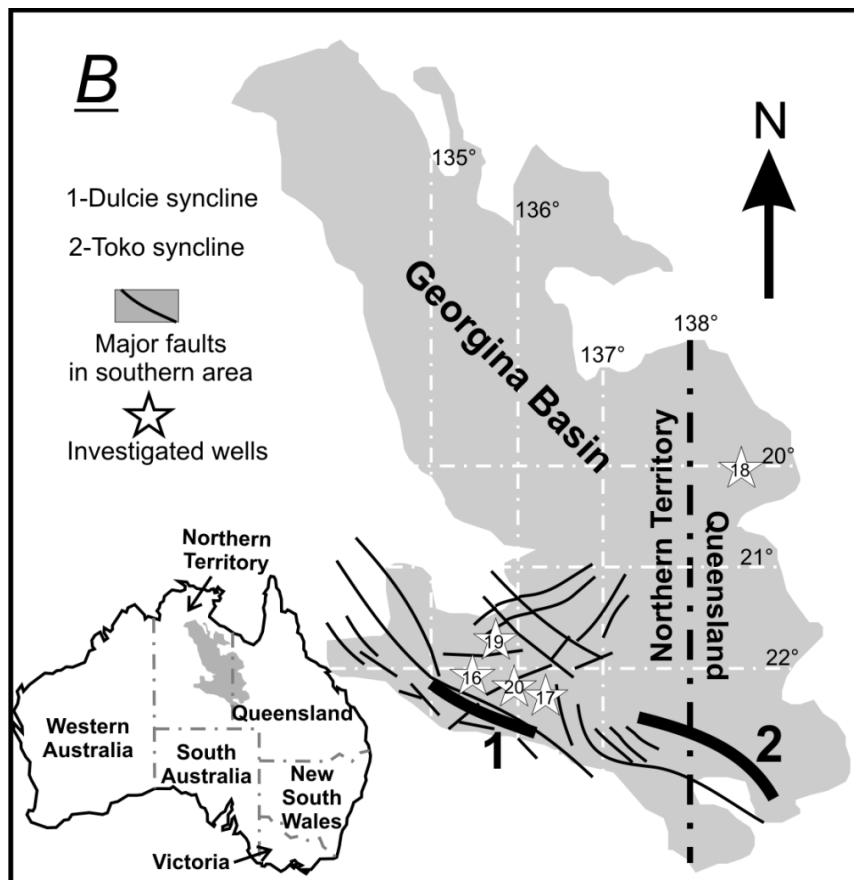
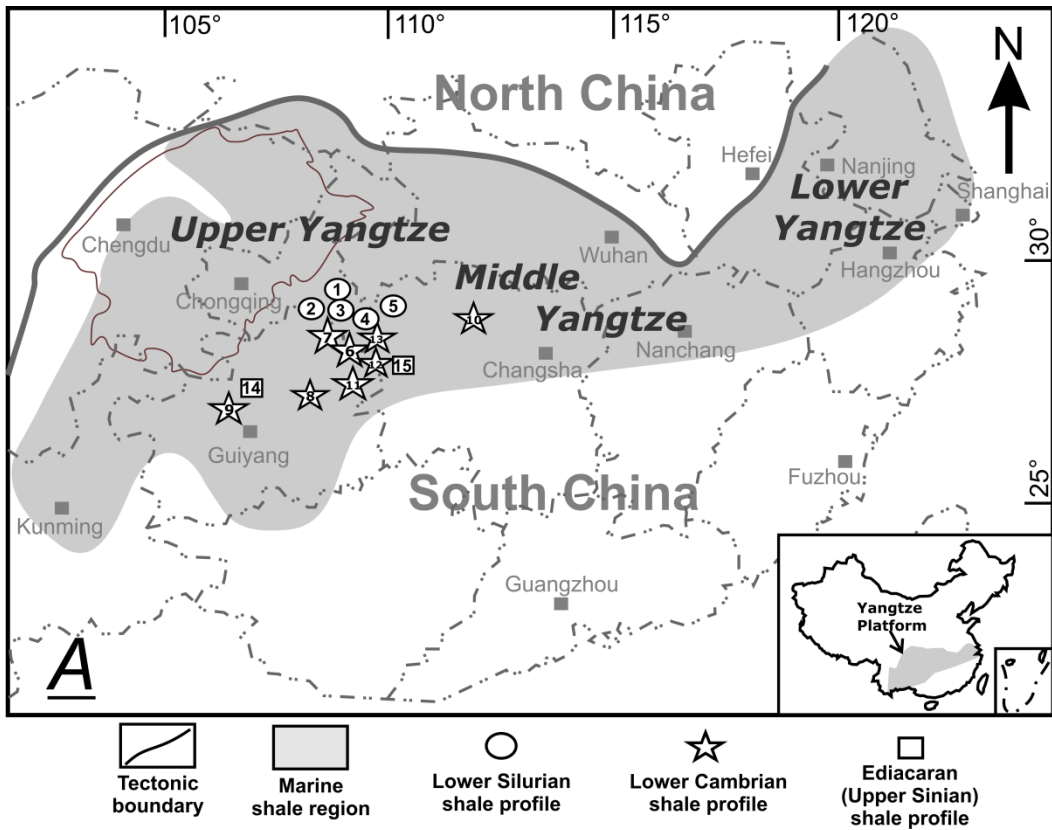


Figure 2.1 Overview maps of the Yangtze Platform, south China (A), and the Georgina Basin, north Australia (B). Numbers show the investigated profiles and wells, and names are listed in Table 2.1.

2.1.2. UYP - Lower Cambrian Shale

30 samples from 6 profiles and 2 wells in the Chongqing area, Guizhou and Hunan province were investigated (Figure 2.1 and Table 2.1). Core samples were recovered from a depth of 22-243m. All Lower Cambrian samples were conducted TOC and Rock-Eval analysis, and most samples were measured XRD, light microscope, and SEM. Some samples from the Rongxi, Jinggang, and Cenggong profiles were performed open py-GC and T_{vap}-GC, while samples from the Jinggang profile and Songqian1 and Yuke1 wells were tested petrophysical and rock mechanical measurements. Moreover, high-pressure methane was measured on 6 samples from the Lower Cambrian shale interval.

2.1.3. UYP - Ediacaran Shale

A total of 15 samples from 2 profiles in the Guizhou and Hunan province and 1 well in the Chongqing area were investigated (Figure 2.1 and Table 2.1). All samples were performed TOC and Rock-Eval analysis, and some of them were measured open py-GC, XRD, light microscope, and SEM. A few of Ediacaran samples were conducted T_{vap}-GC and petrophysical measurements.

2.1.4. AU - Cambrian Shale

AU Cambrian shale samples were taken from a depth range of 101.5 and 887.7m (Figure 2.1 and Table 2.1). A total of 14 Cambrian shale samples from 5 wells in south of the Georgina Basin were investigated organic geochemistry and mineralogy. 1 of them was used as equivalent immature sample of the Lower Cambrian shale in the UYP to investigate the physical properties of the petroleum formed during maturation in the Lower Cambrian shale reservoir in south China. In addition, 2 of immature samples were tested high pressure methane sorption isotherms to investigate the thermal maturity effects on methane sorption capacity.

2.2. Sample Preparation

After detailed macroscopic sample descriptions, large samples were drilled perpendicular to (for most of rock mechanical tests) or parallel to bedding (for most of petrophysical measurements) using a diamond studded drill bit, pre-cut using a diamond saw.

Subsequently the sample was ground to the sizes required for analysis. Specimens for rock mechanical measurements require cylindrical plugs with 25 mm diameter and 50 mm length for uniaxial and triaxial compression tests, or with 25 mm diameter and about 15 mm length for Brazilian disk tensile testing. Specimens for petrophysical measurements are cylindrical plugs with 28.5 mm diameter and 10-30 mm length. After the preparation of plugs, remaining chunks were broken by a hammer to make fragments for mercury injection porosimetry, or were cut into small rectangular strips by a water-cooled saw to make sections for light microscopy and to prepare sample materials for SEM and TEM investigation. Remaining small fragments were crushed to 0.5-1.5 mm diameter (cutting) for helium pycnometry, or were ground to 100-200 μm diameter (powder) for organic geochemical, mineralogical, and adsorption analysis.

2.3. Methodology

2.3.1. Organic Geochemical Measurements

TOC and Rock-Eval

In order to characterise organic matter richness and general organic geochemical properties, all samples were measured TOC and Rock-Eval (Espitalié et al., 1977). The Sub-contractor Applied Petroleum Technology AS (Norway) measured these parameters using a Leco SC-632 and a Rock-Eval 6 device (Behar et al., 2001).

Thermovaporisation Gas Chromatography (Tvap-GC)

Roughly 20-30 mg of finely ground powder was weighed into glass capillaries, which were then sealed by an H₂-flame after reducing the internal volume of the tube from ca. 40 ml to ca. 15 ml with pre-cleaned quartz sand. The sealed tubes were then introduced into a Quantum MSSV-2 Thermal Analyzer pyrolysis oven unit interfaced with an Agilent GC 6890A apparatus equipped with an HP-Ultra 1 column of 50 m length, 0.32 mm internal diameter and 0.52 μm thickness and an FID. The external surfaces of each tube were purged for 5 min at 300°C, during which time volatiles were also mobilised within the tube and thereafter cracked open by a piston device to transfer generated products from within the vessel by a helium-carrier gas with a flow rate of 30 ml/min into a liquid nitrogen-cooled trap. The trapped hydrocarbons were released to the column by ballistic heating of the trap to 300°C, and then thermovaporisation products were recorded. Quantification of individual

Chapter 2 Samples and Methods

compounds and totals was conducted by external standardisation with n-butane. Reproducibility of measured product concentration was generally better than 4% (Schenk et al., 1997). Because of the lower response factor of methane compared to the heavier gases the methane content was multiplied with 1.1.

Open-system Pyrolysis Gas Chromatography (Open-py GC)

Open py-GC was conducted using the Quantum MSSV-2 Thermal Analysis System© interfaced with an Agilent GC-6890A (Horsfield et al., 1989). About 20-30 mg sample was placed into the central part of a glass tube (26 mm long, inner sleeve diameter 3 mm). The remaining volume was filled with purified quartz that had been cleaned by heating at 630°C in air for 30 min. The sample was heated in a flow of helium, all products released up to 300°C being vented (3 min, isothermal). After then, it was pyrolysed at 50°C/min from 300 to 600°C and pyrolysis products were collected in a cryogenic trap (liquid nitrogen cooling at -190 °C, glass beads substrate) for condensation, from which they were later liberated by ballistic heating (held at 300°C for 10 min). AHP-Ultra 1 dimethylpolysiloxane capillary column (50 m length, inner diameter of 0.32 mm, film thickness of 0.52 µm) connected to a Flame-Ionisation-Detector (FID) was used with helium as carrier gas. The GC oven temperature was programmed from 30°C to 320°C at 5°C/minute. Boiling ranges (C₁, C₂₋₅, C₆₋₁₄, and C₁₅₊) and individual compounds (n-alkenes, n-alkanes, alkylaromatic hydrocarbons and alkylthiophenes) were quantified by external standardisation using n-butane. Reproducibility of measured product concentration was generally better than 4% (Schenk et al., 1997). Because of the lower response factor of methane compared to the heavier gases the methane content was multiplied with 1.1.

Bulk Kinetics

Kinetic parameters of primary kerogen to petroleum conversion were assessed by subjecting the same sample to open-system, non-isothermal pyrolysis at four different linear heating rates (0.7, 2, 5, 15°C/min) using a Source Rock Analyser SRA (Humble). Roughly 100 mg of crushed sample material was weighed into small vessels and heated according to the temperature program from 250°C to ~600°C. Generated bulk products were transported to the FID in a constant helium flow of 50 mL/min. The discrete activation-energy (E_a) distribution optimization with a single, variable frequency factor (A) was performed using the KINETICS05 and KMOD® programs (Burnham et al., 1987).

Chapter 2 Samples and Methods

Closed-system Pyrolysis Gas Chromatography (MSSV-py GC)

Non-isothermal closed-system micro-scale-sealed-vessel (MSSV) pyrolysis gas chromatography (principles described in Horsfield et al., 1989) was employed to obtain compositional information on petroleum products as input parameter for phase kinetic modeling. Ca. 20-30 mg of finely ground, whole rock was weighed into glass capillaries, which were then sealed by an H₂-flame after reducing the internal volume of the tube from ca. 40 ml to ca. 15 ml with pre-cleaned quartz sand. Pyrolysis was performed off-line at 0.7K/min to temperatures corresponding to 10, 30, 50, 70, and 90% of transformation ratio (TR) as defined by bulk pyrolysis (SRA), using an external high performance oven. The latter consisted of a massive cylindrical metal block acting as a circular sample holder enclosing a central heating cartridge, which provided a very homogeneous temperature field throughout the core. Excellent temperature control was guaranteed by a thermocouple introduced directly into one sample holder. After removal from the external pyrolysis oven, samples were then performed T_{vap}-GC.

Compositional Kinetic Modeling

Having acquired bulk kinetic parameters (activation energy-E_a and frequency factor-A) of primary petroleum formation and the composition of generated hydrocarbons at 10, 30, 50, 70, and 90% kerogen conversion, a compositional kinetic model for the prediction of hydrocarbon physical properties (GOR, P_{sat}, B_o) under subsurface conditions could be determined using the PhaseKinetics approach established by di Primio and Horsfield (2006). GOR is the gas oil ratio, which is the ratio of total gas hydrocarbons (C₁₋₅) and total liquid hydrocarbons (C₆₊) at standard surface conditions (Sm³/Sm³). B_o is the formation volume factor, which is the ratio of reservoir liquid volume to surface liquid volume in m³/Sm³. P_{sat} is the saturation pressure, the pressure which occurs when oil cannot dissolve any more gas.

As gas composition dominantly controls petroleum phase behaviour, and laboratory pyrolysis results in less dry composition than field data implies, a gas composition correction was performed as described in (di Primio et al., 1998). For basin modeling purposes and assuming a heating rate of 1.5°C/ ma, results were applied to the geological evolution of Cambrian shale within a selected synthetic well located in the UYP (central-south Sichuan Basin; 30.00N; 105.40E).

2.3.2. Microstructural and Mineralogical Examinations

Light Microscopy

Both thin sections and polished sections were prepared for analysis of the mineralogical composition and the structural fabric. Prepared thin sections were investigated at various magnifications under plane-polarized, cross-polarized, and reflected white light using a Zeiss Axiophot Electronic Microscope System. This system was equipped with a Carl Zeiss Axiocam digital camera and a Carl Zeiss Axiovision 2.0 software, and is capable to take high resolution photomicrographs with magnifying lenses of 10×, 20×, 30×, 40×, and 50×. Thin section microscopy was carried out at GFZ Potsdam, while polished sections were studied at RWTH Aachen University.

Scanning Electron Microscopy (SEM)

SEM investigations were conducted on 27 UYP rock samples. Small bars with 0.3-0.5 cm thick, 0.5-1.0 cm width, and >2 cm length were cut during initial preparation. A fresh surface was created by breaking the bar. The samples were dried in an oven at 40 °C for 24 hours to remove fluids. Afterwards, the dried material was mounted on specimen holders using resin. The freshly broken surface was coated with a gold-palladium alloy. Investigations were carried out at GFZ Potsdam using an Ultra 55 plus Carl Zeiss SMT field emission scanning electron microscope (FE-SEM), and images were obtained under high vacuum at 20 kV acceleration voltages using the SE, Inlens-SE, and BSE detectors.

Focused Ion Beam - Transmission Electron Microscopy (FIB-TEM)

FIB is a high precision technique which is able to slice samples in μm or nm scale, while TEM has ample power to magnify a solid-state sample on nm or even atomic scale. Thus a combination of these two emerging techniques allows analysis at extremely high resolution. Detailed methodological descriptions of FIB-TEM are available in Wirth(2004; 2009). On the basis of previous organic geochemical and mineralogical screening results and in order to analyze shale composition, fabric and texture at nm scale, five UYP samples comprising the Lower Cambrian and Lower Silurian shales were selected. FIB thin foils with 15-20 μm wide, 10-15 μm high, and 100-150 nm thick were investigated at GFZ Potsdam, using a FEI Tecnai G2 F20 x-Twin transmission electron microscope (TEM/AEM) that is equipped with a Gatan Tridiem energy filter, a Fishone high-angle annular dark field detector (HAADF), and an energy dispersive X-ray analyzer (EDX).

X-ray Powder Diffraction (XRD)

XRD is a rapid analytical technique used to determine the atomic and molecular structure of a crystalline material. XRD was performed at GFZ Potsdam using a Siemens D5000 powder diffractometer with Cu K α radiation, automatic divergent and antiscatter slits and a secondary graphite monochromator with scintillation counter to determine proportions of matrix minerals. The diffraction data were recorded from 4° to 75° 2 θ with a step width of 0.02° and a counting time of 4 s per step. The generator settings were 40 kV and 30 mA. Measured data were then analyzed qualitatively using the EVA (Bruker) software and quantitatively using AutoQuant software. In addition, XRD results of nearly 700 samples from 20 profiles/wells scattered in the UYP were compiled in order to better define the reservoir mineralogy.

2.3.3. Petrophysical Experiments

Mercury Intrusion Porosimetry (MIP)

Mercury intrusion porosimetry was performed on most of the core samples and several outcrop samples to determine bulk density, equivalent pore radius distribution, and interconnected pores on the μm and nm range. In this procedure mercury is injected into the pore system of a sample at continuously increasing pressure. The mercury volume injected upon a pressure increase from P_i to P_{i+1} is related to the volume of cylindrical equivalent pores with radii ranging from r_i to r_{i+1} by means of the Washburn equation (Washburn, 1921):

$$r = \frac{-2\gamma \cos \omega}{P} \quad (2.1)$$

Here γ is the mercury/air interfacial tension, ω is the contact angle of mercury, and P (MPa) is the injection pressure. The values applied in this study are $\gamma=480\text{dyne/cm}$ (480 mN/m) and $\omega=140^\circ$. The measurements were performed with a Fisons Instruments Mercury Porosimeter. The mercury pressure was increased from 0.0013 up to 200 MPa, corresponding to equivalent pore radii from 58 μm down to 3.7 nm.

Sample fragments with approximately 20 \times 20 mm and 10-20 g were prepared via the initial sample preparation and then were dried in an oven for 24 hours at 50°C. Subsequently, sample fragments were placed into a container (dilatometer), mounted on the apparatus. Then the system was evacuated for 15 minutes prior to the measurement.

Chapter 2 Samples and Methods

Helium Pycnometry

Porosity describes the fraction of pore space in the bulk volume, and can be calculated by:

$$\phi = \frac{V_p}{V_b} = 1 - \frac{V_s}{V_b} = 1 - \frac{\rho_b}{\rho_s} \quad (2.2)$$

Where V_p is the volume of pores in the rock, V_b is the bulk rock volume, and V_s is the volume of solid skeleton. ρ_b is the bulk density, and ρ_s is the skeleton density. The bulk density was determined by mercury intrusion porosimetry, while helium pycnometry was used for accurately measure the skeletal density of irregularly shaped samples. In this study, helium pycnometry was performed on most of the core samples and certain outcrop samples using the pycnometers at RWTH Aachen University and at GFZ-Potsdam. Connected porosity of measured samples was then calculated using formula (2.2).

Gas permeability

Gas permeability measurements were conducted on four UYP samples at RWTH Aachen University. For this purpose, helium was used as permeating fluid because it is inert gas and generally does not alter the structure or solve constituents of the measured sample plug compared to liquid fluids (Wei et al., 1986; Carles et al., 2007). Measured plugs were drilled parallel to beddings with a diameter of 28.5 mm, and then cut to 10-20 mm in length. Plugs were in as-received conditions and measured using a triaxial flow cell, which is designed for confining pressures up to 50 MPa and axial loads up to 100 KN. We applied a non-steady state technique that is described in detail by Ghanizadeh, et al. (2013a; 2013b) to measure apparent gas permeability (k_{gas}) coefficients at different mean pressures (P_{mean}). After installation of the sample plug, the experimental set up was leak tested and the volumes of the top and bottom reservoirs were calibrated ($\pm 0.1 \times 10^{-6} \text{ m}^3$). Non-steady state gas flow tests were then commenced by applying a pressure difference between the upstream (P_{up}) and the downstream (P_{down}) reservoir. Due to this pressure difference, gas flows from high pressure to the low pressure reservoir until an equilibrated pressure is reached. The pressure decline with time at the high pressure reservoir and the pressure incline with time at the low pressure reservoir were automatically recorded using two Keller PAA-33X / 80909 pressure transducers with a precision of 0.05%. From the pressure decline/incline curves at the upstream/downstream reservoirs we calculated k_{gas} according to Ghanizadeh, et al. (Ghanizadeh et al., 2013a). The corrected permeability k_{∞} was calculated using the

Chapter 2 Samples and Methods

formulation of Klinkenberg (1941). In this research, applied confining pressure was 30 MPa at a temperature of 46 °C and 52°C. The pressure difference between the upstream and downstream reservoir at the beginning of each experiment was around 20 bar, except for measurements 5-9 (<5 bar) of sample 43 and sample 58 (120 bar) (Figure 6.10 and Table A7 in appendix). Measurements were repeated at least two times with different flow directions (from the top side of the cell to the bottom and vice versa) in similar conditions in order to achieve a systematical interpretation. For sample 58 (Figure 6.10 and Table A7 in appendix) it was only possible to measure one gas permeability coefficient, because there was no measurable pressure decline/incline of the upstream/downstream reservoir at pressure differences <100 bar.

2.3.4. Rock Mechanical Tests

Rock mechanical measurements on specimens were carried out at GFZ-Potsdam and Geomecon GmbH-Potsdam. Uniaxial compression test, Brazilian disk tensile test (BD), and triaxial compression test with multiple failure were conducted in servo-hydraulically controlled, stiff MTS loading frame (Minneapolis, USA) with a maximum axial load capacity of 4600 kN and a maximum confining (oil) pressure of 200 MPa. The applied load, F , was measured by class I load cells with max. 25 KN for BD and maxum 1000KN for TCT-MF and UCT. Experimental methods and data analysis for measurements of the uniaxial (UCS) and triaxial (TCS-MF) strength are in line with recommendations from the International Society for Rock Mechanics (ISRM) (Ulusay and Hudson, 2007), while the measurements and calculations of the tensile strength (TS) and Mode I fracture toughness (K_{IC}) based on BD testing follow the procedures recommended by ISRM (Bieniawski and Hawkes, 1978) and Guo, et al (1993), respectively. Prior to mechanical measurements, ultrasonic p-wave velocities were measured parallel to the axis of cylindrical samples using piezoceramic transducers. Reported velocities were obtained by averaging about 100 high-pass filtered measurements in each direction.

2.3.5. Methane Sorption Isotherms

Experimental Setup and Procedure

High pressure methane sorption measurements were conducted on a manometric setup, which has been described in detail in a series of publications (Krooss et al., 2002; Weniger et al., 2010; Gasparik et al., 2013). The setup consists of a stainless steel sample cell, two high

Chapter 2 Samples and Methods

pressure shut-off valves, and a high accuracy pressure transducer. These components are connected by 1/16 inch stainless steel tubing, and placed in a thermostatic oven (GC-furnace). A 2- μm filter is equipped on the entrance of the sample cell to prevent shale particles from entering the valves, while a three-port valve is used to link gas supply (helium and methane) and a vacuum pump. The volume between two valves, including the dead volume of the pressure transducer, is regarded as reference volume ($\sim 1.3 \text{ cm}^3$) and determined by helium expansion in a calibration run, whereas temperature is recorded by a high-precision Pt-100 resistance temperature detector (RTD).

In this study, methane sorption isotherms were measured on “as received” samples in a pressure range of 0-25MPa at 46°C. These pressure and temperature conditions should be suitable for reservoirs at a depth between 1 and 2km in the UYP, since the present geothermal gradients are generally between 18 and 33°C/km (Han and Wu, 1993; Xu et al., 2011).

The experimental procedure can be summarized as follows (see Weniger et al., 2010):

- 1) Degas the measuring material by evacuation for 15 min at 1 MPa;
- 2) Conduct leak test using helium at 10 MPa for 2 hours, in order to reach thermal equilibration and guarantee a helium leakage rate less than 500 Pa per hour;
- 3) Determine void volume as well as sample volume using helium expansion. Void volume is calculated using the average value of 10 pressure steps ranging from 1 to 10 MPa with a standard deviation less than 0.05%. In addition, the void volume determination provides the sample volume which can be used to calculate sample skeletal density;
- 4) Evacuation for 60 min at 1 MPa to remove helium;
- 5) Perform methane sorption measurement until pressure goes up to 20-25 MPa.

Results Calculation and Parameterization

The excess sorption amount of adsorbed gas (m_{excess}) is calculated from the difference between the total amount of gas introduced into the system (m_{total}) and the amount of gas that still presents in the void volume (V_{void}), i.e. the amount of gas is not adsorbed by measuring material.

$$m_{\text{excess}} = m_{\text{total}} - \rho_{\text{gas}} V_{\text{void}} \quad (2.3)$$

The void volume was determined by helium expansion at 46°C prior to the sorption measurement, whereas the gas density (ρ_{gas}) was calculated from an equation of state of the

Chapter 2 Samples and Methods

gas for corresponding pressure and temperature conditions. Measured results are in molar units normalized to samples mass (mmol CH₄/g rock).

The Langmuir model is commonly applied to describe the relations between the adsorbed gas on solid surface and the measured pressure at a fixed temperature:

$$n_{excess} = n_L \cdot \frac{p}{P_L + p} \quad (2.4)$$

Here n_{excess} (mmol/g) denotes the excess adsorbed amount of substance at pressure P (MPa). P_L (MPa) is the Langmuir pressure, corresponding to the pressure at which half of the (“monolayer”) sorption sites are occupied and n_L (mmol/g) is the “Langmuir amount of substance” (corresponding to the “Langmuir volume”), denoting the amount adsorbed at full occupancy of the “Langmuir monolayer”.

Because the Langmuir sorption model is a limiting model for low pressure, its application to high-pressure sorption isotherms is not strictly justified (Weniger et al., 2010). Most of the excess sorption isotherms measured in this study exhibit a maximum in the pressure range between 10 and 15 MPa, indicating that the adsorption maximum occurs before the final experimental pressure was reached. At higher experimental pressure the density of the gas phase increases and gradually approaches the density of the adsorbed phase, resulting in a decrease in excess sorption. To approximate measured data of isotherms exhibiting a maximum, a modified Langmuir model was used. This function is given by:

$$n_{excess} = n_L \cdot \frac{p}{P_L + p} \cdot \left(1 - \frac{\rho_g}{\rho_{ads}}\right) \quad (2.5)$$

It contains an additional adjustable parameter, the density of the adsorbed phase (ρ_{ads}). The parameters n_L , P_L , and ρ_{ads} are fitted to the experimental excess sorption data using a least squares minimization procedure.

Equation of State (EOS) Applied of Methane Sorption Isotherm

The equation of state (EOS) developed by Setzmann and Wagner (1991) for methane was applied to calculate the specific density of the free gas phase under experimental pressure and temperature conditions, while the wide-range equation of state GERG 2004 was used to calculate the helium density during void volume evaluation (Michels and Wouters, 1941).

Chapter 3 Geological and Geochemical Characterisation

3.1. Abstract

The Ediacaran (Upper Sinian), Lower Cambrian, and Lower Silurian black shale formations deposited in marine environments are widespread on the Upper Yangtze Platform (UYP), south China. These formations have been recently regarded targets for shale gas exploration. Generally speaking, these black shales are thick successions (10m to over 100m), have a high total organic carbon (TOC) content (>2%), and are at variable but usually high levels of thermal maturity. Burial depths of these formations can be shallow, such as at outcrop in the marginal regions of the Sichuan Basin and in the south-east UYP, or deep, reaching more than 5000 m in some depressions.

Here we report on the shale gas potential of 53 highly mature samples from south-east Sichuan, Chongqing, north Guizhou and Yunnan, and west Hunan and Hubei. Reflected light microscopy, TOC measurement, Rock-Eval, carbon isotope ratio analysis, thermovaporisation gas chromatography (T_{vap}-GC), and open pyrolysis gas chromatography (open py-GC) were used to characterise the organic matter. Measured TOC in this research is normally higher than 2%, and averages 5%. TOC contents are roughly positively correlated with increasing geological age, i.e. Lower Silurian shales exhibit generally lower TOC contents than Lower Cambrian shales, which in turn commonly have lower TOC contents than Ediacaran shales. Kerogen has evolved into metagenesis stage, which was demonstrated by the abundant pyrobitumen on microphotographs, the high calculated vitrinite reflectance ($R_o=3.0\%$) via bitumen reflectance (R_b), as well as the $\delta^{13}C$ of gas (methane) inclusions. Pyrolysates from open py-GC are quantitatively low and qualitatively only light hydrocarbon can be detected.

This chapter is in submission as: Tan, J., Horsfield, B., Mahlstedt, N., Zhang, J., Boreham, C.J., Hippler, D., van Graas, G. and Tocher, B.A., 2014. Shale Gas Potential of the Major Marine Shale Formations in the Upper Yangtze Platform, South China, Part I: Geological and Geochemical Characterisation.

Chapter 3 Geological and Geochemical Characterisation

To help reconstruct the original kerogen properties of the UYP shales, a comparison was made with natural and simulated maturity series from Germany, Australia, Norway, and United States. The UYP shales were revealed to be dominated by type I original kerogen that is possible to be formed in the marine environments via selective accumulation of algal material, based on the analysis of $\delta^{13}\text{C}$ of methane, kerogen, and chloroform bitumen, as well as the correlations with the Australian shale in aromatics generation and aromaticity evolution with the increase in the T_{max} . Type I kerogen containing shale shows significant higher hydrocarbon potential than type II and III, and thus implies massive original petroleum potential. Excellent original hydrocarbon generation was revealed by that TOCo is between 5% and 23%, and S1o+S2o is ranging from 29 to 215 mg HC/g rock.

Keywords

Shale gas; Lower Cambrian shale; Lower Silurian shale; Upper Yangtze Platform; south China

3.2. Introduction

The remarkable success of shale gas exploitation in the United States has led to shale systems becoming increasingly important exploration targets worldwide. In China, different black shale formations ranging from Precambrian to Cenozoic in age are known (Figure 1.2 A-C). Technically recoverable shale gas reserves are estimated to range from 10 to $45 \times 10^{12} \text{ m}^3$ (Zhang et al., 2009; Dong et al., 2010; Liu et al., 2010; EIA, 2011b; Zou et al., 2011). Exploration activities are already underway in southern (Sichuan Basin, Yangtze Platform) and northern (e.g. Ordos Basin, Songliao Basin) parts of the country.

The Upper Yangtze Platform (UYP), where the Sichuan Basin is located, is one of the largest conventional natural gas provinces of China, accounting for 22-43% of the annually produced gas over the last 20 years (National Bureau of Statistics and Energy Bureau, 1991-2010). The recoverable reserves of conventional gas have been estimated at around $1.7 \times 10^{12} \text{ m}^3$, with annual yields exceeding $23 \times 10^9 \text{ m}^3$ in the year 2010 (Ma et al., 2010). In addition to conventional petroleum, the Lower Silurian and Lower Cambrian shale formations have been regarded as two prolific unconventional shale gas reservoirs with recoverable reserves around $19.6 \times 10^{12} \text{ m}^3$ (EIA, 2011b). Although only two formations were reported in that evaluation, and shale gas reserved outside the Sichuan Basin were not considered, reported unconventional reserves are significantly higher than the total reserves of conventional

Chapter 3 Geological and Geochemical Characterisation

petroleum (Ma et al., 2010; EIA, 2011b). Moreover, the Ediacaran and Upper Permian marine shale, the Upper Triassic transitional shale (from marine to lacustrine environment) and the Lower Jurassic lacustrine shale all locally possess shale gas potential in the UYP (Ye and Zeng, 2008; Zou et al., 2010; Chen, 2011; Guo et al., 2011b).

Studies on shale gas plays in the USA have shown that the type, abundance and maturity of organic matter, as well as the grain-size and mineralogy, determine the source, reservoir, and seal properties of gas shales (Schoell, 1980; Martini et al., 1998; Curtis, 2002; Bowker, 2007). Prolific shale plays are normally recognized by certain minimal technical thresholds, which should be fulfilled. These include but are not limited to shale thickness, organic matter richness, maturity, mineralogy, porosity, permeability, pore pressure, and gas-in-place (Curtis, 2002; Bowker, 2007; Jarvie et al., 2007; Strapoc et al., 2010; Miceli Romero and Philp, 2012). Zhao et al (2007) stated that the shale thickness, depth, total organic carbon (TOC) and thermal maturity are the most important geological factors for commercial gas production. The minimum net thickness for a shale gas play to be successfully developed amounts to approximately 10 m, e.g. for the Fayetteville, Antrim and Ohio shale, while the depth can be lower than 200 m in the case of Antrim shale, containing biogenic gas, or up to 5000 m in the case of the Haynesville (Bowker, 2007; Hammes et al., 2011). Meanwhile, exploration targets are usually thick, widespread, gas-saturated, fine-grained, organic rich units with a) significant Type II organic matter in a thermally overmature state, b) rich organic matter of any type that is thermally immature and subject to extensive biogenic decomposition, and/or c) significant Type III organic matter in thermally mature to overmature states (Martini et al., 2003; Hamblin, 2006). Some of these general principles have already been applied to Chinese gas shales. The Ediacaran and Lower Paleozoic black shale intervals in the UYP cover a broad area, have a large thickness and a burial depth ranging from the surface to more than 5000 m, at which depth thermal maturity is high (Cheng et al., 2009; Wang et al., 2009a; Wang et al., 2009b; Wang et al., 2009c; Zhang et al., 2009; Zou et al., 2010; Nie et al., 2011; Zou et al., 2011). In a strict sense, however, issues remain on the composition of the origin kerogen, thermal evolution and maturity, and thus the original hydrocarbon potential and hydrocarbon generation properties have not been clearly clarified.

This study focuses on the generation and storage properties of the Ediacaran and Lower Paleozoic shales in the UYP. The reconstruction of original organic geochemical properties for the shale intervals under study is especially difficult because the organic matter is overmature ($R_o \gg 2.0\%$). Therefore, a series of organic screening methods, e.g. TOC, Rock-

Eval, microcopies, carbon isotope ratio, thermovaporisation gas chromatography (T_{vap}-GC) and open-system pyrolysis gas chromatography (open py-GC), were performed on representative samples from the central area of the UYP. In conjunction with an extensive data compilation, the present organic geochemical properties are then revealed in detail. Followed on, kerogen origin and evolution, and thus the evolution of hydrocarbon generation during maturation were investigated, using open py-GC results of both naturally and artificially matured samples collected from the UYP, Australia, Germany, Norway, New Zealand, and United States. Naturally mature samples cover a maturity range from immature to overmature, whereas artificially matured samples, containing various types of organic matter, are originally immature or low mature, but were heated to different mature levels using the MSSV approach (Horsfield et al., 1989). Finally, original organic abundance and hydrocarbon generative potential were reconstructed via the mass balance models developed by Cooles, et al (1986) and Claypool (in Peters et al., 2005).

3.3. Geological Setting

3.3.1. Tectonic and Sedimentary History

The present-day tectonic framework of China is a mosaic composed of three platforms and fifteen fold systems, and the UYP is located in the western zone of the Yangtze Platform (Zhang et al., 2011) (Figure 1.2D). In the Early Sinian (Late Proterozoic), the basement and boundaries of the Yangtze Craton were created in the course of the Chengjiang tectonic movement (Editorial Committee of the Sichuan Oil & Gas field, 1989; Guo, 1996). The earliest sedimentary rocks within the UYP, consisting of black shales and dolomites, were deposited during a major transgression in the Late Sinian. The Tongwan tectonic movement at the end of the Proterozoic caused a disconformity between the Ediacaran and Lower Cambrian strata (Ma et al., 2007). The second major marine transgression occurred in the Early Cambrian. Sedimentary successions, comprising shale, siltstone, limestone and dolomite, were laterally deposited extensively in open to restricted marine environments. Between the Middle Cambrian and Ordovician, depositional environments were generally maintained and geographically similar in that ancient continent/islands were located in the west, while the littoral, restricted and open marine platform and deep marine shelf were developed southeast towards. Carbonates were therefore deposited in most of the regions, in addition to the deposition of minor amounts of clastic material occurred at the western

Chapter 3 Geological and Geochemical Characterisation

margin. During the Early Silurian, the third major transgression occurred southwest towards resulting in a widespread deposition of black shales that contributed significantly to the charging of oil and gas fields in the eastern Sichuan Basin. However, the Late Caledonian orogeny impacted on the whole area at the end of the Silurian. Structural highs and lows were extensively formed in the central and south UYP, which affected source rock sedimentation and preservation. As a result of the Late Caledonian orogeny and the subsequent Liujiang and Yunnan orogeny, most of the regions in the UYP were in continental environments during the Devonian and Carboniferous. Consequently, Devonian and Carboniferous strata were confined locally to the east and south of the area, whereas the Lower Paleozoic strata underwent prolonged erosion. The fourth major marine transgression commenced during the Early Permian and was interrupted only shortly by the Dongwu uplift in the Middle Permian times. Open to restricted marine environments reestablished again in Late Permian times and persisted until the Middle Triassic. Coal-bearing shales and carbonates were periodically deposited and provided important source and reservoir rocks (Editorial Committee of the Sichuan Oil & Gas field, 1989; Guo, 1996; Ma et al., 2006; Hao et al., 2008).

The Indosinian movement in the Middle-Late Triassic is a pivotal event to the tectonic and environmental evolution. The entire UYP was escalated during the course of the intensive compression between the South China Plate, the North China Plate, and the Pacific Ocean Plate. As a result, marine sedimentation diminished while terrestrial sedimentation prevailed. A series of structural highs and lows were then created during the Yanshanian orogeny in the Middle-Late Mesozoic and the Himalayan orogeny in the Cenozoic, indicating that tectonic and stratigraphic architecture of the UYP were almost formed. In the Sichuan basin thousands of meter of clastic strata were sediments providing important petroleum source, reservoir as well as seal rocks, whereas the regions surrounding the basin in the UYP experienced remarkable erosions (Editorial Committee of the Sichuan Oil & Gas field, 1989; Korsch et al., 1991; Dai et al., 1992; Guo, 1996; Ma et al., 2007; Hao et al., 2008; Ma et al., 2010).

3.3.2. Petroleum Systems of the UYP

In the UYP, marine sediments are characterised by thick carbonates and shale formations, and terrestrial sediments are characterised by fluvio-deltaic strata, coal measures, and lacustrine carbonates or shales (Editorial Committee of the Sichuan Oil & Gas field, 1989). As far as conventional petroleum is concerned, the regional source rocks are the Lower Cambrian, Lower Silurian and Lower Jurassic mudstones and shales, the Lower Permian

Chapter 3 Geological and Geochemical Characterisation

carbonates, and the Upper Permian and Upper Triassic coal-bearing shales (Huang et al., 1997). Principal reservoirs comprise the Changxing (Upper Permian) and Feixianguan (Lower Triassic) carbonates and the Xujiahe (Upper Triassic) and Jurassic terrigenous clastics. They account for over 70% of the total conventional reserves in the Sichuan Basin (Dai et al., 2009; Ma et al., 2010). Significant seal rocks include anhydrite, halite and gypsiferous dolomite, developed in a major marine regression during the Early to Middle Triassic times (Ma et al., 2006; Hao et al., 2008). The earliest thermogenic hydrocarbon generation period has been reported to be during the Silurian when Precambrian and Lower Cambrian source rocks were buried almost 2000 m, ostensibly leading to the formation of small petroleum accumulations in the east and south Sichuan Basin (Huang et al., 1997). However, the major periods of hydrocarbon generation, migration and accumulation are thought to have occurred between the Triassic and Cretaceous when the most important source rocks were buried successively to more than 2000 m, and reservoir seals became effective (Editorial Committee of the Sichuan Oil & Gas field, 1989; Dai et al., 1992; Guo, 1996; Ma et al., 2010) (Figure 3.1).

More than a hundred conventional petroleum fields or structures have been found in the UYP, but most of them are gas fields located in the Sichuan Basin. Within this basin, commercial-scale oil fields are confined to the central area. Gas fields are volumetrically more important and have preponderance in the south, while most giant gas fields (reserves $> 30 \times 10^{12} \text{ m}^3$) are situated in the east of the basin (Editorial Committee of the Sichuan Oil & Gas field, 1989; Zhu et al., 2006; Ma et al., 2010). The basin is therefore normally divided into four petroleum regions according to the prevalent petroleum type (oil or gas) and scale. They are respectively the western gas field region, central oil-gas field region, eastern giant gas field region, and southern gas field region.

3.4. Black Shale Intervals under Investigation

A total of more than 10 black shale formations can be identified in the UYP. The Doushantuo Fm. (Ediacaran), Qiongzusi / Niutitang Fm. (Lower Cambrian), Wufeng Fm. (Ordovician), Longmaxi Fm. (Lower Silurian), Luofu Fm. (Devonian) and Longtan Fm. (Upper Permian) are the major marine/transitional shale formations, whereas the Xujiahe Fm. (Upper Triassic) and Ziliujin Fm. (Lower Jurassic) are the principal lacustrine shale formations (Figure 3.1) (Editorial Committee of the Sichuan Oil & Gas field, 1989; Liang et al., 2008; Dong et al., 2010; Zou et al., 2010). In this paper, we primarily focus on the Lower

Chapter 3 Geological and Geochemical Characterisation

Silurian and Lower Cambrian black shale intervals, and to some extent on the Ediacaran black shale formation that occurs in the upper part of Proterozoic strata.

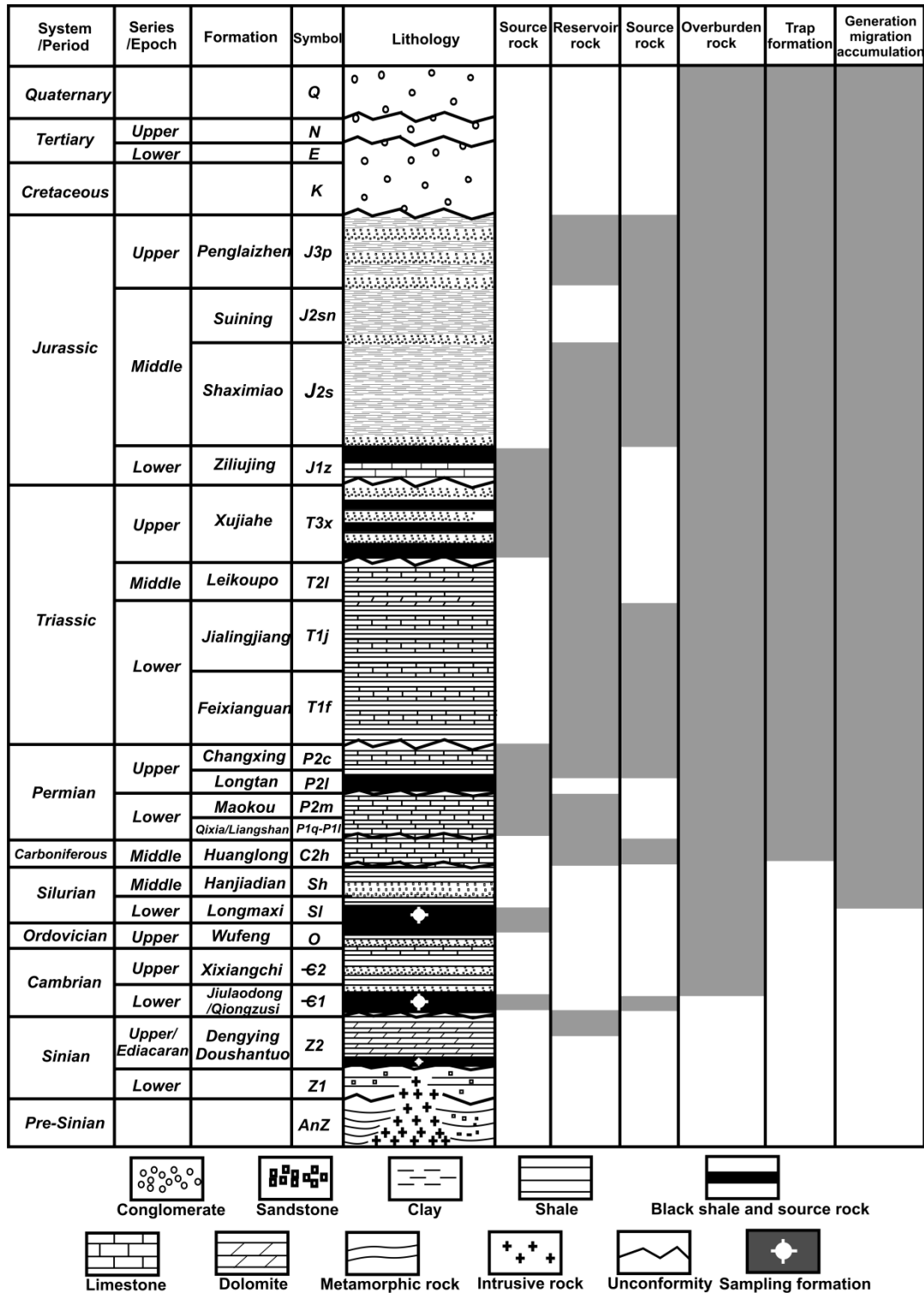


Figure 3.1 Generalized stratigraphic column and petroleum system event chart of the Sichuan Basin, UYP, modified after (Editorial Committee of the Sichuan Oil & Gas field, 1989). Note: The Lower Cambrian shale formation has several local names, usually called Jiulaodong or Qiongzusi in the Sichuan Basin and Niutitang in the Chongqing area and Yunnan and Guizhou province.

Chapter 3 Geological and Geochemical Characterisation

The Lower Silurian shale thickens in the south-east Sichuan Basin, Chongqing area, and west Hubei province (50-200m), but it has lower thickness in most other places in the UYP (Wang et al., 2009b; Dong et al., 2010) (Figure 3.2). This distribution can be traced back to a regression of open marine conditions resulting from uplifts of tectonic blocks in the southern and western UYP. In the Sichuan Basin, the Lower Silurian succession can be subdivided into the Longmaxi Formation and Xiaoheba Formation. The bottom Longmaxi Formation is abundant in Graptolite, e.g. *Glyptograptus persculptus*, *Pristiograptus cyphus*, *Demirastrites triangulates*, and consists of black shale, green sandy shale, siltstone and argillaceous limestone. The top Xiaoheba Formation contains fossils like Graptolites, Trilobites, Brachiopods, etc., and comprises grey-green siltstone, sandstone, shale, and biological limestone lenses with distinct ripples and biological traces (Editorial Committee of the Sichuan Oil & Gas field, 1989). The thickness of the complete Lower Silurian succession ranges between 100m and 500m in the Sichuan Basin, but exceeds 700m in the southeast Sichuan and Chongqing area. In the Longmaxi Formation, organic matter contents decrease while siliceous minerals increase from the bottom upwards. It has been recognized as one of the principal contributors to large- and medium-sized gas fields, e.g. the Puguang and Hechuan giant gas fields (Editorial Committee of the Sichuan Oil & Gas field, 1989; Huang et al., 1997; Wang et al., 2009b; Ma et al., 2010). In this investigation, the analyzed Lower Silurian samples are dominantly siliceous shale/mudstone, and consist of 8 outcrop samples (Sample ID 01-08, Table 3.1) from the Lujiao and Guankou profiles and 6 core samples (Sample ID 09-14) from the YY1 shale gas well (Figures 3.2 and 3.3) with depths ranging from the top down are 136, 207, 267, 276, 285, and 321 m.

The Lower Cambrian black shale usually exhibits gross thicknesses of 50 to 200 m in most of the regions in the Yangtze Platform, but it is thinner in the central Sichuan Basin and the western and southern marginal areas of the UYP (Figure 3.2). This feature can be related to the marine transgression during the Early Cambrian. In the UYP, the presence of thick black shale packages indicates open marine to marine shelf depositional environments, whereas the presence of thin black shale packages indicates littoral depositional environment (Dong et al., 2010). The Lower Cambrian interval disconformably overlays the Ediacaran carbonates (Figure 3.1), with the stratigraphic boundary consisting of phosphate-containing siliceous dolomite, phosphorites, sandy dolomite and calcareous shale. Three subdivisions can be recognized on the basis of lithology, biota and texture: 1) the bottom comprises *Protospongia* containing black shale or carbonaceous shale with pyrite, phosphate and siderite nodules, and exhibits a distinct laminated bedding; 2) the middle is grey-black sandy or silty

shale, accompanied by calcareous sandstone, fine sandstone and dolomite, and rich in fossils, e.g. containing trilobites, sponge spicules, brachiopods, and 3) the top comprises juxtaposed carbonate, siltstone and shale, containing various trilobite species, such as Trilobite, e.g. Eoredlichia, Hebediscus and Yunanocephalus (Editorial Committee of the Sichuan Oil & Gas field, 1989). Organic richness, strata color and lamellation vary gradually from the bottom up (Cheng et al., 2009; Wang et al., 2009b). Black shale occurs primarily in the middle or bottom intervals of the Lower Cambrian formation. It is characterised by high gamma ray responses with values between 70 and 150 API inferring high TOC contents of the shale (Cheng et al., 2009). The Lower Cambrian shale has been recognized as the source rock of the Weiyuan gas field, which possesses the oldest reservoir rock (Ediacaran dolomite) of all Chinese petroleum fields (Editorial Committee of the Sichuan Oil & Gas field, 1989; Xu et al., 1989; Huang et al., 1997; Dai, 2003; Ma et al., 2010). In the research reported here, a total of 15 Lower Cambrian samples comprising siliceous or carbonaceous shale/mudstone and phosphorite were investigated. They were collected from the Rongxi and Jinggang profiles (Sample ID 15-20, Table 3.1) in the Chongqing area, the Cenggong profile in the Guizhou province (Sample ID 21-23), and the Heishapo profile in the Hunan province (Sample ID 24-29) (Figures 3.2 and 3.3).

The Ediacaran black shale has a more restricted distribution than the Lower Silurian and Lower Cambrian shale and locally crop out to the southeast of the Sichuan Basin, north Guizhou province, and west Hunan and Hubei provinces. 24 Ediacaran samples (Sample ID 30-53, Table 3.1) collected from two profiles in Guizhou and Hunan provinces (Figures 3.2 and 3.3) were investigated; here the lithofacies comprised mudstone, shale, chert, and phosphorite (Table 3.1).

3.5. Applied Methods

Samples were cut into small fragments using a water-cooled saw to prepare thin and polished sections, to select minerals, and to fit the grind. Thin sections and polished sections were examined using the Zeiss Axioplan electronic microscope system. Quartz and calcite minerals from four samples were selected for fluid inclusions analysis using the Elemental Analyzer (EA)-IRMS system, which comprises a Crusher, a GC-column, an EA, a ConFloIII interface and a Thermo DeltaplusXL mass spectrometer, allowing to simultaneously measure the stable isotope ratios of gas mixtures consisting of N₂, CH₄, and/or CO₂ (Lüders et al., 2012).

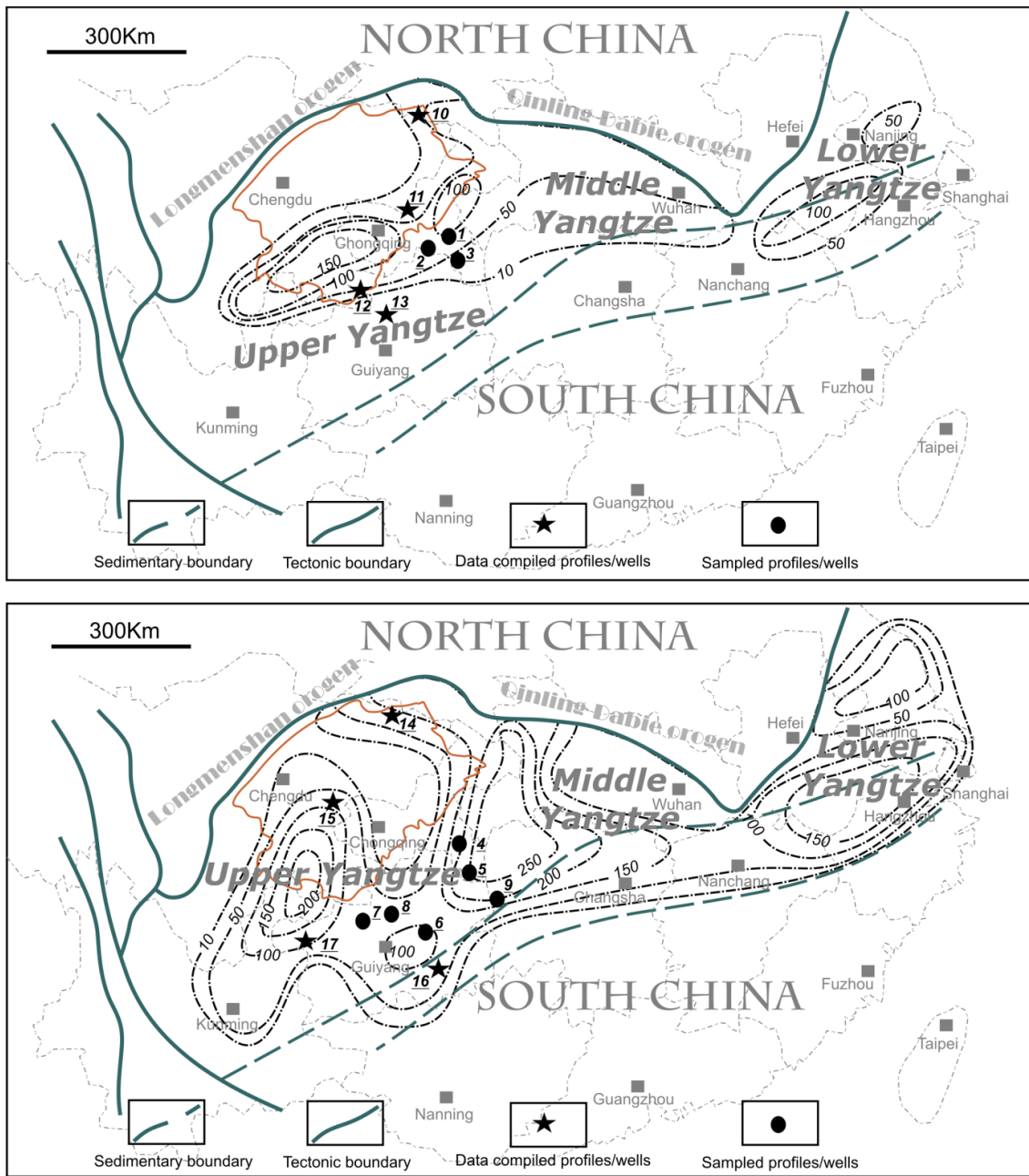


Figure 3.2 Isopach maps of the Lower Silurian (upper) and Lower Cambrian (lower) shale formations in the Yangtze Platform, modified after (Liang et al., 2008; Zou et al., 2011), and the locations of investigated profiles and wells. Sampled Lower Silurian profiles or wells are 1-YY1# well, 2-Guankou, and 3-Lujiao. Sampled Lower Cambrian profiles are 4-Jinggang, 5-Rongxi, 6-Cenggong, and 7-Heishapo. Data compiled Lower Silurian profiles or wells are 10-Zhenba-Guanyin, 11-Shizhu-Qiliao, 12- Shizhu-Dafengao, 13-Dingshan 1# well, 14-Xishui-liangchun 5# well, and 15- Changxin 1# well. Data compiled Lower Cambrian profiles or wells are 16-Nanjiang-Shatang, 17- Guangyuan, 18- Gaoke 1# well, 19-Wei 001-2# well, 20-Fanshen 1# well, and 21-Majiang-Yangtiao. In addition, two sampled Ediacaran profiles denoted in the bottom plot are 8-Maoshi and 9-Lijiatuo.

Chapter 3 Geological and Geochemical Characterisation

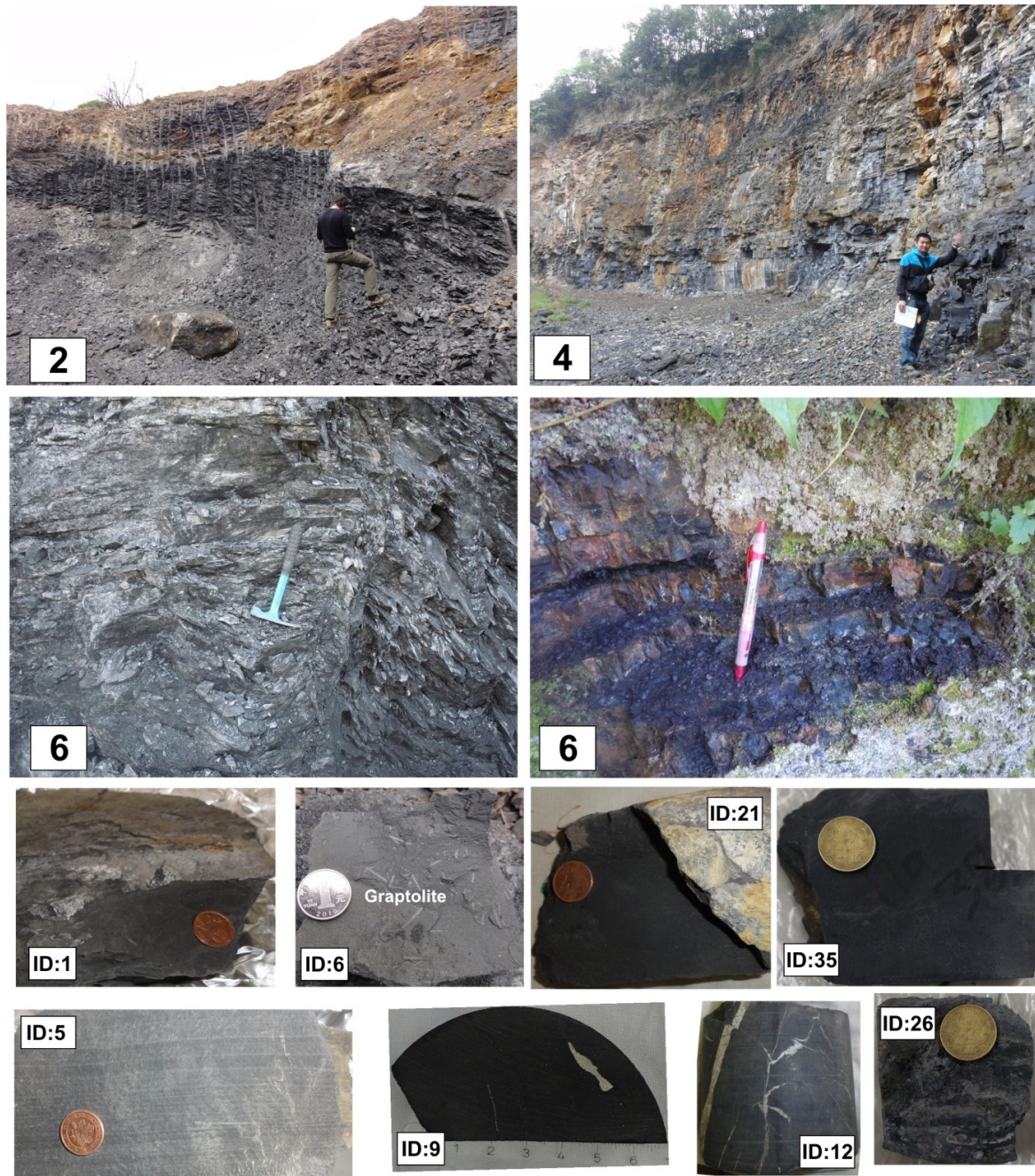


Figure 3.3 Outcrop photographs and selected hand specimens. A-Lower Cambrian shale in the Cengcong profile, Guizhou province; B-Lower Silurian shale in the Guankou profile, Chongqing area; C-Lower Cambrian black (bottom) and silicious (upper) shale in the Jinggang profile, Chongqing area; D-Silicious shale in the Cengcong profile, Guizhou province; E-Lower Silurian calcareous shale sample from the Lujiao profile, Chongqing area; F-Lower Silurian fossiliferous (graptolite) shale sample from the Guankou profile, Chongqing area; G-Lower Silurian mudstone with big pyrite accumulation or segregation, sample from the YY1 well; H-Fractured Lower Silurian mudstone filled with quartz, sampled from the YY1 well; K-Lower Cambrian carbonaceous shale sample from the Cengcong profile, Guizhou area; L-Distinct horizontal laminations in the Lower Cambrian shale, sampled from the Rongxi profile, Chongqing area; M-Ediacaran black shale from the Lijiatuo profile, Hunan province; N-Ediacaran phosphatic shale sample from the Maoshi profile, Guizhou province.

Chapter 3 Geological and Geochemical Characterisation

Table 3.1 Sample information, TOC and Rock-Eval data.

Unit	Profile / Area	Original ID	ID	Depth (m)	TOC (%)	S1 (mg/g)	S2 (mg/g)	Tmax (°C)	HI (mg HC/g TOC)	OI (mg CO ₂ /g TOC)
Lower Silurian-Longmaxi	Lujiao, Chongqing	G009507	1		3.34	0.02	0.28	439	8	14
		G009508	2		3.76	0.05	0.43	598	11	16
		G009509	3		1.68	0.03	0.41	331	24	65
		G009510	4		1.84	0.02	0.31	336	17	20
		G009511	5		0.93	0.02	0.35	599	38	69
	Guankou, Chongqing	G009512	6		3.89	0.02	0.33	601	8	14
		G009513	7		4.00	0.04	0.48	600	12	8
		G009514	8		3.64	0.02	0.33	599	9	23
	YY1 well, Chongqing	G009524	9	136	1.96	0.04	0.37	409	19	35
		G009525	10	207	1.47	0.05	0.42	405	29	31
		G009526	11	267	2.31	0.04	0.43	600	19	22
		G009527	12	276	1.69	0.02	0.33	400	20	20
		G009528	13	285	1.68	0.02	0.26	409	15	22
		G009529	14	321	2.21	0.03	0.34	313	15	45
Lower Cambrian-Niutitang		Rongxi, Chongqing	G009515	15		0.44	0.02	0.38	291	86
	G009516		16		10.20	0.02	0.37	593	4	19
	G009517		17		6.02	0.02	0.33	365	5	8
	Jinggang, Chongqing	G009518	18		7.44	0.05	0.62	281	8	6
		G009519	19		8.15	0.03	0.43	565	5	15
		G009520	20		9.41	0.02	0.35	565	4	4
	Cenggong, Guizhou	G009521	21		5.04	0.03	0.31	600	6	6
		G009522	22		5.79	0.04	0.39	598	7	15
		G009523	23		2.85	0.01	0.23	501	8	48
	Heishapo, Guizhou	He25d	24		0.44	0.03	0.09	445	20	120
		He25e1	25		0.52	0.04	0.11	441	21	76
		He25e2	26		0.39	0.02	0.30	404	77	105
		He29	27		7.79	0.05	0.44	413	6	24
		He30	28		5.80	0.03	0.34	522	6	51
He31		29		7.69	0.01	0.20	411	3	10	
Maoshi, Guizhou		Ma32-2	30		4.42	0.06	0.12	317	3	18
	Ma25	31		2.59	0.02	0.31	403	12	26	
	Ma26	32		3.30	0.08	0.63	421	19	80	
	Ma32-1	33		5.05	0.04	0.39	312	8	19	
	Ma34	34		1.89	0.04	0.39	403	21	61	
	Ma38	35		1.43	0.02	0.38	582	27	18	
	Ediaecran	Li3	36		0.90	0.02	0.05	409	6	30
		Li7b	37		2.10	0.02	0.06	446	3	26
		Li8	38		0.43	0.01	0.27	400	63	288
		Li9a	39		6.15	0.14	0.09	406	1	23
Li12b		40		0.90	0.04	0.05	609	6	49	
Li19a		41		5.90	0.13	0.15	439	3	18	
Li20b		42		1.20	0.02	0.03	413	3	24	
Li21c		43		1.00	0.04	0.21	474	21	199	
Lijiatuo, Hunan		Li22	44		1.73	0.03	0.05	451	3	34
		Li25a	45		12.70	0.46	0.26	283	2	10
		Li26a	46		7.60	0.08	0.09	414	1	28
		Li27	47		13.50	0.23	0.12	422	1	27
		Li28	48		19.00	0.55	0.32	412	2	6
	Li29	49		7.90	0.31	0.16	290	2	4	
	Li30	50		1.30	0.12	0.14	449	11	29	
Li33	51		11.40	0.31	0.09	450	1	16		
Li35	52		4.90	0.05	0.10	467	2	41		
Li37	53		5.30	0.11	0.08	513	2	39		

The location of the profiles and wells are denoted in Figure 3.2.

The remaining rock fragments were then ground to 200-250 μm in an achat-crucible for measuring TOC, Rock-Eval parameters, and volatile compound abundances by thermovaporisation-GC (Tvap-GC), and volatilisable kerogen components using pyrolysis gas chromatography (open py-GC). TOC and Rock-Eval Pyrolysis (Espitalié et al., 1977) were performed on all samples to determine classical screening parameters. For Tvap-GC, roughly 20-30 mg of finely ground powder was weighed into glass capillaries, which were then sealed by an H₂-flame after reducing the internal volume of the tube from ca. 40 ml to ca. 15 ml with pre-cleaned quartz sand. The sealed tubes were then introduced into a Quantum MSSV-2 Thermal Analyzer pyrolysis oven unit interfaced with an Agilent GC 6890A apparatus

Chapter 3 Geological and Geochemical Characterisation

equipped with an HP-Ultra 1 column of 50 m length, 0.32 mm internal diameter and 0.52 μm thickness and an FID. The external surfaces of each tube were purged for 5 min at 300°C, during which time volatiles were also mobilised within the tube and thereafter cracked open by a piston device to transfer generated products from within the vessel by a helium-carrier gas with a flow rate of 30 ml/min into a liquid nitrogen-cooled trap. The trapped hydrocarbons were released to the column by ballistic heating of the trap to 300°C, and then thermovaporisation products were recorded. Py-GC was performed on the remaining powder by heating from 300°C to 600°C using a 50°C/min heating rate (3min, isothermal). Pyrolysis products were again collected in the cryogenic trap and further analyzed using the same GC conditions as for T_{vap}-GC. The GC oven temperature was programmed from 30°C to 320°C at 5°C/min. Quantification of individual compounds and totals was conducted by external standardisation with n-butane. Reproducibility of measured product concentration was generally better than 4% (Schenk et al., 1997). Because of the lower response factor of methane compared to the heavier gases the methane content was multiplied with 1.1.

The artificial maturation products of immature to low mature samples from other parts of the world (Mahlstedt, 2012) were used to help reconstruct the original organic matter type of the generally overmature Paleozoic samples at the UYP. The 4 samples include the type I Green River Shale (USA), the type II Spekk shale (Norway), the type III Are Fm. Coal (Norway), and the type III Westphalian coal (Germany) to represent the classical kerogen types (type I, II and III). Samples were heated to 350, 400, 450 and 500°C using MSSV-pyrolysis (Horsfield et al., 1989) with a starting temperature of 250°C and a heating rate of 1°C/min. Residues were picked and then analyzed as previously described for the Chinese samples.

We also compiled TOC and Rock-Eval data of hundreds of samples from literature about the Lower Cambrian and Lower Silurian profiles or wells in the north, south and east Sichuan Basin (Liang et al., 2008; Liang et al., 2009b) and about typical shales or coals collected in Australia, Germany (Schenk and Horsfield, 1998), New Zealand (Vu, 2008) and the United States (Jarvie, 2008; Kuhn et al., 2010). Finally, the Cooles' method (Cooles et al., 1986) and Claypool's equations (in Peters et al., 2005) were applied to reconstruct original TOC and Rock-Eval parameters of the overmature Chinese samples, and hence the original hydrocarbon generative potential is revealed as input parameter for mass balance calculations.

3.6. Results and Discussions

3.6.1. Organic Matter Richness

Based on thin section and polished section microscopy on 30 samples, the matrix was seen to be composed of quartz and clay minerals, with abundant pyrite and organic material (Figure 3.4). In the thin section photomicrographs (sample 6 and G011315 in Figure 3.4) dark colored amorphous organic matter clusters can be observed within the quartz and clay or shale matrix, as well as along the crinkle to wavy lamination. In polished section photomicrographs (sample 2 and 20 in Figure 3.4) organic matters appear as grey aggregates showing high reflectance (approximately 4%). Organic matters of the examined sample account for 20-30% of the photomicrograph area (sample 20 in Figure 3.4). Its high level of reflectance points to the particles being spent kerogen or pyrobitumen (Tissot and Welte, 1984; Horsfield and Rullkötter, 1994).

The TOC (wt. %) and Rock-Eval data are listed in Table 3.1. Figure 3.5 illustrates that TOC content ranges between 1 and 19%, with TOC content almost positively correlated with increasing geological age, i.e. the Longmaxi shales (Lower Silurian) exhibit generally lower TOC contents than that of the Niutitang shales (Lower Cambrian), which commonly exhibit lower TOC contents than that of the Ediacaran shales. The TOC content of the Longmaxi shales mainly range from 1% to 3% showing the lowest average value of 2.5% of all investigated samples. The TOC values of the Niutitang shales range from 0.4% to 10.2 % possessing an average value of 5.2%. Particularly, the TOC contents of phosphatic samples from the Niutitang interval are lower than 1%. The highest TOC concentration can be found for the Ediacaran shales for which half of samples exhibit more than 4% TOC, with maximum contents exceeding 10% by far, at least in one profile located in the western Hunan. The organic matter richness of the measured samples can thus be described as moderate to very high, which is an important parameter for evaluating either conventional petroleum systems (Tissot and Welte, 1984; Peters and Cassa, 1994; Hunt, 1995; Peters et al., 2005) or unconventional petroleum systems (Curtis, 2002; Montgomery et al., 2005; Jarvie et al., 2007; Kinley et al., 2008; Ross and Bustin, 2008; Rodriguez and Philp, 2010; Hackley, 2012). Clearly, the TOC content of the original immature equivalents of these samples was much higher than the present values, the factor being dependent on original kerogen type. In addition, high TOC may indicate an anoxic environment. The abundance of organic matter thus reflects the fact that the UYP sea floor was at times of deposition likely anoxic, for if the

Chapter 3 Geological and Geochemical Characterisation

sea bottom had been oxic, aerobic bacteria would have thrived and consumed much of the organic material (Tissot and Welte, 1984).

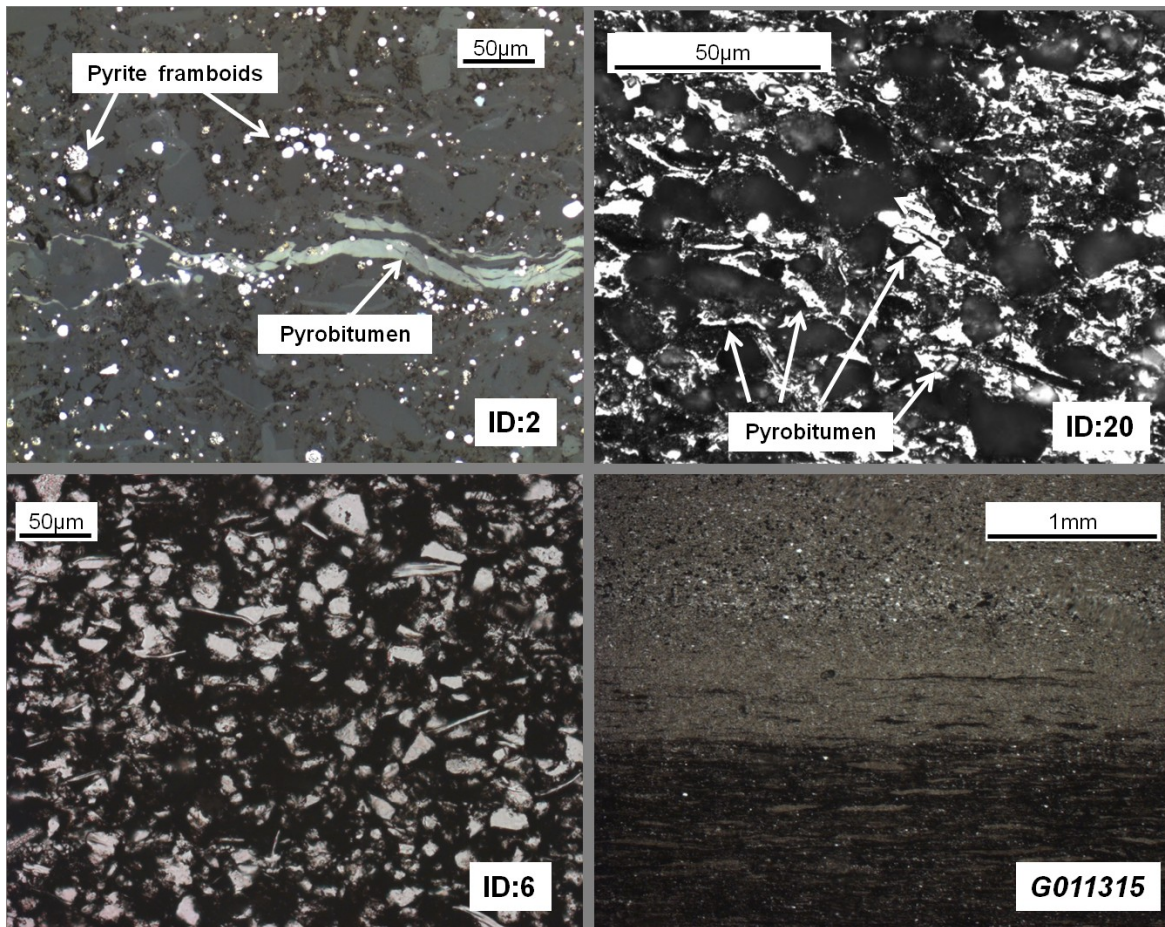


Figure 3.4 Organic matter in section photomicrographs of selected and representative shale samples. 2-Organic matter (pyrobitumen) and pyrite framboids (polished section with reflected light). 20-Disseminated pyrobitumen in shale matrix, with light reflectance of the bitumen is over 4.0 % (polished section, reflected light). 6-Unlaminate siliceous shale showing organic matter (black), platy clay or mica minerals and subrounded to angular detrital quartz grains (white) (thin section, plane polarized light). G011315-Siliceous shale showing graded bedding with crinkle to wavy laminated organic matter in the bottom and lower organic content in the more granular top (thin section, plane polarized light).

Published TOC results support the above findings. High TOC concentration is demonstrated by the hundreds of samples taken from 8 profiles/wells within the UYP (Figures 3.2 and 3.6). Most of the profiles exhibit higher TOC concentrations in the lower part, where black shale is present, and lower TOC concentrations in the upper part, where carbonates, mud, and/or siltstone dominate (Editorial Committee of the Sichuan Oil & Gas field, 1989; Liang et al., 2008; Cheng et al., 2009). Furthermore, those TOC contents fit to the published isopach maps. On the basis of detailed TOC analysis on 3811 marine source rocks collected from 121 profiles/wells in the Yangtze platform (Liang et al., 2008), Cheng et al (2009) and

Dong et al (2010) prepared isopach maps for Lower Cambrian and Lower Silurian black shale successions in southeast Sichuan, Chongqing, north Guizhou, and west Hunan and Hubei, exhibiting thicknesses from 20 to 200 m for shale units with TOC values exceeding 2%.

3.6.2. Thermal History and Maturity

The Ediacaran and Lower Palaeozoic source rocks did not commence to generate considerable thermogenic hydrocarbon until the Late Permian to Early Triassic, as a result of the prolonged uplift in the course of the Late Caledonian and Yunnan orogeny between the Late Silurian and Carbonaceous (Huang et al., 1997; Zhang et al., 2007a; Zhang et al., 2007b; Wang et al., 2009a). The principal period of hydrocarbon generation from kerogen (primary cracking) of the Lower Paleozoic shales was suggested to have occurred between the Late Triassic and Early Jurassic. During this period, these intervals were buried between 2000 m and 4000 m which indicate a geo-temperature range of 120-165°C. In the course of the continuous burial and kerogen conversion secondary cracking processes started to form light hydrocarbon products since the Early Jurassic. By the end of the Jurassic, the Lower Paleozoic shales endured maximum burial of 6000 m and the highest temperature of 220°C (Tan et al., 2013). In this regard, the present organic matter in the investigated Ediacaran and Lower Paleozoic source rocks should have been overmature, having evolved far into the metagenesis stage (Tissot and Welte, 1984; Horsfield and Rullkötter, 1994).

Using microscopic images dark organic clusters can be observed under transmitted light on thin sections and bright-grey organic aggregates with intense bitumen reflectance (as much as 4.0%) can be seen under reflected light on polished sections (Figure 3.4). Rock-Eval Pyrolysis of whole rocks also indicates the high thermal maturity. Investigated samples exhibit, even though organic matter rich, very low S₂ (<0.65 mg HC/g rock) and consequently low HI values (<100 mg HC/g TOC) (Table 3.1). Vitrinite reflectance (R_o) is the most widely used key measure for thermal maturity. Nevertheless, it is not suitable for the Ediacaran and Lower Paleozoic source rocks since vitrinite in its strict sense does not exist in sediments deposited before Devonian times. Nevertheless, methods have been set up to compare equivalent parameters with R_o, for instance, bitumen reflectance (Jacob, 1967; Jacob, 1985; Buchardt and Lewan, 1990; Pawlewicz and King, 1992; Bertrand, 1993) and carbon isotope ratios (Stahl, 1974; Stahl and Carey Jr, 1975; Schoell, 1980; James, 1983; Laughrey and Baldassare, 1998; Prinzhofer et al., 2000).

Chapter 3 Geological and Geochemical Characterisation

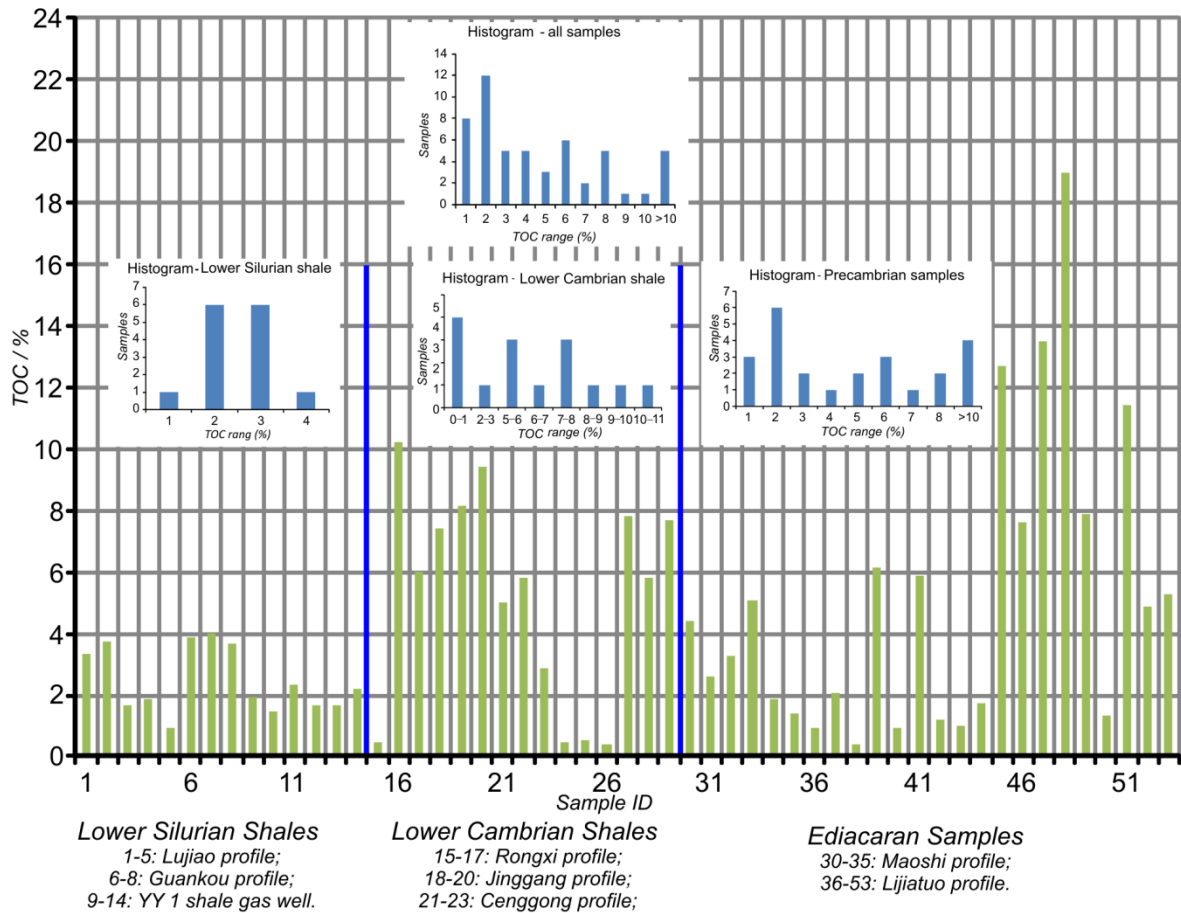


Figure 3.5 Histograms of TOC content in relation to stratigraphic age. The TOC content almost positively correlates with increasing geological age. Sample IDs are denoted Table 3.1.

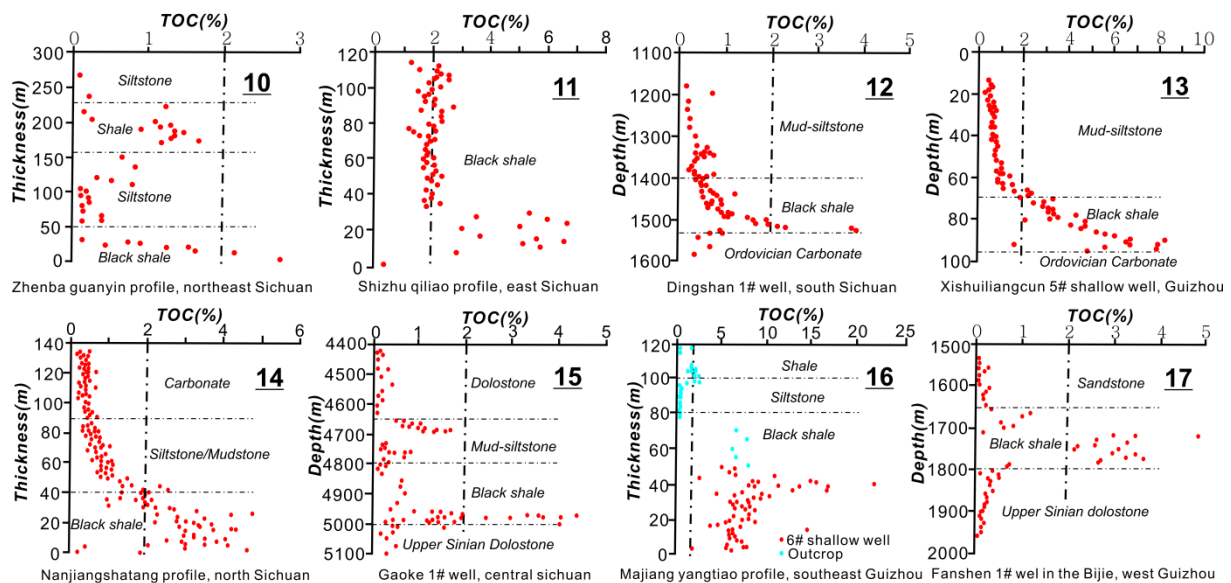


Figure 3.6 TOC content versus stratigraphic depth for 8 sections studied on the UYP. A-H: data compiled profiles from (Liang et al., 2008), 10-13 are the Lower Silurian profiles/wells. 14-17 are the Lower Cambrian profiles/wells. The locations are denoted in Figure 3.2.

Chapter 3 Geological and Geochemical Characterisation

For the Sichuan Basin, UYP, Feng and Chen (1988) reported a formula to calculate R_o via bitumen reflectance (R_b):

$$R_o = 0.3195 + 0.6790R_b \quad (3.1)$$

This formula was deduced from thermal experiments on oil shale, and examined by applying the calculated R_o to the Permian source rocks in the Sichuan Basin. An excellent correlation of the real measured R_o and the calculated R_o was found (Feng and Chen, 1988). Measured R_b of investigated Lower Cambrian shales is, as stated above, as high as 4.0%, which translates to a R_o of about 3.0%.

The isotopic behavior of natural gas can be explained by differences in the binding energy of molecules. Instantaneous methane should, related to the kinetic isotope effect, become increasingly enriched in the ^{13}C isotope with increasing thermal stress, i.e. with increasing maturity of the source rock (Stahl, 1974; Stahl and Carey Jr, 1975). Thus, $\delta^{13}\text{C}$ of methane ($\delta^{13}\text{C}_1$) can be used to deduce R_o and thus reveal thermal maturity. In the current work, $\delta^{13}\text{C}_1$ has been measured for two samples containing methane inclusions. Measured $\delta^{13}\text{C}_1$ values are -33.20‰ for the Lower Silurian shale and -28.99‰ for the Lower Cambrian shale. Figure 3.7 illustrates the correlations between $\delta^{13}\text{C}_1$ and R_o . It shows results of a series of marine source rocks from the Devonian through Carboniferous strata in the Val Verde and Delaware Basins (Barnett shale, USA) (Stahl and Carey Jr, 1975) and a series of German Carboniferous coal samples (Schoell, 1980). The UYP shale samples are obviously in agreement with the Barnett shale, and thermal maturities of the Lower Silurian and Lower Cambrian shale could be extrapolated to a R_o range of 2.5-3.0% and 3.0-3.5%, respectively (Figure 3.7). For the Ediacaran shale, the thermal maturity should be generally higher than that of the Lower Silurian and Lower Cambrian samples, and a R_o range of 3.5-4.0% is assumed according to the modeling results (Tan et al., 2013). The vitrinite reflectance values present here are consistent with those deduced from R_b which have been extensively published (Liang and Chen, 2005; Liang et al., 2009b; Wang et al., 2009a; Wang et al., 2009b; Nie et al., 2011; Huang et al., 2012a; Long et al., 2012; Yu et al., 2012).

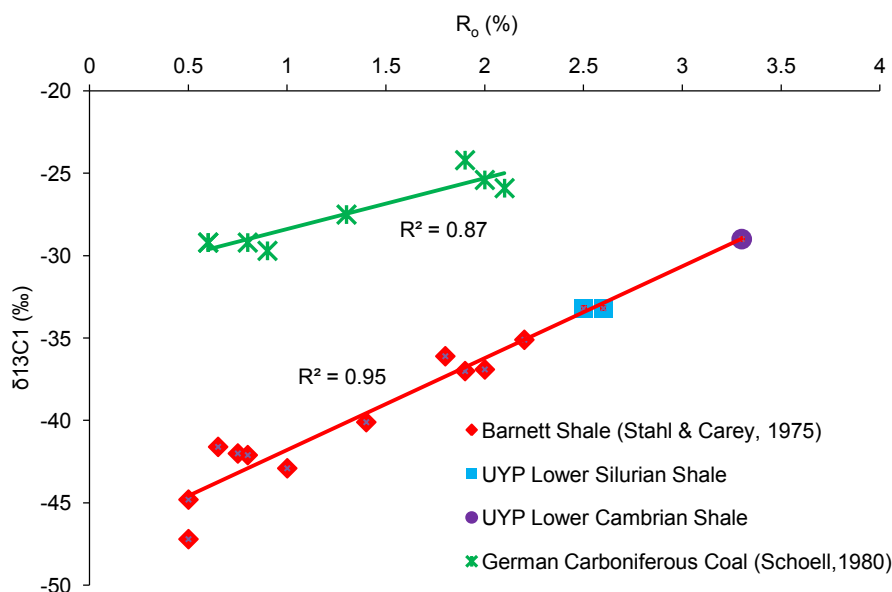


Figure 3.7 Compilation of $\delta^{13}\text{C}$ of methane ($\delta^{13}\text{C}_1$) versus vitrinite reflectance R_o . Carbon isotopic composition of methane and vitrinite reflectance are positively correlated for both marine source rocks as well as terrestrial coal samples, with both arrays being considerably offset. This is reflected in $\delta^{13}\text{C}_1$ -values from marine source rocks being more fractionated than $\delta^{13}\text{C}_1$ -values from terrestrial coal. Values for UYP samples are in agreement with values measured for the Barnett shale (Stahl & Carey, 1975) plotting on the extrapolation towards higher $\delta^{13}\text{C}_1$ and higher vitrinite reflectance, respectively.

3.6.3. Sorbed Hydrocarbon Composition as Revealed by Tvp-GC

Tvp-GC is a method of gas chromatography capable of resolving the S_1 peak of Rock-Eval pyrolysis, which represents the bulk of retained hydrocarbons within the rock. Because free gas is lost either during the sampling or preparation process (crushing), gas measured using Tvp-GC primarily reflects the fraction of sorbed gas which might accumulate on the surfaces of minerals or organic matter and/or retained gas which may be stored in unconnected pores. Mahlstedt and Horsfield (in preparation) have recently outlined how Tvp-GC can be used to screen samples based on their sorption capacity. In the current investigation, 14 samples were subjected to Tvp-GC analysis to quantify the retained/sorbed hydrocarbons that were generated during the early geological history of the rocks (Table 3.2). Because the samples were taken from outcrops or depths shallower than 350 m, the measurable hydrocarbon amounts are less than 10 mg/g TOC, i.e., extremely low. Generally, the Tvp-GC results from the core samples are higher than those from the outcrops. In addition, the detectable hydrocarbons in overmature source rocks were expected to be

Chapter 3 Geological and Geochemical Characterisation

dominated by light hydrocarbons. Hence, the measured products primarily consist of methane (C_1), ethane (C_2), propane (C_3), butane (C_4), pentane (C_5), and benzene. Interestingly, C_1 , C_3 , and C_4 are major components of the core samples. C_5 and benzene are present in high amounts in certain outcrops, whereas the levels of C_2 are low in the majority of the samples (Table 3.2).

Table 3.2 T_{vap}-GC products in ug/g TOC.

Unit	Lower Silurian shale						Lower Cambrian shale					Ediacaran shale		
Sample-ID	9	10	11	12	13	14	16	17	18	19	20	39	41	51
Depth (m)	136	207	267	276	285	321	0	0	0	0	0	0	0	0
TOC (%)	1.97	1.47	2.31	1.69	1.68	2.21	10.20	6.02	7.44	8.15	9.41	6.15	5.90	11.40
C_1	50.66	68.50	13.81	64.56	52.98	75.25	0.79	7.96	7.47	8.98	3.91	8.44	9.71	17.87
C_2	13.55	24.08	15.41	34.97	14.64	26.92	3.02	5.30	4.70	5.55	1.71	7.35	7.17	16.69
C_3	34.47	95.44	45.97	292.01	51.61	180.14	2.36	6.26	7.96	4.66	2.55	15.41	12.78	6.19
C_4	104.62	391.43	212.60	296.75	210.48	393.85	5.30	36.45	19.58	12.17	10.38	45.93	59.81	31.74
C_5	6.19	44.76	35.97	39.70	39.82	111.13	2.71	11.03	57.07	173.87	2.62	126.65	149.83	9.65
Benzene	0.00	32.86	43.72	42.25	23.63	127.01	9.86	40.78	9.33	9.99	5.88	55.56	38.07	35.97
Σ total identified	209.49	657.07	367.49	770.24	393.15	914.30	24.05	107.77	106.12	215.21	27.06	259.35	277.37	118.11
Σ products	1707.56	2551.56	3397.71	6516.98	1610.36	7600.05	44.63	271.81	205.50	401.88	96.17	1189.59	525.49	183.45

3.6.4. Remaining Hydrocarbon Generative Potential as Revealed by open py-GC

The low remaining hydrocarbon generative potential of selected samples is illustrated in Figure 3.8. The HI of the UYP shales is much lower than that of the samples containing types II and III kerogen from the United States, Germany, and New Zealand. Open py-GC was performed on 34 samples to investigate the remaining hydrocarbon generative potential on a molecular level. The pyrolysates are primarily composed of light hydrocarbons, i.e., methane (C_1), ethane and ethene (C_2), propane and propene (C_3), butane and butene (C_4), pentane and pentene (C_5), and benzene (Figure 3.9 and Table 3.3). In general, the Lower Silurian shales are capable of generating higher yields than the Lower Cambrian and Ediacaran shales (Figure 3.9, A and B in Figure 3.10), indicating somewhat lower maturities. C_1 is by far the dominant product, and C_2 and benzene can be detected in relatively high amounts in the pyrolysates from the cores and certain outcrop samples (Figure 3.10C and D). Individual hydrocarbon compounds generated by the core samples display no significant variations with depth (Figure 3.10E), whereas a generally positive correlation between the levels of C_5 and TOC can be observed (Figure 3.10F). In addition, the amount of total hydrocarbon of per gram TOC of the Lower Silurian core samples is higher than that of most outcrop samples (Figure 3.10B).

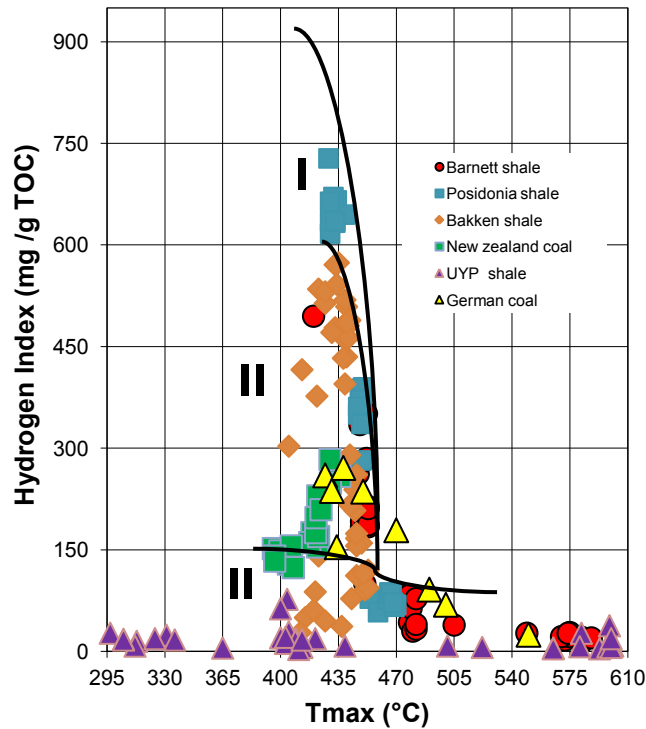


Figure 3.8 HI- T_{max} plot of different source rocks, comprising the UYP shale, Barnett shale (Jarvie, 2008), Bakken shale (Kuhn et al., 2010), Posidonia shale (Schenk and Horsfield, 1998), German coal (Schenk and Horsfield, 1998), and New Zealand coal (Vu, 2008).

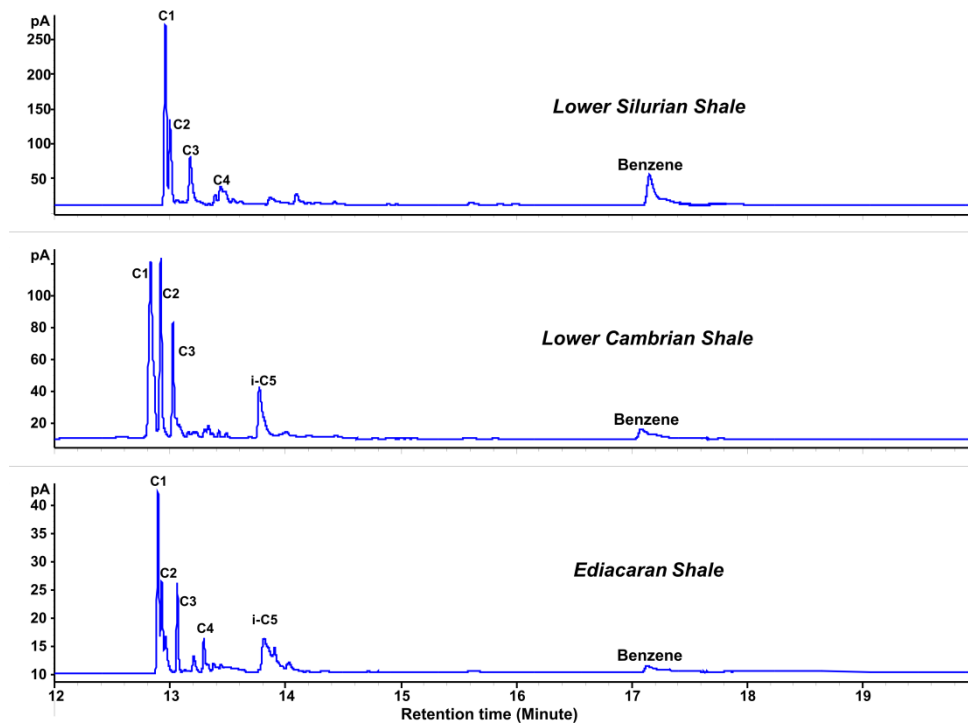


Figure 3.9 The dominant open py-GC pyrolysates of the Lower Silurian, Lower Cambrian and Ediacaran shale sample. Considerable differences in open py-GC pyrolysate composition are found for the respective units. The Lower Silurian sample shows relatively stronger yields than that of the Lower Cambrian sample which in turn has higher yields than the Ediacaran sample.

Chapter 3 Geological and Geochemical Characterisation

Table 3.3 Open py-GC products in ug /g TOC.

	Sample-ID	1	2	3	4	5	6	7	8	9	10	11	12	13	14
Lower Silurian Shale	Depth (m)	0	0	0	0	0	0	0	0	136	207	267	276	285	321
	TOC (%)	3.34	3.76	1.68	1.84	0.93	3.89	4	3.64	1.97	1.47	2.31	1.69	1.68	2.21
	C1	700.8	374.6	320.4	641.4	325.6	140.6	121.2	174.8	395.7	392.9	345.5	359.1	397.9	391.2
	C2	327.6	183.5	120.6	141.1	166.4	165.4	48.5	53.2	174	245.9	200.8	222.8	175.3	160.8
	C3	170.4	108.3		134	153.9	100.1	26.9	22.9	142.8	211.1	71.7	147.8	165.4	83.4
	C4	47.8	36.6			129	66.5	9.3	9.2	101.3	231.9	101.8	160	146.5	235.7
	C5	38.3	44.7	39.1	111.8	76.3	27	20.8	18.5	38.7	74.8	30.4	72.4	57.6	54.3
	C6			18.8			33.6			14.7	19	12.3	15.6	14.9	18.9
	Benzene	27	51.1	76.8	50.5	49.2	117.9	36.2	47.7	240.7	227.8	178.5	207.8	211.1	249.5
	Σ total identified	1311.9	798.8	575.7	1078.7	900.4	651.1	262.9	326.3	1107.9	1403.5	941	1185.5	1168.6	1193.8
	Σ products	1607.6	1688	1439.5	1613.5	1276.3	2865	377	469.7	1740.8	2984.1	2011.8	2252.1	1840.5	2774.2
Lower Cambrian Shale	Sample-ID	15	16	17	18	19	20	21	22	23	26	27	28	29	
	Depth (m)	0	0	0	0	0	0	0	0	0	0	0	0	0	
	TOC (%)	0.45	10.2	6.02	7.44	8.15	9.41	2.85	5.79	5.04	0.39	7.79	5.81	7.69	
	C1	166.9	17.7	18.7	31.5	14.5	16.8	75	106	95	408.2	23.1	262.5	96.2	
	C2	164	8.4	15.9	39.7	15.3	12	70.9	52.2	48.2	670.3	11.7	35.9	36.4	
	C3	83.6		8.7	26.5	7.8	9.1		34.6	24.8	220.5	6.3	15.1		
	C4	55.6		6.3	17.8	3.7	3.5	20.5	7.1	9.8	156.2	4.6	14.7	7.3	
	C5	33.7		14.5	53.6	13.8	31.4	79.4	33.1	60.4	135.5	35	40.1	44.6	
	C6														
	Benzene		5	7.8	6.4	0	3.9	175.4	11	12.9	59.1	4.8	219.8	170.9	
	Σ total identified	503.9	31	72	175.4	55.2	76.7	421.1	243.9	251	1649.7	85.5	588.2	355.4	
Σ products	1339.3	72.9	165.8	464.5	95.7	102.4	1581.5	382.2	389.8	3547.9	143.4	1183.6	787		
Ediacaran Shale	Sample-ID	31	32	33	34	35	38	41							
	Depth (m)	0	0	0	0	0	0	0							
	TOC (%)	2.59	3.3	5.05	1.89	1.43	0.43	6.7							
	C1	37.4	40.6	30	181.4	81.7	515.2	23.3							
	C2	28.3	91.4	20.2	149.1	80.7	510.4	21.9							
	C3	14.7	30.4	12.2	34.7	51.1	258.3	11.1							
	C4	8.7	54.7	7.5		58.4	170.9	4.9							
	C5	22.6	48.3	7.2	110	79.3	244								
	C6														
	Benzene	5.6													
	Σ total identified	117.3	265.3	77.1	475.2	351.2	1698.8	61.2							
Σ products	204.2	520.7	184.6	2823.9	612.4	2919.3	158.8								

The relatively high remaining generative potential of the Lower Silurian shale can be principally attributed to the progressive increase in thermal maturity with geological age, i.e., from the Lower Silurian to Lower Cambrian to Ediacaran strata, although the effects of the mineralogy and weathering on the kerogen decomposition cannot be ruled out. The highest remaining hydrocarbon potential per gram of TOC is observed in the two samples with the lowest TOC concentrations (<0.5%) (Figure 3.10 B). It has been reported, however, that the primary heavy products of whole rocks can be trapped on mineral surfaces or interlayers, which can then be cracked into light hydrocarbon with temperature increases (Eisma and Jurg, 1967; Espitalié et al., 1980; Horsfield and Douglas, 1980). The highest pyrolysis yields from organic matter lean samples may therefore be attributed to the thermal decomposition of formerly retained bitumen, on a TOC normalised basis. Weathering may also impact the properties of the organic matter in the shales. It has been reported that the weathering process could result in decrease of TOC content, enrichment of ¹³C, and variation of kerogen structure (Leythaeuser, 1973; Clayton and Swetland, 1978; Clayton and King, 1987; Littke et al., 1991; Petsch et al., 2000; Wildman et al., 2004; Fischer et al., 2009; Marynowski et al., 2011). A decrease in TOC during weathering is consequently accompanied by a pronounced reduction in the remaining hydrocarbon generative potential, which may be responsible for the

Chapter 3 Geological and Geochemical Characterisation

relatively low TOC content in core samples showing higher generative potentials than most of the outcrops (Figure 3.10A).

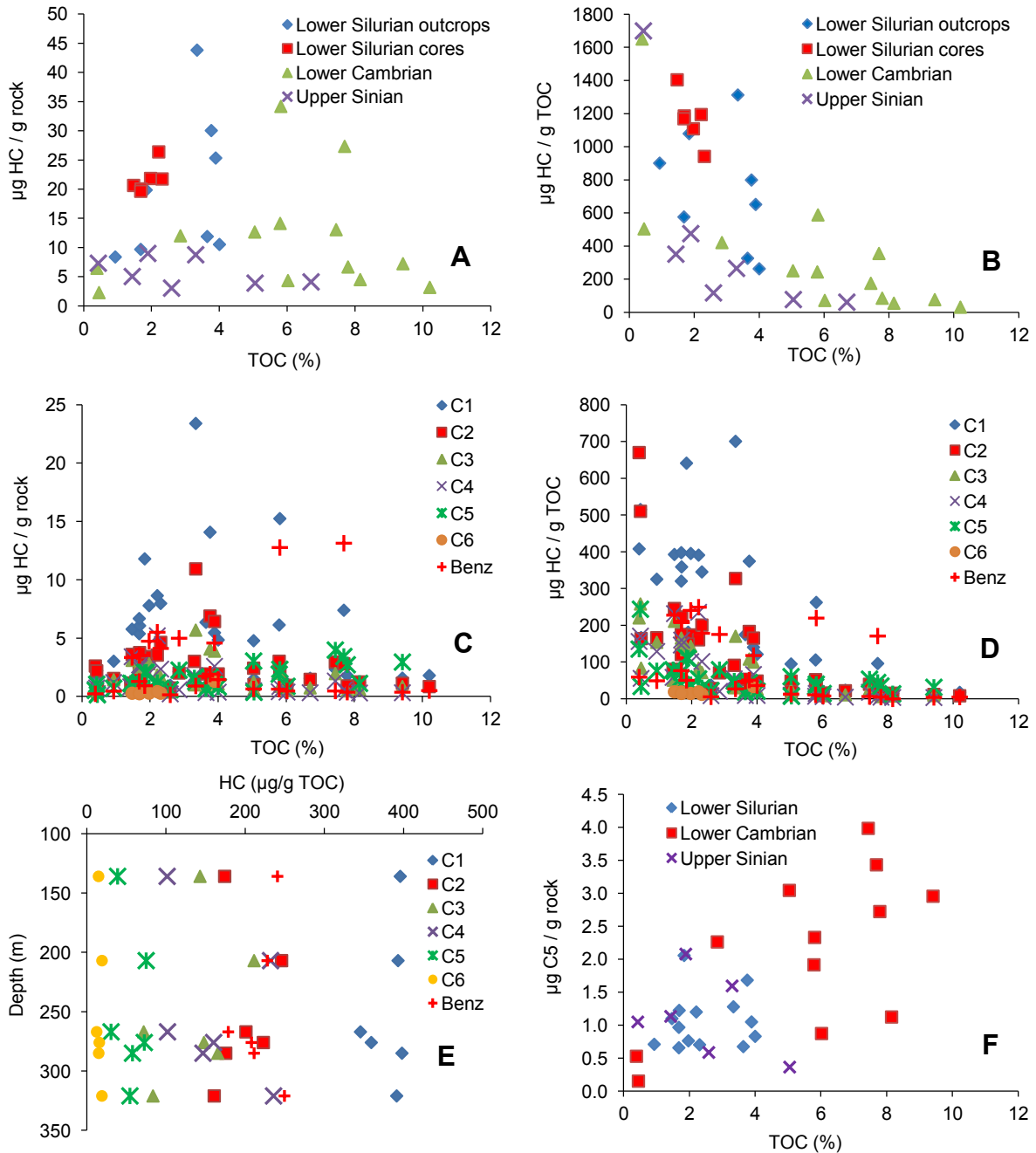


Figure 3.10 Open py-GC products of selected samples. A-Total amount of open py-GC products of per gram rock; B-Total amount of open py-GC products, values were normalized to TOC weight; C-The amount of the identified light hydrocarbons in per gram rock; D-The amount of the identified light hydrocarbons, values were normalized to TOC; E-Light hydrocarbons vs. depth of the core samples; and F-The correlations between C5 and TOC.

3.6.5. Evolution of Kerogen Structure and Hydrocarbon Generation Properties

Because the selected UYP shales were subjected to metagenesis, it is a major challenge to discern their original kerogen properties (generation potential, gas versus oil potential, and thermal lability) based on their present-day organic matter compositions. We have attempted to surmount this problem by comparing their pyrolysis-GC characteristics with those of naturally and artificially matured samples from other parts of the world.

Artificially matured samples

Immature to low-maturity samples containing all of the three classical kerogen types were artificially matured using Micro-Scale-Sealed-Vessel (MSSV) pyrolysis, and the residues were subsequently analysed using open-system py-GC to investigate the evolution of the macromolecular components of the kerogen and hydrocarbon generation properties as the temperature progressively increases. The analysed samples are of low maturity and rich in organic matter (Table 3.4). The results of open py-GC analyses of residues were taken from Mahlstedt (2012), and the TOC contents in the residues were determined in this study in order that the results could be normalised to TOC. The py-GC results of the artificial residues are listed in Table 3.5 and plotted in Figure 3.11 and 3.12. This work was performed based on the assumption that the evolutionary stages of the kerogens at temperatures of 350°C, 450°C and 500°C (heating rate of 1°C/min) roughly correlate with the zones of diagenesis, catagenesis, and metagenesis in sedimentary basins (as defined in Tissot and Welte, 1984).

Table 3.4 Properties of artificially matured samples.

Samples ID	Kerogen type	Basin/Region	Age	Sedimentary environment	TOC (%)	S1 (mg/g)	S2 (mg/g)	S3 (mg/g)	HI (mg HC/g TOC)	OI (mg CO ₂ /g TOC)	Tmax (°C)	PI (wt ratio)
GRS	I	Uinta, USA	Tertiary	Lacustrine	12.82	1.79	99.58	0.73	777	6	445	0.02
Spekk Fm.	II	Haltenbanken, Norway	Late Jurassic	Marine	7.19	2.03	26.65	3.11	371	43	417	0.07
Are Fm.	III	Haltenbanken, Norway	Early Jurassic	Fluvio-deltaic	39.36	4.65	70.87	34.17	180	87	416	0.06
GRS+Are Fm.	I+III				31.3	2.7	82.87	16.39	265	52	434	0.03
Westf. coal	III	Germany	Late Carboniferous	Terrestrial	79.3	3.25	164.9	5.08	208	6	438	0.02

TOC of the residues of the mixed sample (GRS+Are Fm.) is simply estimated by assuming 50% TOC of GRS and 50% of Are Fm. Coal.

Chapter 3 Geological and Geochemical Characterisation

Table 3.5 Open-GC products of the original samples and artificially matured residues.

ID	MSSV-temp	TOC	C1+	C1	C2-C5	C1-C5	C6+	Aromatics	Monoaromatics	Diaromatics	Aromaticity1	Aromaticity2	Gas Wetness	GOR
GRS	200	12.82	908.9	16.7	99.8	116.5	792.3	15.88	14.62	1.26	0.08	0.02	0.86	0.15
	350	13.71	843.3	15.4	95.4	110.8	732.5	13.17	12.11	1.07	0.07	0.02	0.86	0.15
	400	12.73	639.5	15.5	80.6	96.0	543.4	9.57	8.68	0.89	0.07	0.02	0.84	0.18
	450	7.42	139.6	12.9	17.3	30.3	109.3	2.42	1.97	0.45	0.16	0.02	0.57	0.28
	500	5.41	21.3	4.1	2.8	6.8	14.5	0.97	0.58	0.39	0.84	0.07	0.40	0.47
Spekk Fm.	200	7.19	419.6	20.1	62.3	82.5	337.1	15.00	12.81	2.19	0.24	0.04	0.76	0.24
	350	8.12	331.3	17.9	53.7	71.6	239.7	10.26	8.90	1.36	0.22	0.04	0.75	0.28
	400	7.70	174.7	15.5	35.6	51.1	123.6	5.40	4.67	0.73	0.20	0.04	0.70	0.41
	450	6.86	30.5	9.6	7.1	16.7	13.9	1.49	1.21	0.28	0.42	0.11	0.42	1.21
	500	6.94	7.7	2.6	1.1	3.7	4.0	1.12	0.62	0.49	0.80	0.28	0.30	0.92
Are Fm.	200	39.36	168.4	21.6	30.2	51.8	116.6	8.77	6.88	1.90	0.27	0.08	0.58	0.44
	350	50.81	155.7	21.8	26.5	48.4	107.3	7.83	6.17	1.66	0.26	0.07	0.55	0.45
	400	51.88	100.0	20.0	20.3	40.2	59.7	5.13	4.02	1.11	0.29	0.09	0.50	0.67
	450	53.80	43.5	14.0	7.0	21.0	22.6	3.08	2.10	0.98	0.39	0.14	0.33	0.93
	500	52.43	16.9	4.5	1.6	6.1	10.8	3.13	1.92	1.21	0.52	0.29	0.26	0.56
GRS+Are Fm.	200	31.30	263.5	18.3	40.0	58.3	205.2	9.83	8.32	1.51	0.17	0.05	0.69	0.28
	350	32.26	286.2	18.7	38.0	56.7	229.4	7.94	6.67	1.27	0.14	0.03	0.67	0.25
	400	32.31	187.9	18.6	31.4	50.0	137.9	5.77	4.80	0.97	0.15	0.04	0.63	0.36
	450	30.61	55.3	13.2	8.7	21.9	33.4	2.08	1.51	0.58	0.33	0.06	0.40	0.66
	500	28.92	16.9	4.7	1.6	6.3	10.6	2.23	1.16	1.06	0.60	0.21	0.25	0.59
Westf.Coal	200	79.30	140.0	21.2	23.6	44.8	95.2	6.57	5.19	1.39	0.26	0.07	0.53	0.47
	400	83.17	122.9	19.7	19.6	39.3	83.6	5.31	4.12	1.19	0.26	0.06	0.50	0.47
	450	90.07	55.6	14.1	7.3	21.4	34.3	2.82	2.07	0.75	0.36	0.08	0.34	0.62
	500	88.76	12.9	4.7	1.0	5.7	7.3	1.82	1.07	0.76	0.58	0.25	0.17	0.78

MSSV-temp is the temperature (°C) applied to make artificial residues. Unit of TOC is wt.%, and all hydrocarbon products have been normalized to mg HC /g TOC. Total yields are C₁₊. Gas wetness equals (C₂-C₅)/(C₁-C₅). GOR is gas oil ratio that equals (C₁-C₅)/(C₆₊). Aromaticity1 is (aromatics) / (C₆₊ identified components), while aromaticity2 is (aromatics)/(C₆₊).

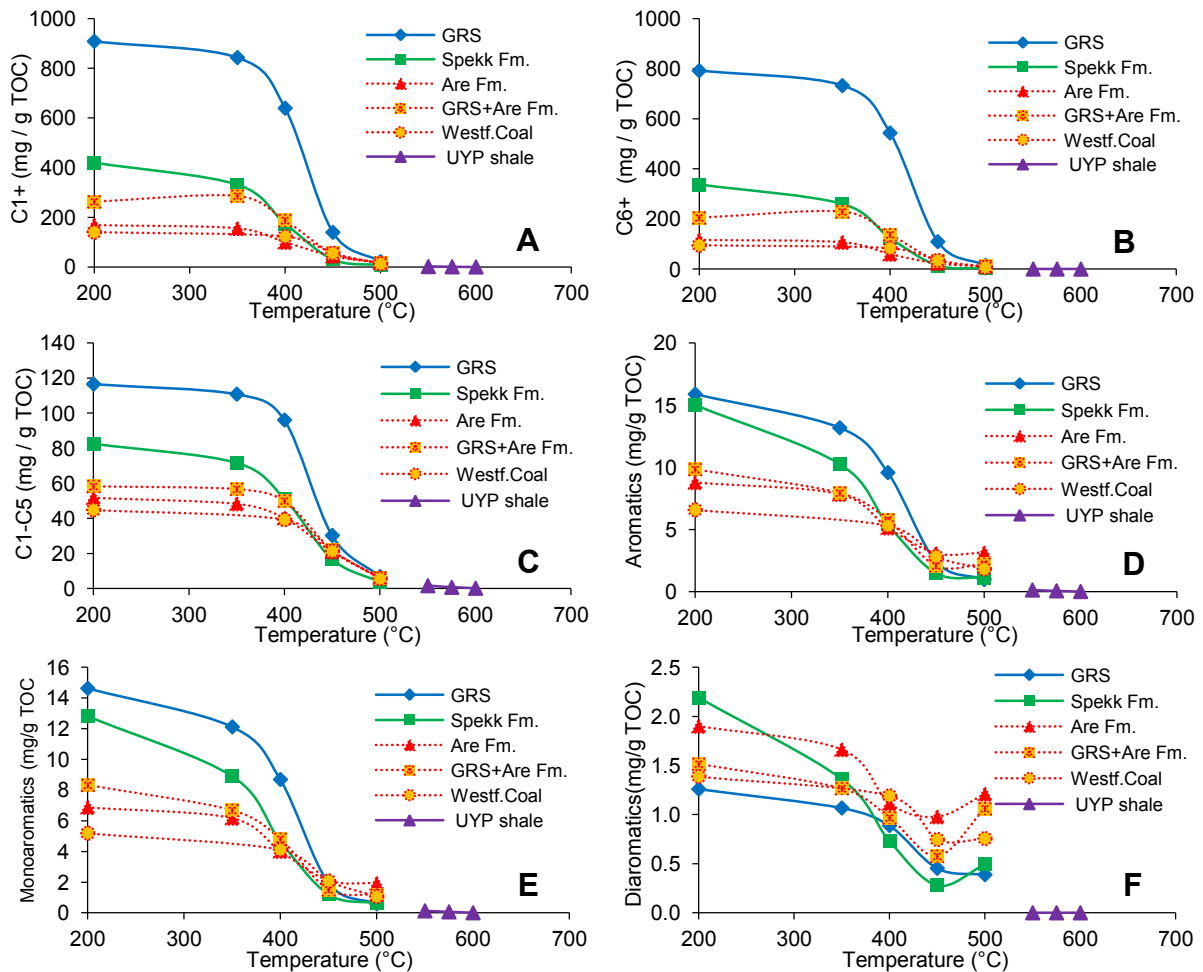


Figure 3.11 X-Y plots of open-py-GC products and temperature illustrating the remaining hydrocarbon generative potential of artificially matured residues.

Chapter 3 Geological and Geochemical Characterisation

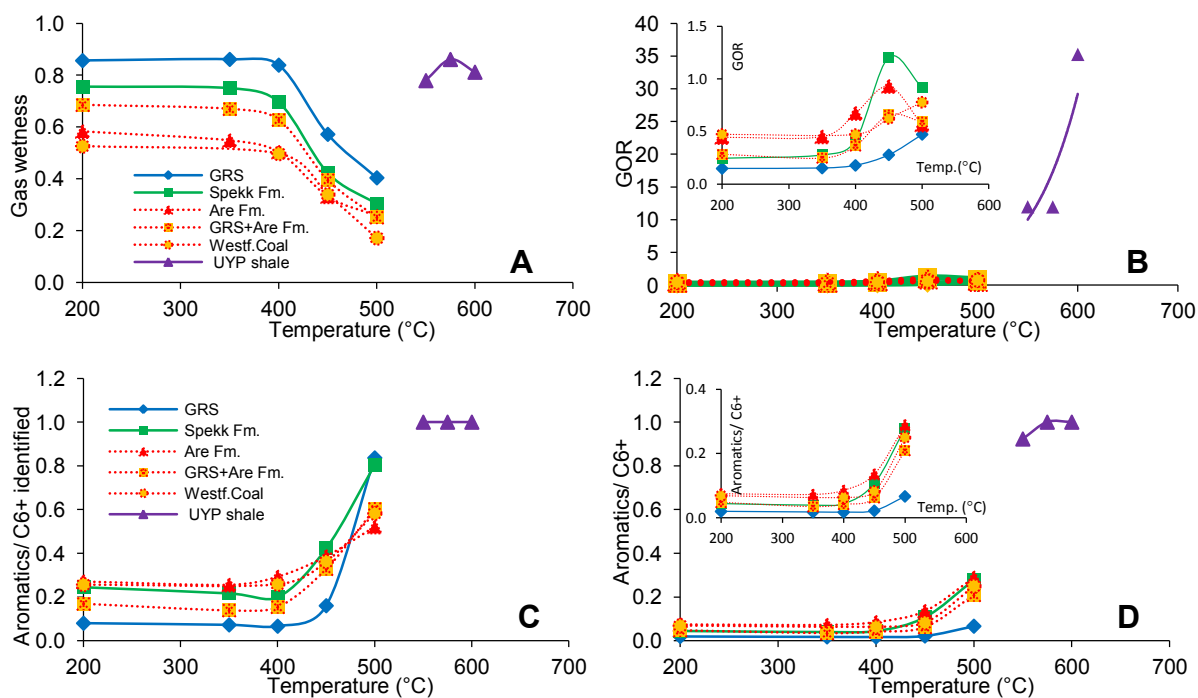


Figure 3.12 Variation gas wetness (A), GOR (B) and aromatics (C and D) of artificially matured residues, as a function of temperature.

The evolutionary paths of these three kerogen types with the increase in temperature are qualitatively comparable, but their quantitative aspects vary from one type to another due to the differences in the original components of the kerogen. Immature type I kerogen is characterised by a high abundance of aliphatics and low amounts of polyaromatics and heteroatomics, with oxygen being present primarily in the ester bonds (Tissot and Welte, 1984; Vandenbroucke and Largeau, 2007). In the measured temperature range, the sample with type I kerogen from the Green River Shale (GRS) consequently exhibits distinctly high levels of total yield, total liquid (C_{6+}), and total gas hydrocarbons (C_{1-5}) (Figure 3.11A-C). As a result, the level of gas wetness is high, and the GOR is low across the entire temperature range (Figure 3.12A and B). In addition, the GRS sample generates the highest absolute amounts of aromatic compounds (Figure 3.11D), although both of the aromaticity ratios, i.e., the sum of the identified aromatics divided by the sum of all identified C_{6+} compounds (defined here as aromaticity1) and the sum of the identified aromatics divided by the sum of C_{6+} (defined here as aromaticity2) are generally low (Figure 3.12C and D). As a result of the abundance of moderately long aliphatic chains and more polyaromatic- and heteroatomic-dominated moieties, the artificially matured sample containing type II kerogen displays a moderate generative potential. The yields of gas, C_{6+} compounds, and aromatic compounds and the product ratios of gas wetness, GOR, aromaticity1, and aromaticity2 fall within the ranges of those obtained from samples containing kerogen of types I and III (Figures 3.11 and

Chapter 3 Geological and Geochemical Characterisation

3.12). The artificially matured samples containing type III kerogen exhibit the lowest generative potential due to a lack of aliphatic moieties in their kerogen structure. The high proportion of oxygenated functional groups and polyaromatics results in a high overall aromaticity. However, the Are Fm. and Westfalian coal samples (type III kerogen) generate more methane over the entire measured temperature range than do other samples and thus exhibit a low gas wetness and a high GOR (Figure 3.12A and B).

Only low amounts of hydrocarbons are generated from artificial residues when the experimental temperature is less than 350°C. In other words, the low temperature does not significantly affect the kerogen structure. Nevertheless, considerable amounts of hydrocarbons are generated between 350°C and 450°C, particularly between 400 and 450°C. The selected parameters, i.e., total hydrocarbon, total liquid, total gas, and total aromatics exhibit sharp decreases (Figure 3.11A-D). In the temperature range of 450-500°C, hydrocarbons are still generated, but to a significantly lower extent than in the former temperature stages. When the temperature increases to over 500°C, all residues display extremely low generative potentials. Interestingly, there are no dramatic changes in the selected ratio parameters (gas wetness, GOR, aromaticity₁, aromaticity₂) until a temperature of 400°C is reached (Figure 3.12). Clear changes therefore occur somewhat later than the onset of hydrocarbon generation, which occurs at approximately 350°C. There is a significant increase in the yield of diaromatic compounds between 450°C and 500°C (Figure 3.11F), and consequently the aromaticity increases distinctly, which reflects an intensified condensation of aromatic rings. The primary stage of hydrocarbon generation or kerogen degradation can therefore be placed at between 350°C and 450°C.

For purposes of comparison, the average values obtained from the natural samples from the Lower Silurian, Lower Cambrian, and Ediacaran intervals are plotted in Figures 3.11 and 3.12, and their MSSV temperatures were simply assumed to be 550°C, 575°C, and 600°C, respectively. It is difficult to closely and directly correlate the UYP shales with any artificially matured samples. Nevertheless, the generation of aromatic compounds and the evolution of aromaticity and GOR may serve as suitable parameters for correlating the UYP shale with the artificially matured residues to a certain extent, as presented in Figures 3.11D-F and 3.12B-D.

Naturally matured samples

A series of naturally matured shale samples from the United States (Bakken and Barnett), Germany (Posidonia), and Australia (denoted as AU shale in Figures 3.13 and 3.14) were selected to investigate the kerogen evolution and hydrocarbon generation properties as a

function of maturity and to compare results with the UYP shale. The thermal maturity is simply represented by the Rock-Eval T_{max} . The Bakken, Barnett, and Posidonia shales contain type II organic matter (Horsfield and Dueppenbecker, 1991; Muscio and Horsfield, 1996; Jarvie et al., 2007), whereas the Cambrian Arthur Creek shales from the Georgina Basin, northern Australia, contain Type I/II microbial organic matter with high initial hydrogen indices (HI) between 600 and 800 mg/g TOC (Ambrose et al., 2001; Boreham and Ambrose, 2007).

The hydrocarbon generation properties of natural samples as a function of T_{max} are shown in Figures 3.13 and 3.14. The variations in hydrocarbon generation properties in immature (400-435°C), mature (435-470°C), and overmature (>470°C) ranges are illustrated. For given similar maturity ranges, selected AU samples generally exhibit relatively lower generation of total hydrocarbon (C_{1+}) (Figure 3.13A), particularly lower generation of total liquid hydrocarbon (C_{6+}) (Figure 3.13C), than the selected Posidonia and Barnett shale samples. In addition, the AU shale generally displays higher GOR and lower gas wetness than other shales (Figure 3.13D and E). The UYP shales are highly similar to the AU shales in terms of most of the parameters presented in Figure 3.13, except for the gas wetness, for which the data from selected samples plot as two groups (Figure 3.13E).

Figure 3.14 shows the generation of aromatic compounds and the evolution of aromaticity ratios as T_{max} increases. The UYP shale appears to be similar to the AU shale regarding most of the indices. Strong power correlations are evident in the plot of total aromatic compound generation ($R^2=0.88$) and in the plot of benzene generation ($R^2=0.83$) (Figure 3.14A and B), whereas only moderate poly correlations are evident in the plots of aromaticity ratios ($R^2\approx 0.7$) (Figure 3.14C and D). There are no distinct correlations between the UYP shale and the Barnett, Bakken, and Posidonia shales.

3.6.6. Kerogen Typing

Kerogen types of the Ediacaran and Lower Palaeozoic shale in the UYP have been speculated to be of type I (Liu et al., 2000; Dai et al., 2003; Zhu et al., 2006), type II (Yin et al., 2001; Liang et al., 2009b; Liu et al., 2011), or type I and II origin (Huang, 1986; Editorial Committee of the Sichuan Oil & Gas field, 1989; Zhang et al., 2008b; Zou et al., 2010). In this study, the Rock-Eval results are characterised by extremely low HI values and a broad

Chapter 3 Geological and Geochemical Characterisation

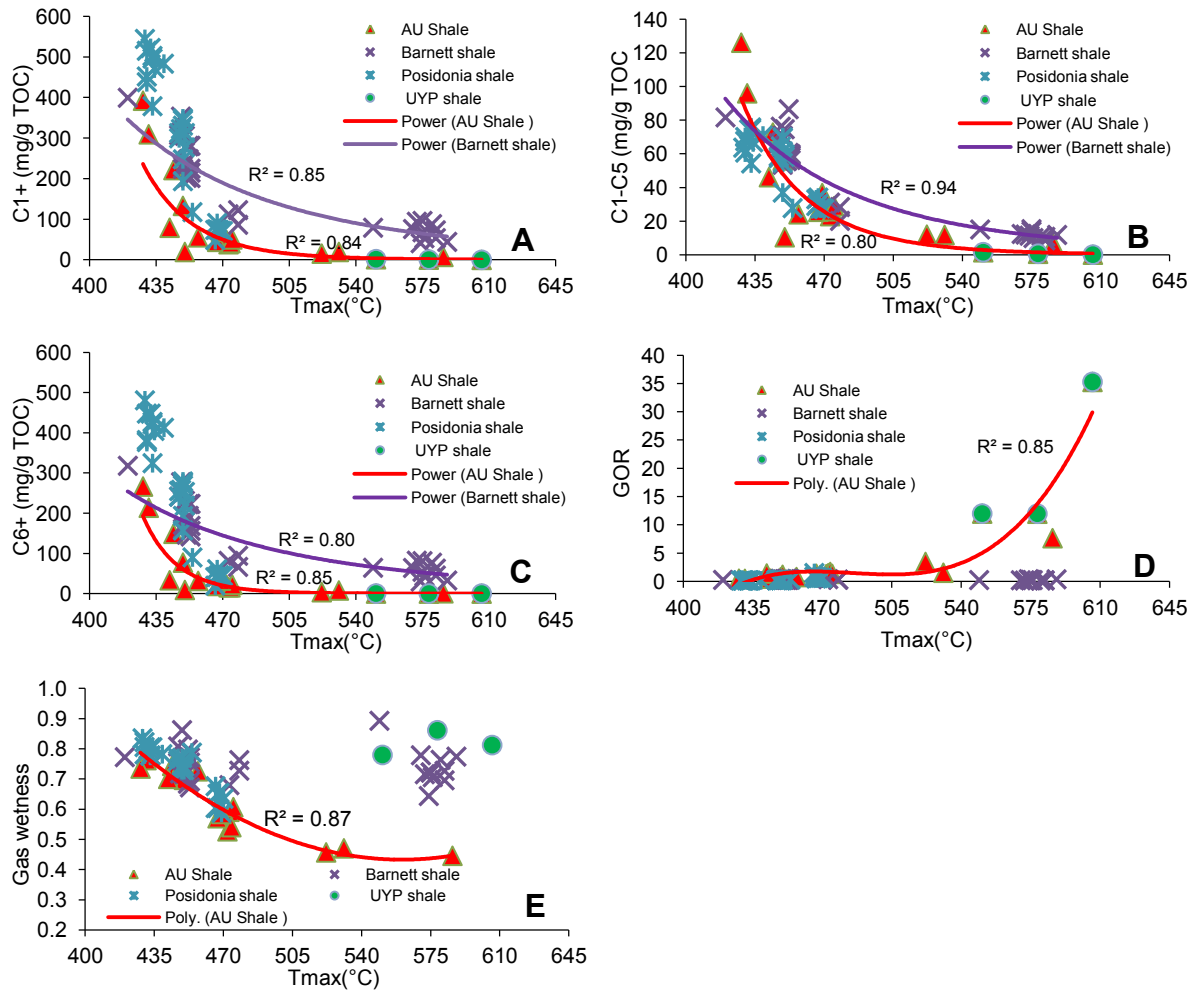


Figure 3.13 Hydrocarbon generation properties with T_{max} increase in natural samples. The UYP shales show possible correlations with the AU shales.

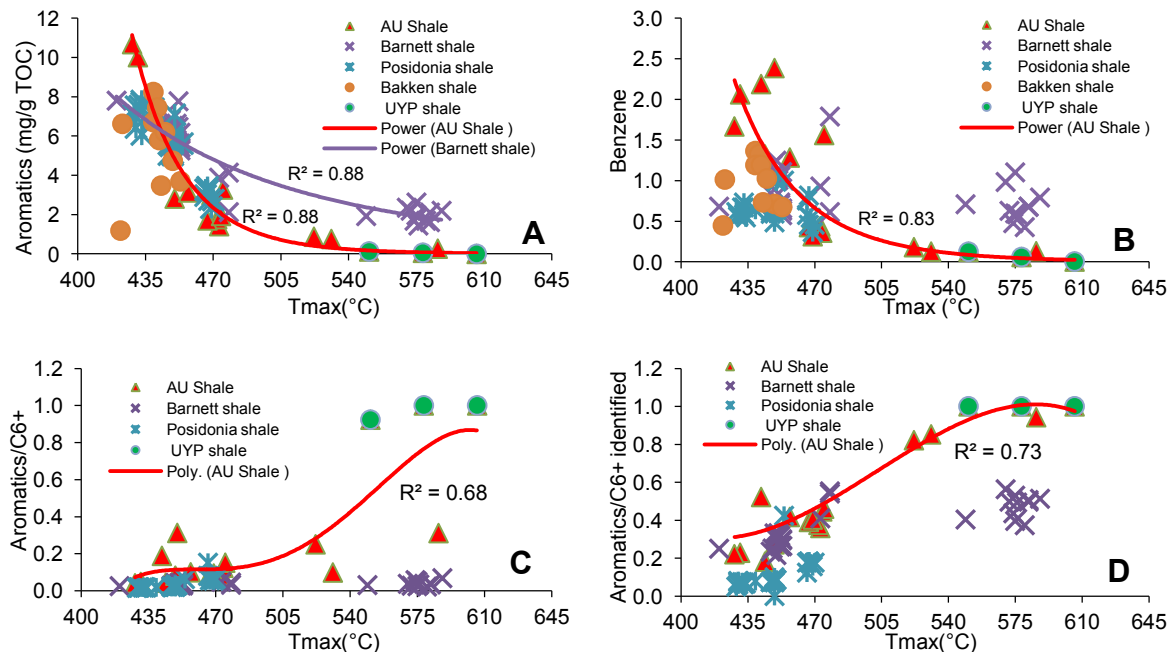


Figure 3.14 Aromatics generation properties with T_{max} increase in natural samples. The UYP shales show possible correlations with the AU shales.

Chapter 3 Geological and Geochemical Characterisation

T_{\max} range (Table 3.1). The original structures of the organic matter within these three intervals must have been altered and lost during the maturation process from diagenesis to metagenesis. Identification of the original kerogen is therefore fraught of difficulties. In the followed paragraphs, we try to identify clues based on the hydrocarbon generation properties during maturation and the carbon isotope ratios of methane, kerogen, and chloroform bitumen.

Revealed by hydrocarbon generation properties

The selected parameters obtained from the natural samples and presented in Figures 3.13 and 3.14 imply that the Australian shale seems a good analogue for the immature composition of the UYP shale, and the UYP shale may then be considered an analogue of the Australian shale in its overmature stage. Most of the selected parameters excluding the gas wetness indicate possible correlations between the AU shales and UYP shales. In this comparison, however, it is worth mention that the thermal maturity is represented simply by T_{\max} , which may be somewhat unreliable when assessing the thermal maturity of overmature samples. In addition, the gas wetness of the UYP shale falls within the range of values observed in the overmature Barnett Shale. The overmature samples of the Barnett Shale, however, generate higher amounts of total hydrocarbons than do the overmature AU shale and UYP shale.

In most cases, aromatisation and polycondensation are primary reactions involving organic matter during metagenesis (Tissot and Welte, 1984), and thus, the properties of aromatic generation and aromaticity evolution may reveal correlations between various overmature source rocks. In this study, parameters related to the generation of aromatic compounds, including the aromaticity, appear to be promising candidates for correlating the UYP shale samples with other samples (Figures 3.11, 3.12, 3.13, and 3.14). Aromatic compound generation and aromaticity evolution with increases in the temperature or T_{\max} suggest that the overmature UYP shale contained an initial kerogen type similar to that in the Australian shales. In support of this inference, the adjacent positions of the South China Plate and Australian Plate during the Cambrian and the similar sedimentary environments of the Cambrian shales in both places imply that a similar type of organic matter could be deposited at least during deposition of the Cambrian shale (Tan et al., 2013). However, more detailed investigation is necessary in the future, and additional methods, i.e., biomarkers or isotope ratios, may provide more information.

Findings from various carbon isotope ratios

The $\delta^{13}\text{C}$ ratios of methane and organic matter in sedimentary rocks are potentially valuable for unravelling the kerogen types. As shown in Figure 3.7, terrestrial source rocks possess remarkable high $\delta^{13}\text{C}$ ratios in methane in contrast to that of marine source rocks, and the ratios of the shale samples from the UYP are clearly in agreement with those of marine shale samples. In addition, the $\delta^{13}\text{C}$ of kerogen and chloroform bitumen in nearly 220 samples consisting of typical marine (Ediacaran, Lower Cambrian, Lower Silurian, and Permian strata) and typical lacustrine (Upper Triassic) source rocks from the UYP were analysed by Liang et al (2009b). Figure 3.15 shows that the $\delta^{13}\text{C}$ of both kerogen and chloroform bitumen increases with decreasing geological age. Assuming that the boundary values of $\delta^{13}\text{C}$ between kerogen type I, II and III are, respectively, -29‰ and -26‰ (Liang et al., 2009b), the kerogens in the Ediacaran and Lower Cambrian shales could be then classified as being of type I origin and of type I/II origin in the Lower Silurian shale (Figure 3.15). Type I kerogen is usually deposited in lacustrine environments (Tissot and Welte, 1984; Vandenbroucke and Largeau, 2007), whereas the selective accumulation of algal material may have also occurred in marine environments (e.g., deposition of tasmanites in southern Australia) (Tissot and Welte, 1984).

3.6.7. Reconstruction of Original Hydrocarbon Generative Potential

The immature and early mature Cambrian shales from northern Australia may therefore be considered immature equivalents of the UYP shale in bulk mass balance models (here that of Cooles et al., 1986). The assumption that dead carbon is simply preserved/concentrated and not neoformed is fundamental to the commonly used mass balance models, although condensation and cross-linking to neoform dead carbon has been reported for the Bakken Shale (Muscio and Horsfield, 1996), New Albany Shale (Lewan et al., 1995), and Barnett Shale (Jarvie and Lundell, 1991). All of these exceptions refer to kerogen that contains aromatic moieties traceable to sulphur-oxidising bacteria active in zones of photic euxinia. Because the immature Australian sample does not appear to contain such moieties, the assumption of dead carbon concentration rather than neoformation is considered valid.

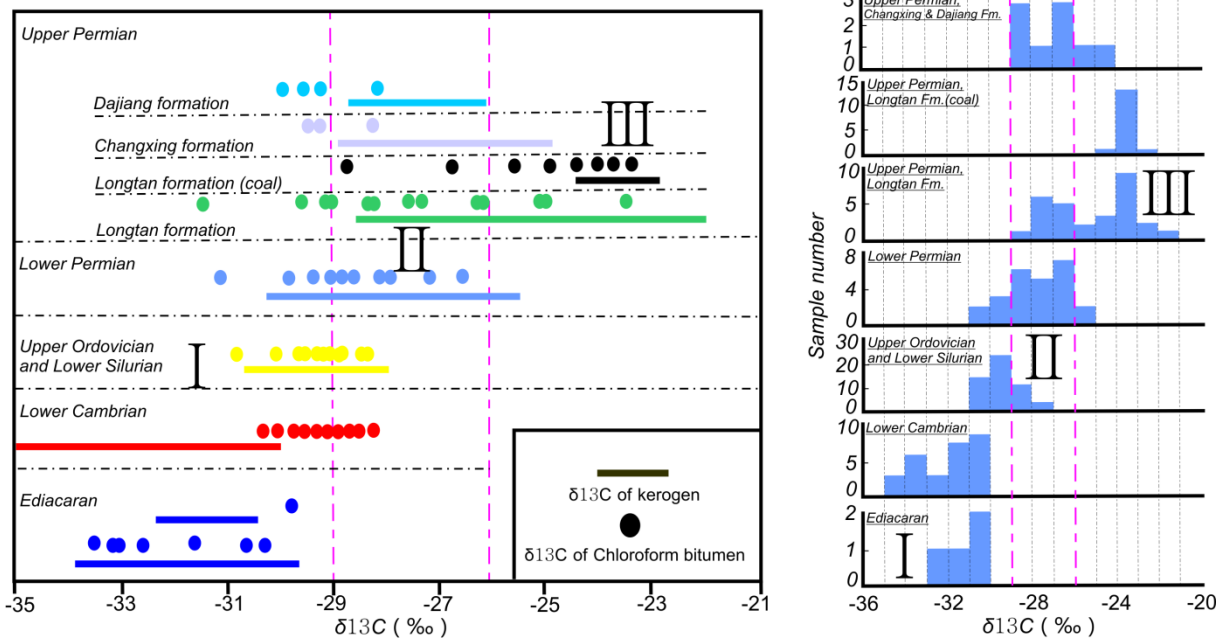


Figure 3.15 $\delta^{13}\text{C}$ of kerogen and extracted bitumen (left) and the histogram of $\delta^{13}\text{C}$ of kerogen (right) in the Palaeozoic source rocks, UYP (Liang et al., 2009b). The $\delta^{13}\text{C}$ of both kerogen and chloroform bitumen increases with decreasing geological age, and different source rocks show variations in $\delta^{13}\text{C}$ values.

The algebraic procedures used in mass balance models for calculating the transformation ratios (TR), original TOC (TOC_0), original petroleum potential ($\text{S1}_0 + \text{S2}_0$), petroleum generation index (PGI), petroleum expulsion efficiency (PEE or ExEf), and the amount of expelled petroleum (S1EX) have been developed and described in detail (Pelet, 1985; Cooles et al., 1986; Santamaria and Horsfield, 2004; Peters et al., 2005). These mass balance calculations are important for constraining the quantity and quality of organic matter in the source rock before maturation. In this study, the input parameters consisted of the measured Rock-Eval data (mean values of shale samples from a given interval), the assumed HI_0 of immature equivalents in the immature Australian samples (601-620 mg HC/g rock) and Green River shale (777 mg HC/g rock), and an assumed PI_0 (0.02), which has been suggested is reasonable for most immature source rocks (Peters et al., 2005). The calculated results (Table 3.6) indicate that the TRs are over 98%, which is in accordance with the overmature kerogen and low remaining generative potential. However, the restored TOC_0 (4.8-23.4%), S1_0 , and S2_0 (29-215 mg HC/g rock) indicate excellent original petroleum potential, and a mass of hydrocarbons must have been generated and expelled upon kerogen maturation, as indicated by the fact that both the PGI and PEE are over 99%. Cooles' method and Claypool's equation yield very similar values of TOC_0 , S1_0 , and S2_0 and high values of TR and PGI. Nevertheless, extremely low expulsion efficiencies (PEE or ExEf) of the Ediacaran shale was

Chapter 3 Geological and Geochemical Characterisation

indicated when Claypool's method was applied. The explanation is that Claypool's method relies on PI and PI_o to calculate the ExEf, whereas the PI of the Ediacaran shale is abnormal high (0.37) and that of the Lower Silurian (0.08) and Lower Cambrian shale (0.09) is low. The high TOC Ediacaran shale samples commonly possess relatively high values of S1 and low values of S2 (Table 3.1), and thus, the measured PI values are abnormal, which may reflect a stronger sorption capacity resulting from the high TOC content. The extrapolated amount of expelled petroleum (S1EX) ranges from 28.91 to 166.02 mg HC/g rock, or nearly 88 mg HC/ g rock on average.

Table 3.6 Mass balance calculations using the different approaches.

Unit	Measured data (mean value)					Assumption		Pelet's equation (Pelet, 1985)		Cooles' method (Cooles et al., 1986)					Claypool's method (in Peters et al., 2006)				
	TOC	S1	S2	HI	PI	HI	PI _o	TR	DCo ratio	DCo	TOC _o	S1 _o +S2 _o	PGI	PEE	TR	TOC _o	S1 _o +S2 _o	S1 EX	ExEf
Lower Silurian	2.5	0.03	0.4	17.43	0.08	900	0.02	99.5	0.22	2.40	10.76	100.66	99.6	99.97	99.5	9.42	86.49	86.07	96.3
						800	0.02	99.3	0.31		7.76	64.54	99.4	99.95	99.3	7.13	58.18	57.75	94.3
						700	0.02	98.9	0.40		6.07	44.16	99.2	99.93	99.0	5.73	40.95	40.51	91.7
						600	0.02	98.5	0.47		5.11	32.66	98.9	99.91	98.6	4.80	29.36	28.91	88.2
Lower Cambrian	5.2	0.03	0.3	17.77	0.09	900	0.02	99.5	0.22	5.15	23.04	215.55	99.8	99.99	99.5	18.17	166.86	166.02	95.3
						800	0.02	99.2	0.31		16.62	138.20	99.8	99.98	99.3	14.16	115.58	114.68	92.8
						700	0.02	98.9	0.40		12.99	94.57	99.7	99.97	99.0	11.60	82.84	81.91	89.5
						600	0.02	98.5	0.47		10.95	69.94	99.5	99.96	98.5	9.82	60.13	59.18	85.1
Ediacaran	5.1	0.12	0.2	9.17	0.37	900	0.02	99.7	0.22	4.98	22.32	208.82	99.9	99.94	99.8	17.97	164.98	164.37	85.8
						800	0.02	99.6	0.31		16.10	133.89	99.9	99.91	99.6	13.99	114.20	113.54	78.2
						700	0.02	99.5	0.40		12.59	91.62	99.8	99.87	99.5	11.45	81.82	81.13	68.4
						600	0.02	99.2	0.47		10.61	67.76	99.7	99.82	99.2	9.70	59.37	58.67	55.4

1) HI is hydrogen index(mg HC/g TOC); TR is transformation ratio(%); PI is production ratio(wt ratio); TOC is total organic carbon (wt. %); S1 is free hydrocarbon and S2 is generated hydrocarbon from kerogen (mg HC/g TOC); S1 EX is expelled petroleum (mg HC/g rock); ExEf is expulsion efficiency(%); DC ratio is dead carbon/total organic carbon; DC is dead carbon wt./rock wt. (%); PGI is petroleum generation index (%); PEE is petroleum expulsion efficiency (%).

2) Pelet's equation: $TR = (1200 \times (HI_o - HI)) / (HI_o \times (1200 - HI))$, where HI_o is hydrogen index of immature sample, HI is hydrogen index of mature sample, and 1200 represents the reciprocal (times 1000) of 0.83, the assumed proportion of carbon in Rock-Eval Pyrolysis products.

3) Cooles' method: $DCo\text{-ratio} = 1 - (C2_o + C1_o) / TOC_o = 1 - (S1_o + S2_o) \times 0.83 / TOC_o / 1000$; $DC = TOC - (C2 + C1) = TOC - (S2 + S1) \times 0.83 / 10$; $TOC_o = (TOC - (C2 + C1)) / DCo = DC / DCo$; $S1_o + S2_o = (C2_o + C1_o) \times 10 / 0.83 = TOC_o \times (1 - DC\text{ ratio}) \times 10 / 0.83$; $PGI = 1 - S2 / (S2_o + S1_o)$; $PEE = ((S2_o + S1_o) - (S2 - S1)) / ((S2_o - S2) + S1_o)$.

4) Claypool's method: $TR = 1 - HI \times (1200 - (HI_o / (1 - PI_o))) / (HI_o \times (1200 - (HI / (1 - PI))))$; $TOC_o = 83.33 \times HI \times TOC / (HI_o \times (1 - TR) \times (83.33 - TOC) + HI \times TOC)$; $S1_o + S2_o = HI_o \times TOC_o / 100 / (1 - PI_o)$; $S1EX = 1000 \times (TOC_o - TOC) / (83.33 - TOC)$; $ExEf = 1 - (1 - f) \times (PI / (1 - PI)) / (f + (PI_o / (1 - PI_o))) \times 100$.

3.7. Conclusions

The Ediacaran, Lower Cambrian, and Lower Silurian black shale intervals were deposited during three major transgressions of the Late Proterozoic and Early Paleozoic. The sedimentary environments were dominated by open- to restricted-marine shelves with deep-water conditions resulting from sea level highstands. The Lower Cambrian shale is distributed throughout most of the UYP and is particularly thick in the southeast Sichuan Basin, Chongqing, north Guizhou, west Hunan, and west Hubei. The Lower Silurian shale, however, is primarily confined to the central UYP, where it underlies the southeast Sichuan Basin and Chongqing area. The depths vary significantly. There are outcrops along the margins of the Sichuan Basin and in the southeast UYP, whereas black shale is encountered at depths exceeding 5000 m in certain depressions. The mineralogy and organic matter vary in upward succession in both the Lower Cambrian and Lower Silurian formations, such that high-TOC black shale is typically situated in the bottom parts, whereas the upper intervals consists of the low-TOC grey shale, siltstone, or carbonate.

The TOC contents in the analysed samples generally exceed 2% and average 5%, and they increase with geological age. For example, the TOC levels in the Lower Silurian shale are lower than those in the Lower Cambrian shale, which are in turn lower than those in the Ediacaran shale in general. The thermal maturity of the kerogen indicates metagenesis, based on the visible organic matter, bitumen reflectance, and $\delta^{13}\text{C}$ of methane. On the basis of the $\delta^{13}\text{C}$ of the methane and the basin modelling results, extrapolated vitrinite reflectances (R_o) of 2.5-3.0% for the Lower Silurian shale, 3.0-3.5% for the Lower Cambrian shale, and 3.5-4.0% for the Ediacaran shale were found. T_{vap}-GC and open py-GC analyses indicate extremely low remaining generated hydrocarbon and low remaining generative potential, and the products are qualitatively dominated by the light hydrocarbons.

Artificially and naturally matured samples from other countries were evaluated to determine the evolution of the kerogen and hydrocarbon generation properties with increases in the temperature and T_{max} and to reveal the origin of the kerogen type of the UYP shale. The organic matter of the UYP shale most likely is predominantly type I original kerogen, which may have formed in a marine environment via selective accumulation of algal material, based on the $\delta^{13}\text{C}$ ratios in the methane, kerogen, and chloroform bitumen and the correlations with the Australian shale in terms of the aromatic generation and aromaticity evolution with the increase in the T_{max} . The original petroleum potential and original organic status were calculated and reconstructed using Cooles' and Claypool's equation. Excellent original

hydrocarbon potential was revealed, based on the values of TOCo between 5% and 23% and S1o+S2o between 29 and 215 mg HC/g rock.

3.8. Acknowledgements

The authors thank Ferdinand Perssen (GFZ-Potsdam) for technical assistance performing experiments and Statoil for financial support and the permission to publish.

Chapter 4 Petroleum Physical Properties

4.1. Abstract

Lower Cambrian shale in the Upper Yangtze Platform (UYP), south China, is an important source rock of many conventional petroleum fields and was recently recognized as a promising unconventional shale reservoir. In this paper, hydrocarbon generation kinetics and petroleum physical properties were investigated using the PhaseKinetics approach (di Primio and Horsfield, 2006) and a Cambrian shale sample from the Georgina Basin, North Territory Australia (NTA), as similar paleogeological and sedimentary environments in Cambrian are found for the UYP and NTA.

The source rock comprises type II kerogen and belongs to an organofacies generating Paraffinic-Naphthenic-Aromatic low wax oil. Bulk petroleum generation can be described by a single frequency factor $A = 8.43E+14$ (1/s) and a dominant activation energy at 56 kcal/mol, which is characteristic for sulphur-poor organic matter deposited in an anoxic marine environment. Onset (transformation ratio TR=10%) and end (TR=90%) of bulk hydrocarbon generation was calculated to take place at 120°C and 165°C respectively for an assumed average geological heating rate of 1.5°C/Ma. Based on the thermal history of a local “model”-well, onset temperature was not reached until the Middle Triassic (241 ma) when sediments were buried more than 2000 m and basalt eruptions caused enhanced heat flows. The main generation stage of primary petroleum took place during the Middle-Late Triassic and ended in the Early Jurassic (187 ma) for burial depths exceeding 4000m (TR 90%; 165°C). Temperatures increased to more than 200°C in the Middle-Late Jurassic leading to secondary cracking of primary products.

Hydrocarbons formed at the onset (TR=10%) of petroleum generation can be characterised by a gas-oil-ratio (GOR) of 63 Sm³/Sm³, a saturation pressure (P_{sat}) of 101bar, and a formation volume factor (B_o) of 1.2 m³/Sm³. Those parameters stay low during primary petroleum generation before 203 ma, at temperatures < 145°C, and at burial depths < 3400m

This chapter has been published as: Tan, J., Horsfield, B., Mahlstedt, N., Zhang, J., di Primio, R., Vu, T.A.T., Boreham, C.J., van Graas, G. and Tocher, B.A., 2013. Physical properties of petroleum formed during maturation of Lower Cambrian shale in the upper Yangtze Platform, South China, as inferred from PhaseKinetics modelling. Marine and Petroleum Geology, 48: 47-56.

(GOR = 176 Sm³/Sm³, P_{sat} = 189 bar, B_o = 1.6 m³/Sm³ at 90%TR). However, predicted parameters increase rapidly (GORs >> 10000 Sm³/Sm³, P_{sat} > 250 bar and B_o > 2.0 m³/Sm³) during secondary cracking starting roughly at 200 ma, 152°C and 3500m burial. Assuming zero expulsion, the shale reservoir position within the sedimentary basin indicates that bubble point pressure was always below reservoir pressure, and fluids in the shale reservoir occurred only as a single, undersaturated phase throughout maturation history. Black oil and volatile oil phases dominated during the primary cracking period, whereas wet gas and dry gas phases dominated during the secondary cracking period.

Keywords

Lower Cambrian shale; south China; Shale gas; Petroleum generation; Phase kinetics; Phase behaviour

4.2. Introduction

In China, the Upper Yangtze Platform (UYP) is one of the major conventional petroleum producing regions, with annual natural gas production accounting for 22-43% of the total national production in the last 20 years (National Bureau of Statistics and Energy Bureau, 1991-2010). Petroleum reservoirs are predominantly composed of the Changxing (Upper Permian) and Feixianguan (Lower Triassic) carbonates and the Xujiache (Upper Triassic) and Jurassic terrigenous clastics, which accounted for over 70% of total reserves (Dai et al., 2009; Ma et al., 2010). Prolific source rocks are the Lower Cambrian, Lower Silurian and Lower Jurassic mud shales, the Lower Permian carbonate, as well as Upper Permian and Upper Triassic coal-bearing shales. Regional seals are mainly consisting of anhydrite, halite, and gypsiferous dolomite that developed in a major marine regression between the Late Early and Middle Triassic (Editorial Committee of the Sichuan Oil & Gas field, 1989; Dai et al., 1992; Huang et al., 1997; Jia et al., 2006; Ma et al., 2006; Hao et al., 2008; Ma et al., 2010) .

As an important regional source rock for many petroleum fields in the Yangtze Platform, Lower Cambrian shales are distributed almost throughout the whole area (Figure 4.1). In the UYP, Lower Cambrian shales usually possess thicknesses between 100 and 200 m in the south and north Sichuan Basin, west Hunan and Hubei Province, and north Guizhou and Yunnan Province (Figure 4.1). In the central Sichuan Basin and the west and south marginal areas of the UYP Lower Cambrian shales are only very thin if present at all. In regions, where thick shale successions predominate, higher average TOC contents > 2%, are encountered

Chapter 4 Petroleum Physical Properties

(Cheng et al., 2009; Liang et al., 2009b). Present organic matter is generally overmature with vitrinite reflectance between 2.0 and 4.0%, and values increasing from west to east (Zhang et al., 2008a; Wang et al., 2009a; Wang et al., 2009b).

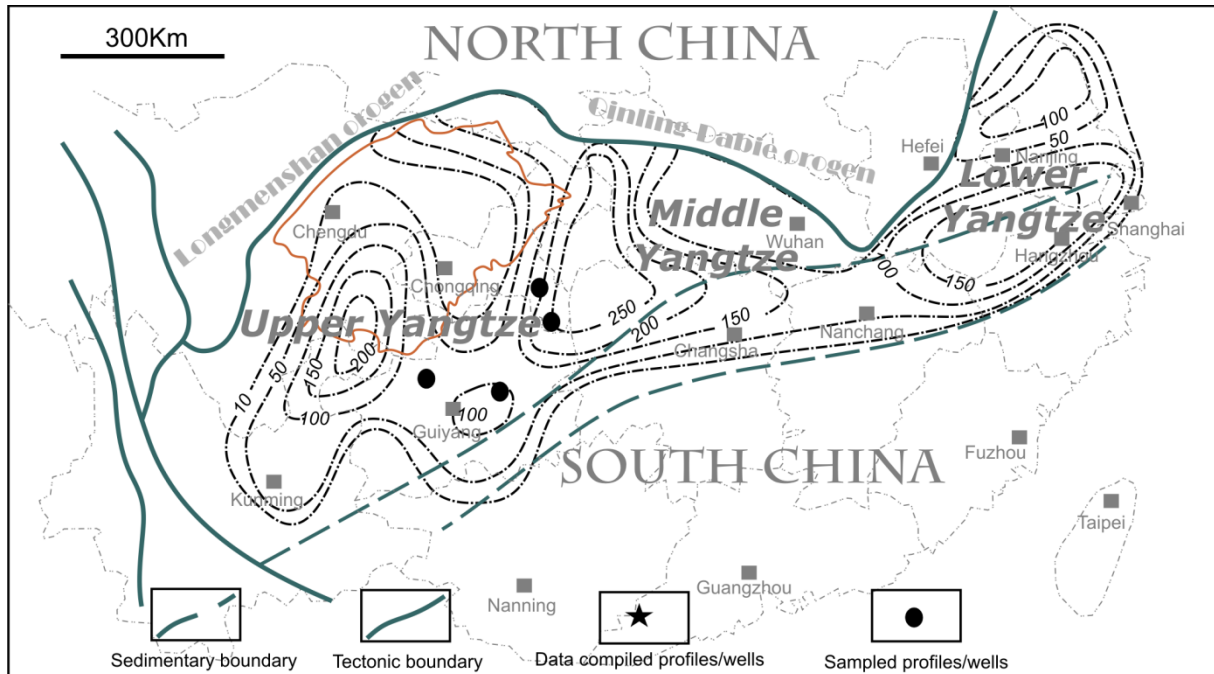


Figure 4.1 Lower Cambrian shale distributions in the Yangtze Platform, modified after (Liang et al., 2008; Zou et al., 2011).

In addition to its importance for conventional petroleum production, Lower Cambrian shale has only recently been recognized as a prolific unconventional resource play (EIA, 2011b). The shale distribution (extent, depth and thickness), sedimentary environment, organic matter richness, thermal maturity, and mineralogical composition can be compared to the Barnett Shale (Zhang et al., 2008a; Cheng et al., 2009; Dong et al., 2010; Zou et al., 2010; Zou et al., 2011; Long et al., 2012), which is often used as an exploitation model.

In both conventional and unconventional petroleum systems, it is important to reconstruct the timing of petroleum generation as well as the changing GOR of the petroleum and its physical properties during maturation. The timing and extent of petroleum generation depends on both the thermal history of the source rock and the reaction kinetics of hydrocarbon generation from kerogen (Behar et al., 1997). Kinetic laws are therefore routinely considered as a very critical element in the modeling of hydrocarbon generation from source rocks (Tegelaar and Noble, 1994; Dieckmann et al., 1998). Kinetic parameters of petroleum generation from kerogen are usually derived by pyrolysis of immature source rocks. In the case of UYP, unfortunately, all published data as well as our own Rock-Eval and Open-

System Thermal Analysis GC-FID results shows that Lower Cambrian shale in the UYP is overmature, and therefore reconstructing the entire petroleum generation history is fraught with difficulty. Here we report how we overcame this problem by using comparable immature samples from Australia. Specifically, Cambrian shale from the Georgina Basin, Northern Territory of Australia was selected because of its paleo-geological and -tectonic position close to the South China Plate throughout the Paleozoic.

4.3. Selection of Cambrian Geological Analogue

Stratigraphic correlations and tectonic analysis indicate that the Yangtze plate of south China can be viewed as a continental fragment caught between the Australian craton and Laurentia during the late Mesoproterozoic assembly of the supercontinent Rodinia (Li et al., 1995). Although the breakup of Rodinia around 0.7 Ga separated south China (Yangtze plus Cathaysia plates) from the other continents, the South China Plate remained adjacent to north Australia for a very long geological time, which lasted throughout the whole Paleozoic (Figure 4.2) (Scotese and McKerrow, 1990; Scotese, 2009). The Precambrian-Paleozoic geology of the Yangtze Plate has therefore already been linked to Australian geology (Li et al., 2003; Steiner et al., 2007), where similar shallow sea sedimentary environments occurred in the Cambrian (Scotese, 2009).

4.3.1. Cambrian Geology - UYP

Tectonically, the UYP comprises the western part of the Yangtze Platform in south China and is enveloped by the Longmenshan orogen in the west and the Qinling-Dabie orogen in the north (Korsch et al., 1991; Meng et al., 2005; Jia et al., 2006; Plesch et al., 2007). It regionally includes the eastern Sichuan, Chongqing area, most of Guizhou, western Hubei and Hunan, and northern Yunnan province. The Tongwan tectonic movement occurring at the end of the Proterozoic resulted in a disconformity between the upper Proterozoic (Sinian) and the Lower Cambrian. The Early Cambrian succession consists of carbonaceous and calcareous shale, carbonate, siltstone and fine stone and was deposited in a major marine transgression from southeast to northwest. The black shale is thickening from northwest to southeast; therefore, the present south and north Sichuan, western Hunan and Hubei, Chongqing and Guizhou contain thick black shale successions deposited in an open marine platform to marine shelf environment, whereas the present western marginal area is

Chapter 4 Petroleum Physical Properties

predominated by clastics and carbonates which were deposited in littoral environments. In the Middle-Late Cambrian, the open marine platform and marine shelf environments were maintained in the western Hunan and Hubei, while in other places a mainly restricted marine platform environment resulted from a regression. Thick Cambrian carbonates were deposited extensively, whose total original thickness would be higher than 2000 m in the south and east UYP if no erosion had resulted from the Late Caledonian Uplift (Editorial Committee of the Sichuan Oil & Gas field, 1989; Korsch et al., 1991; Ma et al., 2007; Hao et al., 2008). In the Sichuan Basin, Lower Cambrian Shale was recognized as one of the major source rocks for many reservoirs, such as the Weiyuan gas field besides others in the eastern part of the basin (Ma et al., 2007; Dai et al., 2009; Ma et al., 2010). Meanwhile, the Middle-Late Cambrian carbonate has good petroleum reservoir characteristics (Editorial Committee of the Sichuan Oil & Gas field, 1989).

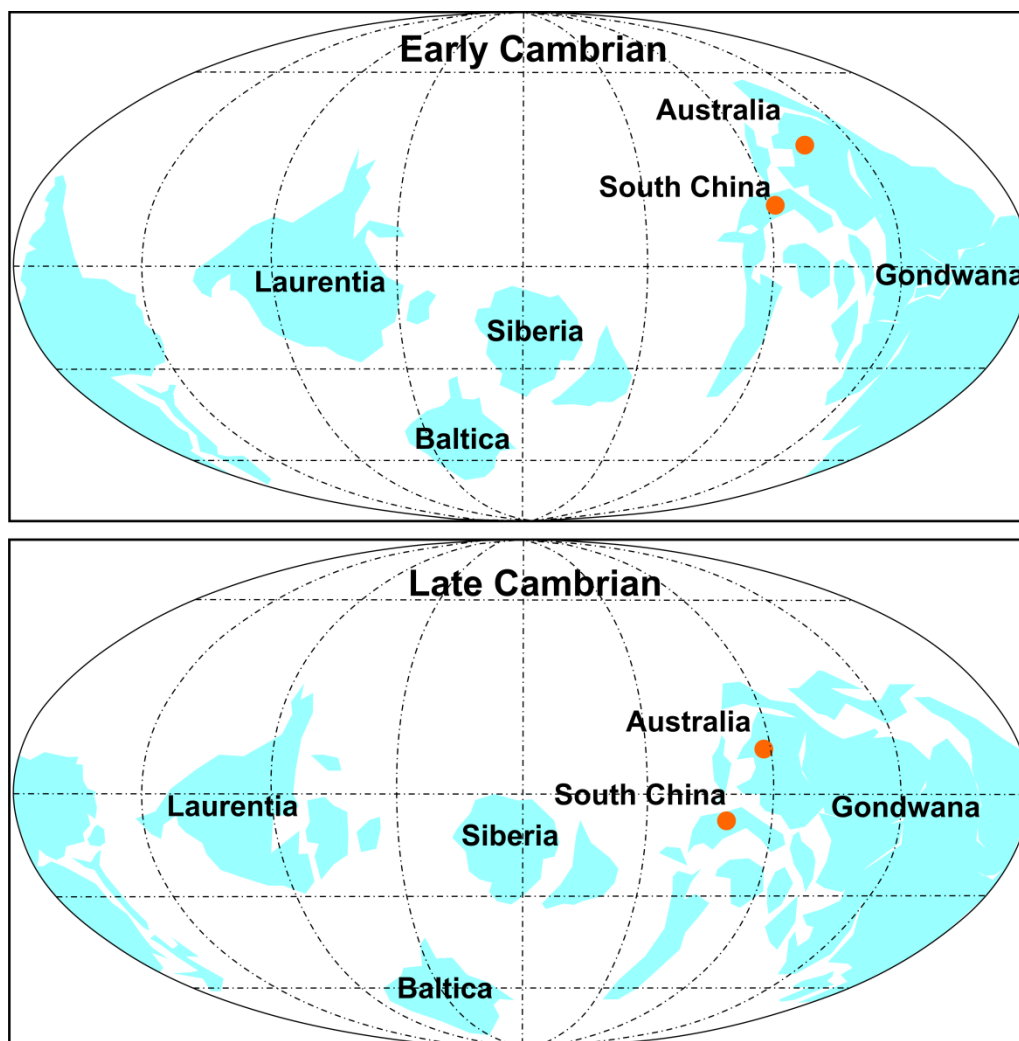


Figure 4.2 Paleogeography in the Cambrian: red points indicate locations of south China and north Australia, modified after (Scotese and McKerrow, 1990).

4.3.2. Cambrian Geology - Georgina Basin

The Georgina Basin covers an area of >100000 km² and is the largest Neo-proterozoic-Paleozoic intracratonic basin in Australia. It evolved after the breakup of the Centralian Superbasin in the Late Neo-proterozoic (Haines et al., 2001; Volk et al., 2007). The present outline is an erosional remnant of a much larger, Vendian-lower Paleozoic sedimentary package, deposited in sub- to supratidal environments across parts of an epicontinental shelf that covered large tracts of central and northern Australia. Cambrian organic rich shales in the Thornton Limestone, Arthur Creek formation and Chabalowe formation provide important source rocks as well as contain the main reservoir targets in the basin. In early Cambrian, the southern basin margin was restricted. Lower Cambrian siliciclastic rocks and carbonates were deposited and unconformably overlay the Neo-proterozoic Elkerka Formation with a total thickness of almost 250m. To Middle Cambrian, sedimentation recommenced during a major transgression and resulted in peritidal to restricted, shallow marine environments and the deposition of the Thornton Limestone. Following basin-wide erosion and the formation of a regional unconformity, deepening marine conditions resulted in the deposition of anoxic, pyritic and carbonaceous, partly dolomitic shale of the basal, up to 60 m thick Arthur Creek formation acting as the main source rock unit. A thick Late Cambrian succession of mixed peritidal carbonate rocks and redbeds of the Chabalowe Formation was deposited in an extensive and intermittently emergent epeiric sea. The basal Hagen Member deposited mainly in the southwest, comprises reservoir-quality dolostone, with subordinate grainstone at the base, overlain by massive anhydrite, which acts as a seal. The Chabalowe Formation is in turn overlain by carbonate and siliciclastic rocks of the Arrinthrunga Formation (Ambrose and Putnam, 2005; Boreham and Ambrose, 2007).

4.4. Selection of Shale Samples

4.4.1. Lower Cambrian Shale Samples from the UYP

Organic richness, maturity, kerogen type as well as free hydrocarbons and kerogen quality have already been assessed for fifteen samples collected from four Lower Cambrian shale profiles throughout the Chongqing area and Guizhou province (Figure 4.1). Results are described in detail in Tan et al. (in review) and can be summarized as follows. The TOC content in many profiles ranges between 5 and 10% with the organic matter itself being

overmature ($R_o \gg 2\%$). This causes very low residual-genetic potentials precluding the direct identification of original kerogen type. Previous researches suggested a mixed type I/II alginitic/bacterial kerogen leading to Lower Cambrian shale being viewed as an important source rock in the UYP (Liang et al., 2009b; Zou et al., 2010).

4.4.2. Cambrian Shale Sample from the Georgina Basin, north Australia

The basal Arthur Creek Fm. is up to 60 m thick and comprises mainly algal/bacterial (type I/II kerogen) organic matter with TOC contents in the range of 0.5-16% and HIs higher than 600 mg HC/g TOC (Ambrose et al., 2001; Ambrose and Putnam, 2005; Volk et al., 2007). An immature core sample (HI=601mg/g TOC, TOC=15.8%, $T_{max}=428^{\circ}\text{C}$) taken from a depth of 107 m of a well located in the southern Georgina Basin was therefore chosen as a source rock equivalent for Lower Cambrian Shales in the central UYP.

4.5. Analytical and Modelling Methods

PhaseKinetics is a compositional kinetic modelling method that is based on pyrolysis gas chromatography to establish Petroleum Type Organofacies, bulk flow pyrolysis to determine bulk petroleum generation parameters, MSSV pyrolysis to determine bulk compositions at selected Transformation Ratios, and finally, tuning to configure results in a PVT-amenable format. Here we perform this workflow on an Australian sample, and then apply the results in a 1-D petroleum system model of a local well within the UYP.

4.5.1. Open-system Pyrolysis Gas Chromatography (open-Py)

Pyrolysis gas chromatography was performed on the immature whole rock sample from Georgina Basin using the Quantum MSSV-2 Thermal Analysis System© interfaced with an Agilent GC-6890A (Horsfield et al., 1989). About 30 mg sample was placed into the central part of a glass tube (26 mm long, inner sleeve diameter 3 mm). The remaining volume was filled with purified quartz that had been cleaned by heating at 630°C in fair of 30 min. The sample was heated in a flow of helium, all products released up to 300°C being vented (3 min, isothermal). After then, it was pyrolysed at $50^{\circ}\text{C}/\text{min}$ from 300 to 600°C and pyrolysis products were collected in a cryogenic trap (liquid nitrogen cooling at -190°C , glass beads

substrate) for condensation, from which they were later liberated by ballistic heating (held at 300°C for 10 min). AHP-Ultra 1 dimethylpolysiloxane capillary column (50 m length, inner diameter of 0.32 mm, film thickness of 0.52 mm) connected to a Flame-Ionisation-Detector (FID) was used with helium as carrier gas. The GC oven temperature was programmed from 30°C to 320°C at 5°C/minute. Boiling ranges (C₁, C₂₋₅, C₆₋₁₄, and C₁₅₊) and individual compounds (n-alkenes, n-alkanes, alkylaromatic hydrocarbons and alkylthiophenes) were quantified by external standardisation using n-butane. Response factors for all compounds were assumed the same, except for methane whose response factor was 1.1.

4.5.2. Bulk Kinetics

Kinetic parameters of primary kerogen to petroleum conversion were assessed by subjecting the same sample to open-system, non-isothermal pyrolysis at four different linear heating rates (0.7, 2, 5, 15°C/min) using a Source Rock Analyser SRA (Humble). Roughly 100 mg of crushed sample material was weighed into small vessels and heated according to the temperature program from 250°C to ~600°C. Generated bulk products were transported to the FID in a constant helium flow of 50 mL/min. The discrete activation-energy (E_a) distribution optimization with a single, variable frequency factor (A) was performed using the KINETICS05 and KMOD® programs (Burnham et al., 1987).

4.5.3. Closed-system Pyrolysis Gas Chromatography (MSSV-Py)

Non-isothermal closed-system micro-scale-sealed-vessel (MSSV-) pyrolysis gas chromatography (principles described in Horsfield et al., 1989) was employed to obtain compositional information on petroleum products as input parameter for phase kinetic modeling. Ca. 20 mg of finely ground, whole rock was weighed into glass capillaries, which were then sealed by an H₂-flame after reducing the internal volume of the tube from ca. 40 ml to ca. 15 ml with pre-cleaned quartz sand. Pyrolysis was performed off-line at 0.7K/min to temperatures corresponding to 10, 30, 50, 70, and 90% TR as defined by bulk pyrolysis (SRA), using an external high performance oven. The latter consisted of a massive cylindrical metal block acting as a circular sample holder enclosing a central heating cartridge, which provided a very homogeneous temperature field throughout the core. Excellent temperature control was guaranteed by a thermocouple introduced directly into one sample holder. After removal from the external pyrolysis oven, samples were introduced into the Quantum MSSV-

2 Thermal Analyzer pyrolysis oven unit interfaced with an Agilent GC 6890A apparatus equipped with an HP-Ultra 1 column of 50 m length, 0.32 mm internal diameter and 0.52 mm thickness and an FID. The tubes were purged 5 minutes at 300°C to remobilize generated products and then cracked open by a piston device to transfer generated products from within the vessel by a helium-carrier gas with a flow rate of 30 ml/min into a liquid nitrogen-cooled trap. The trapped hydrocarbons were released to the column by ballistic heating of the trap to 300°C. The GC oven temperature was programmed from 30°C to 320°C at 5°C/min. Quantification of individual compounds and totals was conducted by external standardisation with n-butane. Reproducibility of measured product concentration is generally better than 4% (Schenk et al., 1997). Because of the lower response factor of methane compared to the heavier gases the methane content was multiplied by 1.1.

4.5.4. Compositional Kinetic Modelling

Having acquired bulk kinetic parameters (activation energy- E_a and frequency factor- A) of primary petroleum formation and the composition of generated hydrocarbons at 10, 30, 50, 70, and 90% kerogen conversion, a compositional kinetic model for the prediction of hydrocarbon physical properties (GOR , P_{sat} , B_o) under subsurface conditions could be determined using the PhaseKinetics approach established by di Primio and Horsfield (2006). GOR is the gas oil ratio, which is the ratio of total gas hydrocarbons (C_{1-5}) and total liquid hydrocarbons (C_{6+}) at standard surface conditions (Sm^3/Sm^3). B_o is the formation volume factor, which is the ratio of reservoir liquid volume to surface liquid volume in m^3/Sm^3 . P_{sat} is the saturation pressure, the pressure which occurs when oil cannot dissolve any more gas.

As gas composition dominantly controls petroleum phase behaviour, and laboratory pyrolysis results in less dry composition than field data implies, a gas composition correction was performed as described in (di Primio et al., 1998). For basin modeling purposes and assuming a heating rate of 1.5°C/ma, results were applied to the geological evolution of Cambrian shale within a selected synthetic well located in the UYP (central-south Sichuan Basin; 30.00N; 105.40E).

4.5.5. 1-D Petroleum System Modelling

A synthetic well located in the central-south Sichuan Basin, UYP (Figure 4.1), was selected for applying the PhaseKinetics model using 1D modelling (Figure 4.3). Lower

Cambrian shale is overlying Ediacaran carbonate, and is covered by Paleozoic carbonate and shale and Mesozoic sandstone and shale. There are three shale formations respectively in the Lower Cambrian, Upper Permian and Upper Triassic succession. The deepest burial depth of Lower Cambrian shale was close to 6000 m with maximum temperatures around 220°C in the Late Jurassic. At present, the depth and temperature of this formation near the well ranges from 4600 to 4900 m and 140°C to 160°C (Wang et al., 2009a; Xu et al., 2011). Three major uplift and erosion periods occurred from the end of the Silurian to Carboniferous, during the Late Permian, and from Cretaceous to present times. During burial, the Lower Cambrian Shales within the well in the Sichuan Basin experienced relative slow heating rates between 1 and 2°C/ma, only accelerated by the Emeishan magmatic activity in Middle-Late Permian times (Zhu et al., 2010). A continuous, long period of subsidence commenced in the Permian and continued until the Late Jurassic. Here and which will be shown in the following in more detail, primary hydrocarbon generation most likely occurred, i.e. between the Middle Triassic and Early Jurassic.

4.6. Results and Discussions

4.6.1. Petroleum Type Organofacies

The sample from the Georgina Basin has a very high petroleum potential (HI=601 mg/g TOC), and comprises type II kerogen (Espitalié et al., 1984) (Figure 4.4). Pyrolysis products are dominated by light hydrocarbons and show a notable presence of 1, 2, 3, 4-tetramethylbenzene (Figure 4.5), which is suggestive of photic zone euxinia during deposition (Hartgers et al., 1994; Muscio et al., 1994; Jia et al., 2007). In Figure 4.6 a paraffinic-naphthenic-aromatic low wax oil petroleum type can be inferred (Horsfield, 1989), but with a pyrolysate composition very close to the boundary of the gas condensate petroleum type organofacies field (Figure 4.6). The ability of marine source rocks to generate anomalously high amounts of light hydrocarbons could be an important characteristic of high quality gas shales in general.

Chapter 4 Petroleum Physical Properties

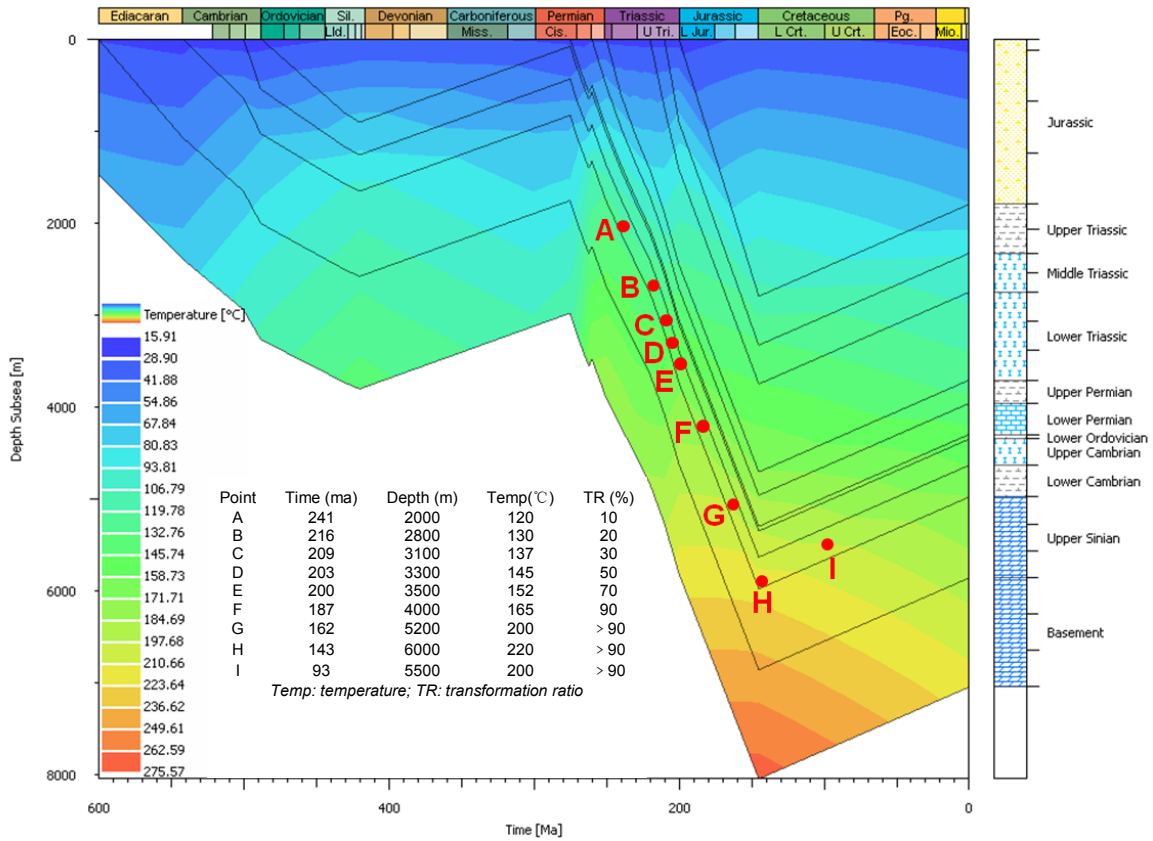


Figure 4.3 1D results in central-south Sichuan Basin, UYP. Reservoir conditions of the Lower Cambrian shale represented by red points are respectively: A – 2000m, 241 ma, and 120°C; B – 2800m, 216 ma, and 130°C; C – 3100m, 209 ma, and 137°C; D – 3300 m, 203 ma, and 145°C; E – 3500m, 200 ma, and 152°C; F – 4000 m, 187 ma, and 165°C; G – 5200 m, 162 ma, and 200°C; H – 6000m, 143 ma, and 223°C; I – 5500 m, 93 ma, and 200°C.

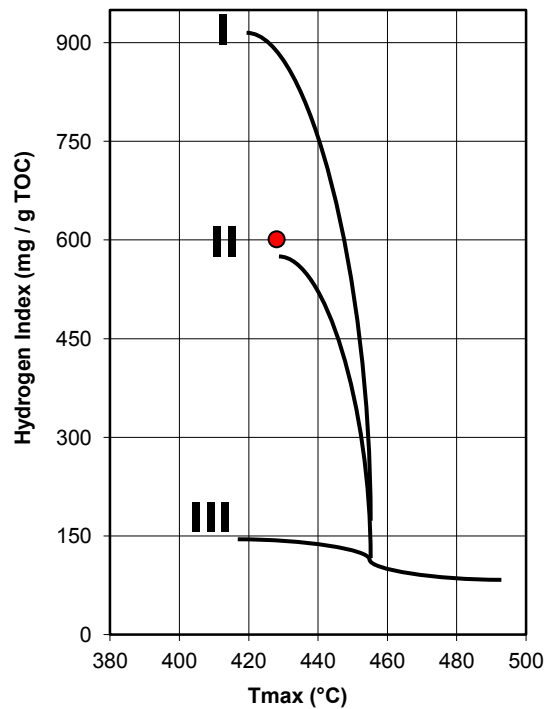


Figure 4.4 OI versus HI.

Chapter 4 Petroleum Physical Properties

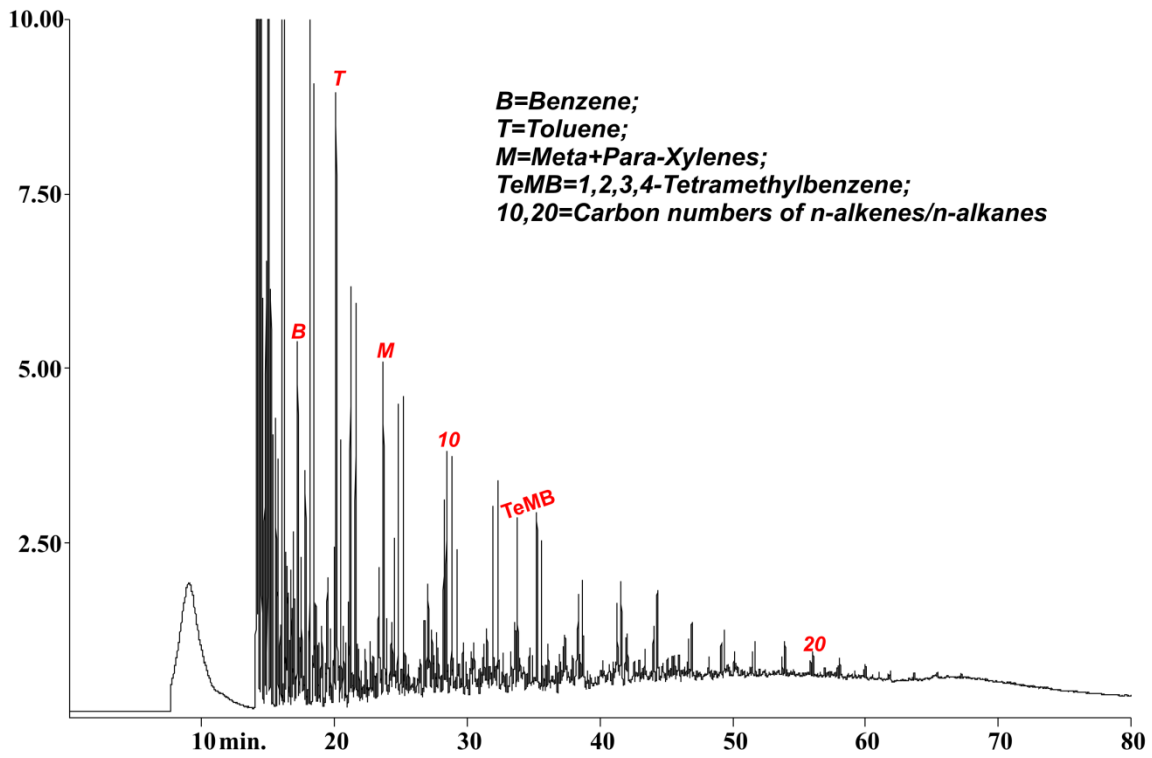


Figure 4.5 Pyrolysis gas chromatogram of the sample from Georgina Basin.

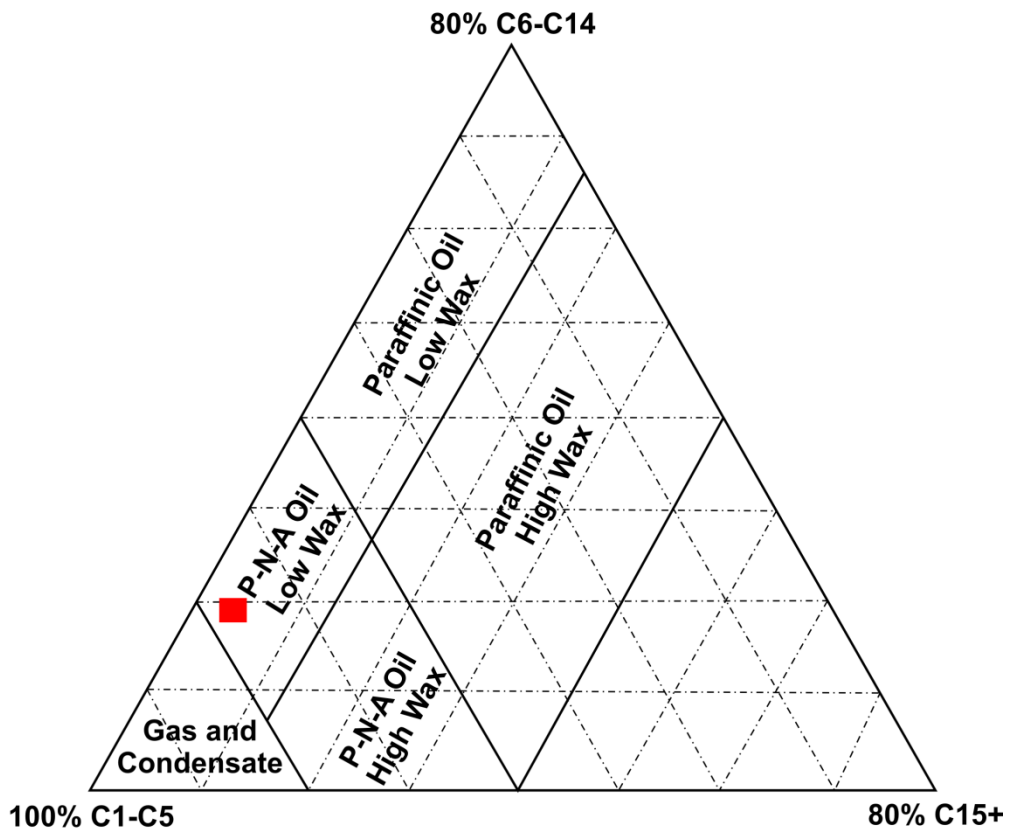


Figure 4.6 Petroleum type organofacies.

4.6.2. Bulk Maturation Characteristics

Bulk kinetic parameters for primary kerogen conversion are given in Table 4.1 and Figure 4.7. Hydrocarbon generation can be described by a single frequency factor of $A=8.429E+14$ 1/sec and an activation energy distribution ranging from 44 to 67 kcal/mol. The main activation energy at 56 kcal/mol, accounting for 36.5% of the bulk reaction, is higher than commonly assumed for oil and gas formation from marine, clastic source rocks. Compared to type II model source rocks (51-54 kcal/mol) (Braun and Burnham, 1992), Jurassic Posidonia Shale (52-54 kcal/mol) (Dieckmann et al., 1998), or a series of sample from different facies (48-55 kcal/mol) investigated by di Primio and Horsfield (2006), organic matter within the old Cambrian shale shows higher stabilities than organic matter within younger ones (Devonian to Mesozoic source rocks). Extrapolation to a geological heating rate of 1.5°C /ma, which fits the averagely experienced thermal stress of Lower Cambrian shale in the UYP, indicates an onset temperature of hydrocarbon generation (TR=10%) near 120°C, while the end of generation (TR=90%) can be expected for temperatures around 165°C (Figure 4.8). The latter prediction is characteristic for marine but sulphur-poor organic matter if compared the data of Tegelaar and Nobel (1994) or di Primio and Horsfield (2006).

Table 4.1 Bulk kinetics parameters of total hydrocarbon potential (%), frequency factor $A=8.429E+14$ (1/s).

Ea (kcal/mol)	44	45	46	47	48	49	50	51	52	53	54	55	56	57	58	59	60	61	62	63	64	65	66	67
Fraction (%)	0.25	0.15	0.41	0.33	0.64	0.62	1.18	1.15	2.53	3.67	12.01	9.59	36.50	14.05	7.46	4.91	1.07	2.03	0.09	0.87	0.00	0.00	0.00	0.49

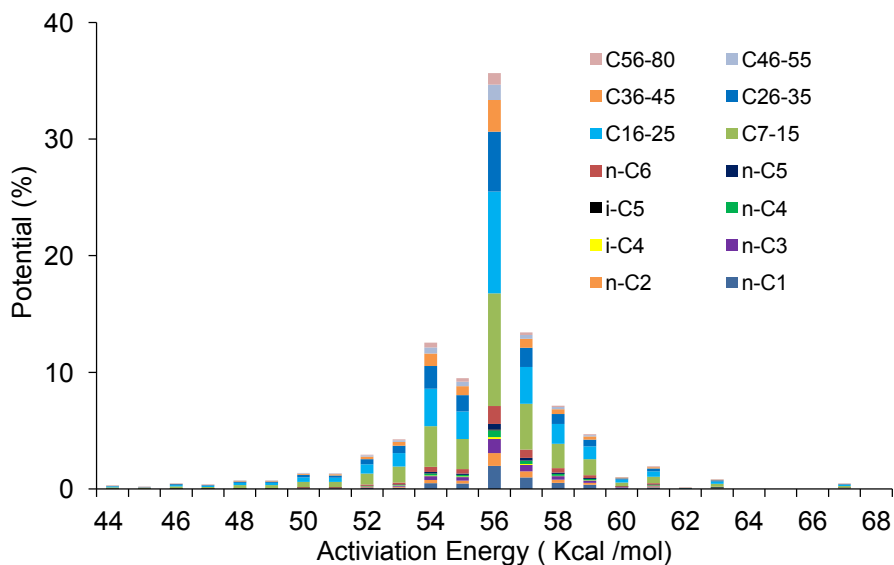


Figure 4.7 Activation energy distribution populated by MSSV data.

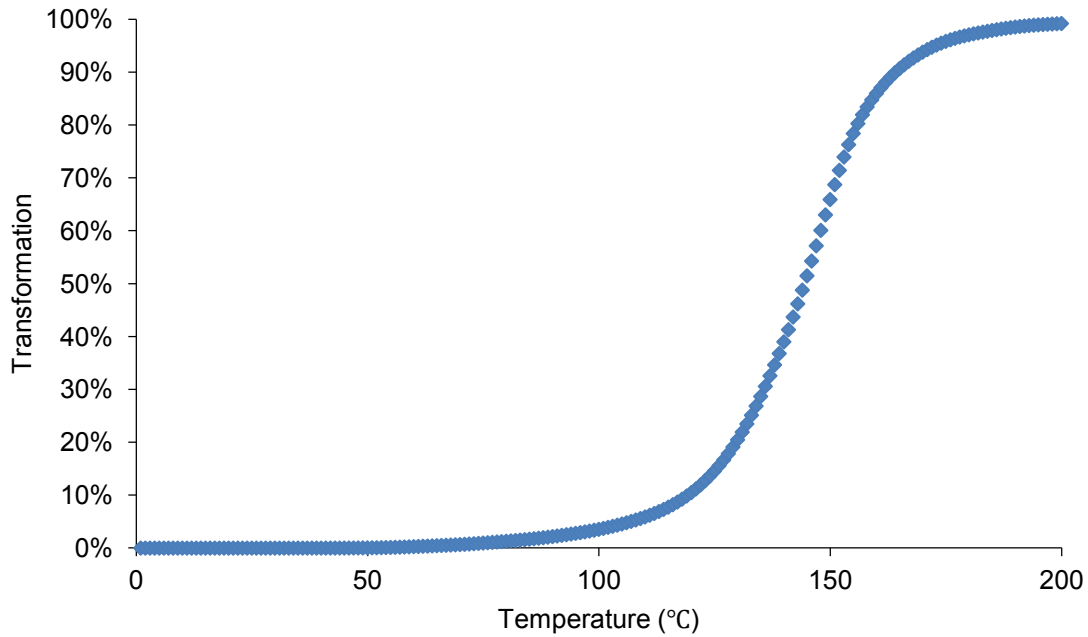


Figure 4.8 Predicted TR evolution with a function of temperature for a heating rate of 1.5 °C/ ma.

4.6.3. Compositional Kinetics

The activation energy distribution populated by MSSV data is given in Figure 4.7. The gases are predominated by n-C₁, n-C₂ and n-C₃, while liquids are predominated by lumped boiling ranges C₇₋₁₅ and C₁₆₋₂₅. The influence of the measured and corrected petroleum composition on the physical properties of the primary formed fluid is displayed in Figure 4.9 in which the evolution of GOR, P_{sat} and B_o as a function of maturity, defined by TRs, is shown. For TRs between 10 and 90% GOR ranges between 63-176 Sm³/Sm³, P_{sat} ranges between 101-189 bar, and B_o ranges between 1.2-1.6 m³/ Sm³, respectively. Thus, black oil (GORs up to 200 Sm³/Sm³) is generated throughout primary kerogen conversion, which might be secondarily cracked to gas in-source or in-reservoir. As high thermal maturities are reached for Lower Cambrian Shale in the UYP, modeled evolution of GORs including secondary composition are displayed in Figure 4.10 for an assumed heating rate of 1.5°C /ma as a function of temperature. It can be deduced from rapidly increasing GORs that secondary cracking starts at temperatures close to 150°C, whereas primary hydrocarbon generation proceeds up to 165°C (compare Figure 4.8 TR 90%). This means that secondary cracking starts when TR reaches ~60%, i.e. before primary cracking of kerogen is completed. In Figure 4.11 the predicted relationship between P_{sat} and B_o for Lower Cambrian shale in the UYP (pink line), with P_{sat} increasing from 101 to 300 bar and B_o increasing from 1.2 to 2.3 m³/Sm³ for increasing maturity levels, is compared to measurements on hundreds of samples from the

Chapter 4 Petroleum Physical Properties

Northern Sea, Norway. The fluid properties evolution curve seems to fit the natural case very well, with black oil being generated at low mature stages and gas condensates at overmature stages when secondary cracking predominates.

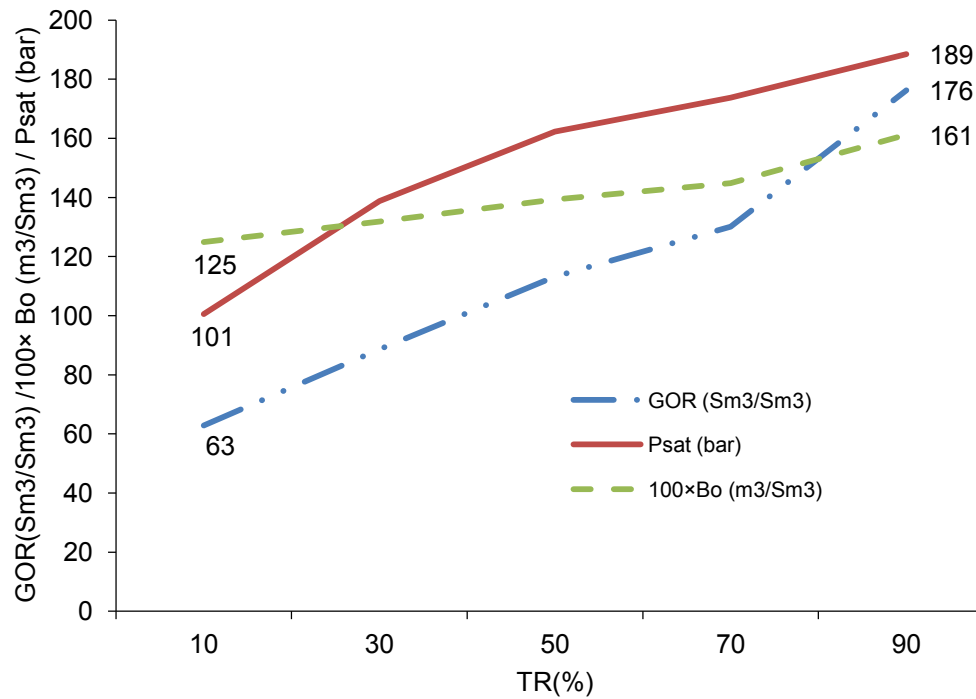


Figure 4.9 Calculated GOR, P_{sat} , B_o evolution with a function of TR.

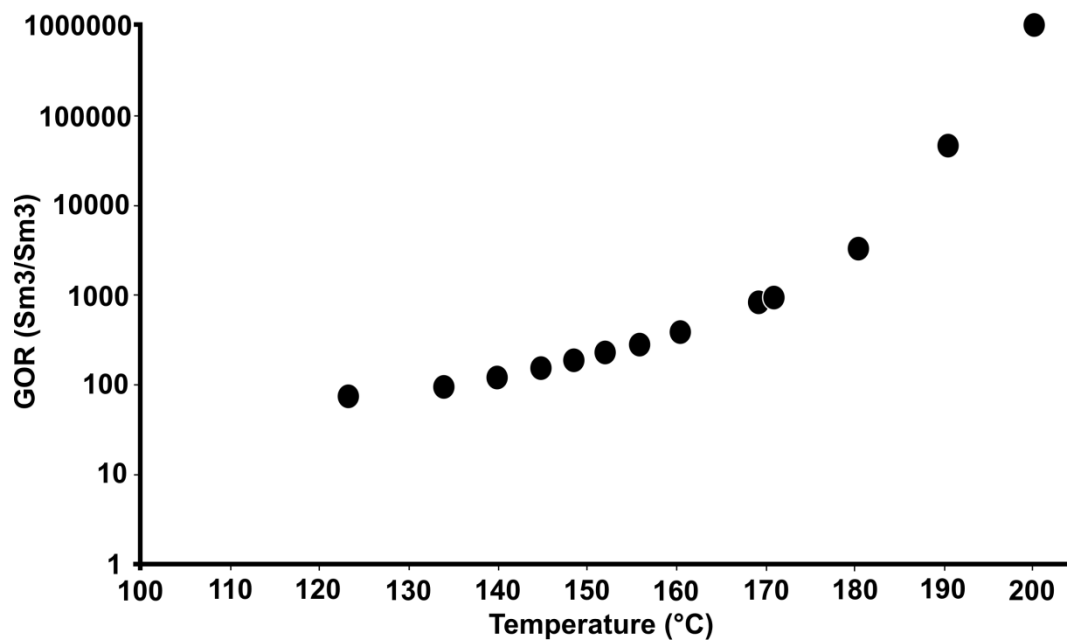


Figure 4.10 Predicted GOR evolution with a function of temperature for a heating rate of 1.5 °C/ ma.

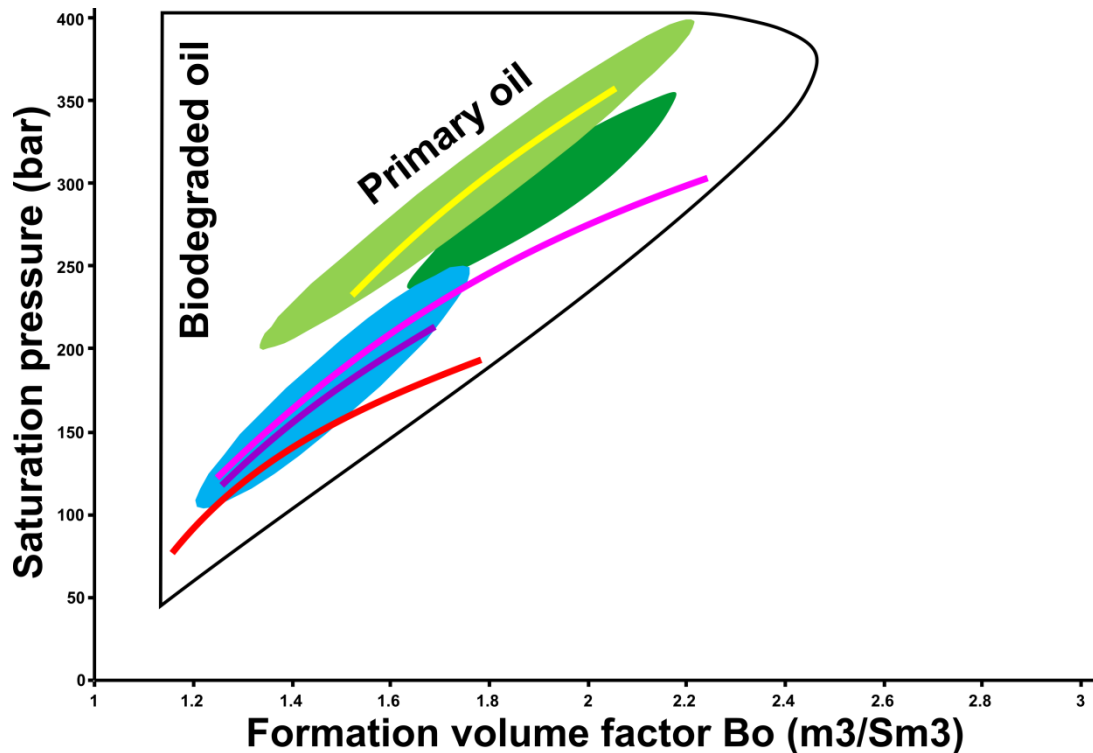


Figure 4.11 Predicted P_{sat} and B_o for a heating rate of $1.5\text{ }^{\circ}\text{C}/\text{ma}$. Ellipses are the ranges of natural oils from the Central Graben) (di Primio and Neumann, 2008), Viking Graben (Bhullar et al., 2003) and Tampen Spur (di Primio et al., 1998) in the Northern Sea, Norway, from the top down. Curves are the predicted ranges of natural oils in the Central Graben, Lower Cambrian shale in the UYP, natural oils in the Tampen Spur (di Primio and Skeie, 2004) and Bakken shale (Kuhn et al., 2010), from the top down.

4.6.4. Petroleum Phase Behaviour Prediction in the UYP

Petroleum phase behaviour of fluids potentially generated during maturation of the UYP Cambrian shale was defined for the temperatures 120, 130, 137, 145, 152 and 165°C (Figure 4.12), which are respectively corresponding to 10, 20, 30, 50, 70 and 90% TR (Figure 4.8). For the present case study it is assumed that all products are retained in the shale reservoir and nothing is expelled. Reservoir pressure applied in the model was calculated only based on the reservoir depths in Figure 4.3 (red points, A-F) and assuming a geo-pressure gradient of 100 bar/km.

Subsequent to basalt eruption in Permian, the onset of primary hydrocarbon generation occurred in the Middle Triassic (241 ma) at a burial depths around 2000 m (Figure 4.3). Here and as shown in Figure 4.12A, the phase envelope of the generated fluid indicates petroleum with a GOR lower than $100\text{ Sm}^3/\text{Sm}^3$ (compare Figure 4.10) and a bubble point pressure (P_b) around 120 bar, which is much lower than the shale reservoir pressure (P_r). The bubble point

Chapter 4 Petroleum Physical Properties

pressure P_b corresponds to the pressure for which gas dissolves from the oil phase. The generated black oil ($GOR < 200 \text{ Sm}^3/\text{Sm}^3$ in Figure 4.10) therefore existed as a single oil phase at shale reservoir conditions. In the case of expulsion of this undersaturated black oil and migration into overlying strata in which lower reservoir pressures existed, a 2-phase system would be reached at 120 bar. Based on the kinetics black oil generation continued to the Late Triassic (203 ma) for burial depths up to 3300 m and temperatures around 145°C (Figures 4.3 and 4.12D). In that period, although P_b has increased to over 260 bar, the shale reservoir pressure P_r was still much lower. Thus, petroleum occurred only as a single liquid phase in the shale reservoir position. When burial depth and temperature increased to 3500 m and 152°C respectively (200 ma) (Figures 4.3 and 4.12E), the reservoir liquid phase became gassier and GORs started to increase rapidly due to the beginning of secondary cracking of oil compounds (Figures 4.3, 4.10 and 4.12 E). Black oil has evolved to volatile oil but P_b (290 bar) was still lower than P_r . The single oil phase under shale reservoir conditions was therefore maintained.

Later, at Early Jurassic times (187 ma) temperatures increased to 165°C for burial depth around 4000 m (Figures 4.3 and 4.12 F). Assuming that all compounds stayed in place, fluid in the reservoir changed from undersaturated liquid (volatile oil) into undersaturated gas (wet gas). P_b was reduced to ~ 200 bars, and started to decrease continuously from an increasing process from A to E. In that case, a single gas phase could change into a gas-oil phases when 200 bar of P_b reached. With a continuous increase of burial depth and temperature in the Middle-Late Jurassic, GORs climbed rapidly (Figure 4.10) by secondary cracking of the remaining oil compounds. P_b decreased to lower than 100 bar while P_r increased to ~ 600 bar by the end of the Jurassic (Figures 4.3 and 4.12 G and H). Fluids under the shale reservoir conditions occurred as a gas phase predominated by methane with only minor amounts of light hydrocarbons being present. Thus, although Lower Cambrian shale in the UYP has been significantly uplifted since Cretaceous (Figure 4.3 I), only the vapor phase (dry gas) reservoir could form within this formation.

Bubble point pressures were significantly below corresponding reservoir pressures in the whole burial process for each stage (Figures 4.3 and 4.12). As a result from constant burial from Permian to Jurassic times, the formation experienced the highest temperatures of $\sim 220^\circ\text{C}$ by the end of the Jurassic, and lasted for 60-70 ma in a high temperature zone ($>200^\circ\text{C}$) (from G to I in Figure 3). When organic matter suffers such high temperatures over a long time span, hydrocarbons formed in the shale reservoir can be only gases regardless how the pressure changes (Figures 4.12G and H).

Chapter 4 Petroleum Physical Properties

Thus, only a single phase would have existed in the Lower Cambrian shale assuming hydrocarbons were completely preserved in the source rock within an unconventional system. A liquid phase (black oil and volatile oil) would have dominated during the primary generation process and a gas phase (wet gas and dry gas) during the secondary generation process. However, phase separation of the fluid into an oil leg and a gas cap would have occurred if the liquid petroleum had migrated during early maturation stages to a shallower, for example conventional reservoir in which bubble point pressure might have been higher than the corresponding reservoir pressure.

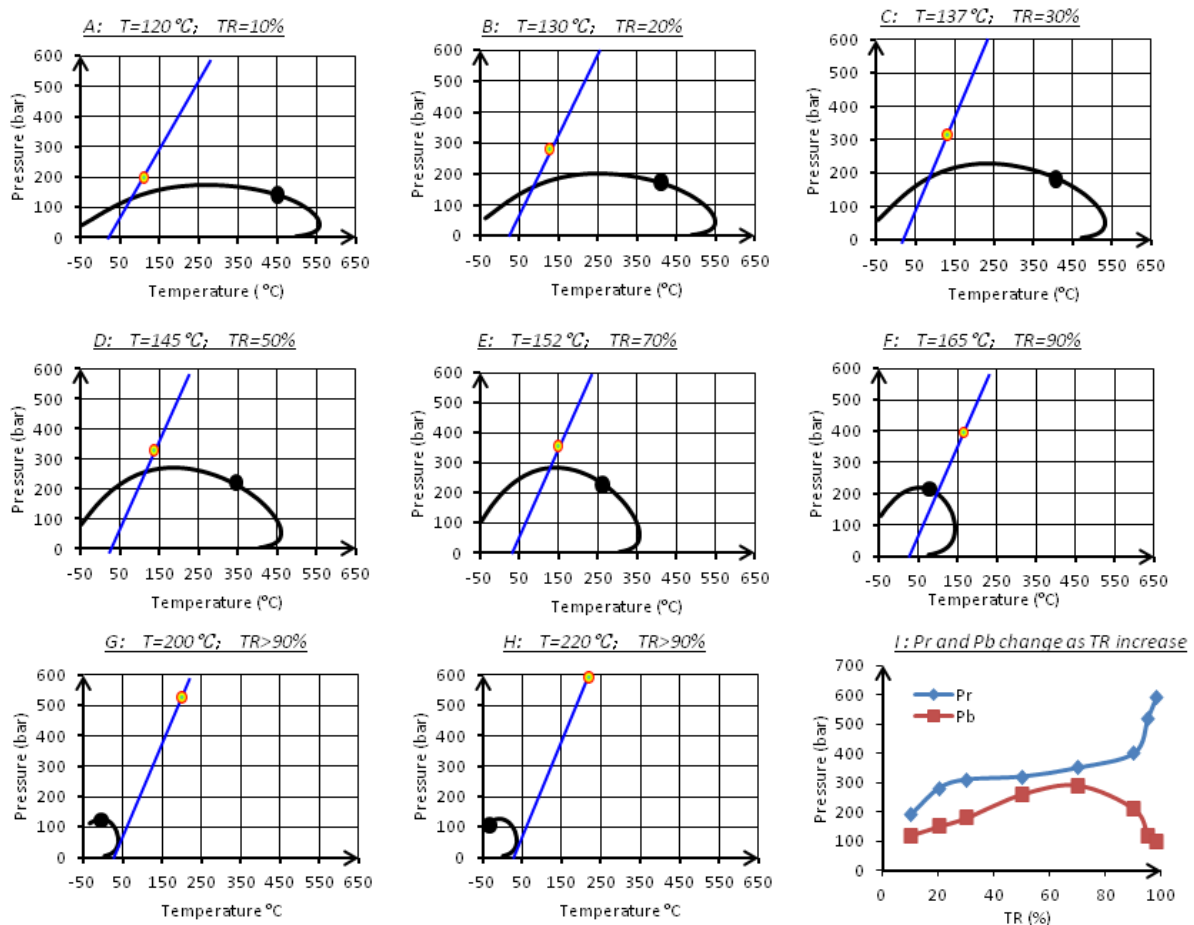


Figure 4.12 Phase behavior evolution with burial depth and temperature increasing of Lower Cambrian shale in the UYP. Diagonals are the temperature-pressure gradients in reservoir conditions; Points on the diagonal are the reservoir conditions in given times; Curves are the phase envelopes; Points on the envelope are bubble points; Plots A-H are corresponding to the six reservoir positions in Figure 4.3.

4.7. Conclusions

Geological temperature-depth history of a well located in the UYP showed that the Lower Cambrian shale succession was influenced strongly by uplifts between the end of the Silurian and Carboniferous, which resulted in erosion of younger sediment packages. The sedimentation generally continued from Permian to Jurassic, with an interruption by a short uplift phase during Middle to Late Permian times. The deepest burial depth of 6000 m with a maximum temperature of 220°C occurred during the Late Jurassic. From then on, the UYP entered into the third uplift period commencing in the Cretaceous. At present, organic matter in Lower Cambrian shale contains normally between 5-10% TOC which is overmature. It possesses only very low remaining petroleum generation potential, but huge amounts of hydrocarbons must have been generated during geological history.

Based on the adjacent tectonic position and comparable Cambrian geology of north Australia and south China, an immature Cambrian Shale sample from the Georgina Basin was used to investigate the petroleum generation kinetics of the Lower Cambrian shale in the UYP, as well as petroleum phase evolution within an unconventional shale reservoir in this formation. The analysis on source rock characteristics suggested a type II kerogen and an organofacies inferring paraffinic-naphthenic-aromatic low wax oil generation. Hydrocarbon generation can be described by a single frequency factor of $A=8.429E+14$ 1/sec and an activation energy distribution ranging from 44 to 67 kcal/mol. The main activation energy of 56 kcal/mol is higher than commonly assumed oil and gas formation from marine, clastic source rocks, and indicated presence of marine but highly stable, sulphur-poor organic matter in the Cambrian shale. The onset temperature of hydrocarbon generation (TR=10%) is ~120°C, while end of generation (TR=90%) can be expected for temperatures around 165°C for a geological heating rate of 1.5 °C/Ma.

Phase behaviour properties for onset and end of bulk hydrocarbon generation from kerogen can be described by a GOR of $63\text{Sm}^3/\text{Sm}^3$, P_{sat} of 101bar and B_o of $1.2\text{ m}^3/\text{Sm}^3$ at 10% TR, and a GOR of $176\text{ Sm}^3/\text{Sm}^3$, P_{sat} of 189 bar and B_o of $1.61\text{ m}^3/\text{Sm}^3$ at 90% TR. Onset occurred in the Middle Triassic (241 ma) at burial depths around 2000 m for temperature close to 120°C. Before 203 ma, for temperatures <145°C, burial depth <3300 m, and TR <50%, phase behaviour of generated black oil was defined by primary product evolution. Secondary cracking of oil to gas predominated with increasing burial depth and temperature in Middle-Late Jurassic times. Kerogen conversion was completed in the Early Jurassic (187 ma) at depths close to 4000 m and temperatures around 165°C.

Chapter 4 Petroleum Physical Properties

In the Lower Cambrian shale reservoir, bubble point pressure was much lower than the reservoir pressure during the whole maturation process. Unconventional shale resources can therefore only be present as a single phase, and were dominated by a single liquid phase (black oil and volatile oil) during the primary generation process and a single vapor phase (wet gas and dry gas) during secondary cracking processes.

Limitations of the model exist with respect to hydrocarbon expulsion since generated hydrocarbons were regarded as retained petroleum. In addition, the predicted petroleum physical properties rely on local geological background and original kerogen type, hence, the applicability of the conclusions presented in this paper has to be considered prudently when apply to other unconventional shale system.

4.8. Acknowledgements

The authors thank Statoil for funding and publication permission. We are grateful to Ferdinand Perssen (GFZ-Potsdam) for his technical assistance. Further thanks go to all anonymous reviewers for their constructive comments and suggestions.

Chapter 5 Methane Sorption Capacity

5.1. Abstract

The marine black shale formations on the Upper Yangtze Platform (UYP), south China are exploration targets for shale gas. Here, we report on the methane sorption capacity of thermally overmature samples from the Lower Silurian and Lower Cambrian black shale intervals in the UYP (UYP-samples). Two immature shale samples from the Middle Cambrian formation in the Georgina Basin, north Australia (AU samples) were also tested to investigate the effect of thermal maturity on sorption isotherms. Excess sorption isotherms were performed over a pressure range of 0-25 MPa at 46°C. The effects of TOC content, thermal maturity, clay minerals, moisture content, pore properties, particle size, temperature, and pressure on methane sorption capacity were analysed. In addition, thermovaporisation gas chromatography (T_{vap}-GC) was used to measure the residual gas that is stored in the samples under atmospheric pressure and temperature conditions.

The results indicate that the maximum methane excess sorption of the Lower Silurian samples is between 0.045 and 0.064 mmol/g rock and that of Lower Cambrian samples is between 0.036 and 0.210 mmol/g rock. The Langmuir sorption capacity of the Lower Silurian samples ranges from 0.096 to 0.115 mmol/g rock, whereas that of the Lower Cambrian shale ranges from 0.077 to 0.310 mmol/g rock. These results are close to the sorption capacities of the Barnett (U.S.), Devonian-Mississippian (Western Canada), and Alum (Southern Scandinavia) shale samples. The shape of the sorption isotherms and methane sorption capacity vary from sample to sample. Under the measured pressure range, the isotherms of the selected immature AU Cambrian samples increase monotonously with pressure, whereas the overmature UYP samples exhibit maxima. The methane sorption capacity of the measured samples positively correlates with TOC content and exhibits a distinct linear relation. The TOC-normalised sorption capacity shows a positive correlation with thermal maturity; however, the corresponding pressure of maximum excess sorption and Langmuir pressure

This chapter has been published as: Tan, J., Weniger, P., Krooss, B., Merkel, A., Horsfield, B., Zhang, J., Boreham, C. J., van Graas, G. and Tocher, B.A., 2014. Shale Gas Potential of the Major Marine Shale Formations in the Upper Yangtze Platform, South China, Part II: Methane Sorption Capacity. Fuel, , 129:204-218.

Chapter 5 Methane Sorption Capacity

decrease substantially with increasing thermal maturity. The clay minerals show a positive effect on the TOC-normalised sorption capacity. The sorption capacity of clay minerals, however, should have been reduced by the moisture content. The two Lower Cambrian samples that have similar maturities were measured for porosity and pore-size distribution. The sample with a high TOC content shows a high total cumulative pore volume, surface area, total porosity and thus a higher sorption capacity than the sample with less TOC. In addition, larger-sized particles show slightly less sorption capacity than smaller-sized particles. The T_{vap}-GC results show that the residual gas content of core samples is evidently higher than that of the outcrop samples, which implies a remarkably negative effect of the weathering process.

Keywords

Methane sorption capacity, sorption isotherm, shale gas, Lower Cambrian shale, Lower Silurian shale, south China

5.2. Introduction

Shales are generally characterised by low porosity and permeability, and the natural gas may be stored in organic rich shales as free gas, adsorbed gas, and/or dissolved gas (Schettler and Parmoly, 1990; Martini et al., 1998; Curtis, 2002; Ross and Bustin, 2009). In general, the free gas is primarily responsible for the gas-in-place of shale gas plays, whereas the adsorbed gas partially determines the longevity of shale gas producing wells (Zhang et al., 2012b). For the Antrim, Ohio, New Albany, Barnett, and Lewis shale gas plays, the adsorbed gas accounts for 20-85% of the total gas (Curtis, 2002), and the adsorbed gas is higher than 50% of the total gas for the Devonian shale in the Appalachian Basin (Lu et al., 1995). Thus, gas adsorption is one of major gas storage mechanisms in shale systems. On the other hand, the methane sorption capacity of shale samples has been widely recognised as varying significantly with the constituents (organic and inorganic) of the samples, moisture content, porosity and pore properties, particle size, and experimental conditions, e.g., temperature and pressure (Lu et al., 1995; Chalmers and Bustin, 2007b; Ross and Bustin, 2007; Chalmers and Bustin, 2008; Ross and Bustin, 2009; Gasparik et al., 2012; Ji et al., 2012; Zhang et al., 2012b; Gasparik et al., 2013; Wang et al., 2013a).

The methane adsorption in the shale samples is the accumulation of methane molecules on the surface of organic matter and minerals, and it is intrinsically related to the micropores

Chapter 5 Methane Sorption Capacity

(diameter, $D < 2$ nm) that have larger internal surface areas and greater sorption energies than the large pores (Dubinin, 1975; Ross and Bustin, 2009). Therefore, the methane sorption capacity of shale samples is positively correlated with factors that have or could create more micropores, whereas it is negatively correlated with factors that could reduce or block micropores. The organic matter properties, e.g., organic richness, thermal maturity, and organic type, have critical effects on the methane sorption capacity of shale samples (Chalmers and Bustin, 2007b; Chalmers and Bustin, 2008; Ross and Bustin, 2009; Zhang et al., 2012b; Gasparik et al., 2013). As the maturity increases, additional micropores may be created in the organic matter during the process of organic matter degradation, hydrocarbon generation and expulsion (Gan et al., 1972; Prinz et al., 2004; Prinz and Littke, 2005; Ross and Bustin, 2009). Therefore, the overmature and high TOC content samples generally show higher sorption capacity than the low mature and low TOC samples (Chalmers and Bustin, 2008; Ross and Bustin, 2009; Gasparik et al., 2013). The methane sorption capacity of type III organic matter is significantly higher than that of type I and II organic matter (Zhang et al., 2012b). For type III organic matter, the sorption capacity of vitrinite-rich coals is higher than that of inertinite-rich coals at the same rank (Lamberson and Bustin, 1993; Bustin and Clarkson, 1998; Crosdale et al., 1998; Mastalerz et al., 2004; Hildenbrand et al., 2006). The effect of organic matter type may be the result of the microporous vitrinite rather than other maceral constituents (Lamberson and Bustin, 1993; Beamish and Crosdale, 1995) or the higher composition of aromatic compounds in type III organic matter than in type I and II (Zhang et al., 2012b). The impact of clay minerals on sorption capacity is significant because of their crystal layers or porous structures; therefore, they generally provide more adsorption sites and large surface areas than other minerals (Aringhieri, 2004; Cheng and Huang, 2004; Wang et al., 2004). The sorption capacity of the montmorillonite and illite/semectite mixed layer is evidently higher than that of kaolinite, chlorite, and illite in the dry state because of the typical three layer crystal structure (Ji et al., 2012). Nevertheless, the sorption capacity of clay may be reduced significantly when water is present in the sample, which is ascribed to its hydrophilic nature. Generally, the presence of water may result in the swelling of clay minerals, taking of sorption sites, and blocking of the pore system, which negatively affects the methane sorption capacity (Krooss et al., 2002). Above a certain moisture concentration, however, the methane adsorption capacity does not decrease any further because all possible adsorption sites for water are occupied, so the water present in excess of the adsorbed water has no effect on the methane sorption (Joubert et al., 1974; Levy et al., 1997; Bustin and Clarkson, 1998).

Chapter 5 Methane Sorption Capacity

The marine black shales are widely distributed on the Upper Yangtze Platform (UYP), south China, particularly in the Lower Paleozoic formations. The Lower Silurian and Lower Cambrian shale intervals have been regarded as prolific shale gas plays (EIA, 2011b; EIA, 2013b). They are generally characterised by a large distribution, big thickness, high TOC content, high quartz content and low clay content (Zhang et al., 2008a; Long et al., 2009; Wang et al., 2009b; Wang et al., 2009c; Zou et al., 2010; Nie et al., 2011; Zou et al., 2011; Huang et al., 2012b; Chen et al., 2013; Tian et al., 2013). Until recently, shale gas was produced from these formations in the Sichuan Basin. Nevertheless, the methane sorption capacity of these shale intervals is still poorly understood. The objectives of this study are to 1) investigate the sorption capacity of shale samples from the Lower Silurian and Lower Cambrian formations in the UYP and 2) analyse the major factors influencing sorption capacity. High-pressure (up to 25 MPa) methane sorption isotherms were measured at 46°C on overmature samples from the UYP, and two immature shale samples from the Middle Cambrian formation in the Georgina Basin, north Australia were measured to study the effect of thermal maturity on sorption capacity. We have already reported on the petroleum phase behaviour of these shale samples (Tan et al., 2013), while their organic geochemical properties, mineralogical composition, lithofacies, petrophysical and rock mechanical properties will be reported in other publications (Tan et al., 2014a; Tan et al., 2014b).

5.3. Samples and Methods

5.3.1. Sample Characterisation

The measured samples are black shales deposited in marine environments from the Upper Yangtze Platform, south China (UYP samples) and from the Georgina Basin, north Australia (AU samples) (Figure 5.1). The detailed geochemical and mineralogical results are listed in Table 5.1. These samples are selected on the basis of the TOC content, thermal maturity, and mineral contents.

The UYP samples are Lower Cambrian and Lower Silurian black in age: seven are outcrops from the profiles in the Chongqing area and Guizhou Province, whereas two are cores from the Yuke-1 well (47.5 m) in the Chongqing area and Songqian-1 well (109.4 m) in the Guizhou Province (Figure 5.1A). The equivalent vitrinite reflectance values of these samples based on the carbon isotope ratio of methane are between 2.5 and 3.0% for the Lower Silurian shales and between 3.0 and 3.5% for the Lower Cambrian shales, which indicates

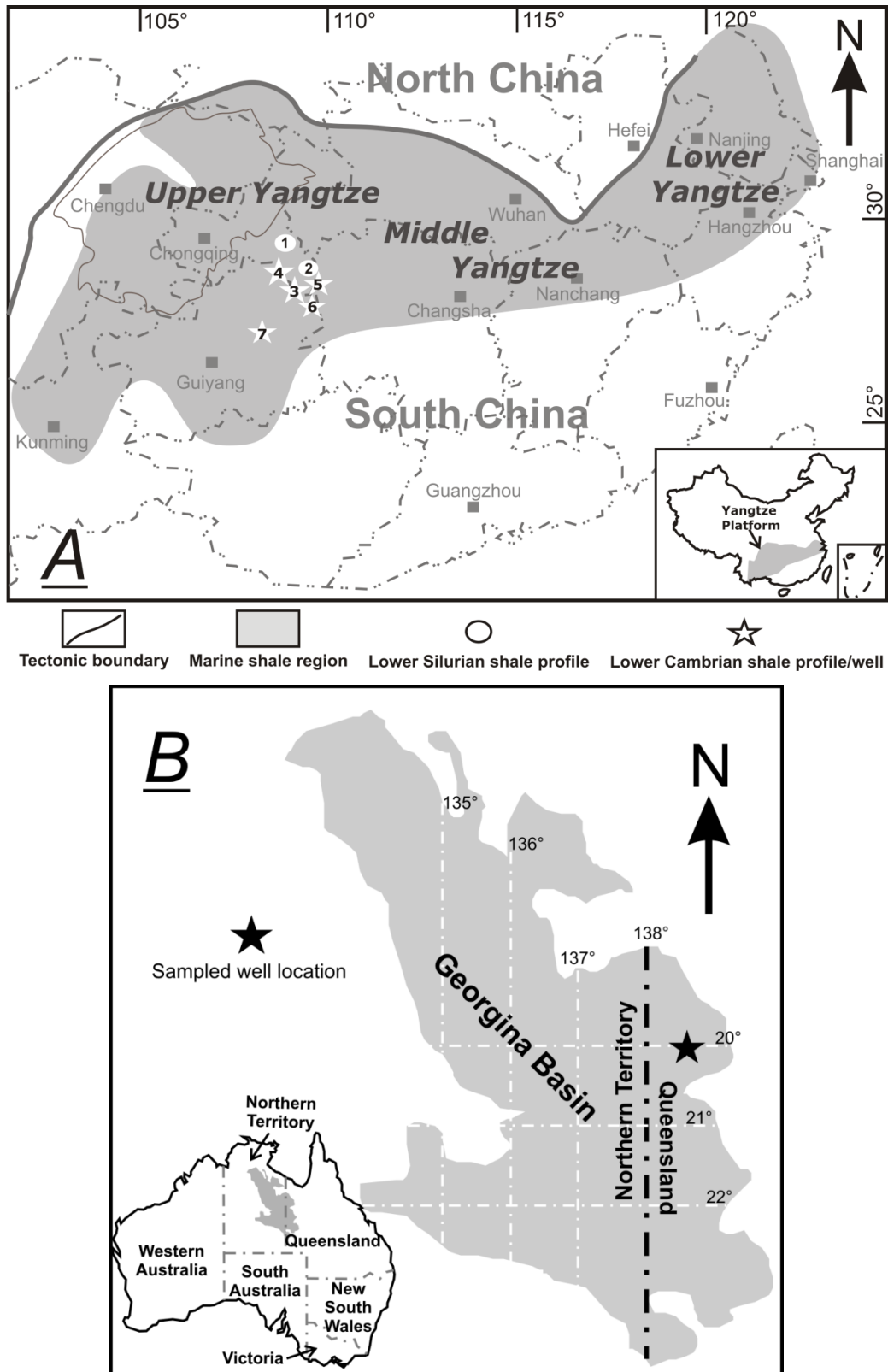


Figure 5.1 Locations of the sampled profiles and wells in the Upper Yangtze Platform, south China (A) and Georgina Basin, north Australia (B). Profiles and wells in the Chongqing area are the 1-Lujiao profile, 2-Datianba profile, 3-Rongxi profile, 4-Jinggang profile, and 5-Yuke1 well; however, the 6-Songqian1 well and 7-Cenggong profile are located in the Guizhou Province. The AU Middle Cambrian shale samples are from the BMR Mt Isa 1 well in the Georgina Basin.

Chapter 5 Methane Sorption Capacity

Table 5.1 Samples measured for the methane sorption isotherms.

Sample ID	Formation	Depth (m)	Maturity (R_{∞} %)	Minerals (%)							Moisture (%)	TOC (%)	Porosity (%)	Particle size
				Quartz	Clay	Carbonate	Feldspar	Mica	Pyrite	Others				
G009507	LMX	0	2.5-3.0	40.8	21.08	8.06	8.15	15.83	6.08	NA	0.53	3.34	N.A	<200 μ m
G009509	LMX	0	2.5-3.0	41.07	28.88	7.62	9.15	11.3	1.99	NA	0.43	1.68	N.A	<200 μ m
G011298	LMX	0	2.5-3.0	74.28	8.53	NA	5.09	8.96	0.49	2.65	0.62	4.15	N.A	<200 μ m
G009517	NTT	0	3.0-3.5	33.57	5.97	NA	31.48	20.52	1.25	7.21	1.45	6.02	N.A	<200 μ m
G009518	NTT	0	3.0-3.5	31.16	7.25	11.88	29.16	14.55	6.01	NA	0.64	7.44	N.A	<200 μ m
G009520	NTT	0	3.0-3.5	41.68	8.7	NA	28.38	15.32	5.92	NA	0.58	9.41	N.A	<200 μ m
G009521	NTT	0	3.0-3.5	45.13	19.81	NA	17.17	17.89	NA	NA	0.93	2.85	N.A	<200 μ m
G011313-1	NTT	109.4	3.0-3.5	42.83	23.28	NA	13.25	17.45	3.19	NA	2.28	1.38	2.02	<0.5mm
G011313-2	NTT	109.4	3.0-3.5	42.83	23.28	NA	13.25	17.45	3.19	NA	2.28	1.38	2.02	0.5-1 mm
G011319	NTT	47.5	3.0-3.5	66.44	11.3	2.27	6.74	8.75	4.5	NA	0.62	13.2	9.13	<200 μ m
G006491	AU	101.5	0.6	22.98	5.57	43.82	18.68	8.03	0.93	NA	0.72	9.04	N.A	<200 μ m
G006492	AU	107.5	0.5	26.7	6.85	26.75	21.7	16.33	1.67	NA	0.99	15.8	N.A	<200 μ m

LMX-Longmaxi formation, Lower Silurian, Upper Yangtze Platform; NTT-Niutitang formation, Lower Cambrian, Upper Yangtze Platform; AU-Arthur creek formation, Middle Cambrian, north Australia; Vitrinite reflectance (R_{∞}) of the UYP shale is deduced from carbon isotope ratio of methane, and of the AU shale is calculated from T_{\max} .

high maturity levels. The mineral constituents are characterised by a high proportion of quartz, moderate content of clay, and low abundance of carbonates. With the exception of two of the Lower Cambrian shales, the samples show moisture content less than 1%. The TOC content of the Lower Silurian samples is between 1.68 and 4.15% (wt %), whereas that of the Lower Cambrian samples increases gradually from 1.38 to 13.20% (Table 5.1).

To evaluate the effect of the thermal maturity of organic matter on the sorption capacity, two immature AU samples were measured. Because the Cambrian shales from the UYP and Georgina Basin possess similar original organic matter types but underwent a rather different burial history (Tan et al., 2013); thus the organic matter of the AU Cambrian shale is still immature, whereas that of the UYP Cambrian shale is overmature. These two AU samples were recovered from the Middle Cambrian Arthur Creek formation in the southern Georgina Basin at depths of 101.5 m and 107.5 m, respectively (Figure 5.1B). The vitrinite reflectance values, calculated from the T_{\max} values of Rock-Eval pyrolysis, are between 0.5 and 0.6%. Compared to the UYP samples, the mineral constituents of the AU samples are characterised by a higher content of carbonates and relatively a lower content of quartz and clay. In addition, these two samples have a moisture content less than 1% and TOC content higher than 9.0% (Table 5.1).

5.3.2. Sample Preparation

Most of the samples were crushed to pass through a sieve size of 200 μ m, and the methane sorption isotherms were measured in the “as received” moisture state, i.e., without drying in the laboratory. To evaluate the effect of particle size on sorption capacity, the G011313 core was measured two times with cutting sizes of 0.5-1 mm and less than 0.5 mm (Table 5.1).

5.3.3. Experimental Setup and Procedure

The high-pressure methane sorption measurements were conducted on a manometric setup, which has been described in detail in a series of publications (Krooss et al., 2002; Weniger et al., 2010; Gasparik et al., 2013). The setup consists of a stainless steel sample cell, two high-pressure shut-off valves, and a high-accuracy pressure transducer connected by 1/16 inch stainless steel tubing and placed in a thermostatic oven (GC-furnace). A 2- μm filter is equipped on the entrance of the sample cell to prevent shale particles from entering the valves, whereas a three-port valve is used to link the gas supply (helium and methane) and a vacuum pump. The volume between the two valves, including the dead volume of the pressure transducer, is regarded as the reference volume ($\sim 1.3 \text{ cm}^3$) and determined by the helium expansion in a calibration run, whereas the temperature is recorded by a high-precision Pt-100 resistance temperature detector (RTD).

5.3.3. Experimental Setup and Procedure

The high-pressure methane sorption measurements were conducted on a manometric setup, which has been described in detail in a series of publications (Krooss et al., 2002; Weniger et al., 2010; Gasparik et al., 2013). The setup consists of a stainless steel sample cell, two high-pressure shut-off valves, and a high-accuracy pressure transducer connected by 1/16 inch stainless steel tubing and placed in a thermostatic oven (GC-furnace). A 2- μm filter is equipped on the entrance of the sample cell to prevent shale particles from entering the valves, whereas a three-port valve is used to link the gas supply (helium and methane) and a vacuum pump. The volume between the two valves, including the dead volume of the pressure transducer, is regarded as the reference volume ($\sim 1.3 \text{ cm}^3$) and determined by the helium expansion in a calibration run, whereas the temperature is recorded by a high-precision Pt-100 resistance temperature detector (RTD).

In this study, the methane sorption isotherms were measured for “as received” samples in a pressure range of 0-25 MPa at 46°C. These pressure and temperature conditions should be suitable for reservoirs at a depth between 1 and 2 km in the UYP because the present geothermal gradients are generally between 18 and 33°C/km (Han and Wu, 1993; Xu et al., 2011).

The experimental procedure can be summarised as follows (see Weniger et al., 2010):

- 1) Degas the measuring material by evacuation for 15 min at 1 MPa;
- 2) Conduct a leak test using helium at 10 MPa for 2 hours to reach thermal equilibration and guarantee a helium leakage rate less than 500 Pa per hour;

Chapter 5 Methane Sorption Capacity

- 3) Determine the void volume as well as the sample volume using helium expansion. Void volume is calculated using the average value of 10 pressure steps ranging from 1 to 10 MPa with a standard deviation less than 0.05%. In addition, the void volume determination provides the sample volume which can be used to calculate sample skeletal density;
- 4) Evacuate for 60 min at 1 MPa to remove the helium; and
- 5) Perform the methane sorption measurement until the pressure increases to 20-25 MPa.

5.3.4. Results Calculation and Parameterisation

The excess sorption amount of adsorbed gas (m_{excess}) is calculated from the difference between the total amount of gas introduced into the system (m_{total}) and the amount of gas that is still present in the void volume (V_{void}), i.e., the amount of gas that is not adsorbed by the measuring material.

$$m_{\text{excess}} = m_{\text{total}} - \rho_{\text{gas}} V_{\text{void}} \quad (5.1)$$

The void volume is determined by helium expansion at 46°C prior to the sorption measurement, whereas the gas density (ρ_{gas}) is calculated from an equation of the state of the gas for the corresponding pressure and temperature conditions. The measured results are in molar units normalised to the sample's mass (mmol CH₄/g rock).

The Langmuir model is commonly applied to describe the relations between the adsorbed gas on a solid surface and measured pressure at a fixed temperature:

$$n_{\text{excess}} = n_L \cdot \frac{P}{P_L + p} \quad (5.2)$$

Here, n_{excess} (mmol/g) denotes the excess adsorbed amount of substance at pressure P (MPa). P_L (MPa) is the Langmuir pressure and corresponds to the pressure at which half of the (“monolayer”) sorption sites are occupied and n_L (mmol/g) is the “Langmuir amount of substance” (corresponding to the “Langmuir volume”), which denotes the amount adsorbed at full occupancy of the “Langmuir monolayer.”

Because the Langmuir sorption model is a limiting model for low pressure, its application to high-pressure sorption isotherms is not strictly justified (Weniger et al., 2010).

Chapter 5 Methane Sorption Capacity

Most of the excess sorption isotherms measured in this study exhibit a maximum in the pressure range between 10 and 15 MPa, which indicates that the adsorption maximum occurs before the final experimental pressure was reached. At higher experimental pressure, the density of the gas phase increases and gradually approaches the density of the adsorbed phase, which results in a decrease of the excess sorption. To approximate the measured data of the isotherms exhibiting a maximum, a modified Langmuir model was used. This function is given by the following:

$$n_{excess} = n_L \cdot \frac{p}{P_L + p} \cdot \left(1 - \frac{\rho_g}{\rho_{ads}}\right) \quad (5.3)$$

The function contains an additional adjustable parameter, which is the density of the adsorbed phase (ρ_{ads}). The parameters n_L , P_L , and ρ_{ads} are fitted to the experimental excess sorption data using a least squares minimisation procedure.

5.3.5. Equation of State (EOS)

The equation of state (EOS) developed by Setzmann and Wagner (1991) for methane was applied to calculate the specific density of the free gas phase under experimental pressure and temperature conditions, whereas the wide-range equation of state GERG-2004 was used to calculate the helium density during the void volume evaluation (Michels and Wouters, 1941).

5.3.6. Thermovaporisation Gas Chromatography (T_{vap}-GC)

Thermovaporisation gas chromatography (T_{vap}-GC) was measured using a Quantum MSSV-2 Thermal Analyser pyrolysis oven unit interfaced with an Agilent GC 6890A apparatus. An HP-Ultra 1 dimethylpolysiloxane capillary column (50 m long, 0.32 mm inner diameter, and 0.52 μm film thickness) connected to a flame-ionisation-detector (FID) was used with helium as a carrier gas. Approximately 20-30 mg of finely ground powder was weighed into glass capillaries that were then sealed by an H₂-flame after reducing the internal volume of the tube from ca. 40 ml to ca. 15 ml with pre-cleaned quartz sand. The sealed tubes were then introduced into the GC unit. The external surfaces of each tube were purged for 5 min at 300°C, during which time the volatiles were also mobilised within the tube. Afterwards, the tube was cracked open by a piston device. The generated products from within the vessel

were then transferred into a liquid nitrogen-cooled trap using a helium-carrier gas with a flow rate of 30 ml/min. The trapped hydrocarbons were released to the column by ballistic heating of the trap to 300°C, and the thermovaporisation products were quantified using gas chromatography.

5.4. Results

5.4.1. Methane Sorption Isotherm Results

The methane sorption isotherms are shown in Figure 5.2, in which the excess adsorbed amount of methane is normalised to the sample weight (mmol CH₄/g rock) and TOC (mmol CH₄/g TOC). All of the Lower Silurian and Lower Cambrian samples from the UYP exhibit maxima in the excess sorption isotherms, whereas this is not the case for the immature AU Cambrian samples. Under the measured pressure range, the maximum methane sorption capacities are between 0.045 and 0.064 mmol/g rock (1.537 and 2.690 mmol/g TOC) for the Lower Silurian shales, between 0.036 and 0.210 mmol/g rock (1.206 to 2.696 mmol/g TOC) for the Lower Cambrian shales, and between 0.105 and 0.162 mmol/g rock (1.026 and 1.158 mmol/g TOC) for the AU Cambrian shales (Table 5.2). The pressures at which the excess sorption maxima occur (P_{excess}) of the UYP samples are between 8.8 and 14.2 MPa. Nevertheless, the sorption isotherms of immature AU samples monotonously increase with pressure; therefore, the maxima appear at the highest applied pressures (~22 MPa). Interestingly, the rock-normalised isotherms of all samples shift upward as TOC increases (plots on the left of Figure 5.2). The TOC-normalised isotherms, however, generally shift downward as TOC increases (plots on the right of Figure 5.2), with the exception of certain Lower Cambrian samples. These phenomena imply that the TOC content has a significant effect on the methane sorption of measured shale samples, whereas other effects, e.g., thermal maturity, mineralogy, moisture content, and porosity, might also affect the measured results. For the Lower Silurian samples, the P_{excess} of G009507 (10.9 MPa) is obviously less than that of G009509 (13.4 MPa), which may result from the hydrophilic properties of clay minerals (Ross and Bustin, 2009) and affinity of methane molecules for the sorption sites of organic matter (Ji et al., 2012). For the Lower Cambrian samples, G009521 (outcrop) has a higher TOC content, lower moisture content and smaller particle sizes compared to G011313-1 and G011313-2 (core). Their rock-normalised sorption isotherms, however, are very close. This

Chapter 5 Methane Sorption Capacity

phenomenon may reflect the effects of weathering on the quality of the organic and inorganic constituents of outcrop samples and thus affect the sorption isotherm and capacity.

The measured methane isotherms can be well fitted by the modified Langmuir function (formula 3). The calculated Langmuir sorption capacity (n_L), Langmuir pressure (P_L), and densities of the adsorbed gas (ρ_{ads}) and sample (ρ_{sample}) are listed in Table 5.2. The Langmuir sorption capacities normalised to the sample weight range from 0.077 to 0.310 mmol/g, whereas when the results are normalised to TOC, the capacities range from 1.536 to 6.097 mmol/g. The Langmuir pressures are between 3.0 and 14.0 MPa. The Langmuir pressures of immature AU samples are higher than that of most of the overmature Lower Cambrian and Lower Silurian shale samples.

5.4.2. T_{vap}-GC Results

Fourteen samples were measured by T_{vap}-GC analysis to quantify the retained/sorbed hydrocarbons (Tan et al., 2014b). The measured hydrocarbon gases are characterised by extremely low detectable quantities, which are between 9.8 and 29.0 $\mu\text{g/g}$ rock (0.5-1.4 mg/g TOC) for the Lower Silurian core samples and between 2.5 and 20.8 $\mu\text{g/g}$ rock (0.02-0.34 mg/g TOC) for the Lower Cambrian and Ediacaran outcrop samples. All samples show gas wetness values higher than 80% (Table 5.3), indicating a high content of C₂-C₅ and a low content of C₁. It should be noted that only three samples were measured by both the T_{vap}-GC and sorption isotherms, which resulted from different selection criteria. The samples for T_{vap}-GC were selected based on the S₁ of the Rock-Eval results, whereas the samples for sorption isotherms were selected based on the TOC, mineralogy, etc.

Table 5.2 Maxima in excess sorption isotherms (46°C) and Langmuir fitting parameters by the fit of three parameters.

Unit	Sample ID	n_{excess}		P_{excess} MPa	n_L		P_L MPa	ρ_{ads} Kg/m ³	ρ_{sample} g/cm ³
		mmol/g rock	mmol/g TOC		mmol/g rock	mmol/g TOC			
Lower Silurian	G009507	0.060	1.790	10.9	0.115	3.438	4.9	302.3	2.47
	G009509	0.045	2.690	13.4	0.096	5.697	6.9	322.1	2.71
	G011298	0.064	1.537	13.1	0.110	2.652	4.9	433.7	2.59
Lower Cambrian	G009517	0.073	1.206	8.8	0.124	2.067	3.0	273.5	2.62
	G009518	0.103	1.388	13.7	0.177	2.384	4.6	414.6	2.68
	G009520	0.121	1.289	12.4	0.195	2.068	3.8	431.3	2.46
	G009521	0.036	1.276	14.2	0.105	3.687	14.0	311.5	2.56
	G011313-1	0.037	2.696	10.5	0.084	6.097	6.7	262.8	2.74
	G011313-2	0.036	2.607	10.9	0.077	5.595	6.2	276.2	2.75
	G011319	0.210	1.589	12.2	0.310	2.352	2.6	445.7	2.50
AU Cambrian	G006491	0.105	1.158	22.4	0.229	2.529	11.9	507.6	2.33
	G006492	0.162	1.026	22.5	0.243	1.536	7.5	1429.4	2.05

Chapter 5 Methane Sorption Capacity

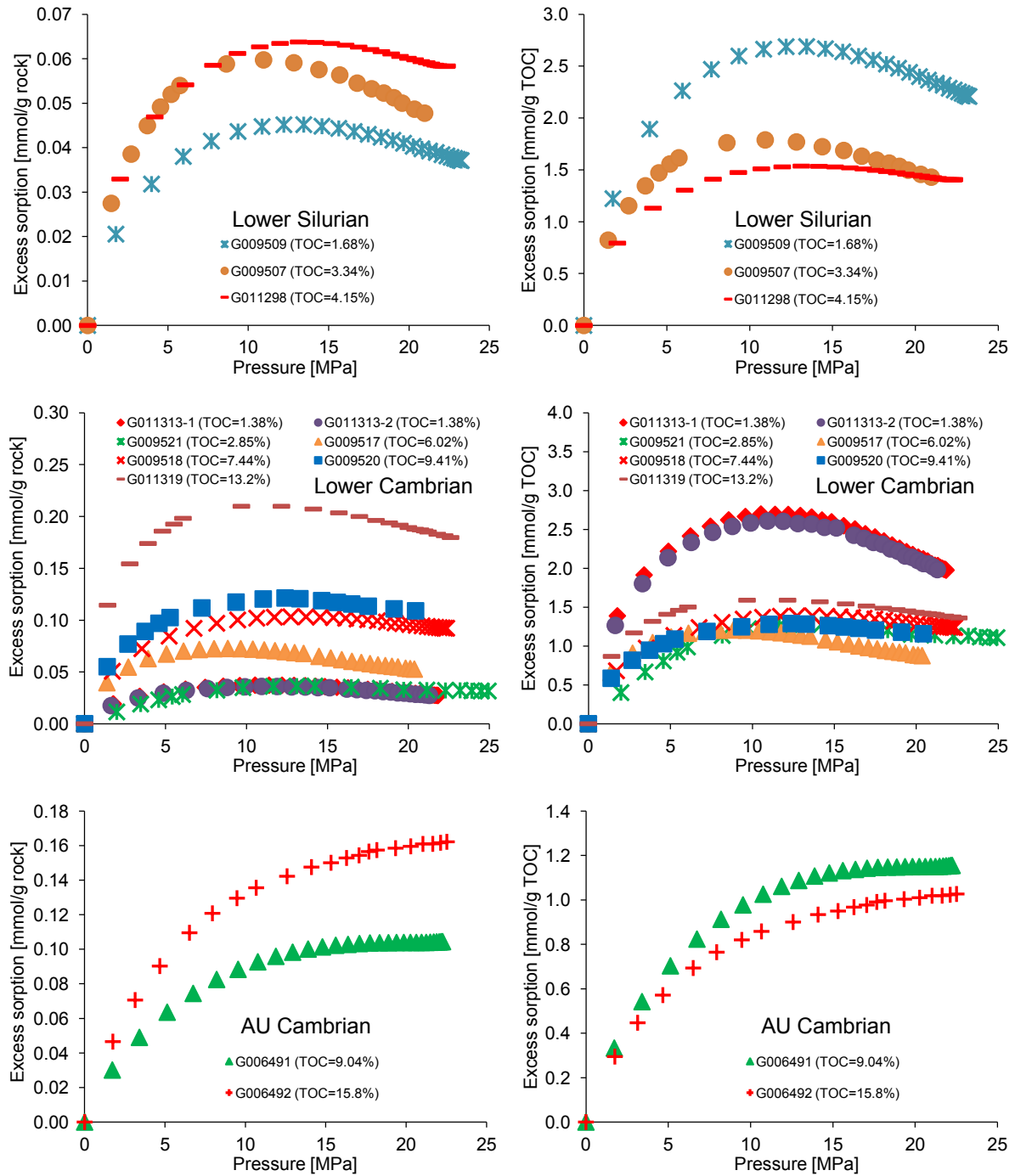


Figure 5.2 Methane excess sorption isotherms at 46°C measured on the received samples. The plots on the left are in mmol/g rock and on the right were normalised to TOC in mmol/g TOC.

Table 5.3 T_{vap}-GC and XRD results of selected samples.

Sample	Depth (m)	Fm.	TOC (%)	Retained gas hydrocarbon (µg/g rock)			Retained gas hydrocarbon (µg/g TOC)			Wetness (%)	Minerals (%)					
				C1	C2-C5	Total retained gas	C1	C2-C5	Total retained gas		Quartz	Feldspar	Pyrite	Clay	Mica	Carbonate
G009524	136	Lower Silurian (YY1 well)	1.97	1.0	8.8	9.8	50.7	447.7	498.3	89.8	30.0	7.0	4.6	40.3	16.5	1.6
G009525	207		1.47	1.0	12.7	13.7	68.5	864.3	932.8	92.7	39.6	11.6	1.5	26.4	14.7	6.2
G009526	267		2.31	0.3	16.6	16.9	13.8	718.0	731.8	98.1	42.8	9.0	1.8	20.8	9.8	15.9
G009527	276		1.69	1.1	23.4	24.5	64.6	1384.9	1449.4	95.5	41.0	12.4	3.2	22.9	14.7	5.8
G009528	285		1.68	0.9	9.5	10.4	53.0	563.9	616.9	91.4	42.2	9.6	1.7	27.7	14.8	4.1
G009529	321		2.21	1.7	27.3	29.0	75.2	1236.2	1311.4	94.3	39.2	8.3	2.5	32.0	13.8	4.3
G009516	0	Lower Cambrian	10.20	0.1	2.4	2.5	0.8	23.3	24.0	96.7						
G009517	0		6.02	0.5	6.4	6.9	8.0	107.0	115.0	93.1	33.6	31.5	8.5	6.0	20.5	0.0
G009518	0		7.44	0.6	11.4	12.0	7.5	153.6	161.1	95.4	31.2	29.2	6.0	7.3	14.6	11.9
G009519	0		8.15	0.7	20.0	20.7	9.0	245.0	254.0	96.5						
G009520	0		9.41	0.4	6.0	6.4	3.9	63.9	67.8	94.2	41.7	28.4	5.9	8.7	15.3	0.0
G007901-A	0		Ediacaran	6.15	0.5	20.3	20.8	8.4	330.5	338.9	97.5					
G007903-D	0	5.90		0.6	19.5	20.1	9.7	330.2	339.9	97.1						
G007922-C	0	11.40		2.0	10.8	12.8	17.9	94.8	112.7	84.1						

5.5. Discussions

5.5.1. Effect of Organic Matter Richness

The TOC content has a significant effect on the methane sorption isotherms. As illustrated in Figure 5.2, the rock-normalised excess sorption isotherms of samples from the same formation show an increase with increasing TOC. Similar correlations between sorption isotherm and TOC content have been observed in samples from around the world (Chalmers and Bustin, 2008; Gasparik et al., 2013). This phenomenon implies that the high TOC content samples can adsorb more methane for almost the entire measured pressure range (Figure 5.2). The significant influences from TOC on sorption capacity are clearly demonstrated in Figure 5.3. Both the maximum excess sorption and Langmuir sorption capacity show a positive linear correlation with TOC (Figure 5.3 A-B). The sorption capacities of samples that have similar clay content, thermal maturity and moisture content exhibit even stronger positive linear correlations with TOC (Figure 5.3 C).

Based on these experimental results, two linear regressions are provided to empirically estimate the maximum excess sorption and Langmuir sorption capacity of the Lower Paleozoic shale samples in the UYP according to their TOC content.

$$n_L = 0.018 \times \text{TOC} + 0.046 \text{ (mmol/g rock)} \quad (R^2=0.9428) \quad (5.4)$$

$$n_{\text{excess}} = 0.014 \times \text{TOC} + 0.0049 \text{ (mmol/g rock)} \quad (R^2=0.9456) \quad (5.5)$$

These correlations are obtained from sorption isotherms (46°C) measured on overmature Lower Paleozoic UYP shale samples that have moisture content between 0.43 and 2.28%.

By way of comparison, the Devonian shale samples from basins in north-eastern America exhibited positive linear correlations between the TOC and adsorption capacities at a given temperature of 37.8°C and given pressures of 3.45 and 6.89 MPa (Lu et al., 1995). Chalmers and Bustin (2008) and Ross and Bustin (2009) reported positive correlations between the TOC and sorption capacities of shale samples from the Western Canadian Sedimentary Basin, which they attributed to the pore structure evolution of organic matter during the maturation process. The maximum excess sorption capacities of samples with moisture content ranging from 0.92 to 3.62% from the Parana Basin, Brazil also increased

linearly with TOC content (Weniger et al., 2010). More recently, similar correlations were reported in a series of samples from China (Sichuan Basin) (Wang et al., 2013a), Germany (Gasparik et al., 2013), and the United States (Zhang et al., 2012b). However, the effect of organic matter on sorption capacity is not only caused by TOC content but also by organic matter type (Crosdale et al., 1998; Chalmers and Bustin, 2008; Zhang et al., 2012b). Based on the methane sorption isotherms of isolated organic matter measured at 50°C and pressures up to 15 MPa, the sorption capacity of type III organic matter was revealed as significantly higher than that for type II and type I organic matter, and may be related to the high content of aromatic compounds of type III organic matter (Zhang et al., 2012b). The investigations on the effect of maceral types of coals on methane sorption capacity have also found that bright, vitrinite-rich coals have a higher methane sorption capacity than dull, inertinite-rich coals at the same maturity level (see Chalmers and Bustin, 2007a and references therein).

5.5.2. Effect of Thermal Maturity

The effect of the thermal maturity of organic matter on the sorption isotherms are displayed in Figure 5.2. The isotherms of immature AU Cambrian samples monotonously increase within the measured pressure range, whereas overmature samples from the UYP exhibit maxima between 8.8 and 14.2 MPa (Table 5.2). Gasparik et al. (2013) report that TOC-normalised isotherms of overmature samples are generally higher than those of low mature or immature samples. Figure 5.4 illustrates the effect of thermal maturity on the maximum excess sorption (TOC-normalised) and its corresponding pressure (Figure 5.4 A and B) and its effect on the Langmuir sorption capacity (TOC-normalised) and Langmuir pressure (Figure 5.4 C and D). Compared to the immature shale samples from Australia, the overmature UYP samples have a higher maximum excess sorption of methane, whereas this increment is ambiguous between samples with R_o between 2.8 (medium value of the Lower Silurian samples) and 3.3% (medium value of the Lower Cambrian samples) (Figure 5.4 A). In addition, the Langmuir sorption capacity generally increases with increasing thermal maturity, but three overmature samples exhibit a relatively lower Langmuir sorption capacity than the immature samples (Figure 5.4 C). Both the pressure of maximum excess sorption and Langmuir pressure distinctly decrease from the immature to overmature samples, whereas this correlation is not clear between the samples in a R_o range of 2.8-3.3% (Figure 5.4 B and D), and one overmature sample shows a distinctly high Langmuir pressure (Figure 5.4 D).

Chapter 5 Methane Sorption Capacity

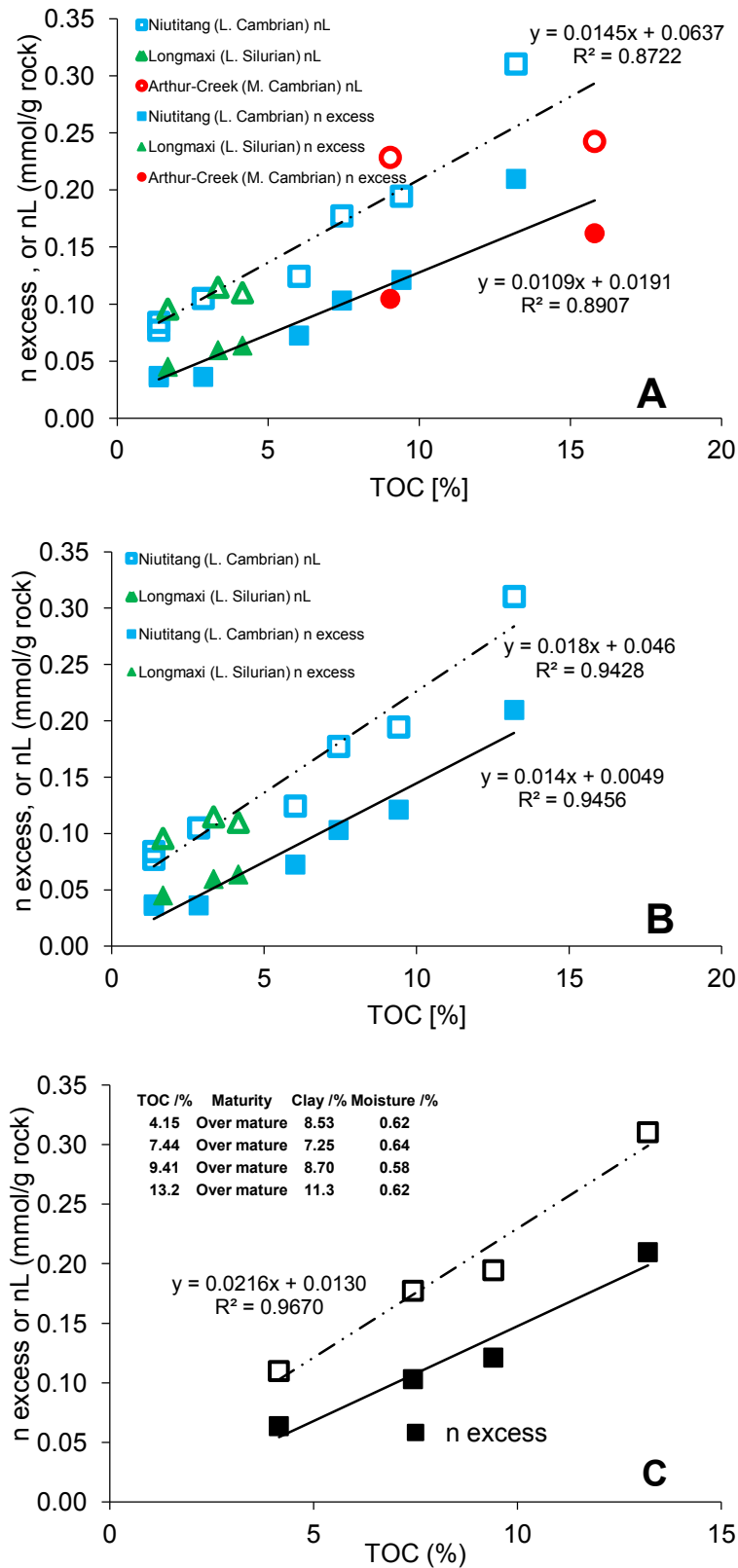


Figure 5.3 Measured maximum excess sorption capacity (n_{excess}) and Langmuir sorption capacity (n_L) as a function of TOC. Plot A contains all the measured samples, plot B contains all the UYP samples, and plot C contains samples that have similar thermal maturity, clay, and moisture content.

Chapter 5 Methane Sorption Capacity

The current investigation is consistent with previous studies. For shale samples from the Western Canadian Sedimentary Basin, the TOC-normalised sorption capacity of overmature Devonian-Mississippian shale samples ($1.6\% < R_o < 2.5\%$) is higher than for Jurassic shale samples that are relatively low mature ($R_o < 1.2\%$) (Ross and Bustin, 2009). This phenomenon was related to structural transformation of organic matter, creation of new sorption sites, and/or heterogeneity decrease of pore surface upon thermal maturation. Zhang et al. (2012b) related the high sorption capacity of overmature samples to the extensive aromatisation from immature to overmature organic matter. The remarkable reduction of the Langmuir pressure of overmature samples indicates that more methane can be adsorbed at low pressure (Zhang et al., 2012b). Gasparik and coworkers (2013) reported a power-law decrease trend of the Langmuir pressure upon maturation, whereas the sorption capacity distinctly increases from immature to a R_o of 2%. Nevertheless, this increase correlation for sample within overmature range are not clear, and most likely decrease again when R_o increases from nearly 2% to 4.2% (Gasparik et al., 2013). In many cases, the increase of methane sorption capacity with thermal maturity has been related to micropores (Bustin and Clarkson, 1998; Laxminarayana and Crosdale, 1999; Chalmers and Bustin, 2007a; Ross and Bustin, 2009), which increase progressively during the maturation process (Gan et al., 1972; Prinz et al., 2004; Prinz and Littke, 2005).

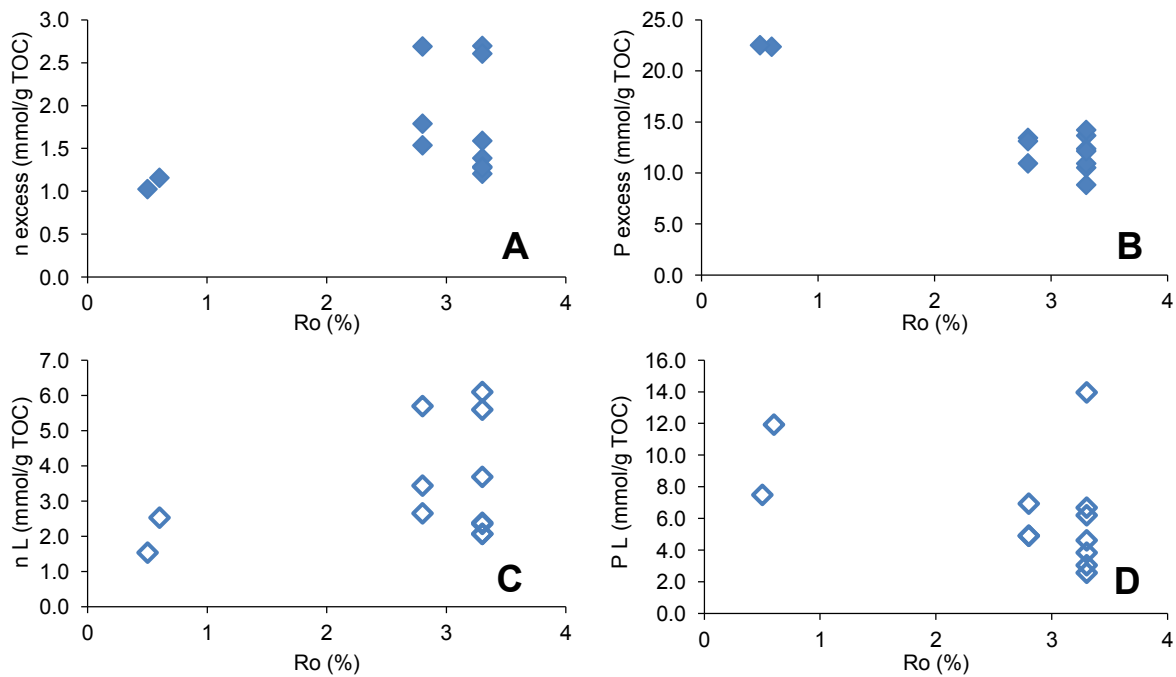


Figure 5.4 Effect of thermal maturity on the maximum excess sorption (A) and its corresponding pressure (B) and on the maximum Langmuir sorption capacity (C) and the Langmuir pressure (D). The sorption capacities are TOC-normalised. The R_o of the Lower Silurian shale was presented by 2.8%, whereas that of the Lower Cambrian shale was represented by 3.3%.

5.5.3. Effect of Mineral Content

The mineral constituents, in particular the clay minerals, have been widely regarded as a significant factor effecting the sorption capacity of shale samples (Lu et al., 1995; Chalmers and Bustin, 2008; Gasparik et al., 2012; Ji et al., 2012). The investigation on the dry Paleozoic shale samples from the Sichuan Basin, south China showed a negative correlation between the clay content and sorption capacity (Wang et al., 2013a). In the present study, the rock-normalised maximum excess sorption and Langmuir sorption capacity of methane are negatively correlated with clay minerals (Figure 5.5 A and B). Nevertheless, this phenomenon is most likely caused by a strong effect of TOC, e.g., the high clay concentration samples have obviously lower TOC content compared to the samples that have less clay minerals. Therefore, plot A and B illustrate that the effect of clay minerals on sorption capacity of the measured samples is relatively insignificant compared to the TOC content. Because of the significant impacts of organic matter richness, such a secondary effect on sorption capacity might be reflected more clearly when data are normalised to TOC. The TOC-normalised maximum sorption and Langmuir sorption capacity are therefore plotted in Figure 5.5 C and D; when the clay minerals increase, both values increase following polynomial-law relations. Thus, clay minerals also show effects on the methane sorption capacity, but are secondary in importance compared to the TOC content.

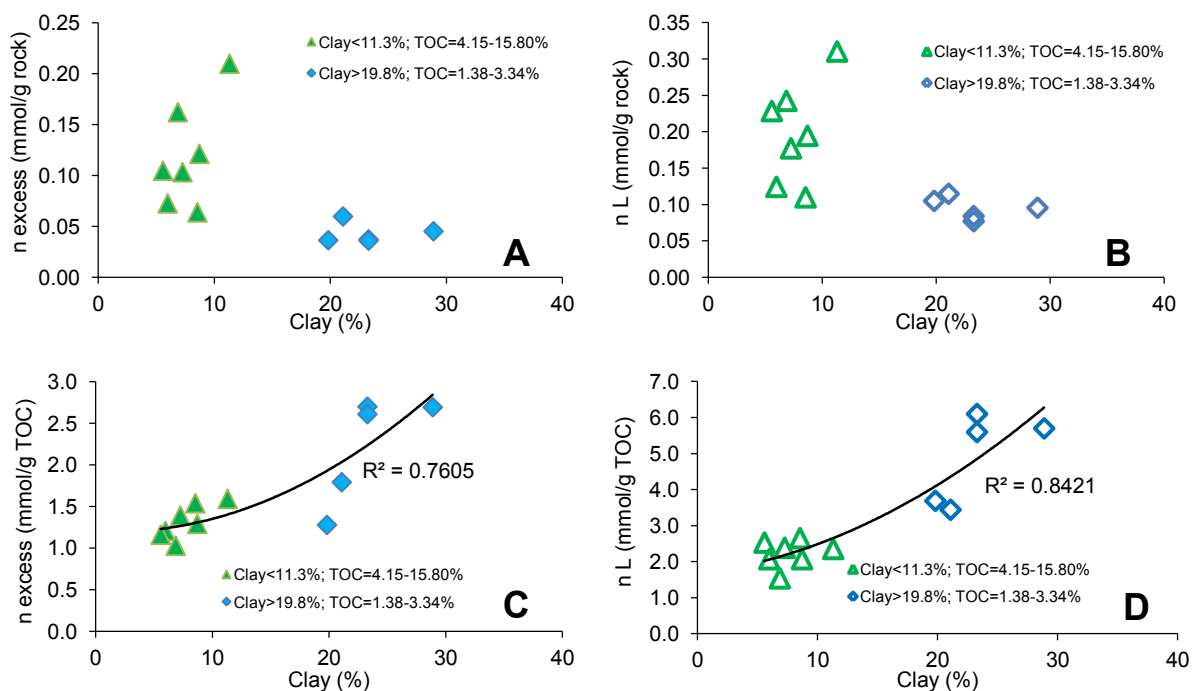


Figure 5.5 Effects of clay on the maximum excess sorption capacity (A and C) and Langmuir sorption capacity (B and D). TOC-normalised and rock-normalised values are presented.

The effect of clay minerals in the measured samples might be reduced by the moisture content, although the moisture content of most samples is less than 1%. As reported by Chalmers and Bustin (2008), there were no correlations between the TOC-normalised sorption capacity and clay content on the moisture equilibrated samples, whereas positive correlations were observed on the dry samples. The presence of water in clay-rich rocks might render many microporous sorption sites unavailable to methane by filling pore throats or occupying sorption sites (see Ross and Bustin, 2009 and references therein), which is attributable to the hydrophilic nature of clay minerals. Nevertheless, methane sorption could be positively related to clay minerals if the dry samples are measured because considerable micropores might be abundant in clay minerals, which results in a high internal surface area and sorption energy (Chalmers and Bustin, 2008; Ross and Bustin, 2009; Ji et al., 2012). Thus, certain organic lean samples with high clay content might have larger sorption capacity than organic rich samples with low clay content if they are measured in the dry state (Gasparik et al., 2012). The methane sorption capacity of dried clay-rich rocks was revealed to descend in the order of montmorillonite>illite/semectite mixed>kaolinite>chlorite>illite (Ji et al., 2012). For the Lower Paleozoic shales in the UYP, however, illite is by far the most prevalent clay mineral, whereas montmorillonite is not normally present in detectable quantities (Tan et al., 2014b).

5.5.4. Effect of Moisture Content

It has been widely recognised that moisture content negatively influences the methane sorption capacity of coal (Joubert et al., 1974; Levy et al., 1997; Bustin and Clarkson, 1998; Clarkson and Bustin, 2000; Krooss et al., 2002; Day et al., 2008). The methane sorption capacity of shale samples from the West Canada Sedimentary Basin measured in the dry state ranges from 0.4 to 4 cm³/g and is substantially higher than moisture equilibrated samples, which is between 0.1 and 2 cm³/g (Ross and Bustin, 2009). The sorption capacity of Posidonia and Alum shale samples is reduced by 45 to 60% when the moisture content increases to between 2.2 and 5.5% from the dry state. The critical moisture content, e.g., a certain moisture content beyond which further moisture increases cannot affect the sorption capacity, was observed at between 2.4 and 5.5% in terms of the measured Alum shale samples (Gasparik et al., 2013). In contrast, shale samples from north-eastern British Columbia, Canada measured by Chalmers and Bustin (2008) showed no clear correlation between

Chapter 5 Methane Sorption Capacity

methane sorption capacity and moisture content, and samples with high moisture content also had high methane sorption capacities. This phenomenon implies that water and methane molecules occupy different sorption sites. The presence of water in shale samples has more significant impacts on clay minerals than organic matter because the sorption sites on clay minerals are relatively hydrophilic, whereas in organic matter, they are relatively hydrophobic. Thus, the methane adsorption of moisture equilibrated samples is mainly attributable to the adsorption of organic matter because clay minerals are most likely blocked, whereas the adsorption of dry samples includes contributions from both organic matter and clay (Ji et al., 2012).

The effect of moisture content on methane sorption capacity is partially illustrated in this study because the samples were not measured at different moisture levels. It can be concluded that the moisture content in governing methane sorption capacity is less than that of the TOC and clay content. Both the TOC-normalised and rock-normalised excess sorption and Langmuir sorption capacity of methane with increasing moisture content are shown in Figure 5.6. The TOC-normalised capacity decreases following polynomial-law relations with the moisture content increase (Figure 5.6 A and B). This correlation, however, is significantly impacted by the clay content. The sorption capacities of the samples that have clay content higher than 20% are remarkably higher than the samples with less clay content. This phenomenon may also imply that the moisture content of the measured samples are much lower than the critical moisture because clay still plays an important role in the TOC-normalised sorption capacity. Compared to the TOC-normalised values, the rock-normalised excess sorption and Langmuir sorption capacity show only weak correlations with moisture content increasing. However, these correlations are remarkably influenced by the TOC content (Figure 5.6 C and D). The sorption capacities of high TOC content samples (>7.4%) are obviously higher than those of low TOC content samples (<6.1%). This phenomenon may suggest that the effect of moisture content on organic matter is less than it is on clay minerals.

5.5.5. Effect of Pressure and Temperature

The methane sorption isotherms of immature samples monotonously increase with a pressure increase over the measured pressure range (0-25 MPa), whereas the sorption capacity of all overmature samples positively increases with pressure only until the maxima and decreases thereafter (Figure 5.2). Similar trends have already been observed on shale samples from other places using high-pressure methane (to 20-25 MPa) (Gasparik et al., 2012;

Chapter 5 Methane Sorption Capacity

Gasparik et al., 2013), whereas the maxima cannot be observed in many sorption isotherms that are conducted in relatively lower pressure conditions (to 6-15 MPa) (Ross and Bustin, 2009; Zhang et al., 2012b; Wang et al., 2013a).

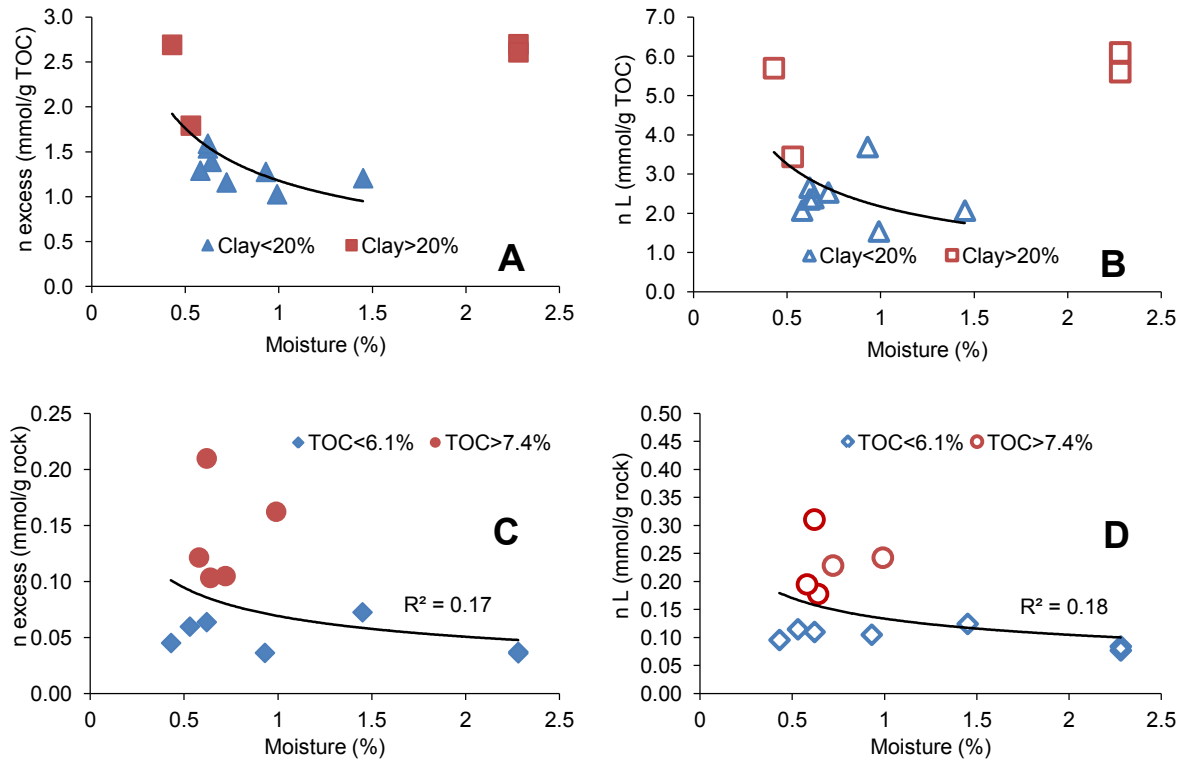


Figure 5.6 The effect of moisture content on the maximum excess sorption (A and C) and Langmuir sorption capacity (B and D). TOC-normalised and rock-normalised values are presented.

The effect of temperature on sorption capacity has been summarised by Yee et al. (1993). Higher temperatures favour more gas in the free state than in the sorbed state and are attributed to the temperature dependence of the Langmuir coefficient (e.g., the reciprocal of the Langmuir pressure in Eq. 2). This constant coefficient decreases as temperatures increase and results in a lower initial slope of the isotherm. Consequently, at higher temperatures, the isotherms are more linear and the samples adsorb less gas (Bustin and Clarkson, 1998). Similarly, Xia et al. correlated the Langmuir constant with the heat and standard entropy of adsorption to describe the temperature dependence of the sorption process (Xia et al., 2006; Xia and Tang, 2012). Linear decreases in methane adsorption capacity of 0.12 m³/ton per 1°C increase in temperature over the temperature range of 20-65°C at 5 MPa were observed for the Australian coal samples (Levy et al., 1997), and similar trends were repeatedly observed by Bustin and Clarkson (1998) over the temperature range of 25-50°C as pressure increased to 10 MPa. In addition, Weniger et al. (2012) reported a similar decreasing tendency for moisture-equilibrated Carboniferous coals from Europe. Recent studies on shale samples and

clay-rich rocks have also shown that the sorption capacity decreases with temperature increase (Ji et al., 2012; Zhang et al., 2012b; Gasparik et al., 2013). High-pressure and high-temperature methane sorption isotherms measured for Posidonia shale samples showed that the occurrence and location of maxima of excess sorption isotherms are temperature related. At low temperatures, the excess sorption maxima occurred in a relatively low pressure range, whereas at higher temperatures, the maxima could either move to the high-pressure range or even disappear when the temperature increases to 100 or 150°C (Gasparik et al., 2013).

Some of the Lower Cambrian and Lower Silurian shale samples from the UYP were measured under a maximum pressure of 11 MPa and temperature of 60°C by Wang et al. (2013a) (Figure 5.7). Compared to the excess sorption isotherms in that research, our samples show a maximum sorption capacity over a pressure range of 8.8-14.2 MPa, whereas the published results exhibit a monotonous increase, e.g., no maxima occurred in the sorption isotherms. Lower pressure and higher temperatures of the sorption experiments compared to the present work might explain why no maxima were observed by Wang et al.(2013a).

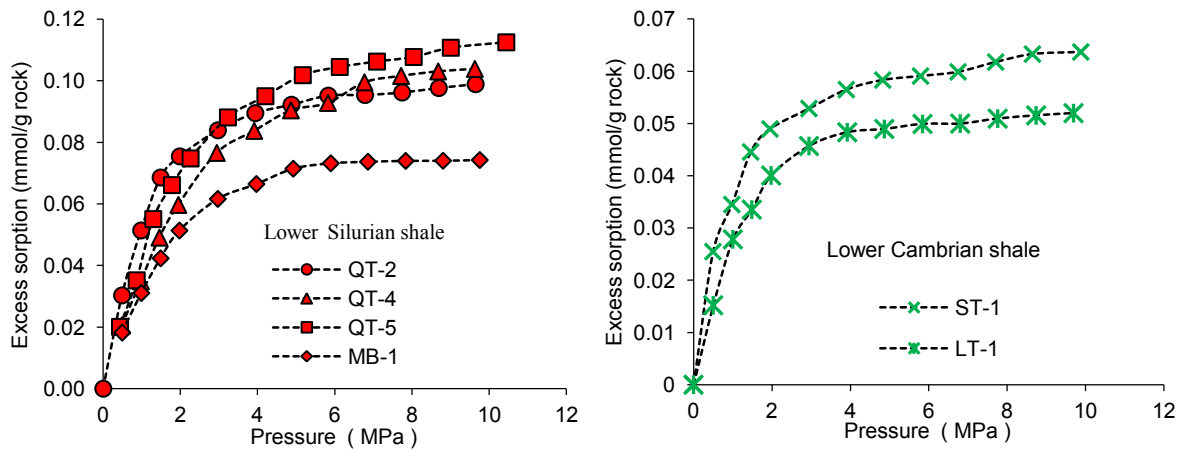


Figure 5.7 Methane excess sorption isotherms at 60°C measured on dry samples (Wang et al., 2013a). QT-2, QT-4, QT-5, and MB-1 are the sample IDs of Lower Silurian samples, and ST-1 and LT-1 are the sample IDs of Lower Cambrian samples.

5.5.6. Effect of Pores and Particle Size

Mercury injection porosimetry and helium pycnometry were performed on two Lower Cambrian core samples (G011313 and G011319) that have similar maturity to determine the total porosity and interconnected pore size distribution properties, as shown in Table 5.4 and Figure 5.8. The high TOC content sample (G011319) has an obviously higher total cumulative pore volume, total surface area, and porosity and a lower density; consequently, it has a higher sorption capacity compared to the sample with a low TOC content (G011313)

Chapter 5 Methane Sorption Capacity

(Tables 5.2 and 5.4). However, this stronger sorption capacity might also be impacted by the moisture content and clay content, which are less in G011319 while high in G011313. In addition, the high TOC content sample has more pores with diameters less than 100 nm, whereas the low TOC content sample has relatively more pores with a diameter larger than 1 μm (Figure 5.8).

Table 5.4 Pore structural properties of the selected samples, as determined by mercury injection porosimetry and helium pycnometry.

ID	TOC (%)	Total cumulative volume* (mm ³ /g)	Total surface area *(m ² /g)	Bulk density* (g/cm ³)	Skeleton density# (g/cm ³)	Hg-P*(%)	He-P#(%)	D-value (%)
G011313	1.38	0.95	0.06	2.69	2.75	0.26	2.02	1.77
G011319	13.20	3.35	0.42	2.33	2.57	0.78	9.34	8.56

Vaues with * are measured by mercury injection porosimetry (MJP) and with # are helium pycnometry (HP) applied. Hg-P is porosity measured by MJP, while He-P means HP applied to calculate the porosity. De-value is the porosity differential values between Hg-P and He-P.

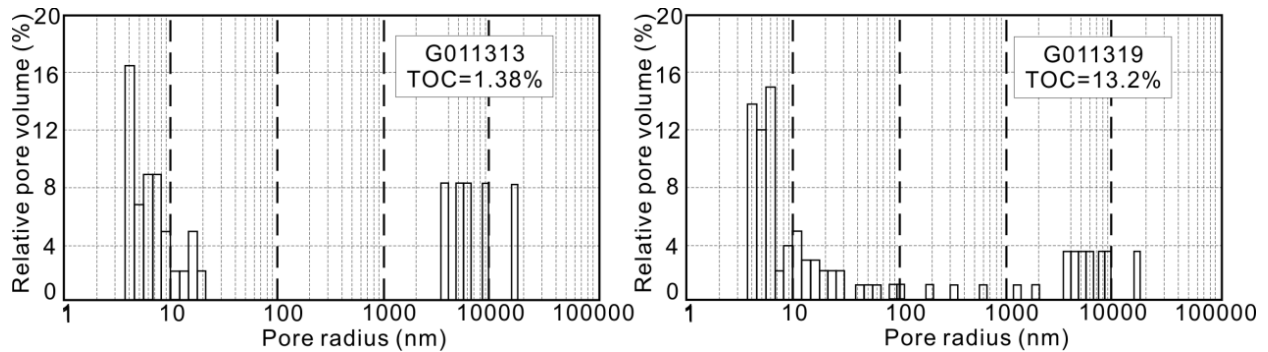


Figure 5.8 Pore size distribution of selected samples measured by mercury inject porosimetry.

Pore size and pore structure have been shown to have the most important direct and indirect effects on the gas sorption capacity of coals (Clarkson and Bustin, 1999a; Clarkson and Bustin, 1999b; Chalmers and Bustin, 2007b; Chalmers and Bustin, 2008) and shales (Ross and Bustin, 2007; Chalmers and Bustin, 2008; Ross and Bustin, 2009; Ji et al., 2012). Micropores are able to offer more surface area and have a greater sorption energy than large pores (Dubinin, 1975; Ross and Bustin, 2009); therefore, they have a more significant effect on sorption capacity (Clarkson and Bustin, 1999a; Chalmers and Bustin, 2007b). In shale samples, most of the micropores are related to both clay minerals and organic matter (Loucks et al., 2009; Slatt and O'Brien, 2011; Chalmers et al., 2012; Curtis et al., 2012; Loucks et al., 2012; Milliken et al., 2013). Investigations performed on the selected UYP Lower Silurian shale samples indicated that 31-62% of total porosity is contributed by organic matter,

Chapter 5 Methane Sorption Capacity

whereas as much as 50-60% of the total surface area is contributed by micropores that have a diameter less than 2 nm (Tian et al., 2013). In this regard, micropores in organic matter of the UYP shales could represent a significant control of the sorption capacity. Even other effects on sorption capacity, e.g., organic matter richness, thermal maturity, clay minerals, and moisture content can be intrinsically ascribed to the change of pore properties of the measured sample. For instance, the positive correlation between the TOC content and sorption capacity is attributed to the micropore abundance in the organic matter and more internal surface area. During the maturation process, organic matter could create additional micropores, which would increase the sorption capacity.

To investigate the possible influences of particle size on sorption capacity, G011313 was measured in particle size fractions of 0.5-1 mm and in a powdered sample with a particle size of less than 0.5 mm. The measured results showed that the powdered sample with a relative smaller size had a slightly higher sorption capacity than the larger-sized fraction (Figure 5.9). Similar phenomena have been observed on the Posidonia and Alum shale samples that were measured in powder with particle sizes less than 80 μm and on cutting with sizes between 0.5 and 1 mm at 45°C and 65°C (Gasparik et al., 2013) as well as on the clay-rich rocks with various particle sizes at 50°C (Ji et al., 2012). The reason for this slightly higher sorption capacity may be the result of a larger and more accessible micropore surface of the powdered sample. The difference between isotherms of different particle size samples, however, is not significantly larger than the experimental error of the isotherm measurements.

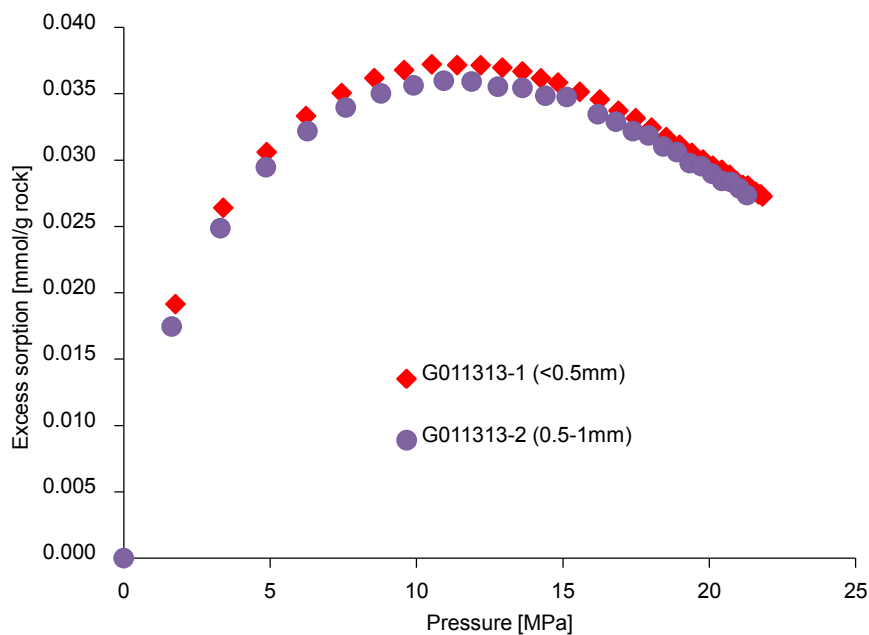


Figure 5.9 Effect of particle size on the excess sorption.

5.5.7. T_{vap}-GC Measured Gas

In contrast to methane sorption isotherms, T_{vap}-GC measures the retained hydrocarbons within the rock (Lafargue et al., 1998). For gas hydrocarbons of measured core samples, a large amount of gas should have been lost during the sampling process, i.e., gas is lost significantly as pressure decreases from the reservoir depth to surface, or cutting and grinding process, which could create more open pores to release gas. In terms of the gas hydrocarbons of measured outcrop samples, the amount of lost gas resulting from the pressure reduction should be much less than that for the core samples; however, weathering may significantly affect the total residual gas. Thus, gas hydrocarbon measured by T_{vap}-GC is relatively lower than the gas-in-place of outcrop samples, whereas it is significantly less than the gas-in-place of core samples. T_{vap}-GC measured gas hydrocarbon might represent the remaining sorbed gas under atmospheric conditions, but it may also include the free gas that is trapped in unconnected pores and dissolved gas in bitumen.

The rock-normalised and TOC-normalised gas hydrocarbon of T_{vap}-GC is shown in Figure 5.10 (vs. TOC) and Figure 5.11 (vs. clay content). The TOC content shows negatively weak influences on the T_{vap}-GC measured gas. The rock-normalised gas weakly decreases as TOC increases, whereas the TOC-normalised result decreases following exponential laws (Figure 5.10). Consequently, high TOC content samples exhibit a low amount of measured gas. Nevertheless, it is notable that the samples with high TOC content are outcrops from the Lower Cambrian and Ediacaran intervals, whereas samples with less TOC are cores from the Lower Silurian interval. Compared to the TOC, there is a positive correlation between clay minerals and measured gas. Both rock-normalised and TOC-normalised values increase with a clay increase (Figure 5.11). However, it is also notable that the high clay content samples are cores from the Lower Silurian interval, whereas samples with little or non-existing clay minerals are outcrops from the Lower Cambrian or Ediacaran intervals. All samples were stored in the laboratory for at least one year; therefore, the T_{vap}-GC results presented in this paper illustrate the residual gas of measured samples under air conditions. Obviously, the weathering process should have strongly reduced the residual gas of the outcrop samples.

5.5.8. Data Comparison

Measured results are used to compare the methane sorption data of a series of shale samples from North America and Europe and several shale samples from the Sichuan Basin, UYP. The sorption capacities are normalised to m³ STP/ton rock and plotted in Figure 5.12.

Chapter 5 Methane Sorption Capacity

The general properties and experimental conditions of the selected samples are listed in Table 5.5. In the dry state, Jurassic shale samples from the Western Canadian Basin exhibit the lowest sorption capacities because of the low clay content (Table 5.5). Although the measured samples in this research have a moisture content of 0.43-2.28%, their sorption capacities are close to those of the Barnett, Alum, and Devonian-Mississippian shale (Figure 5.12 A). However, the different measured temperature should be noted and are listed in Table 5.5. In a moist state, the sorption capacities of UYP samples are significantly high compared to the moist samples from the Western Canadian Basin (Figure 5.12 B), which is because the moisture content of selected Canadian samples is generally much higher than the UYP samples. For the Lower Cretaceous samples, the data show sorption capacities at 6 MPa, which may be much lower than the expected sorption capacities.

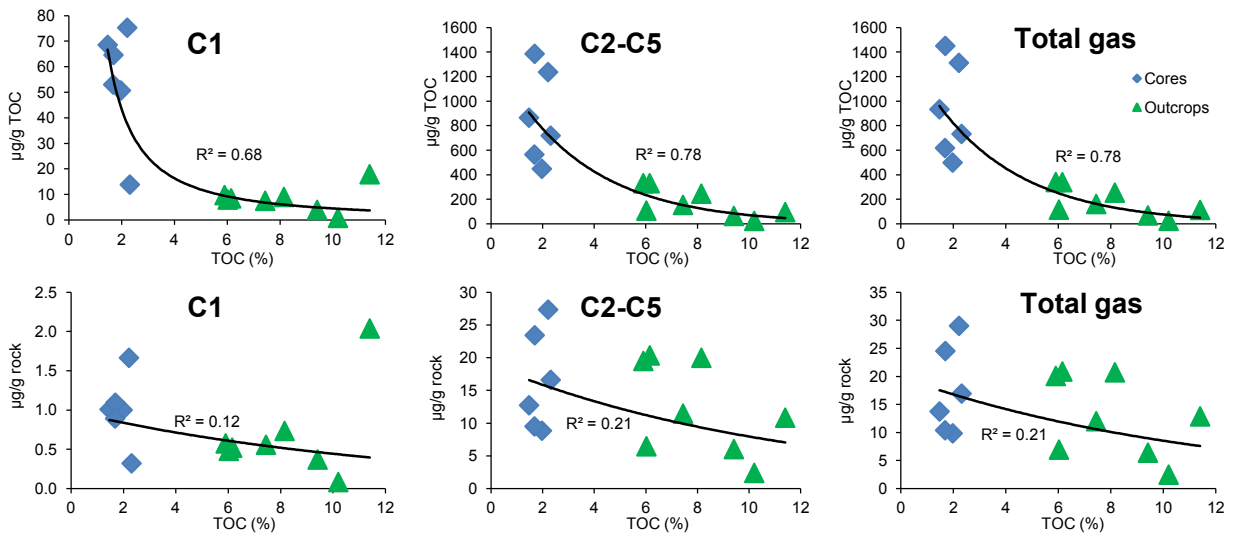


Figure 5.10 Effect of TOC on Tvp-GC measured gas hydrocarbon.

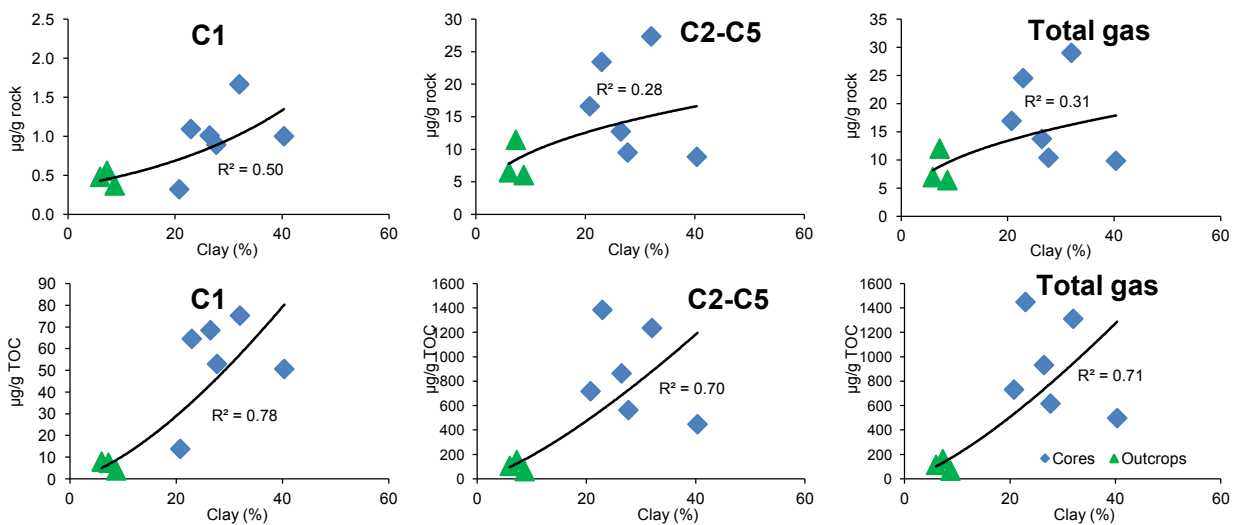


Figure 5.11 Effect of clay on Tvp-GC measured gas hydrocarbon.

Chapter 5 Methane Sorption Capacity

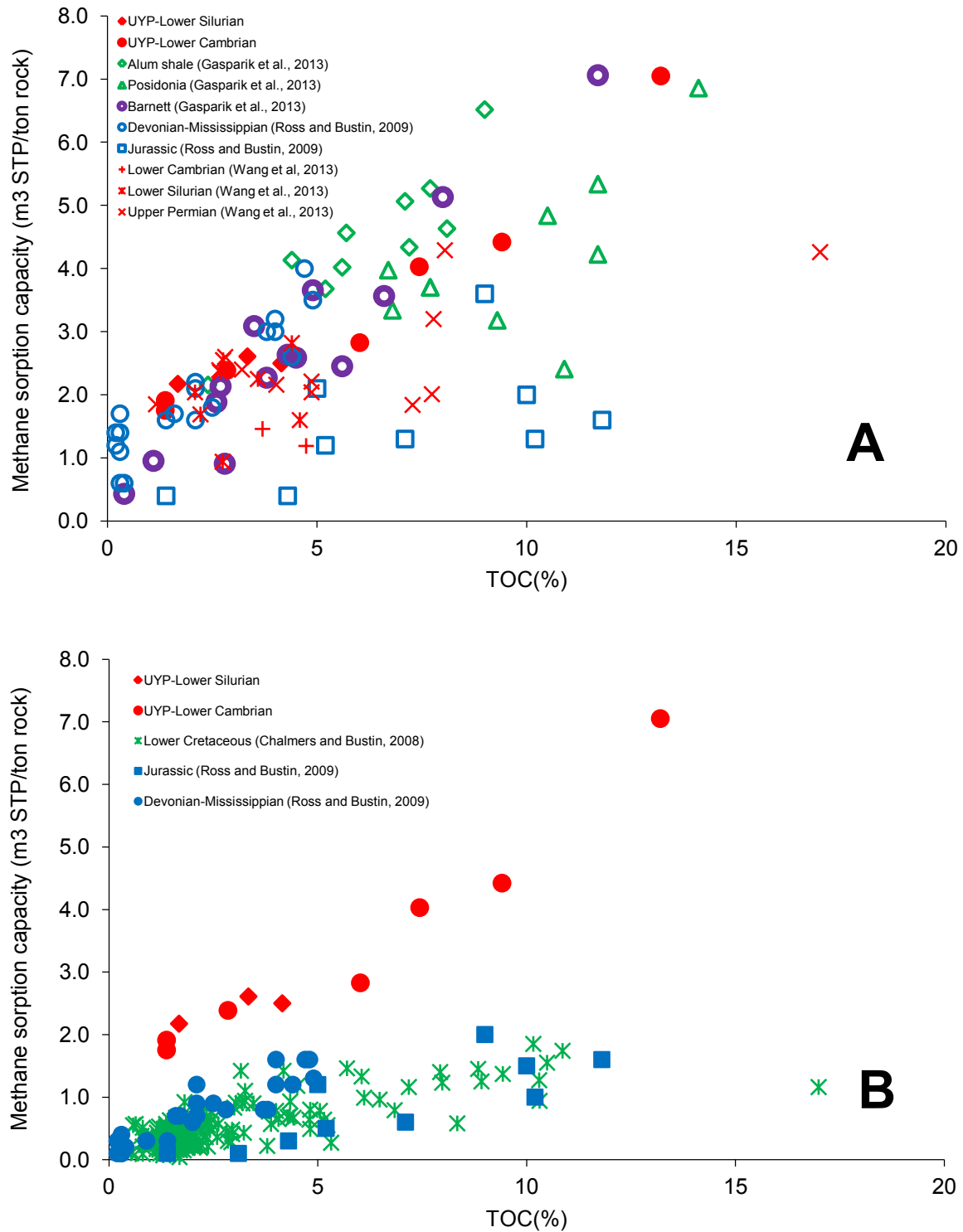


Figure 5.12 Comparison of methane sorption capacity of shale samples from China, Canada, Europe, and U.S. Plot A: Data in this research vs. published data of dry samples. Plot B: Data in this research vs. published data of moist samples. The sorption capacities of the samples from the Sichuan and Lower Cretaceous samples from the Western Canadian Basin have values of 10 and 6 MPa, respectively, whereas other samples show theoretical sorption capacities. Published results are from (Chalmers and Bustin, 2008; Ross and Bustin, 2009; Gasparik et al., 2013; Wang et al., 2013a).

Chapter 5 Methane Sorption Capacity

Table 5.5 Properties and experimental conditions of the compared samples in Figure 5.12.

Sample	Experimental conditions		Maturity (R _o ,%)	Moisture (%)	Clay (%)	Particle size (mm)	References
	Temperature (°C)	Pressure (Mpa)					
UYP-Lower Cambrian	46	0-25	3.0-3.5	0.43-0.62	8.5-28.9	<0.2	This research
UYP-Lower Silurian			2.5-3.0	0.58-2.28	6.0-23.28		
Devonian-Mississippian (W Canada)	30	0-6	1.6-2.5	1.6-5.2	1.7-24.1	<0.25	(Ross and Bustin, 2009)
Jurassic (W Canada)			0.7-2.5	0.6-8.5	1.0-15.3		
Lower Cretaceous (W Canada)			0.33-1.41 ^I	1.5-11.0	14-77 ^{II}		
Lower Cambrian (Sichuan Basin)	60	0-11	3.0-3.5		50.0-60.4	<0.15	(Wang et al., 2013a)
Lower Silurian (Sichuan Basin)			2.5-3.0	0	35.1-62.5		
Upper Permian (Sichuan Basin)			0.7-1.2 ^I		3.0-54.1		
Barnett (U. S.)	65	0-25	0.7-1.0		0.6-56.9	0.5--1	(Gasparik et al., 2013)
Alum (S Scandinavia)			0.5-2.4	0	7.5-60.7		
Posidonia (NW Germany)			0.5-1.5		15.6-39.7		

I: equivalent R_o was calculated from T_{max}, based on R_o=0.018×T_{max}-7.16 (Jarvie et al., 2001)

II: volume percentage

The sorption capacity of shales is intrinsically controlled by many factors, and the experimental conditions and calculative methods used to measure methane sorption capacity may be different. The measured methane sorption results by different laboratories, therefore, cannot be simply compared with each other. Chalmers et al. (2008) measured more than 200 shale samples that were collected from north-eastern British Columbia, Canada. The measurements were performed only on moisture samples, and the published results are the sorption capacities at 6 MPa. Wang et al. (2013a) measured only the dry samples, and the results are sorption capacities at 10 MPa. Shale samples from the Jurassic and Devonian-Mississippian formations in western Canada were measured in both dry and moisture states by Ross and Bustin (2009). These measurements were performed only at 30°C and until 6 MPa. In addition, some of the Barnett and European shale samples were measured under different temperature and moisture levels in the same laboratory as the current research (RWTH Aachen) (Gasparik et al., 2013); however, more systematic measurements are still required. Therefore, the data comparison in this paper is simple, and additional measurements should be performed on the UYP samples in the future.

5.6. Conclusions

The high-pressure (up to 25 MPa) methane sorption isotherms were measured for shale samples from the Lower Silurian and Lower Cambrian formations in the UYP. The results indicate that the excess methane sorption capacity of the Lower Silurian shale is between 0.045 and 0.064 mmol/g rock and that of the Lower Cambrian shale is between 0.036 and 0.210 mmol/g rock. The measured isotherms can be well fitted by the corrected Langmuir function. The Langmuir sorption capacity is between 0.096 and 0.115 mmol/g rock for the

Chapter 5 Methane Sorption Capacity

Lower Silurian shale, whereas it ranges from 0.077 to 0.310 mmol/g rock for the Lower Cambrian shale. The shape of the sorption isotherms and sorption capacity vary from sample to sample and might be affected by the TOC content, thermal maturity, clay minerals, moisture content, particle size, pore properties, as well as the measured temperature and pressure conditions.

Under the measured pressure range, the sorption capacity of selected immature AU Cambrian samples increases monotonously with increasing pressure, whereas that of UYP overmature samples shows a maxima during a pressure range of 8.8-14.2 MPa. The TOC content shows a significant effect on methane sorption capacity. With a TOC content increase, the sorption capacity increases positively, exhibiting a distinct linear correlation. The TOC-normalised sorption values increase positively with thermal maturity. In contrast, the corresponding pressure of the maximum excess sorption and Langmuir pressure clearly decrease with thermal maturity. The effect of clay minerals is clearly revealed by the TOC-normalised sorption values; however, it showed relatively less of an effect compared to the TOC content. The measured samples have a moisture content between 0.43 and 2.28%, which reduces the impact of clay minerals on the sorption capacity. The measured high TOC content sample shows a high total cumulative pore volume, surface area, total porosity, and thus higher sorption capacity compared to the similar mature sample that has less TOC. In addition, the particle size has a slight effect on the sorption capacity.

The T_{vap}-GC measured gas hydrocarbons are characterised by extremely low detectable quantities between 9.8 and 29.0 µg/g rock (0.5-1.4 mg/g TOC) of the Lower Silurian core samples and between 2.5 and 20.8 µg/g rock (0.02-0.34 mg/g TOC) of the Lower Cambrian and Ediacaran outcrop samples. Contrary to the sorption isotherms, the TOC content is negatively correlated with the measured gas, which most likely was impacted by weathering processes. Nevertheless, clay minerals show a strong effect on the T_{vap}-GC results.

5.7. Acknowledgements

We are grateful for the financial support from Statoil, and would like to thank Matus Gasparik and Yves Gensterblum (RWTH Aachen) for detailed discussions.

Chapter 6 Mineralogy, Lithofacies, Petrophysics, and Rock Mechanics

6.1. Abstract

The marine black shale formations on the Upper Yangtze Platform, south China, are currently exploration targets for shale gas. Here, we report on the mineralogy, lithofacies, petrophysics, and rock mechanics of samples collected from the Ediacaran (Ediacaran), Lower Cambrian, and Lower Silurian black shale intervals. All three formations are composed of high proportion of quartz, low content of clay, and rare or non-existent content of carbonates. The Ediacaran and Lower Cambrian shales deposited in restricted deep water marine platform to marine basin environments are characterised by a higher quartz content and lower clay content than the Lower Silurian shales that were deposited in a more restricted marine basin environment. The carbonate content varies from 0 to over 50%, with the higher values measured in the Lower Silurian samples. These stratigraphic units were formed during bottom water anoxic conditions; therefore, they were rarely influenced by bioturbation. Lithologically, laminated and non-laminated siliceous mudstones predominate, with minor contributions of other lithotypes.

Pores generally have diameters in the nanometer (nm) to micrometer (μm) range, and numerous pores occur in organic matter. Most of the measured samples have porosities less than 4%, although a few samples show porosity in excess of 10%. Pores with radii less than 50 nm contribute significantly to total pore volume and total porosity. Permeability is extremely low, and helium permeability coefficients (Klinkenberg corrected permeability coefficient) are less than 20.2 nD (nano-Darcy, $\sim 2 \times 10^{-20} \text{ m}^2$). The rock mechanical properties of the samples are characterised by high brittle behavior, which coincides with their high compressive and tensile strengths and elastic properties. The Lower Cambrian shale is

This chapter has been published as: Tan, J., Horsfield, B., Fink, R., Krooss, B., Schulz, H.-M., Rybacki, E., Zhang, J., Boreham, C.J., van Graas, G. and Tocher, B.A., 2014. Shale Gas Potential of the Major Marine Shale Formations in the Upper Yangtze Platform, South China, Part III: Mineralogical, Lithofacial, Petrophysical, and Rock Mechanical Properties. Energy & Fuels, 28:2322-2342.

generally more brittle than the Lower Silurian shales, which possess a relatively higher content of clay minerals. The rock mechanical properties of the measured samples, however, depend on the overall mineral compositions and physical properties.

Keywords

Mineralogy, Lithofacies, Petrophysics, Rock Mechanics, Shale Gas, South China

6.2. Introduction

Unconventional shale gas plays are unique in that they contain three of the classical elements of petroleum systems: source-, reservoir-, and seal-rock (Curtis, 2002; Jarvie et al., 2007; Loucks and Ruppel, 2007). To understand and therefore predict the viability of an unconventional shale reservoir, it is important to estimate the gas-in-place (GIP), both vertically and laterally, and establish the optimum method of producing the gas by simulation techniques. In addition, the heterogeneity of the target formation must be taken into account and a number of important parameters that relate to successful shale plays should be characterised, e.g., sedimentological architecture, organic richness, thermal maturity, mineralogical composition, lithofacies, as well as petrophysical and rock mechanical properties. As a result of generally low permeability and sorption mechanisms playing important roles in a shale gas play, key technologies for successful shale gas production are necessary, i.e., horizontal drilling and hydraulic fracturing. It is thus mandatory that detailed investigations of the mineral constituents, texture, fabric and physical and mechanical properties of shales should be conducted to successfully exploit the shale reservoir. A well-considered completion strategy entails evaluating the role of these properties for the susceptibility of a shale play to successful stimulation (Grieser and Bray, 2007; Sierra et al., 2010; Harris et al., 2011; Slatt and Abousleiman, 2011). Nevertheless, these rock properties must be considered in a larger geological context of stress fields. Having all the optimum properties with poorly defined stress fields could result in poor wells even in good shale gas regimes.

Shale gas exploration in China is in its infancy. Marine black shales, which comprise the Ediacaran, Lower Cambrian, and Lower Silurian shale intervals, are found throughout the Upper Yangtze Platform (UYP) in south China. These sediments have long been known to be the principal source rocks for conventional petroleum fields in the Sichuan Basin (Editorial

Committee of the Sichuan Oil & Gas field, 1989) and have been more recently recognized to host promising unconventional shale gas potential (Zhang et al., 2008a; Zou et al., 2010; Zou et al., 2011). The GIP of the Lower Cambrian and Lower Silurian shale has been estimated at 349 and 343 trillion cubic feet, respectively (EIA, 2011b). Despite their tremendous potential, the petrophysical and rock mechanical properties are poorly documented. The mineralogical composition of the Lower Silurian and Lower Cambrian shale has recently been used as a proxy for brittleness based on a “ternary comparison” of carbonate, quartz and clay content (Wang et al., 2009a; Wang et al., 2009c; Jiang et al., 2010; Chen et al., 2011; Zou et al., 2011; Li et al., 2012a). Nevertheless, comprehensive and systematic investigations are rare, resulting in indistinct correlations of these major rock physical properties. In this paper, we present new insights into the lithofacies, petrophysics, and rock mechanical properties of these Pre- to Early Paleozoic marine shale intervals.

Samples collected from 15 profiles/wells in the core area of the UYP were examined from the centimeter scale (cm, hand specimen and light microscopy) down to the nm scale (Transmission Electron Microscope, TEM). The results were correlated with the data of mineralogical composition, porosity and permeability and the elastic properties and mechanical strengths gained by a series of rock mechanical experiments. Additionally, published data, including the XRD results of nearly 700 samples from more than 20 profiles/wells scattered on the UYP, were compiled with the purpose of characterising mineralogical properties. Furthermore, samples from the Georgina Basin, north Australia were also investigated because Cambrian shale in the Georgina Basin is considered an immature equivalent of the overmature Cambrian shale on the UYP in terms of its organic geochemical composition (Tan et al., 2013).

6.3. Experimental Details

6.3.1. Analyzed Samples

The analyzed sample set is composed of rocks from the UYP, south China (UYP samples) and Georgina Basin, north Australia (AU samples) (Figure 6.1 and Table 6.1). The UYP samples were collected from the Lower Silurian, Lower Cambrian, and Ediacaran black shale formations. The investigated profiles and wells are located in the central area of the UYP where the succession of marine black shale is generally more than a hundred meters thick (Liang et al., 2008; Cheng et al., 2009; Wang et al., 2009b; Zou et al., 2011). In contrast,

the AU shale samples were recovered from the Cambrian Arthur Creek Formation, which hosts one of the major regional source rocks for conventional petroleum (Ambrose et al., 2001; Ambrose and Putnam, 2007; Boreham and Ambrose, 2007) and has been regarded as a major unconventional petroleum target (Bennett et al., 2010; Boreham et al., 2013) in the southern Georgina Basin, north Australia (Figure 6.1). For all the samples that were amenable to laboratory tests, various measurements were performed. A total of 73 samples were investigated in terms of mineral constituents, texture and fabric, porosity, permeability and rock mechanical properties (Table 6.1).

6.3.2. Sample Preparation

After detailed macroscopic sample descriptions, large samples were drilled perpendicular (for most of rock mechanical tests) or parallel to the bedding (for most of the petrophysical measurements) using a diamond-studded drill bit and pre-cut using a diamond saw. Subsequently, the sample was ground to the size required for analysis. The specimens for rock mechanical measurements required either cylindrical plugs of 25 mm diameter and 50 mm length for uniaxial and triaxial compression tests or plugs with 25 mm diameter and approximately 15 mm length for Brazilian disk tensile testing. The specimens for petrophysical measurements are cylindrical plugs with 28.5 mm diameter and 10-30 mm length.

After the preparation of plugs, the remaining chunks were broken by a hammer to make fragments for mercury injection porosimetry or cut into small rectangular strips by a water-cooled saw to create sections for light microscopy and prepare sample materials for SEM and TEM investigation. The remaining small fragments were crushed to a 0.5-1.5 mm diameter (cutting) for helium pycnometry or ground to a 100-200 μm diameter (powder) for XRD. Small samples that were not suitable for preparation of standard specimens were analyzed by mineralogy, microscopy, mercury intrusion porosimetry, and helium pycnometry.

6.3.3. Methodology

Light microscopy

To analyze the sample composition and structural fabric, thin-sections and polished-sections were prepared for most of samples and then examined using a Zeiss Axiophot Electronic Microscope System, which was equipped with a Carl Zeiss Axiocam digital

camera and Axiovision 2.0 software and was capable of taking high resolution photomicrographs with magnifying lenses of 10×, 20×, 30×, 40×, and 50×.

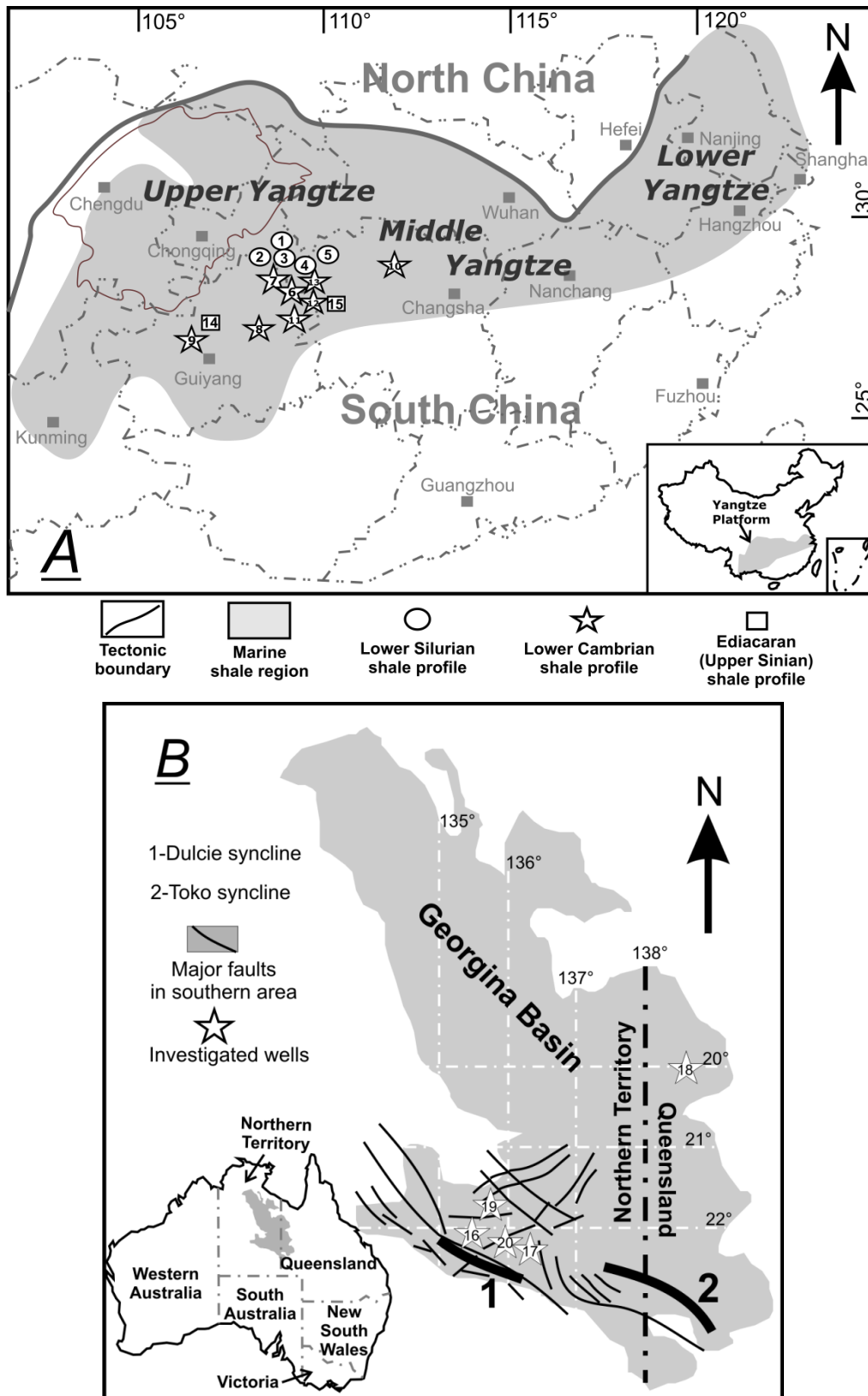


Figure 6.1 Overview maps of the Yangtze Platform, south China (A), and the Georgina Basin, north Australia (B). Numbers show the investigated profiles and wells, and names are listed in Table 6.1.

Chapter 6 Mineralogy, Lithofacies, Petrophysics, and Rock Mechanics

Table 6.1 Investigated samples and applied measurements.

ID	Original ID	Depth/m	Age	Formation	Profile/wells (Coordinates)	Area	Location	Country	Mineralogy		Microscopy			Petrophysics			Rock mechanics					
									XRD	LM	SEM	TEM	MIP	HP	GP	UC	TC	BD	UV			
1	G009507	Outcrop	Early Silurian	Longmaxi	1-Lujiao	UYP	Chongqing	China														
2	G009508	Outcrop		Longmaxi		UYP	Chongqing	China														
3	G009509	Outcrop		Longmaxi		UYP	Chongqing	China														
4	G009511	Outcrop		Longmaxi	UYP	Chongqing	China															
5	G009512	Outcrop		Longmaxi	2-Guankou	UYP	Chongqing	China														
6	G009514	Outcrop		Longmaxi		UYP	Chongqing	China														
7	G009524	136		Longmaxi	UYP	Chongqing	China															
8	G009525	207		Longmaxi	UYP	Chongqing	China															
9	G009526	267		Longmaxi	3-YY 1	UYP	Chongqing	China														
10	G009527	276		Longmaxi		UYP	Chongqing	China														
11	G009528	285		Longmaxi		UYP	Chongqing	China														
12	G009529	321		Longmaxi		UYP	Chongqing	China														
13	G011296	Outcrop		Wufeng	UYP	Chongqing	China															
14	G011297	Outcrop		Wufeng	UYP	Chongqing	China															
15	G011298	Outcrop		Wufeng	UYP	Chongqing	China															
16	G011299	Outcrop		Longmaxi	UYP	Chongqing	China															
17	G011300	Outcrop		Longmaxi	UYP	Chongqing	China															
18	G011301	Outcrop		Longmaxi	UYP	Chongqing	China															
19	G011302	Outcrop		Longmaxi	UYP	Chongqing	China															
20	G011303	Outcrop		Longmaxi	5-Hongyanxi	UYP	Hunan	China														
21	G011304	Outcrop		Longmaxi		UYP	Hunan	China														
22	G009515	Outcrop	Niutitang	UYP	Chongqing	China																
23	G009516	Outcrop	Niutitang	6-Rongxi	UYP	Chongqing	China															
24	G009517	Outcrop	Niutitang		UYP	Chongqing	China															
25	G009518	Outcrop	Niutitang	UYP	Chongqing	China																
26	G009519	Outcrop	Niutitang	7-Jinggang	UYP	Chongqing	China															
27	G009520	Outcrop	Niutitang		UYP	Chongqing	China															
28	G009521	Outcrop	Niutitang	8-Cenggong	UYP	Guizhou	China															
29	G009522	Outcrop	Niutitang		UYP	Guizhou	China															
30	G009706	Outcrop	Zhujiaping	UYP	Guizhou	China																
31	G009709	Outcrop	Shiyantou	9-Heishapo	UYP	Guizhou	China															
32	G009712	Outcrop	Shiyantou		UYP	Guizhou	China															
33	G009715	Outcrop	Shiyantou		UYP	Guizhou	China															
34	G011305	Outcrop	Niutitang	10-Ligonggang	UYP	Hunan	China															
35	G011306	Outcrop	Niutitang		UYP	Hunan	China															
36	G011307	Outcrop	Niutitang	UYP	Guizhou	China																
37	G011308	Outcrop	Niutitang	11-Bahuang	UYP	Guizhou	China															
38	G011309	Outcrop	Niutitang		UYP	Guizhou	China															
39	G011310	Outcrop	Niutitang		UYP	Guizhou	China															
40	G011311	Outcrop	Niutitang		UYP	Guizhou	China															
41	G011312	53.1	Bianmachong	12-Songqian 1	UYP	Guizhou	China															
42	G011313	109.4	Bianmachong		UYP	Guizhou	China															
43	G011314	166.5	Bianmachong	UYP	Guizhou	China																
44	G011315	200.3	Bianmachong	13-Yuke 1	UYP	Guizhou	China															
45	G011316	243.8	Bianmachong		UYP	Guizhou	China															
46	G011317	22.5	Mingxinsi/ Jindingshan	13-Yuke 1	UYP	Chongqing	China															
47	G011318	32.0	Mingxinsi/ Jindingshan		UYP	Chongqing	China															
48	G011319	47.5	Niutitang	UYP	Chongqing	China																
49	G011320	65.1	Niutitang	13-Yuke 1 well	UYP	Chongqing	China															
50	G011321	77.7	Niutitang		UYP	Chongqing	China															
51	G009694	Outcrop	Doushantuo	14-Maoshi	UYP	Guizhou	China															
52	G009697	Outcrop	Doushantuo		UYP	Guizhou	China															
53	G009703	Outcrop	Doushantuo	15-Lijiatuo	UYP	Hunan	China															
54	G009718	Outcrop	Liuchapo		UYP	Hunan	China															
55	G011322	86.1	Dengying	13-Yuke 1 well	UYP	Chongqing	China															
56	G011323	162.9	Doushantuo		UYP	Chongqing	China															
57	G011324	271.7	Nantuo	13-Yuke 1 well	UYP	Chongqing	China															
58	G011325	326.0	Nantuo		UYP	Chongqing	China															
59	G011326	351.5	Nantuo	UYP	Chongqing	China																
60	G006484	766.7	Arthur Creek	16-MacIntyre 1 well	UYP	North Territory	Australia															
61	G006485	782.6	Arthur Creek		UYP	North Territory	Australia															
62	G012285	790.8	Arthur Creek	17-Baldwin 1	UYP	North Territory	Australia															
63	G006486	797.7	Arthur Creek		UYP	North Territory	Australia															
64	G006487	803.2	Arthur Creek	18-BMR Mt Isa 1	UYP	North Territory	Australia															
65	G006488	879.2	Arthur Creek		UYP	North Territory	Australia															
66	G006489	883.8	Arthur Creek	19-NTGS Elkedra 3	UYP	North Territory	Australia															
67	G006490	887.7	Arthur Creek		UYP	North Territory	Australia															
68	G006491	101.5	Current Bush Lst	20-Hunt 1	UYP	Queensland	Australia															
69	G006492	107.5	Current Bush Lst		UYP	Queensland	Australia															
70	G012286	107.6	Current Bush Lst	19-NTGS Elkedra 3	UYP	Queensland	Australia															
71	G006493	114.4	Current Bush Lst		UYP	Queensland	Australia															
72	G006496	113.4	Arthur Creek	20-Hunt 1	UYP	North Territory	Australia															
73	G012284	345.4	Arthur Creek		UYP	North Territory	Australia															

Scanning electron microscopy (SEM)

SEM investigations were conducted on 27 UYP rock samples. Small bars at 0.3-0.5 cm thick, 0.5-1.0 cm width, and >2 cm length were cut during initial preparation. The samples were dried in an oven at 40°C for 24 hours to remove fluids. Investigations were carried out at GFZ Potsdam using an Ultra 55 plus Carl Zeiss SMT field emission scanning electron microscope (FE-SEM), and images were obtained under high vacuum at 20 kV acceleration voltages using the SE, Inlens-SE, and BSE detectors.

Focused ion beam - transmission electron microscopy (FIB-TEM)

Five UYP samples were selected for focused ion beam - transmission electron microscopy (FIB-TEM) analysis. FIB thin foils that were 15-20 µm wide, 10-15 µm high, and 100-150 nm thick were investigated at GFZ Potsdam using a FEI Tecnai G2 F20 x-Twin transmission electron microscope (TEM/AEM) equipped with a Gatan Tridiem energy filter, Fishone high-angle annular dark field detector (HAADF), and energy dispersive X-ray analyzer (EDX). The detailed methodological descriptions are available in Wirth(2004; 2009).

X-ray powder diffraction (XRD)

XRD was performed on most of the samples using a Siemens D 5000 powder diffractometer with Cu-K α radiation, automatic divergent and antiscatter slits, and a secondary graphite monochromator with a scintillation counter to determine proportions of matrix minerals. The diffraction data were recorded from 4° to 75° 2 θ with a step width of 0.02° and a counting time of 4 s per step. The generator settings were 40 kV and 30 mA. Measured data were then analyzed qualitatively using the EVA (Bruker) software and quantitatively using the AutoQuant software.

Mercury intrusion porosimetry (MIP)

Mercury injection porosimetry was performed on most of the core samples and several outcrop samples to determine the bulk density, equivalent pore radius distribution, and

Caption of Table 6. UYP: the Upper Yangtze Platform; AU: Australia (the Georgina Basin); XRD: X-ray powder diffraction; LM: Light microscope; SEM: Scanning electron microscopy; TEM: Transmission electron microscopy; MIP: Mercury injection porosimetry; HP: Helium pycnometry; GP: Gas (helium) permeability; UC: Uniaxial compression test; TC: Triaxial compression test; BD: Brazilian disk tensile test; UV: Ultrasonic velocity.

Chapter 6 Mineralogy, Lithofacies, Petrophysics, and Rock Mechanics

interconnected pores in the μm and nm range. Sample fragments with approximately 20×20 mm and 10-20 g were prepared and dried in an oven for 24 hours at 50°C . Subsequently, sample fragments were placed in a container (dilatometer) and mounted on the apparatus. The measurements were performed using a Fisons Instruments Mercury Porosimeter, and the results were calculated using the Washburn equation (Washburn, 1921). The mercury pressure increased from 0.0013 up to 200 MPa, which corresponds to an equivalent pore radius from $58 \mu\text{m}$ down to 3.7 nm .

Helium pycnometry

Helium pycnometry was performed on most of the core samples and certain outcrop samples using the pycnometers at RWTH Aachen University and GFZ-Potsdam to determine the skeletal density of the sample. Measured materials were cuttings with a diameter between 0.5 and 1.0 mm, and they were dried in vacuum conditions at 105°C .

Helium permeability

Helium permeability measurements were conducted on four UYP samples at RWTH Aachen University. Plugs were in as-received conditions and measured using a triaxial flow cell, which was designed for confining pressures up to 50 MPa and axial loads up to 100 kN. We applied a non-steady state technique that is described in detail by Ghanizadeh et al. (2013a; 2013b) to measure apparent gas permeability (k_{gas}) coefficients at different mean pressures (P_{mean}). k_{gas} was calculated from the pressure decline/incline curves at the upstream/downstream reservoirs we calculated according to Ghanizadeh et al. (Ghanizadeh et al., 2013a), and the corrected permeability k_{∞} was calculated using the formulation of Klinkenberg (1941). In this research, the applied confining pressure was 30 MPa at temperatures of 46°C and 52°C . The pressure difference between the upstream and downstream reservoir (ΔP) at the beginning of each experiment was approximately 20 bar, excluding certain measurements of sample 43 (<5 bar) and sample 58 (120 bar). Measurements were repeated at least two times with different flow directions (from the top side of the cell to the bottom and vice versa) in similar conditions to achieve a systematic interpretation. For sample 58, it was only possible to measure one gas permeability coefficient because there was no measurable pressure decline/incline of the upstream/downstream reservoir at pressure differences <100 bar.

Rock mechanical measurements

The rock mechanical measurements for the specimens were carried out at GFZ-Potsdam and Geomecon GmbH-Potsdam. The uniaxial compression test, Brazilian disk tensile test (BD), and triaxial compression test with multiple failures were conducted in a servo-hydraulically controlled stiff MTS loading frame (Minneapolis, USA) with a maximum axial load capacity of 4600 kN and maximum confining (oil) pressure of 200 MPa. The applied load, F , was measured by class I load cells with a maximum of 25 kN for BD and 1000 kN for TCT-MF and UCT. Experimental methods and data analysis for measurements of the uniaxial (UCS) and triaxial (TCS-MF) strength are consistent with recommendations from the International Society for Rock Mechanics (ISRM) (Ulusay and Hudson, 2007), whereas the measurements and calculations of the tensile strength (TS) and mode I fracture toughness (K_{IC}) based on the BD testing followed the procedures recommended by ISRM (Bieniawski and Hawkes, 1978) and Guo et al (1993), respectively. Prior to the mechanical measurements, ultrasonic p-wave velocities were measured parallel to the axis of cylindrical samples using piezoceramic transducers. The reported velocities were obtained by averaging approximately 100 high-pass filtered measurements in each direction.

6.4. Results

6.4.1. Mineralogy

The investigated samples are primarily composed of siliciclastic sediments and carbonates (Table 6.2). Detrital quartz is the dominant mineralogical constituent of the siliciclastic sediments, although subordinate amounts of feldspar and minor fraction of apatite are also present. The clay minerals consist primarily of illite and mica with minor amounts of chlorite and kaolinite. Carbonates in the UYP samples are mostly composed of calcite, whereas dolomite or ankerite dominates in the AU rocks. Pyrite is variably abundant in most of the samples, and the XRD bulk abundance ranges from 0.5% to 27%. The UYP rocks are frequently characterised by a higher content of clay minerals and mica compared to the AU rocks, which contain relatively higher amounts of carbonates.

Ternary diagrams composed of the measured XRD results and the compiled XRD data (Jiang et al., 2010; Zou et al., 2010; Chen et al., 2011; Guo et al., 2011a; Li et al., 2012a; Li et al., 2012b; Long et al., 2012; Chen et al., 2013; Han et al., 2013; Li et al., 2013; Nie et al., 2013; Wang et al., 2013b; Wu et al., 2013) show relative proportions of minerals in the quartz

group (quartz, feldspar, apatite, and pyrite), carbonate group (calcite, dolomite, ankerite, and siderite), or clay group (clay and mica) (Figure 6.2). Both the analytical results and compiled data show that the carbonate content of the UYP rocks is generally less than 30%, quartz group mineral content is higher than 30%, and clay mineral content is between 20-60% (Figure 6.2A). The clay minerals are relatively high in the Lower Silurian samples, whereas the quartz-related minerals are relatively high in the Lower Cambrian and Ediacaran samples. Carbonate, however, is low in both sample sets. Currently, shale gas was primarily produced from the Lower Silurian shale in the UYP. The difference of mineral composition between these shale formations may reflect that the production time of the Lower Cambrian shale might be longer than that of the Lower Silurian shale.

Although there is a broad variability of mineralogical composition, certain general conclusions can be drawn for the mineral data about the Lower Silurian and Lower Cambrian samples. Interestingly, more than 70% of the Lower Silurian samples are located in the C zone of Figure 6.2 B, and more than 70% of the Lower Cambrian samples are present in the C zone of Figure 6.2 C, which illustrate the typical mineral composition of samples from these two formations.

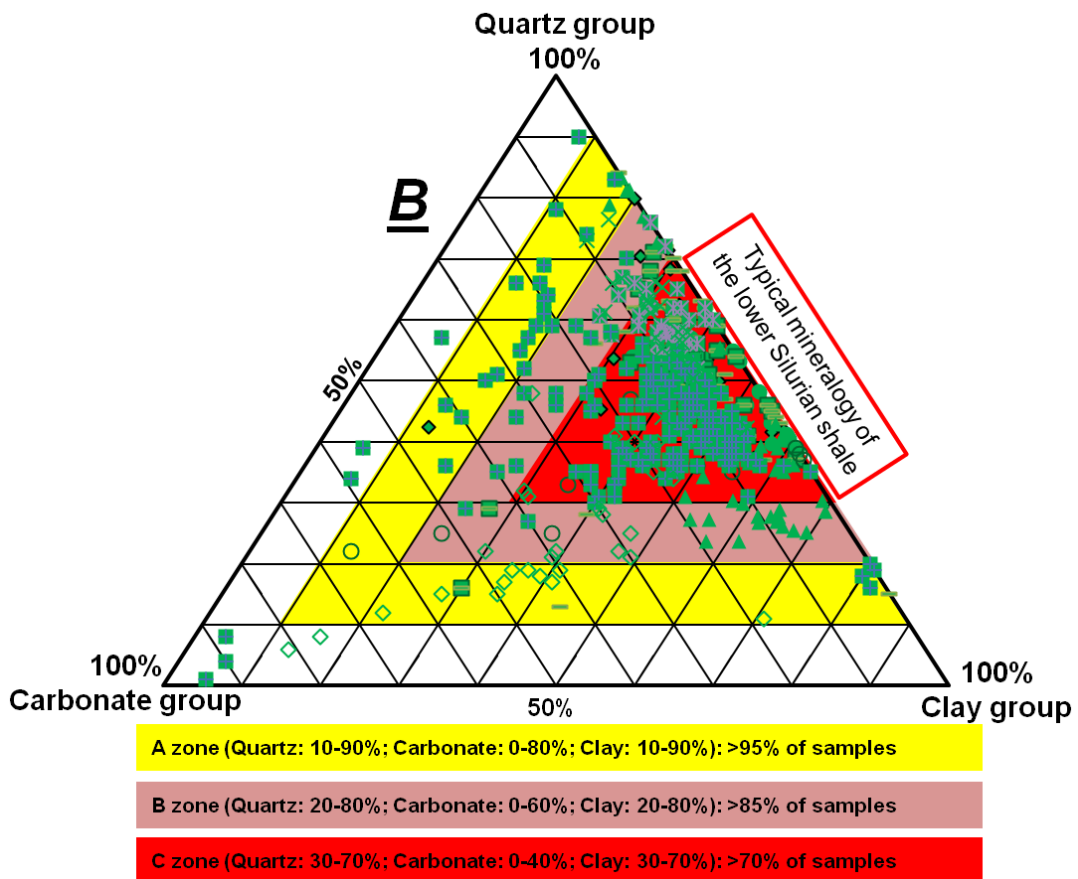
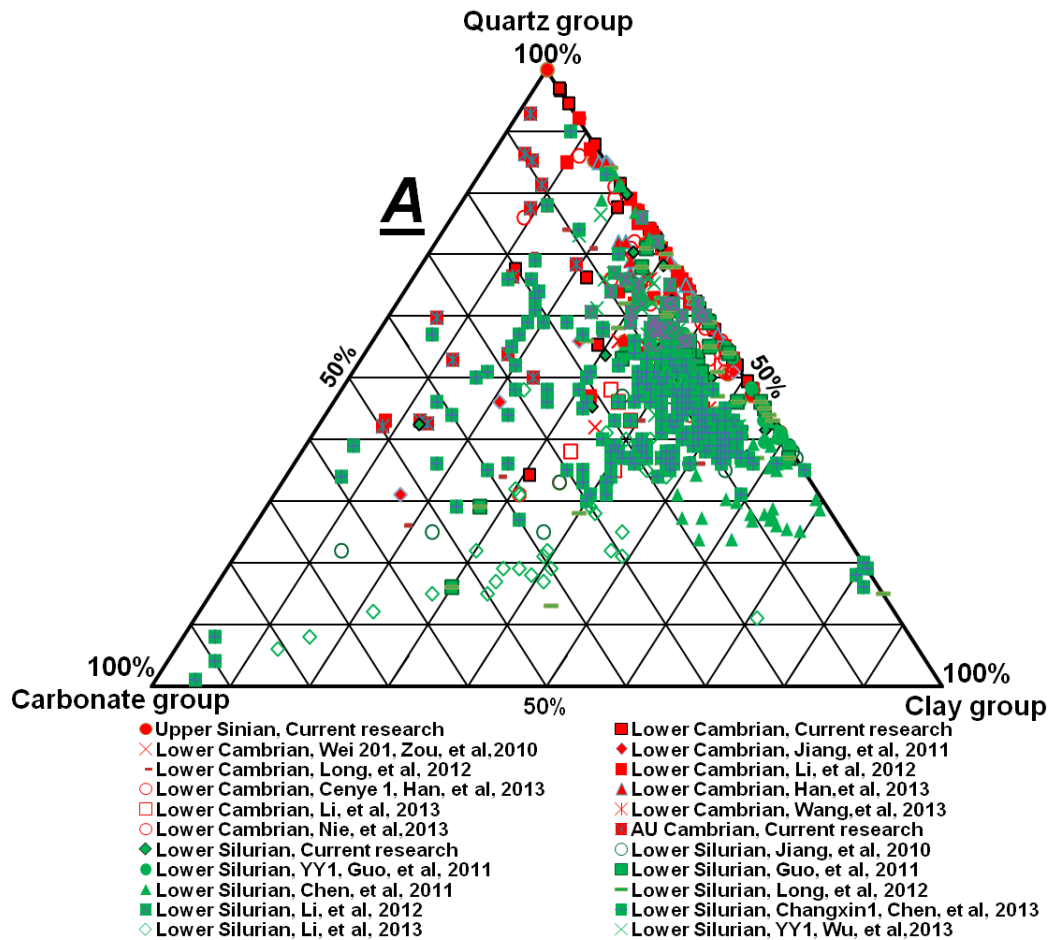
6.4.2. Lithofacies

The analyzed samples are composed of fine-grained (clay- to silt-sized) sediments that reflect a variety of lithofacies. Based on the XRD analysis (Table 6.2) and thin-section examination (Figures 6.3 and 6.4) and on a case study of the Barnett Shale (Hickey and Henk, 2007; Loucks and Ruppel, 2007; Abouelresh and Slatt, 2012), five different lithofacies can be distinguished for the analyzed UYP and AU rocks: 1) laminated siliceous mudstone, 2) non-laminated siliceous mudstone, 3) siliceous calcareous mudstone, 4) calcareous mudstone, and 5) phosphorite (Tables 6.2 and 6.3 and Figures 6.3-6.5). Other deposits such as carbonate laminae, reworked shaley, and lag deposits are rare to absent. Although only a few UYP samples show macroscopically visible laminae, a faint to well-developed laminated texture exists on the μm -scale for 60% of the samples (Table 6.3). Hence, the investigated UYP black shale intervals are dominated by laminated mudstone. Natural fractures are common and are currently tight by predominantly calcite or quartz (Table 6.3, Figure 6.5). These fractures are nearly perpendicular to the lamination. Minerals veins and en echelon fractures, which indicate extensional stress regimes, are also present. In certain cases, stylolites and load casts are noted (Figure 6.5).

Chapter 6 Mineralogy, Lithofacies, Petrophysics, and Rock Mechanics

Table 6.2 Results of TOC (wt %) and XRD mineralogy (wt %).

Interval	ID	TOC	Quartz	Feldspar	Apatite	Pyrite	Clay	Mica	Carbonate	Q+F+A+P	C+M	Lithofacies	Comment
Lower Silurian	1	3.3	40.8	8.2	<0.5	6.1	21.1	15.8	8.1	55.0	36.9	Siliceous	
	3	1.7	41.1	9.2	<0.5	2.0	28.9	11.3	7.6	52.2	40.2	Siliceous	
	4	0.9	29.9	14.7	<0.5	0.8	22.5	10.5	21.7	45.4	33.0	Siliceous calcareous	
	5	3.9	52.5	7.8	<0.5	2.2	20.3	14.2	3.1	62.4	34.5	Siliceous	
	6	3.6	56.6	9.6	<0.5	2.1	14.1	16.3	1.2	68.3	30.5	Siliceous	
	7	2.0	30.0	7.0	<0.5	4.6	40.3	16.5	1.6	41.6	56.8	Siliceous	
	8	1.5	39.6	11.6	<0.5	1.5	26.4	14.7	6.2	52.7	41.1	Siliceous	
	9	2.3	42.8	9.0	<0.5	1.8	20.8	9.8	15.9	53.6	30.6	Siliceous calcareous	
	10	1.7	41.0	12.4	<0.5	3.2	22.9	14.7	5.8	56.6	37.6	Siliceous	
	11	1.7	42.2	9.6	<0.5	1.7	27.7	14.8	4.1	53.4	42.5	Siliceous	
	12	2.2	39.2	8.3	<0.5	2.5	32.0	13.8	4.3	50.0	45.8	Siliceous	
	13	3.4	65.8	3.2	<0.5	1.5	11.3	14.3	4.0	70.4	25.6	Siliceous	
	14	3.3	65.7	4.1	<0.5	1.5	14.8	13.9	<0.5	71.3	28.7	Siliceous	
	15	4.2	74.3	5.1	<0.5	0.5	11.2	9.0	<0.5	79.9	20.2	Siliceous	
	16	4.0	29.6	10.8	<0.5	2.2	7.0	5.5	45.0	42.5	12.6	Calcareous	
	17	0.5	33.7	19.3	<0.5	1.3	19.6	21.1	5.0	54.4	40.6	Siliceous	
	18	0.5	35.2	21.2	<0.5	0.5	20.5	18.2	4.4	56.9	38.7	Siliceous	
	19	0.4	26.9	9.3	<0.5	1.2	37.4	19.2	6.1	37.3	56.6	Siliceous	
	20	0.4	41.2	<0.5	<0.5	0.7	25.1	33.0	<0.5	41.9	58.1	Siliceous	
	21	0.4	28.4	8.6	<0.5	1.6	24.8	36.7	<0.5	38.6	61.4	Siliceous	
	Average		2.1	42.8	9.4	<0.5	2.0	22.4	16.2	7.2	54.2	38.6	
Lower Cambrian	22	0.4	94.8	0.9	1.0	<0.5	<0.5	3.4	<0.5	96.6	3.4	Siliceous	
	24	6.0	33.6	31.5	<0.5	8.5	6.0	20.5	<0.5	73.5	26.5	Siliceous	
	25	7.4	31.2	29.2	<0.5	6.0	7.3	14.6	11.9	66.3	21.8	Siliceous calcareous	
	27	9.4	41.7	28.4	<0.5	5.9	8.7	15.3	<0.5	76.0	24.0	Siliceous	
	28	2.9	45.1	17.2	<0.5	<0.5	19.8	17.9	<0.5	62.3	37.7	Siliceous	
	29	5.8	52.6	22.6	<0.5	6.2	8.0	10.6	<0.5	81.4	18.6	Siliceous	
	30	0.4	29.2	<0.5	64.8	0.6	<0.5	5.4	<0.5	94.6	5.4	Phosphatic	
	31	7.8	55.6	<0.5	<0.5	2.1	22.0	20.3	<0.5	57.7	42.3	Siliceous	
	33	7.7	53.1	<0.5	<0.5	0.0	25.0	21.8	<0.5	53.1	46.9	Siliceous	
	34	1.7	46.3	5.2	<0.5	3.0	15.1	30.4	<0.5	54.5	45.5	Siliceous	
	35	2.5	38.7	10.8	<0.5	2.5	15.8	32.3	<0.5	51.9	48.1	Siliceous	
	36	4.9	44.7	22.4	<0.5	5.5	16.3	11.1	<0.5	72.6	27.4	Siliceous	
	37	3.8	51.6	16.2	<0.5	4.6	16.2	11.5	<0.5	72.3	27.7	Siliceous	
	38	4.2	48.0	16.6	<0.5	9.6	15.7	10.0	<0.5	74.2	25.8	Siliceous	
	39	6.4	40.3	18.7	<0.5	11.2	16.0	13.9	<0.5	70.1	29.9	Siliceous	
	40	0.3	80.1	7.5	<0.5	<0.5	2.3	9.8	<0.5	87.9	12.1	Siliceous	
	41	1.6	45.2	13.9	<0.5	2.3	19.8	18.9	<0.5	61.3	38.7	Siliceous	
	42	1.4	42.8	13.3	<0.5	3.2	23.3	17.5	<0.5	59.3	40.7	Siliceous	
	43	1.8	30.9	13.8	<0.5	3.4	31.2	20.6	<0.5	48.1	51.9	Siliceous	
	44	1.2	34.6	11.0	<0.5	3.8	30.9	19.7	<0.5	49.5	50.5	Siliceous	
	45	1.9	21.3	10.5	<0.5	2.5	14.4	16.2	35.1	34.3	30.6	Calcareous	
46	5.7	43.0	8.4	<0.5	4.0	18.3	10.4	15.9	55.4	28.7	Siliceous calcareous		
47	3.2	40.0	10.7	<0.5	3.8	14.8	22.5	8.3	54.5	37.3	Siliceous		
48	13.2	66.4	6.7	<0.5	4.5	11.3	8.8	2.3	77.7	20.1	Siliceous		
49	1.1	66.2	<0.5	<0.5	1.3	4.4	7.9	20.2	67.6	12.2	Siliceous calcareous	Dolomitic	
50	2.1	96.4	0.5	<0.5	<0.5	<0.5	3.0	<0.5	97.0	3.0	Siliceous		
Average		4.0	49.0	12.1	2.5	3.7	14.5	15.2	3.6	67.3	29.7		
Ediacaran	51	3.3	30.8	31.1	4.1	5.7	14.3	12.4	1.7	71.7	26.6	Siliceous	
	52	5.1	45.6	25.2	11.4	3.1	5.9	7.4	1.4	85.3	13.3	Siliceous	
	53	1.4	44.0	17.1	<0.5	3.9	15.1	20.0	<0.5	65.0	35.0	Siliceous	
	54	0.4	78.9	19.4	<0.5	1.6	0.0	0.0	<0.5	100.0	<0.5	Siliceous	
	55	14.5	33.4	14.4	<0.5	7.9	13.2	18.6	12.5	55.7	31.8	Siliceous calcareous	Dolomitic
	56	1.3	57.9	8.8	<0.5	<0.5	12.5	20.6	<0.5	66.9	33.1	Siliceous	
	57	0.4	28.9	13.1	<0.5	1.1	30.9	20.2	5.8	43.1	51.1	Siliceous	
	58	0.3	34.2	15.4	<0.5	0.9	20.2	27.4	1.8	50.6	47.6	Siliceous	
	59	0.5	30.7	14.8	<0.5	1.5	23.9	28.4	0.7	47.1	52.3	Siliceous	
	Average		3.0	42.7	17.7	1.7	2.9	15.1	17.2	2.7	65.0	32.3	
Middle Cambrian	60	1.2	42.2	9.3	<0.5	1.4	3.7	7.9	35.5	52.9	11.6	Siliceous calcareous	Dolomitic
	61	1.0	92.8	0.0	<0.5	<0.5	0.5	1.0	5.7	92.9	1.5	Siliceous	
	62	2.1	36.0	14.6	<0.5	3.2	5.4	12.7	28.1	53.8	18.1	Siliceous calcareous	Dolomitic
	63	8.7	9.7	10.7	12.0	27.2	6.3	0.0	34.1	59.7	6.3	Calcareous	Dolomitic
	64	5.3	70.0	8.0	5.7	1.5	<0.5	5.5	9.3	85.2	5.5	Siliceous	
	65	5.5	75.3	<0.5	<0.5	2.2	<0.5	9.2	13.3	77.5	9.2	Siliceous calcareous	Dolomitic
	66	11.0	70.7	8.0	<0.5	2.6	<0.5	8.6	10.1	81.3	8.6	Siliceous calcareous	Dolomitic
	67	10.9	82.9	2.5	<0.5	0.9	<0.5	4.1	9.7	86.3	4.1	Siliceous	
	68	9.0	23.0	18.7	<0.5	0.9	5.6	8.0	43.8	42.6	13.6	Calcareous	Dolomitic
	69	15.8	26.7	21.7	<0.5	1.7	6.9	16.3	26.8	50.1	23.2	Calcareous	Dolomitic
	70	1.0	42.5	<0.5	<0.5	0.6	4.6	7.8	44.6	43.1	12.4	Calcareous	Dolomitic
	71	0.5	27.6	14.1	<0.5	0.5	3.2	5.0	49.7	42.1	8.2	Calcareous	Dolomitic
	72	12.2	38.9	26.2	<0.5	3.3	5.2	14.2	12.2	68.4	19.4	Siliceous calcareous	Dolomitic
	73	10.7	45.3	18.7	<0.5	2.5	2.4	10.1	21.2	66.4	12.4	Siliceous calcareous	Dolomitic
Average		6.8	48.8	10.9	<0.5	3.5	3.1	7.9	24.6	64.4	11.0		



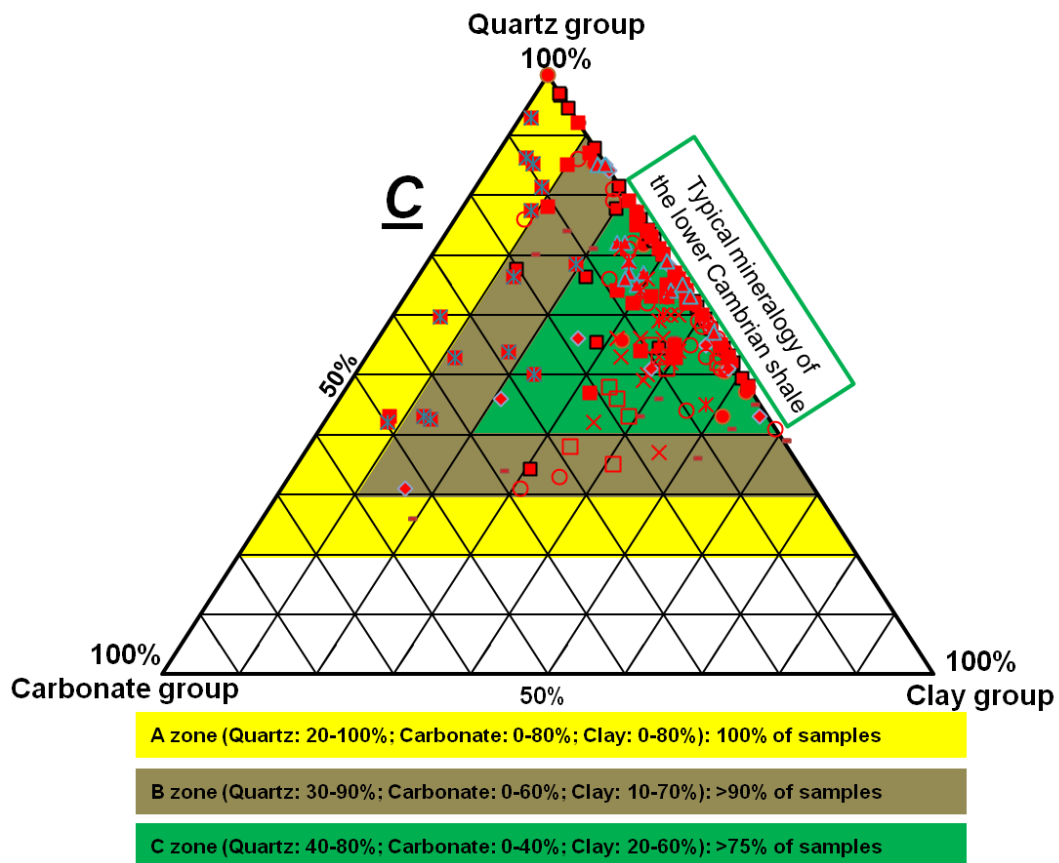


Figure 6.2 Mineralogical compositions according to XRD results. A: All measured samples and compiled data; B: Lower Silurian samples; C: Lower Cambrian samples. Basically, “quartz group minerals” include quartz, feldspar, apatite, and pyrite; “clay group minerals” comprise clay and mica; and carbonates consist of calcite, dolomite, ankerite, and siderite. Plot A and C contains 14 AU Cambrian samples.

Laminated siliceous mudstone

Laminated siliceous mudstone is the most common lithofacies in the Ediacaran, Lower Cambrian, and Lower Silurian UYP rocks, but it is less abundant in the AU Cambrian samples (Table 6.3 and Figures 6.3 and 6.4). The sediments of this lithofacies are commonly faintly to well-laminated depending on the orientation of the interbedded quartz and organic matter bands. The contacts between mineral laminae and organic laminae can be sharp or gradational. Burrows are scarce, indicating rare to absent bioturbation because of bottom water anoxia. The content of quartz is obviously higher than carbonate, clay, or any other terrigenous minerals, e.g., feldspar or mica. Organic material commonly appears in the form of aggregates and disseminated particles, and intact organic fossils are rare because of alteration, replacement, or crystallization. The TOC content is highly variable and ranges from less than 1% to higher than 10%.

Non-laminated siliceous mudstone

The non-laminated siliceous mudstone lithofacies is less common than the laminated siliceous mudstone facies but more frequent than other lithofacies of the UYP rocks. The sediments are poorly laminated and exhibit a homogenous matrix that consists of quartz, clay, and organic matter. In certain cases, mica, feldspar, or carbonate minerals are frequent (Figures 6.3 and 6.4). Burrows and fossil traces are extremely rare. The mineral composition resembles the siliceous shale facies and is dominated by quartz, which includes detrital grains and microcrystalline diagenetic quartz. Pyrite can occur in high concentrations and are commonly small framboids (Figure 6.3), especially in layers with high TOC content. Generally, fine organic matter aggregates or particles are distributed without orientation in the matrix, and the TOC content is relatively higher than in the siliceous shale facies (generally more than 5% TOC).

Siliceous calcareous mudstone

Poorly to well-laminated siliceous calcareous mudstones are characterised by a high content of quartz and a carbonate content of more than 10%. Only 11% of the UYP rocks can be classified as this lithofacies, whereas it is the dominant lithofacies of the AU rocks represents more than 43% of the analyzed samples (Table 6.3). Carbonate minerals may form part of the matrix and/or occur as bright laminae in siliceous calcareous mudstone (Figure 6.3). Dolomite or ferroan dolomite (ankerite) predominates in the Lower Cambrian and Ediacaran samples, whereas calcite is the dominant carbonate phase in the Lower Silurian samples.

Calcareous mudstone

Samples of this study are classified as calcareous mudstone when carbonate concentrations are higher than quartz and/or clay content. Thus this lithofacies can be commonly recognized by a light-gray or a brown color. Only two samples of the UYP rocks belong to this group (Figures 6.3 and 6.4), whereas 36% of the AU rocks are made up of such composition (Table 6.3). Carbonates of the calcareous samples from the UYP are mainly composed of calcite, whereas dolomite and ankerite dominate in AU samples. Samples with a high TOC content but few well-shaped microfossils indicate diagenetic alteration of the organic rich shale in the form of strong recrystallization and replacement by microcrystalline dolomite.

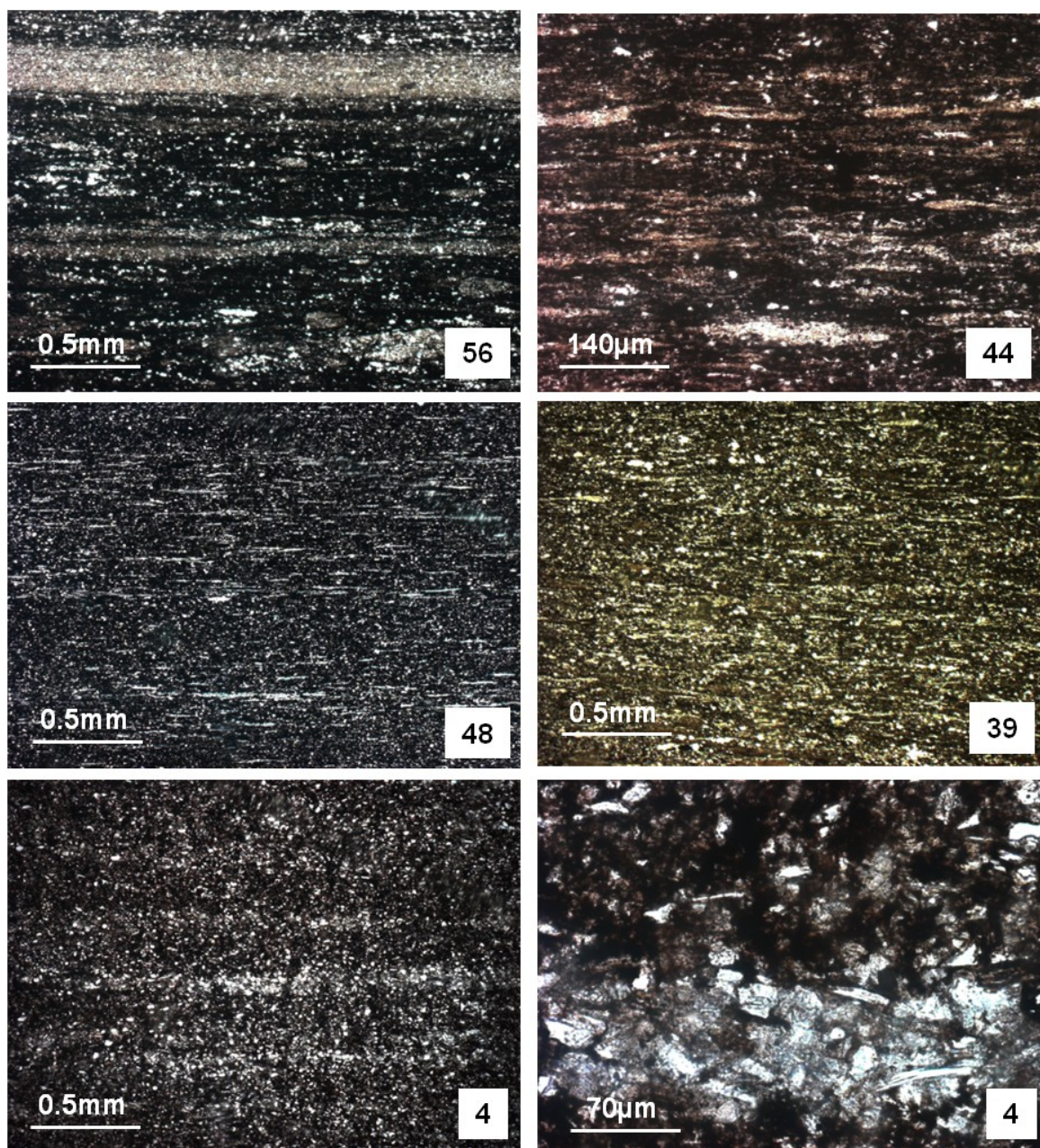


Figure 6.3 Microphotographs of laminated siliceous mudstone and siliceous calcareous mudstone. 56 (sample ID)-Ediacaran siliceous mudstone: Quartz and mica concentrate in the white laminae, while clay and organic matter concentrate in the black laminae in microphotograph; 44-Lower Cambrian siliceous mudstone: Discontinuous laminae can be seen in microphotograph; 48- Lower Cambrian siliceous mudstone: Faint laminae are shown by the orientation of quartz (66.4%, wt) and organic matter (13.2% TOC); 39-Lower Cambrian siliceous mudstone: It shows similar texture as the sample 48, but has obviously high content of pyrite (11.2%), concentrating to form thin laminae; 4-Lower Silurian siliceous calcareous mudstone: Faintly rhythmic lamination texture is illustrated by the alternating clay-rich (dark) and ankerite-rich (bright) laminae; 43-Lower Cambrian siliceous mudstone (reflected light): Organic matter (grey part) occupies significant area in the texture, and concentrates to form thin laminae; and 48 (bottom)-Lower Cambrian siliceous mudstone (reflected light): Organic matter (grey part) occupies significant area in the texture, but scatters in the matrix. The pyrite could occur either as framboids (yellow arrows in 43 and 48), or single crystals (blue arrows in 43 and 48). Samples for these microphotographs were cut perpendicular to bedding planes.

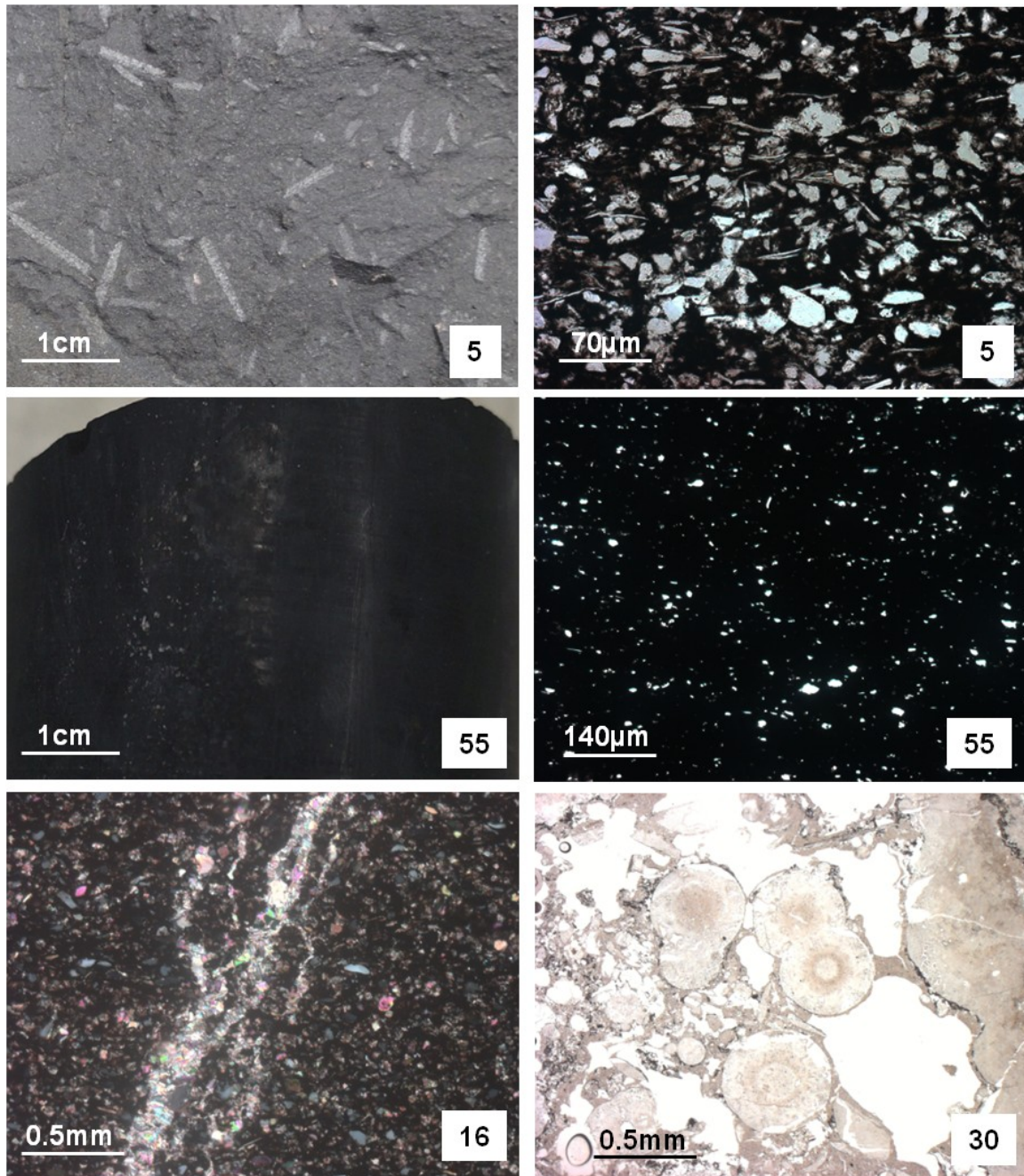


Figure 6.4 Sample slabs and microphotographs of non-laminated siliceous mudstones and phosphatic concretion. 5 (Sample ID)-Lower Silurian non-laminated siliceous mudstone: Graptolite fossils randomly distribute in hand specimen (left), while the microphotograph exhibits homogeneous matrix comprising subangular quartz grains, clay, mica, and organic matter (right); 55-Ediacaran non-laminated siliceous calcareous mudstone: Core photograph shows a dark and massive texture (left), and fine-grained dolomite minerals scatter in a dark (TOC=14.5%) and clayey matrix (right); 16-Lower Silurian non-laminated calcareous mudstone: Microphotograph shows calcite matrix and mineral veins (sealed fractures); 30-Lower Cambrian phosphatic concretion: Appearance of phosphatic pellets in microphotograph. Excluding the photograph of 5-left, samples were cut perpendicular to bedding planes.

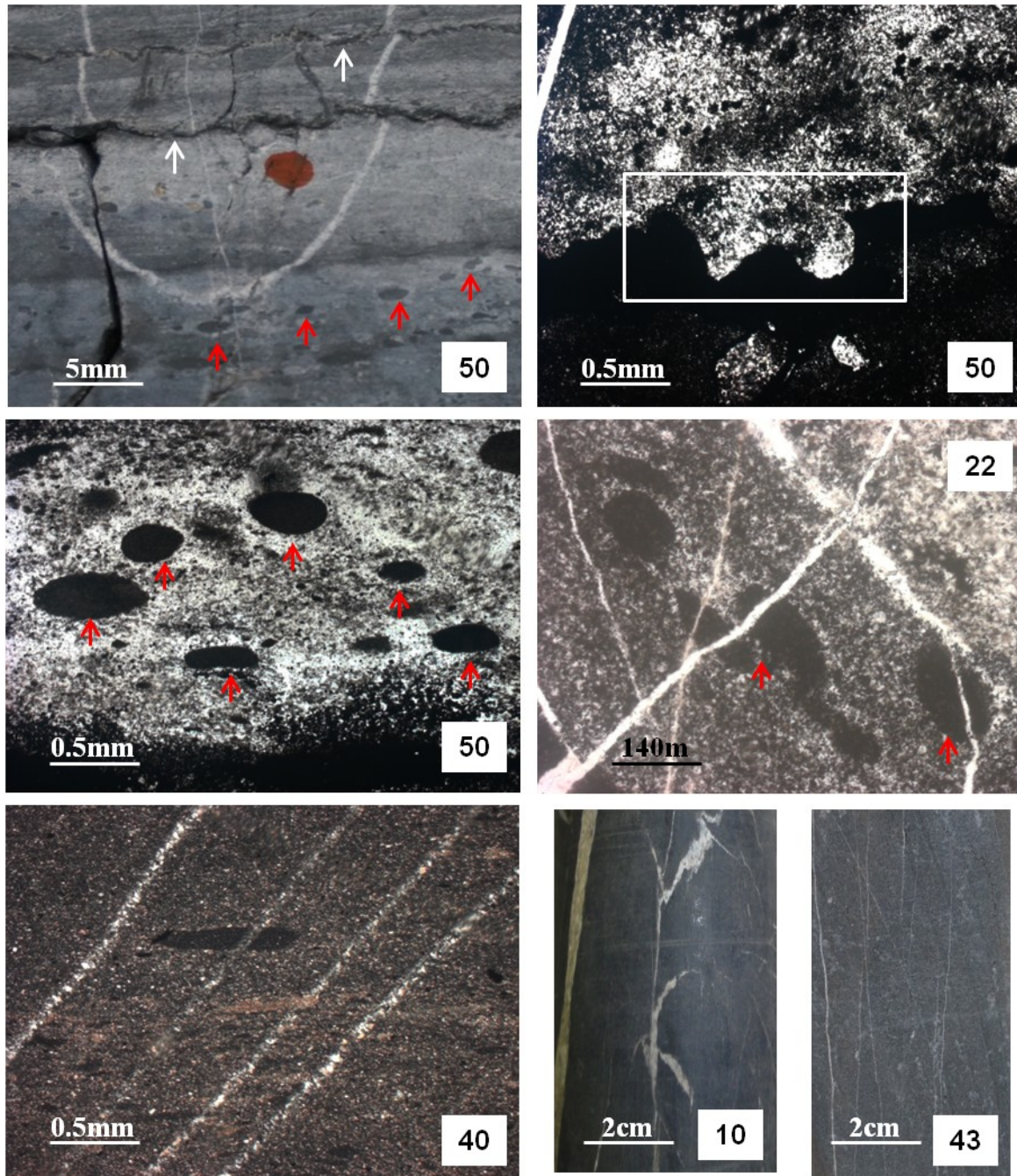


Figure 6.5 Fracture photographs. 50 (sample ID): Stylolites (white arrows) in a chert matrix, with mineral veins and pellets (red arrows) (upper left); Microphotographs of the same sample shows load casts (upper right), and exhibits dark elliptic pellets (red arrows) in a chert matrix (middle left). 22- Crossed fracture system cuts through pellets (red arrows). 40: Mineral veins (sealed fractures) show in a siliceous mudstone sample. 10 and 43: Vertical sealed fractures occur frequently in the Lower Silurian shales (e.g., 10) or in the Lower Cambrian shales (e.g., 43).

Table 6.3 Lithofacies statistics.

Type	Number analyzed	Analyzed item	Classification	Sample account	Percentage (%)	Applied Method
UYP rock	33	Lamina	Laminated	20	60.6	Sample description+light microscopy
			Non-laminated	13	39.4	Sample description+light microscopy
	33	Fracture	Non-fracutred	21	63.6	Sample description+light microscopy
			Fractured	12	36.4	Sample description+light microscopy
	55	Mineral	Siliceous	46	83.6	Light microscopy+XRD
			Siliceoue calcareous	6	10.9	Light microscopy+XRD
			Calcareous	2	3.6	Light microscopy+XRD
			Phosphatic	1	1.8	Light microscopy+XRD
			Siliceous	3	21.4	Light microscopy+XRD
	AU rock	14	Mineral	Siliceoue calcareous	6	42.9
Calcareous				5	35.7	Light microscopy+XRD

Phosphorite

The phosphatic lithofacies is composed of phosphatic concretions, nodules (Figure 6.4), and pellets (Figure 6.5). Both colorless phosphatic aggregates and light- to medium-brown nodules were observed. Layers of phosphatic concretions are oriented parallel to the bedding and elliptic phosphatic nodules. Phosphatic pellets appear as minor to common grains in siliceous mudstone and are distributed discretely or as lenses.

6.4.3. Petrophysics

Pore types

Pores are not recognized at the centimeter scale on core slabs or on the millimeter (mm) to micrometer (μm) scale in thin-sections (Figures 6.3-6.5). The samples exhibit a tight texture, although open fractures occur in several samples. Based on Loucks et al (Loucks et al., 2012), various porosity types are recognized: organic-matter pores (organopores), intraparticle pores (within mineral grains), interparticle pores (between grains), and also microfractures. Such porosity types have been proven using high-resolution microscopes, e.g., SEM, TEM, and FE-SEM (Figures 6.6 and 6.7). As the images show, organic material or organic-dominated patches are discernible from the matrix by their darker gray-scale value. Pyrite is highlighted by its obvious white color, and the mineral matrix is characterised by different grey colors that represent varying amounts of clay, carbonate, and quartz.

In the mineral matrix, intraparticle pores appear in calcite or quartz grains, whereas interparticle pores can occur between various mineral grains or clay flakes (Figures 6.6 and 6.7). Microfractures are present along mineral boundaries or along clay flakes, but it is

unclear whether they are artificial or natural fractures. In general, the diameters of these pores are developed from the μm to nanometer (nm) scale. However, along with intraparticle and interparticle pores, a large number of pores were observed within the organic matter (Figure 6.7). In the Lower Silurian shales, circular or irregular organopores occur on the order of tens to hundreds of nm in diameter. Organopores can be elongated along the orientation of organic bands or randomly distributed. In addition, interparticle pores between organic matter and clay flakes occur. In the Lower Cambrian shale, nm or even μm -large circular pores are randomly located in the organic matter, whereas significant organopores can also occur between pyrite framboids or between pyrite crystals and clay flakes. Overall, the observed organopores in selected samples are at the nm scale, with few having μm diameters. In certain cases, the pores are well connected, and pore throats occur between the organopores (Figure 6.7 B).

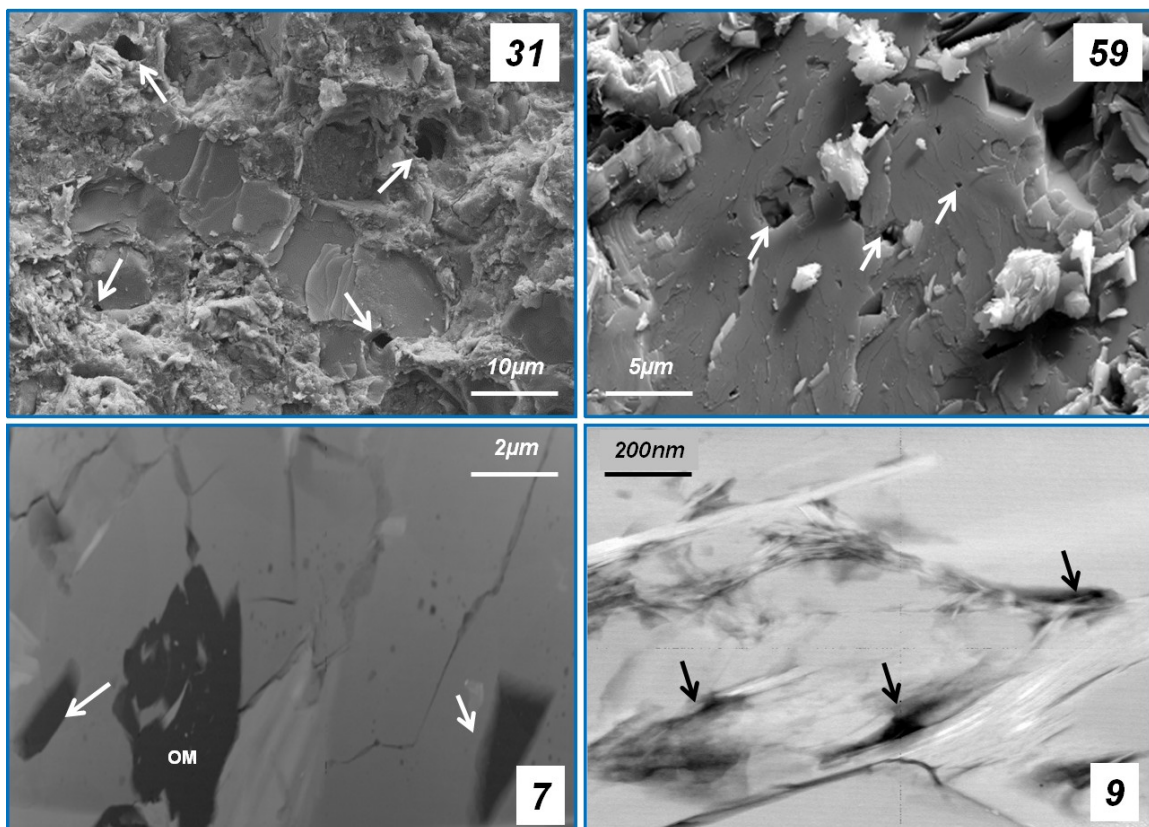


Figure 6.6 Pores in the mineral matrix. 31 (sample ID) - Micrometer scale matrix pores (white arrows, SEM); 59-Intraparticle pores (white arrows) in a quartz grain (SEM); 7-Organic matter, angular-subangular pores (white arrows), fractures (artificial or natural?), and fluid inclusions in the matrix (FIB-TEM); 9- Elongate pores (black arrows) distribute between clay flakes (FIB-TEM).

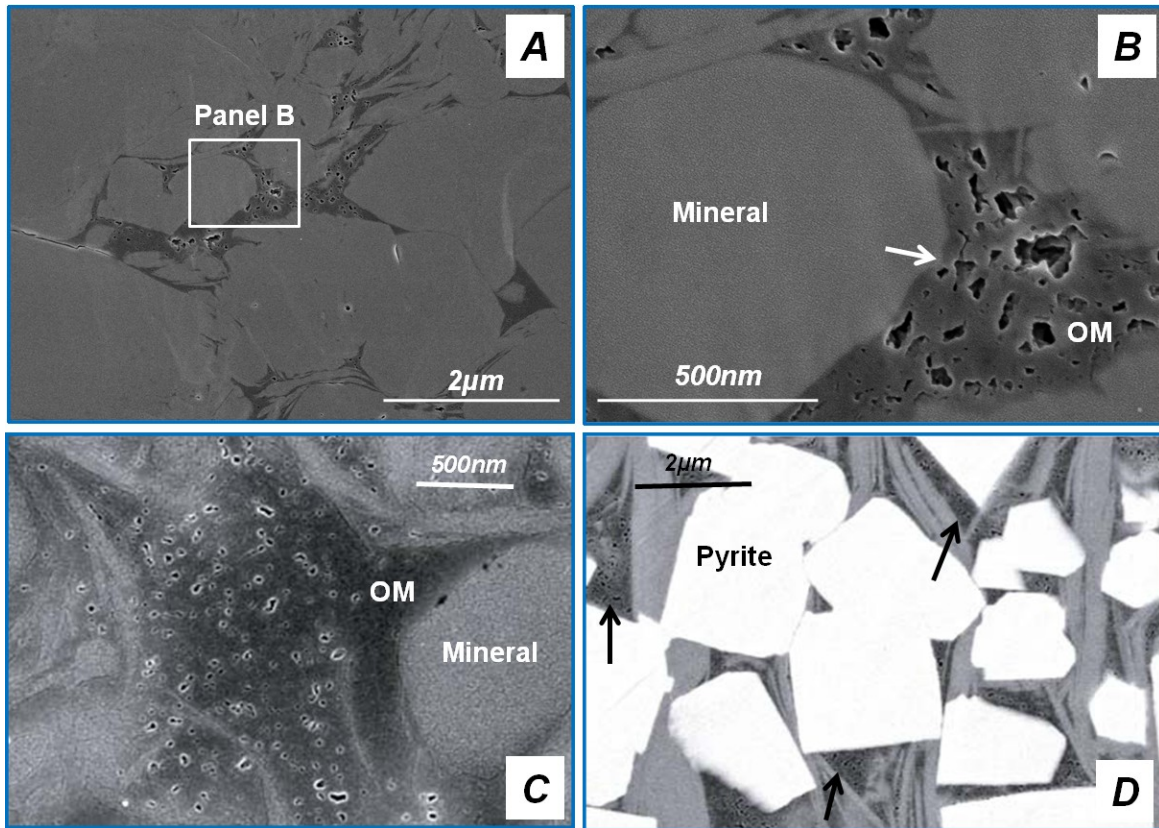


Figure 6.7 Pore in the organic matter. A and B—Nanometer to micrometer scale pores are abundant in the organic matter, and rarely occur in the mineral matrix, FE-SEM image of a Lower Silurian shale sample (courtesy of Tian, and from Tian, et al (2013)); C and D—Nanometer scale pores are abundant in the pyrobitumen between silt minerals, or in the pyrobitumen that is located between pyrite and clay flakes of a Lower Cambrian shale sample (courtesy of Zou, and from Zou, et al (Zou et al., 2010)).

Porosity

The measured porosities via MIP (Hg-porosity) of most samples are lower than 1%, with two AU Cambrian samples ranging from 1.5% to 3.5% (Table 6.4 and Figure 6.8 A). The Hg-porosity of the Lower Cambrian samples positively correlates with an increase of TOC (Figure 6.8 A), whereas the bulk density of all UYP samples distinctly decreases with an increase of TOC (Figure 6.8 B). In contrast to the low Hg-porosity, the porosity (He-porosity) that was calculated via the density results from MIP and helium pycnometry of most samples are relatively high (Table 6.4 and Figure 6.8 C). The He-porosity of most samples is between 1% and 4%, whereas four samples are in excess of 10%, which indicates large variation. This considerable variation might result from mineral constituents, although the mineral composition shows no systematic influences on porosity. In addition, the He-porosity shows a positive weak correlation with TOC increase (Figure 6.8 C). Presumably, porosity involves a

considerable contribution from small pores (radius <3.7 nm), which are not assessed using MIP but can be reflected by He-porosity.

The size distribution of pores with a radius larger than 3.7 nm was investigated using MIP, and the cumulative pore volume and relative pore volume of the selected Lower Silurian and Lower Cambrian sample are shown in Figure 6.9. The results show that considerable contributions of pore volume are from smaller pores, i.e., pores with a radius between 3.7 nm and 50 nm are primary contributors to the total pore volume (Figure 6.9). Another major contribution appears to be from pores with a radius between 3 μm and 30 μm , and two selected samples show a significant relative pore volume in this range. Nevertheless, it is difficult to determine whether such macropores (diameter >10 μm) are actual pores within the sample or result from measurement error. Cracks or an incomplete vacuum may be induced when the pressure increases (Jüntgen and Schwuger, 1966), and artificial intergranular pores may be produced by a partial filling of the penetrometer during the preparation stage of analysis (Chalmers et al., 2012). However, porosity contributions from such macropores of all measured samples are very low, and their influences on total porosity of any measured sample are within the error margin.

Gas permeability

The measured samples have Klinkenberg-corrected gas permeability coefficients (k_{∞}) ranging from near 0 to 20.2 nano-Darcy (nD) and a Klinkenberg slip factor (b) for helium between 0.32 and 0.55. The apparent gas permeability coefficients (k_{gas}) under applied experimental conditions range from 0.06 to 52.7 nD (Table 6.5 and Figure 6.10). Different measurements performed on the same sample exhibit similar k_{∞} values with the highest difference being 3 nD.

Samples 25 and 29 (Figure 6.10) were measured under similar conditions ($T \approx 46^{\circ}\text{C}$, $P_{\text{conf}} \approx 30$ MPa, $\Delta P \approx 20$ bar) but show different permeability coefficients (K_{∞} or K_{gas}). In contrast to sample 29, K_{gas} differences existing between two measurements of sample 25 are more evident. Sample 43 was measured at a higher ambient temperature (52°C) than samples 25 and 29 and repeated at ΔP lower than 5 bar (rectangle) and approximately 20 bar (rhombus). However, it can be observed that quite similar K_{∞} values were achieved by two measurements, although the measured conditions were changed both in the flow direction and pressure difference between the two reservoirs (Table 6.5 and Figure 6.10). Sample 58 is almost impermeable. Even if the pressure difference increases to 120 bar, only a slight

pressure change can be observed in the upstream and downstream reservoir, and thus only a very low apparent gas permeability (0.06 nD) was calculated (Figure 6.10).

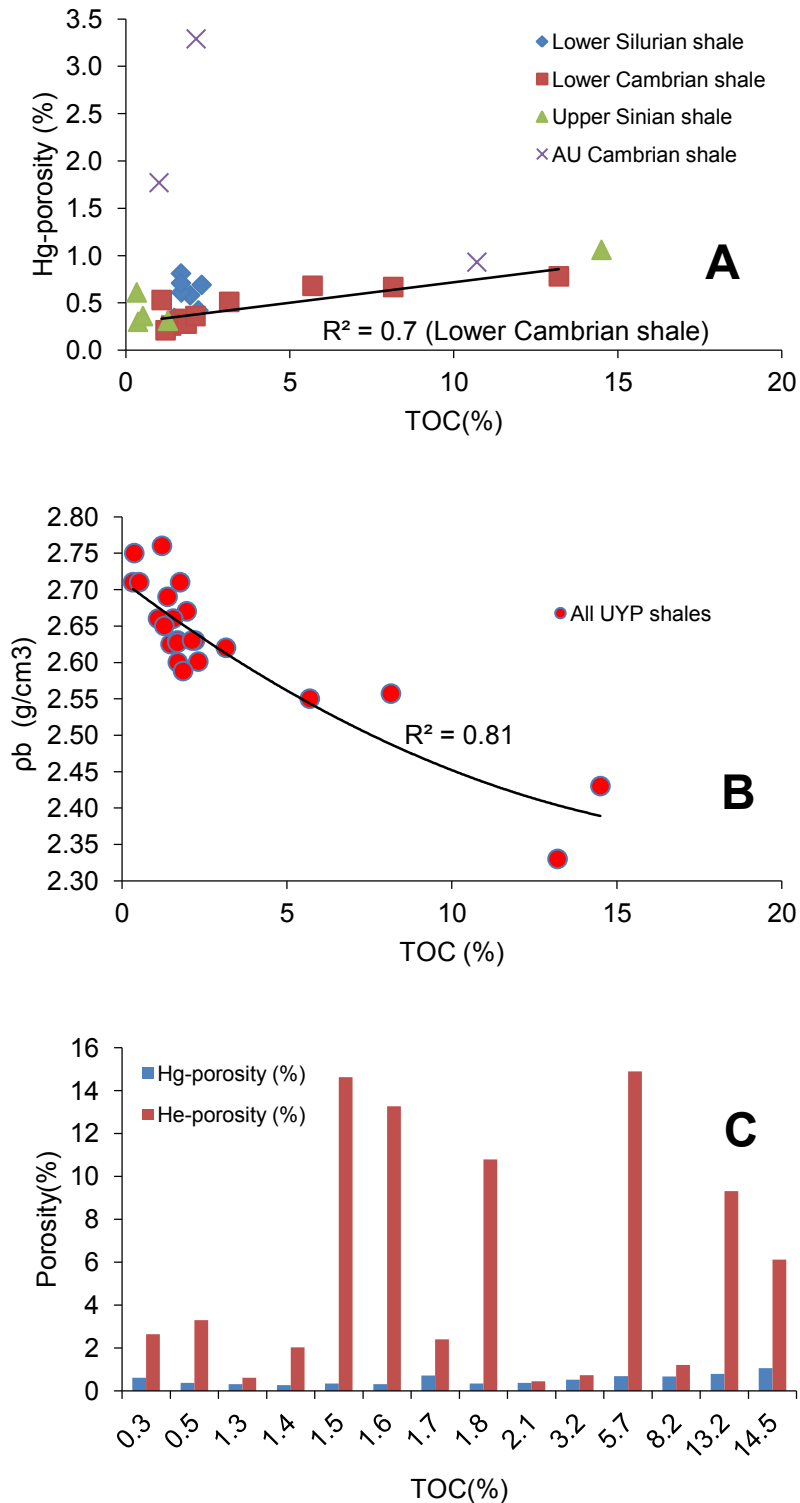


Figure 6.8 Porosity and bulk density, and their correlations with TOC. A: Hg-porosity versus TOC; B: Correlations between bulk density (ρ_b) and TOC; C: Hg-porosity versus He-porosity.

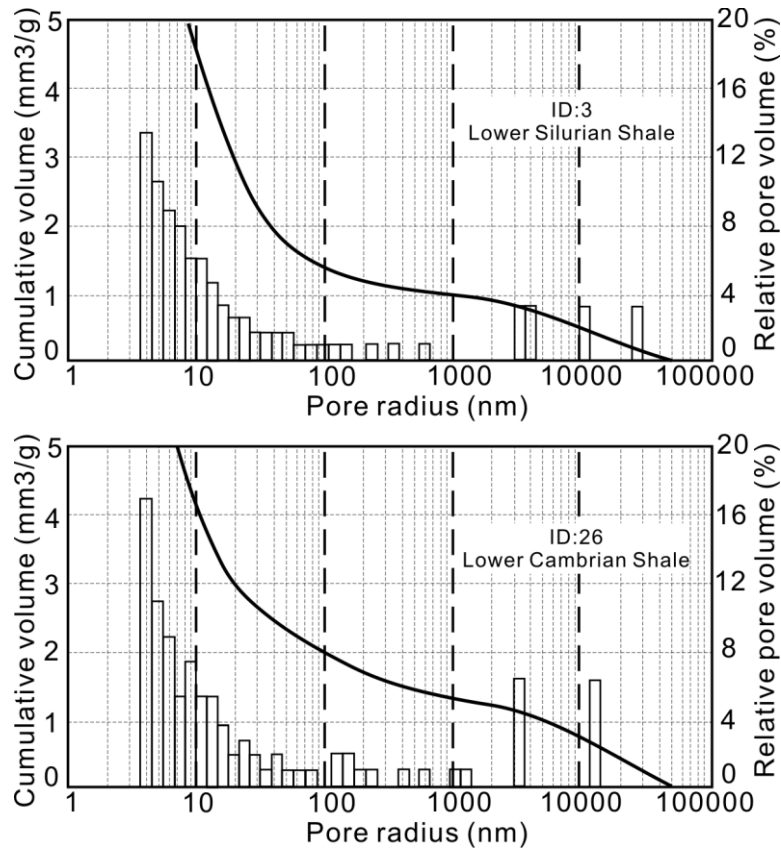


Figure 6.9 Pore size distribution and cumulative pore volume of the selected Lower Silurian (upper) and Lower Cambrian (lower) shale sample.

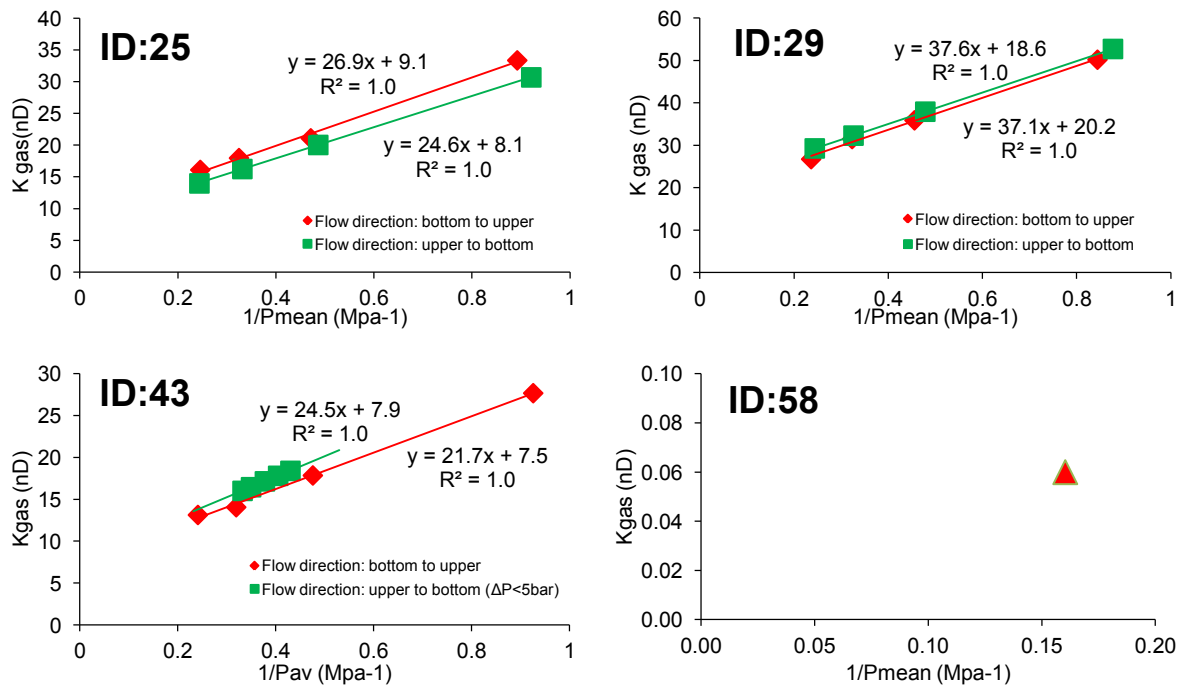


Figure 6.10 K_{gas} vs. $1/P_{\text{mean}}$ (Klinkenberg-plot) for sample 25, 29, 43 and 58. The intercepts between the linear regressions and the y-axis are the Klinkenberg corrected permeability coefficients k_{∞} . For sample 58 it was not possible to calculate k_{∞} , because at lower P_{mean} could not detect a pressure decline/incline at the upstream/downstream reservoirs.

6.4.4. Rock Mechanics

Compressive strength

At atmospheric pressure, the samples show brittle behavior with a minor inelastic deformation before failure resulting in axial splitting. The peak stresses range from 94 to 169 MPa for the Lower Silurian shale and from 167 to 234 MPa for the Lower Cambrian shale (Figure 6.11). The uniaxial compression strengths (UCS) negatively correlate with the weak constituents (clay, mica, TOC) and porosity but show positive correlations with the amount of carbonate and feldspar or the total amount of minerals excluding the weak constituents (Figure 6.12 A, B). Hence, both the sample composition and the porosity affect the uniaxial strength.

The brittle character was also revealed by a triaxial compression test with confining pressure increasing up to 36 MPa. Most of the investigated samples were failed by an abrupt drop in load. With regard to the measured UYP outcrops, samples 3 and 26 exhibit low and high strength, respectively. In terms of the measured AU Cambrian samples, sample 70 shows distinct strain softening at the highest applied confining pressure, and the strength at all pressures is lower than most of the other samples (Figure 6.13). The triaxial compression strengths (TCS) of samples that exhibit brittle failure range from 200 to 380 MPa and are negatively correlated with clay and mica and positively correlated to the amount of carbonate and feldspar or the total amount of minerals excluding the weak minerals (Figure 6.14 A-C). In contrast, the coefficient of internal friction (μ) increases with the total content of clay, mica, and TOC, whereas it decreases with the quantity of carbonate or the total amount of minerals excluding the weak constituents (Figure 6.14 D).

Elastic properties

Static Young's moduli (E) measured at atmospheric pressure are between 13 and 24 GPa (Figure 6.12 C and D) and those measured at 12 MPa confinement (E12) range from 12 to 26 GPa (Figure 6.15 A). In addition, both sets increase with strength increase. Similar to the UCS, the static Young's moduli shows a strong negative correlation with porosity (Figure 6.12 D). The dynamic Young's moduli could not be calculated because only the P-wave velocity was measured perpendicular to the bedding (V_p). Nevertheless, the V_p correlates well with the static Young's moduli (Figure 6.15 B). In addition, two samples were measured for Poisson's ratio by simultaneous records of the vertical and parallel deformation during two

UCS measurements at atmospheric confinements. The Poisson's ratio of the Lower Silurian sample (0.33; ID 4) is higher than that of the Lower Cambrian sample (0.25; ID 29).

Tensile strength

Indirect (Brazilian disk) tensile tests were performed on 2-8 specimens drilled out of selected cores and yield relatively high tensile strength values with considerable scatter. Fracture initiation starts in the center of most specimens and generally displays continuous fracture propagation. Hence, the measured results are suitable for the evaluation of tensile strength (σ_t) and mode I fracture toughness (K_{IC}). As shown in Figure 6.16, σ_t ranges between 10 and 20 MPa, whereas K_{IC} ranges from 1.0 to 1.7 MPa.m^{1/2}. These values are relatively high compared to those for Woodford shales (Sierra et al., 2010). Evidently, no clear correlation between σ_t or K_{IC} and the mineral content exist in relation to carbonates or clay and mica (Figure 6.16). However, the tensile strengths tend to increase with increasing uniaxial compressive strength and Young's modulus, although they are obscured by a large scatter (Figure 6.15 C and D).

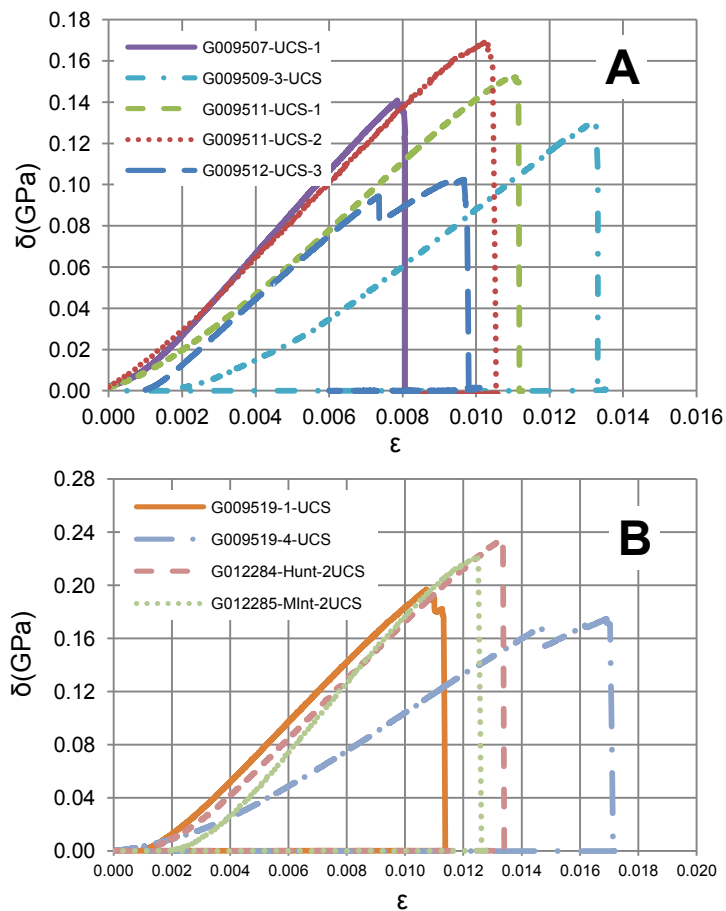


Figure 6.11 Stress (δ)-strain curves (ϵ) of selected samples. A-Lower Silurian shale and B-Cambrian shale.

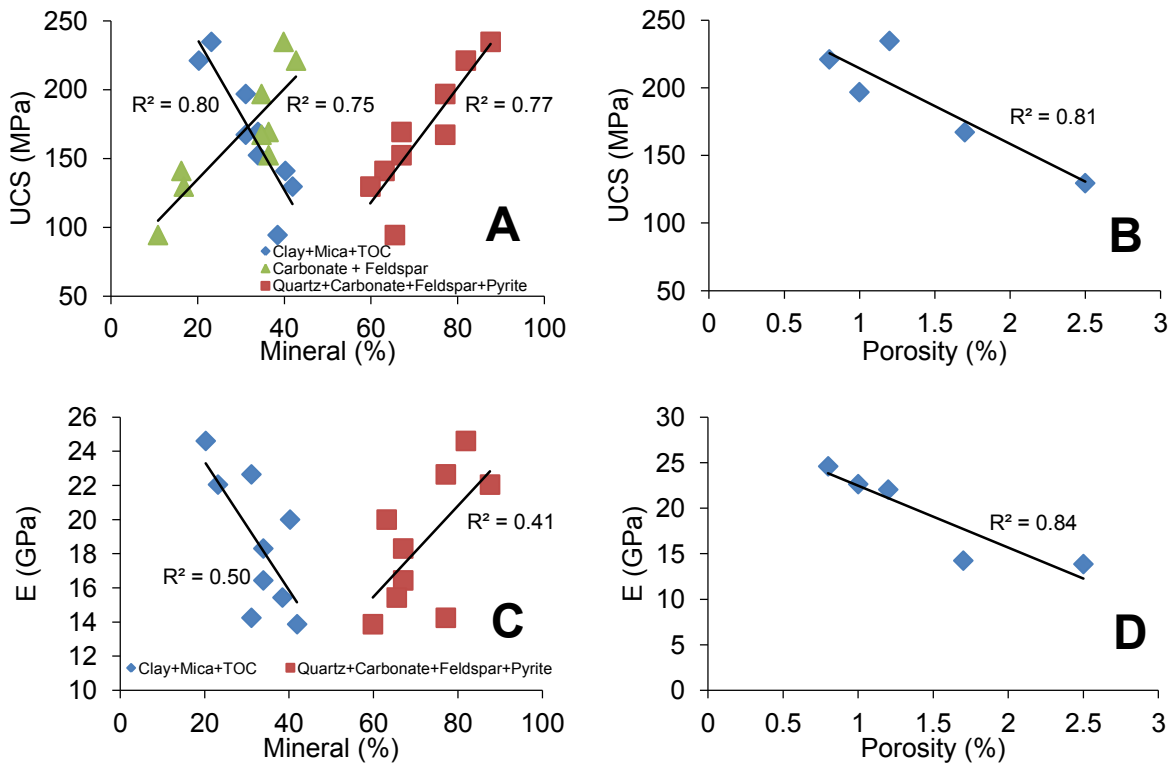


Figure 6.12 Uniaxial compression strength (UCS) and Young's modulus (E) and their correlations with mineral content and porosity.

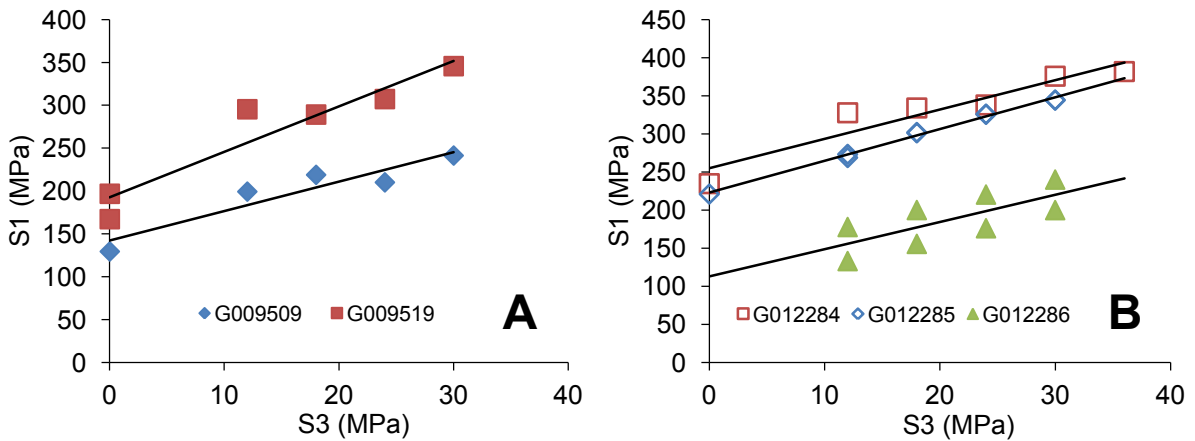


Figure 6.13 Confining pressure (S3) vs. maximum stress (S1) of triaxial compression test with multiple failure. A-UYP outcrops, B-AU Cambrian cores.

Chapter 6 Mineralogy, Lithofacies, Petrophysics, and Rock Mechanics

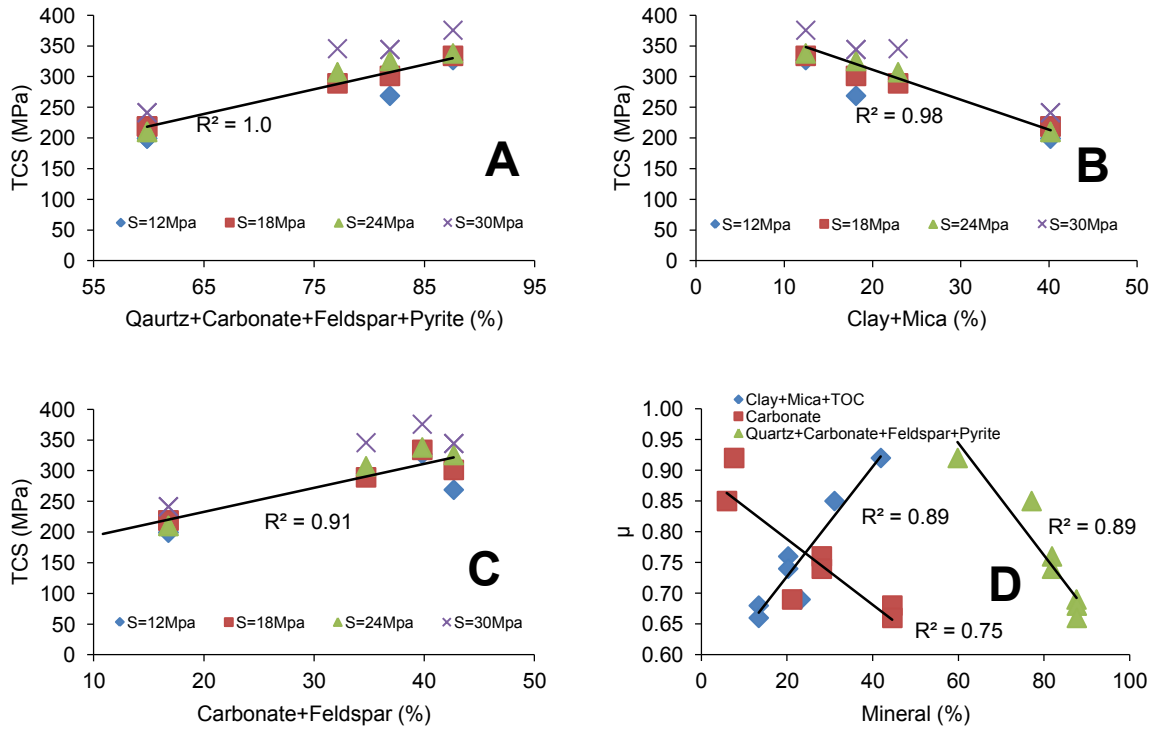


Figure 6.14 Mineral influences on the triaxial compression strength (TCS, A-C) and the internal friction coefficient (μ , D).

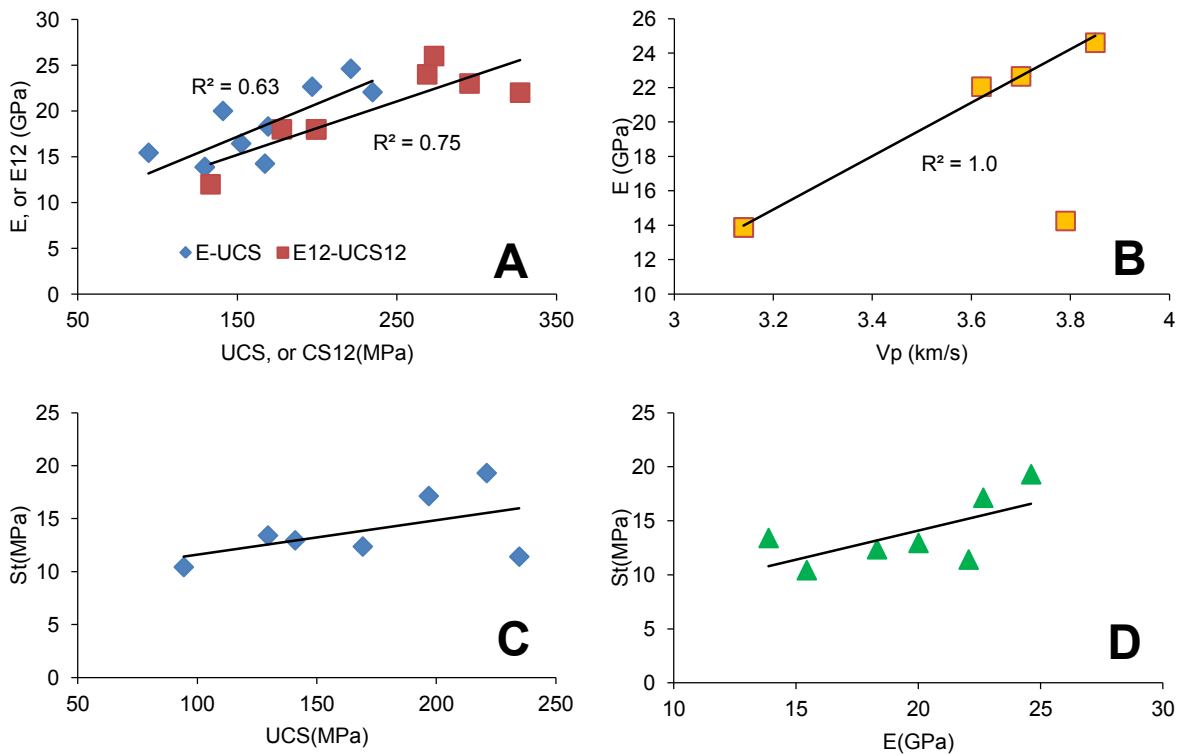


Figure 6.15 Correlations between Young's modulus and compression strength (A), Young's modulus and P-wave velocity perpendicular to bedding (V_p) (B), tensile strength and uniaxial compressive strength (C), and tensile strength and Young's modulus (D). E12 and CS12 mean Young's modulus and compression strength measured at 12 MPa confinements.

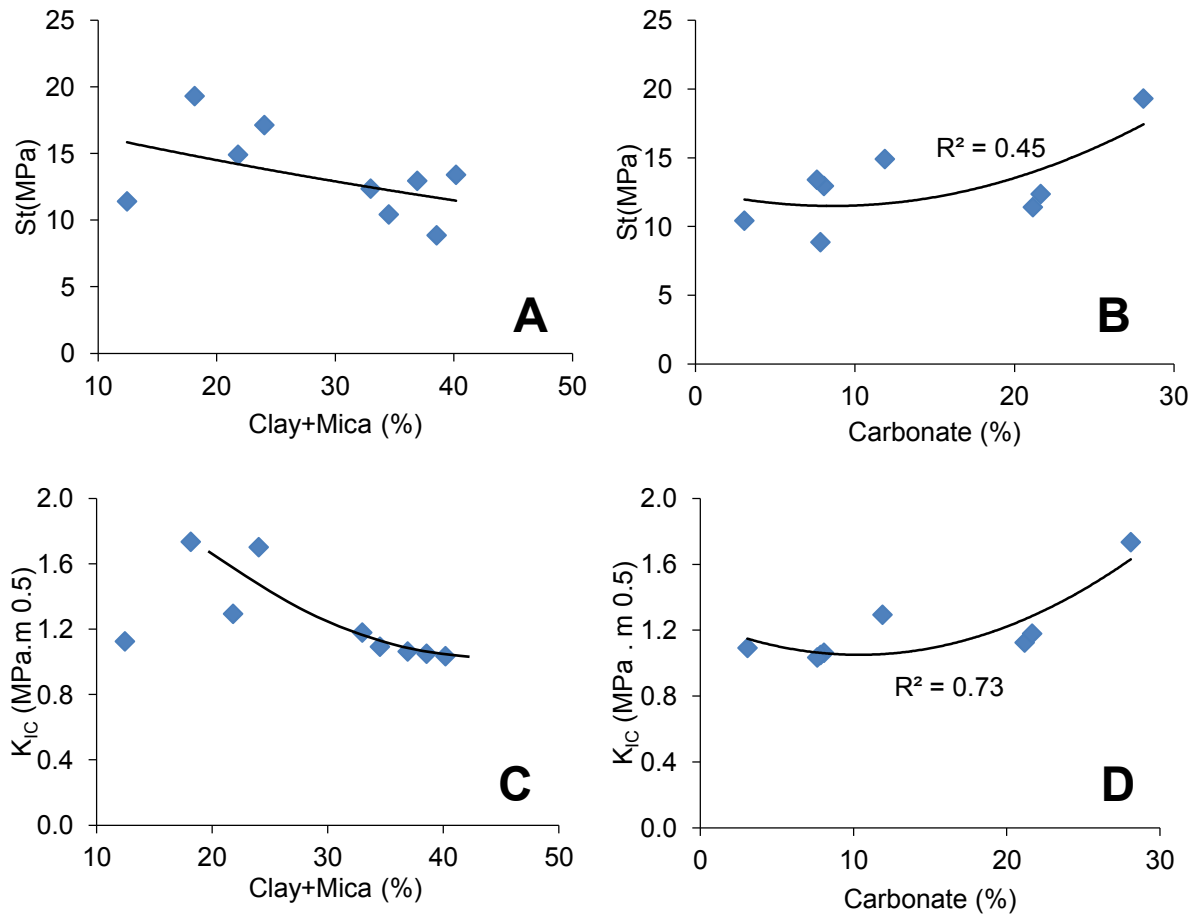


Figure 6.16 Tensile strength (St) and model I fracture toughness (K_{IC}), and their correlations with minerals.

6.5. Discussions

6.5.1. Mineralogy and Lithofacies: Implications for Sedimentary Environments

The Lower Cambrian shale is composed of a higher content of quartz-related minerals than the Lower Silurian shale, which is characterised by a relatively higher content of clay (Figure 6.2). The difference in mineral composition may reflect different depositional environments (Figure 6.17). The selected Lower Cambrian samples were deposited in restricted deep water marine platform to marine basin environments (Figure 6.17 B), whereas the Lower Silurian samples were formed in a more restricted marine basin environment (Figure 6.17 D).

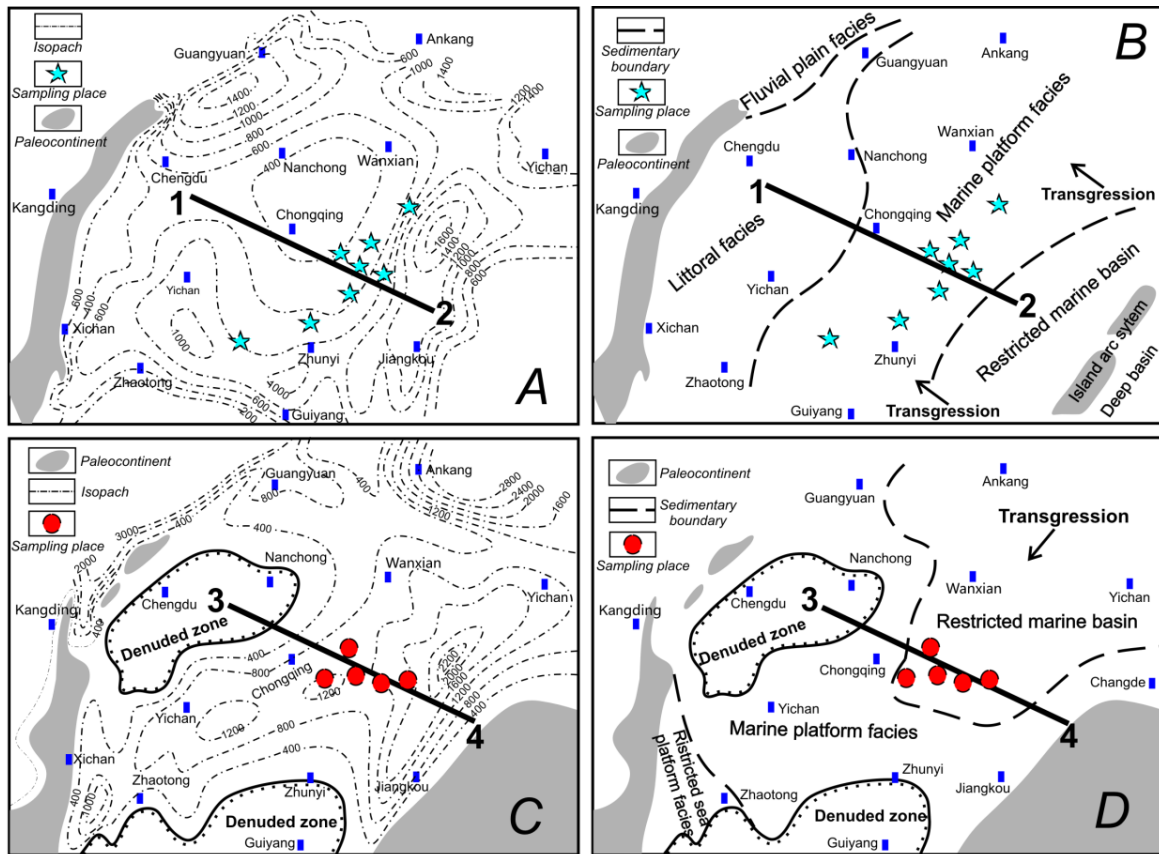


Figure 6.17 Thickness and sedimentary environments of the Lower Cambrian shale (A and B) and the Lower Silurian shale (C and D), modified after (Editorial Committee of the Sichuan Oil & Gas field, 1989).

During the Early Cambrian, the whole UYP could be considered a pericontinental marine shelf. The paleocontinent was located in the west, and the depositional environments gradually changed to a marine platform, restricted marine basin, former island arc system, and deep marine setting towards the southeast (Figures 6.17 B and 6.18 A). The presence of the island arc system most likely limited the interconnection of the UYP with open marine. The detrital components of the Lower Cambrian sediments were sourced from the paleocontinent in the west and island arc system in the southeast and deposited in restricted marine platform to marine basin settings during a major transgression from the southeast. This transgression resulted in flooding in the entire region, and the water depth increased to approximately 90-300 m (Zhang et al., 1996; Guo et al., 2011a). The anoxic bottom water conditions and a chemocline within the water column were present in most of places in the UYP (Goldberg et al., 2007), which are consistent with the extremely rare biturbation traces in our samples. The anoxic bottom water condition has been widely documented by previous studies. Steiner et al. (Steiner et al., 2001) reported that the anoxic condition or even euxinic condition in the bottom of the water column occurred in that period because the enrichment of trace elements,

e.g., V, Cd, Mo, U, and Se, are consistent with a hydrogenous precipitation under expanded anoxic, partly euxinic conditions. Moreover, the positive $\delta^{34}\text{S}$ values of sulfide, high degree of pyritization, high total organic carbon (TOC), and widespread phosphogenesis in the lowermost formation also reflected a largely anoxic and most likely sulfidic deeper water body (Goldberg et al., 2007). Phytoplankton and zooplankton blooms occurred in the surface water and provided high primary productivity of organic material, which could have gradually led to the bottom water anoxia caused by the aerobic degradation of organic matter during its passage to the sea floor (Demaison and Moore, 1980).

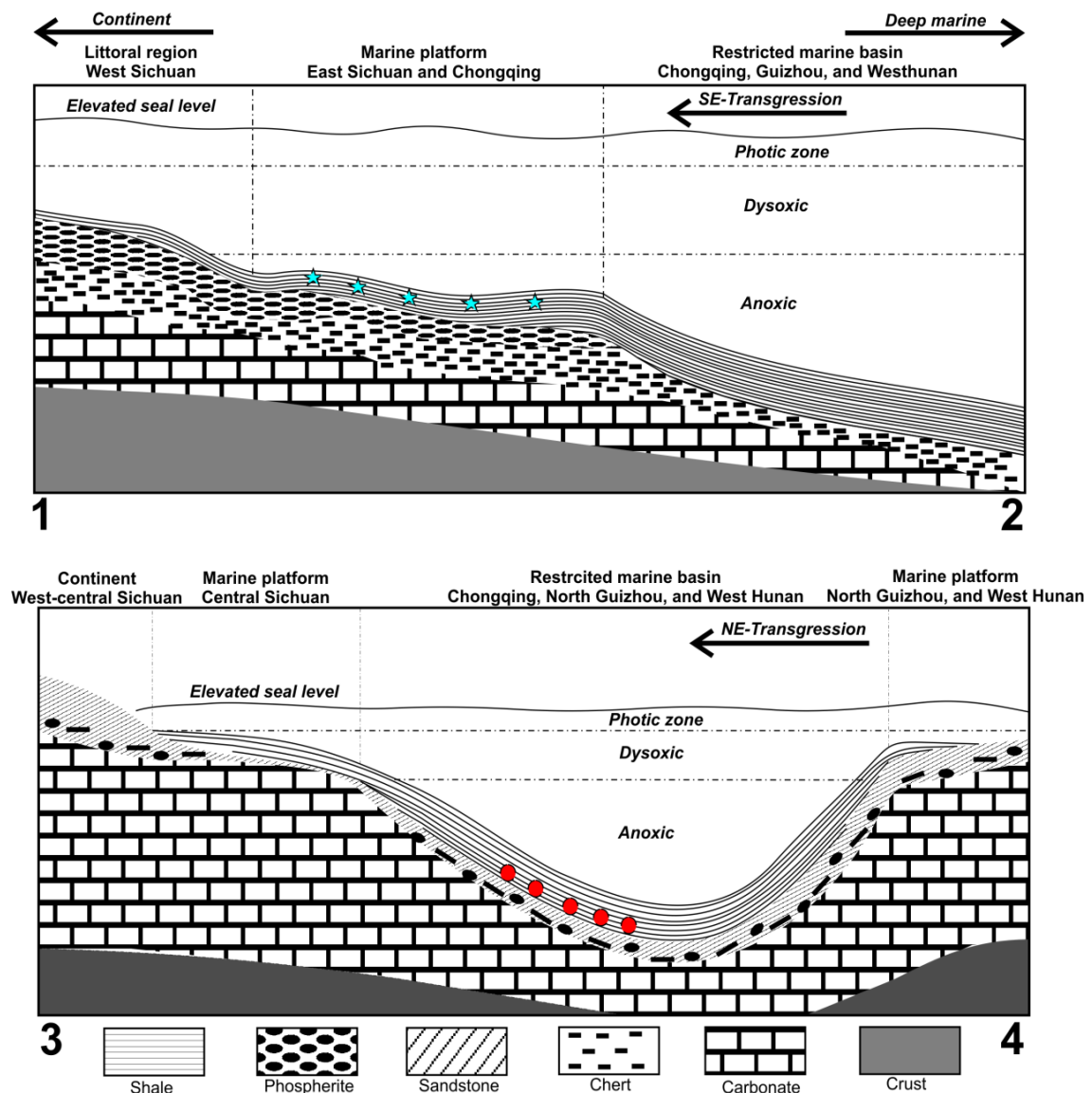


Figure 6.18 Depositional models of the lower Cambrian shale (upper) and the lower Silurian shale (lower), profiles and sampled places are denoted in Figure 6.17.

Chapter 6 Mineralogy, Lithofacies, Petrophysics, and Rock Mechanics

In the Early Silurian, however, most of the UYP region was covered by an epicontinental marine shelf, and the major transgression was from the northeast. Tectonic blocks to the west of the Sichuan Basin and in the north and southeast of the UYP uplifted. Thus, this area was more restricted than in the Early Cambrian and had sedimentary material sourced from a more diverse provenance (Figures 6.17 D and 6.18 B). The sedimentary region was dominated by a marine platform and a restricted marine basin, and the sedimentary conditions were characterised by low energy, reducing bottom water conditions, and slow sedimentation (Mu et al., 1981; Chen et al., 1987). It has been reported that the water depth reached approximately 60-200 m (Wang et al., 1997; Liang et al., 2009a).

Although the analyzed sediments can be classified into different lithofacies, mostly faint to well-laminated mudstone predominates, suggesting suspension settling as the main sedimentary mechanism (Loucks and Ruppel, 2007). Evidence of this mechanism includes the fine laminations and fine grain sizes. Many of the laminae are comprised of extrabasinal mineral, e.g., clay, quartz, and feldspar, whereas certain laminae are composed of intrabasinal mineral of mostly calcite or dolomite (Figures 6.3 and 6.4). These sediment particles were most likely transported from shallower water sources to the deeper basin floor. Three main processes are capable of eroding, transporting, and depositing these sediments: hemipelagic settling, bottom currents, and episodic re-sedimentation processes (Reading, 2009).

6.5.2. Porosity and Permeability of the Shale Reservoir

In general, pores provide storage space for free gas and surface area for sorbed gas, whereas permeability directly determines the capability of gas transport within pore networks. In shale gas systems, pores are commonly dominated by those with a diameter in the nm to μm scale, and pores within organic matter are widely documented as a significant contributor to pore networks (Loucks et al., 2009; Slatt and O'Brien, 2011; Chalmers et al., 2012; Curtis et al., 2012; Loucks et al., 2012; Milliken et al., 2013; Tian et al., 2013). Because a considerable amount of pores are organic matter-hosted while pore sizes approach nm scale, mechanisms of pore connectivity, gas storage, and gas transportation in the pore network are more complex compared to conventional petroleum systems. A large proportion of connected pores in highly porous organic matter could produce pathways for gas transportation within shale (Curtis et al., 2012). Although fractures and interconnected interparticle pores in the matrix are likely important contributors to the conductivity in a shale gas reservoir, in many cases, significant contributions can be attributed to interconnected organopores (Loucks et al.,

2012). The matrix permeability of shale is generally in the sub-nD to micro-Darcy (μD) range, and gas transport in the network is most likely controlled by a diffusion mechanism (Amann-Hildenbrand et al., 2012). In addition, the surface area becomes important and considerably influences the proportion of free gas and sorbed gas as well as the gas flow mechanism in the system (Ambrose et al., 2010). As organopores are able to account for as high as 62% of the total porosity of the Lower Silurian shale samples from the UYP (Tian et al., 2013), a significant portion of the total gas in-place appears to be associated with interconnected organopores. Such small pores can lead to different fluid phase behaviors or form different gas density profiles in the reservoir, and thus significantly impact the gas in-place evaluation of shale gas plays (Ambrose et al., 2012).

In this research, analyzed samples show extremely low permeability, which was confirmed by nm to μm scale observed pores (Figures 6.6 and 6.7) and low measured porosity (Figure 6.8). The pores with a diameter lower than 100 nm are major contributors to the total pore volume (Figure 6.9). The influences of organic matter on porosity are significant because observed pores or measured porosities are positively correlated with increases in the TOC, whereas the correlations between minerals and porosity are not remarkable. The results of this investigation are consistent with the results published by Tian et al (2013), who reported that the He-porosity of the selected Lower Silurian shales from the Sichuan Basin ranges from 2.6% to 4.7% and that the TOC shows positive correlations with both porosity and surface area (Tian et al., 2013). Extremely tight textures, however, lead to an extremely low permeability of the UYP shale and thus the measured intrinsic permeability coefficients of selected samples at a confining pressure of 30 MPa are lower than 20.2 nD ($2 \times 10^{-20} \text{m}^2$) (Figure 6.10). Similar measurements were performed on a series of shale samples from Germany (Possidonia), Sweden (Alum), Denmark (Alum), and the United States (Barnett) in the same laboratory, and the permeability coefficients ranged from 0.4 nD ($4 \times 10^{-22} \text{m}^2$) to 0.97 μD ($9.7 \times 10^{-17} \text{m}^2$) (Ghanizadeh et al., 2013a; Ghanizadeh et al., 2013b). In the current research, however, more systematic measurements are required because only four samples were measured; therefore, logical comparisons of the possible effects of TOC, maturity, minerals, moisture, temperature, and permeating fluids, among others on permeability are difficult to perform.

6.5.3. Physical Properties of the Shale Reservoir

Identifying mechanically brittle shale intervals may help in shale reservoir simulation, whereas rock mechanical parameters, e.g., Poisson's ratio and Young's modulus, helps identify ductile or brittle behavior (Grieser and Bray, 2007; Rickman et al., 2008). Rock

Chapter 6 Mineralogy, Lithofacies, Petrophysics, and Rock Mechanics

brittleness may be higher for shales with a high Young's modulus and low Poisson's ratio (Rickman et al., 2008), although the physical reason for this apparent correlation remains unclear. These parameters can be estimated from well logging data (Jacobi et al., 2009; Zhu et al., 2011) or directly measured in cores (Abousleiman et al., 2007; Sondergeld and Rai, 2011), and they commonly show close correlations with mineral composition as well as rock texture and fabric (Rickman et al., 2008; Britt and Schoeffler, 2009; Slatt and Abousleiman, 2011). Based on geomechanical investigations conducted on the eight shale gas plays in North America, Britt and Schoeffler (2009) suggested that prospective shales are those with a 1) limited amount of clay minerals of generally less than 40%, 2) static Young's modulus in excess of 20 GPa, and 3) fairly isotropic properties on the core plug scale.

As much as 50% of the Lower Silurian shales and 80% of the Lower Cambrian shales contain less than 40% clay minerals and a relatively high amount of brittle minerals. The measured compressive strength and Young's modulus are negatively correlated with the total amount of the weak constituents, e.g., clay, mica, and organic matter, and are positively correlated with the sum of carbonate and feldspar or the total amount of minerals that excludes the weak constituents. In contrast, the internal friction coefficient positively correlates with the constituents of clay, mica, and TOC, whereas it negatively correlates with carbonate or the total amount of minerals excluding the weak constituents (Figures 6.11 and 6.14). In addition, the tensile strength and model I fracture toughness are high but without an obvious correlation with any mineral constituents (Figure 6.16). Strong minerals, e.g., quartz, feldspar, and pyrite, imply a positive correlation with compressive strength and Young's modulus; nevertheless, this is not the case in this research because either quartz alone or the sum of strong minerals (quartz, feldspar, and pyrite) does not show any correlation with UCS, E, E12, and μ (Figure 6.19). Carbonate exhibits a positive correlation with the internal friction coefficient (Figure 6.14 D) but not with UCS, E, and E12 (Figure 6.19). Therefore, the rock mechanical properties of shale intrinsically rely on the overall composition and physical properties of the measured material, and simplified classifications may be misleading. The proxy of brittleness, e.g., the ternary plot of mineral constituents, should be used carefully.

Our samples deformed at room temperature and show brittle behavior with up to 36 MPa confining pressure (Figures 6.11-6.14). Although the compressive strength and Young's moduli of the Lower Cambrian shales are higher than for the Lower Silurian shales, both shale types show brittle behavior. This suggests that the value of Young's modulus alone is not indicative of the 'brittleness'. The measured Poisson's ratio of the Lower Cambrian shale is 0.25 and of the Lower Silurian shale is 0.33, whereas the reported values range from 0.18 to

0.26, respectively (Chen and Jin, 2012; Huang et al., 2012b; Li et al., 2012c). However, half of the measured samples in this research were collected from outcrops, which may have altered the rock mechanical properties because of conditions such as weathering. In addition, the mechanical behavior is expected to be more ductile at in-situ temperatures because they facilitate plastic deformation processes. Detailed well logging was performed in a well in the Weiyuan gas field, Sichuan Basin, using techniques such as caliper, electric resistivity, gamma ray, sonic, radioelement, elemental capture spectroscopy sonde, and so on; thus, a series of lithological, petrophysical, and rock mechanical parameters were estimated (Wu et al., 2011; Chen and Jin, 2012; Li et al., 2012c). The results indicate that in the selected interval, the bottom zone shows an obviously higher concentration of brittle minerals, TOC and uranium content, and Young's moduli, and lower values of Poisson's ratio and densities compared to the upper zone. However, the calculation of the so-called "brittle index" in these studies (Wu et al., 2011; Chen and Jin, 2012; Li et al., 2012c) is uncertain because the experience from the Barnett Shale was arbitrarily applied to the black shale intervals in south China.

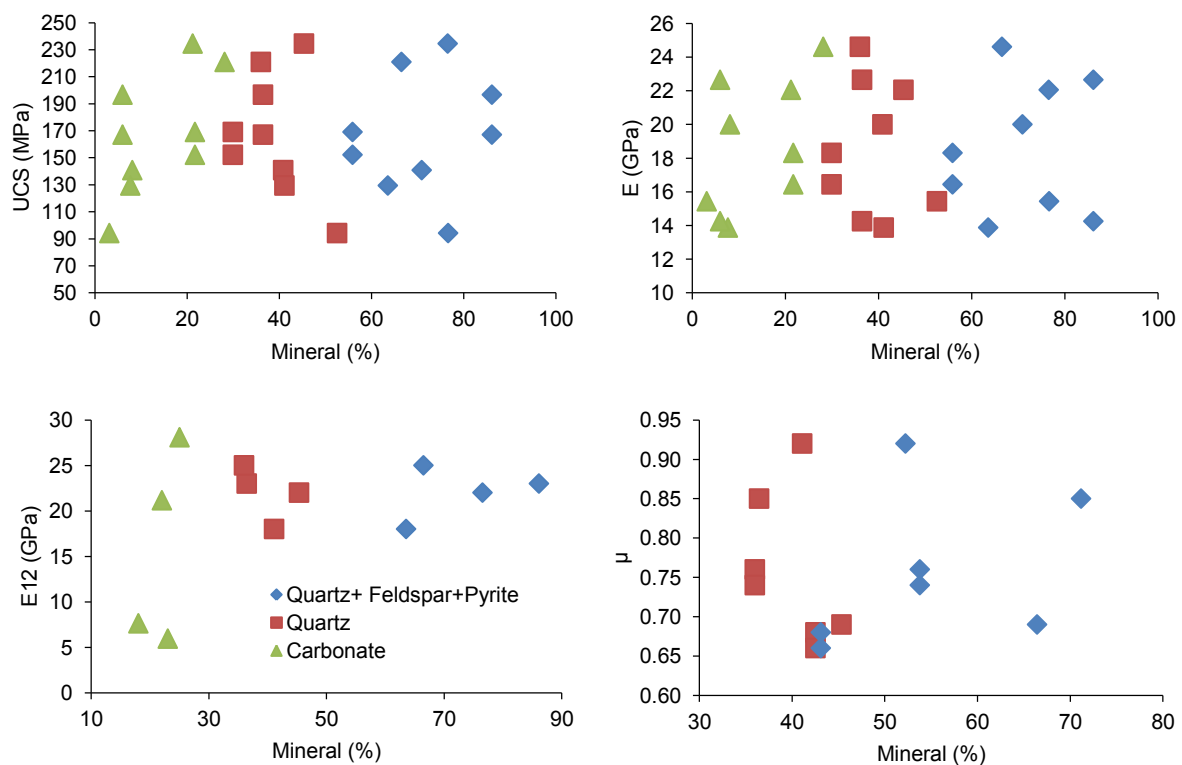


Figure 6.19 Measured rock mechanical parameters vs. minerals. In contrast to Figure 13 and 15, no correlations can be observed in these plots because a different mineral grouping method, e.g., clay, mica, and organic matter represent weak constituents; quartz, feldspar, and pyrite represent strong constituents; and carbonates are in between the weak and strong constituents.

6.6. Conclusions

Investigations of mineralogical composition, lithofacies, petrophysics, and rock mechanics on selected samples from the Ediacaran, Lower Cambrian, and Lower Silurian intervals at the UYP indicate the following:

1) Minerals typical of siliciclastic sediments (quartz, feldspar, and pyrite) dominate in the analyzed formations. Clay minerals occur in moderate concentrations, whereas carbonates are generally rare or absent. Furthermore, the Ediacaran and Lower Cambrian shales generally possess more siliceous minerals and less clay mineral than the Lower Silurian shales.

2) Lithofacies analysis revealed that laminated and non-laminated siliceous mudstones predominate, and there are minor contributions from calcareous shale-mudstone and others. The Ediacaran and Lower Cambrian shales were deposited in restricted deep-water marine platform to marine basin environments, whereas the Lower Silurian shales were deposited in a more restricted marine basin environment. Nevertheless, the high TOC content in all formations are a consequence of bottom water anoxia devoid of significant bioturbation.

3) Most samples show an extremely tight matrix characterised by nm to μm scale pores, Hg-porosity lower than 1%, and He-porosity ranging from 1% to 4%, with only a few samples having a porosity value in excess of 10%. The porosity and the pore volume is significantly dependent on the occurrence of pores with a diameter lower than 100 nm. Numerous small pores are within the organic matter; therefore, the porosity correlates positively with TOC content and not with mineral content. The intrinsic matrix permeability coefficients measured on four plugs at 30 MPa confining pressure are less than 20.2 nD ($2 \times 10^{-20} \text{m}^2$). Compared to the production of shale gas plays in the U.S., the matrix permeability is rather low.

4) The rock mechanical measurements are characterised by high compressive strength, Young's modulus, tensile strength, and mode I fracture toughness but low Poisson's ratio. Consistent with mineral properties, the Lower Cambrian shale is commonly more brittle than the Lower Silurian shale. Nevertheless, the rock mechanical properties of the measured samples depend on the overall compositions and physical features.

In terms of the petrophysical and rock mechanical properties of rocks that have such low porosity and permeability, a much larger dataset is required to account for the

heterogeneity of rocks and variation of rock physical properties at the reservoir scale. On the other hand, fluid transport processes in these types of rocks are still poorly understood. In practice, such measurements are technically difficult and sensitive to experimental conditions and sample quality. Nevertheless, the measurements and results attained in this research significantly contribute to the understanding of the hot black shale formations in south China and the amount of published data.

6.7. Acknowledgements

We are grateful to Statoil for funding and publication permission. The authors thank Drs. Rudolf Naumann, Helga Kemnitz, Richard Wirth, and Andreas Reinicke (GFZ-Potsdam) for their help on XRD, SEM, TEM, and Rock mechanics, and Amin Ghanizadeh and Alexej Merkel (RWTH Aachen) for their help on petrophysical measurement and sample preparation.

Chapter 7 Summary and Outlook

The objective of this dissertation is to evaluate the gas-in-place and fraccability of the Ediacaran, Lower Cambrian, and Lower Silurian marine shale formations in the UYP, south China. These assessments of resource potential and developmental prospect inherently relate to the geological setting, organic geochemical characteristics, petroleum physical properties, methane sorptive capacity, mineralogical constituents, lithofacies, petrophysical features, and rock mechanical properties. It can be concluded that the major tasks were completed in the course of the project, and the research objectives were achieved.

7.1. Summary

7.1.1. Geological Characterisation

The Ediacaran, Lower Cambrian, and Lower Silurian black shale intervals were deposited during three major transgressions of the Late Proterozoic and Early Paleozoic. The sedimentary environments were dominated by open- to restricted-marine shelves with deep-water conditions resulting from sea level highstands, and hence oxygen and biomass were extremely lack. The Lower Cambrian shale is distributed throughout most of the UYP and is particularly thick in the southeast Sichuan Basin, Chongqing, north Guizhou, west Hunan, and west Hubei. The Lower Silurian shale, however, is primarily confined to the central UYP, where it underlies the southeast Sichuan Basin and Chongqing area. The depths vary significantly. There are outcrops along the margins of the Sichuan Basin and in the southeast UYP, whereas black shale is encountered at depths exceeding 5000 m in certain depressions. The mineralogy and organic matter vary in upward succession in both the Lower Cambrian and Lower Silurian formations, such that high-TOC black shale is typically situated in the bottom parts, whereas the upper intervals consists of the low-TOC grey shale, siltstone, or carbonate.

7.1.2. Organic Geochemical Properties

The TOC contents in the analysed samples generally exceed 2% and average 5%, and they increase with geological age. For example, the TOC levels in the Lower Silurian shale are lower than those in the Lower Cambrian shale, which are in turn lower than those in the Ediacaran shale in general. The thermal maturity of the kerogen indicates metagenesis, based on the visible organic matter, bitumen reflectance, and $\delta^{13}\text{C}$ of methane. On the basis of the $\delta^{13}\text{C}$ of the methane and the basin modelling results, extrapolated vitrinite reflectances (R_o) of 2.5-3.0% for the Lower Silurian shale, 3.0-3.5% for the Lower Cambrian shale, and 3.5-4.0% for the Ediacaran shale were found. T_{vap}-GC and open py-GC analyses indicate extremely low remaining generated hydrocarbon and low remaining generative potential, and the products are qualitatively dominated by the light hydrocarbons.

Artificially and naturally matured samples from other countries were evaluated to determine the evolution of the kerogen and hydrocarbon generation properties with increases in the temperature and T_{max} and to reveal the origin of the kerogen type of the UYP shale. The organic matter of the UYP shale most likely is predominantly type I original kerogen, which may have formed in a marine environment via selective accumulation of algal material, based on the $\delta^{13}\text{C}$ ratios in the methane, kerogen, and chloroform bitumen and the correlations with the Australian shale in terms of the aromatic generation and aromaticity evolution with the increase in the T_{max} . The original petroleum potential and original organic status were calculated and reconstructed using Cooles' and Claypool's equation. Excellent original hydrocarbon potential was revealed, based on the values of TOC_o between 5% and 23% and S_{1o}+S_{2o} between 29 and 215 mg HC/g rock.

7.1.3. Petroleum Physical Properties in the Shale Reservoir

Based on the adjacent tectonic position and comparable Cambrian geology of north Australia and south China, an immature Cambrian Shale sample from the Georgina Basin was used to investigate the petroleum generation kinetics of the Lower Cambrian shale in the UYP, as well as petroleum phase evolution within an unconventional shale reservoir in this formation. The analysis on source rock characteristics suggested a type II kerogen and an organofacies inferring paraffinic-naphthenic-aromatic low wax oil generation. Hydrocarbon generation can be described by a single frequency factor of $A=8.429\text{E}+14$ 1/sec and an activation energy distribution ranging from 44 to 67 kcal/mol. The main activation energy of 56 kcal/mol is higher than commonly assumed oil and gas formation from marine, clastic

Chapter 7 Summary and Outlook

source rocks, and indicated presence of marine but highly stable, sulphur-poor organic matter in the Cambrian shale. The onset temperature of hydrocarbon generation (TR=10%) is ~120°C, while end of generation (TR=90%) can be expected for temperatures around 165°C for a geological heating rate of 1.5 °C/Ma.

Phase behaviour properties for onset and end of bulk hydrocarbon generation from kerogen can be described by a GOR of 63Sm³/Sm³, P_{sat} of 101bar and B_o of 1.2 m³/Sm³ at 10% TR, and a GOR of 176 Sm³/Sm³, P_{sat} of 189 bar and B_o of 1.61 m³/Sm³ at 90% TR. Onset occurred in the Middle Triassic (241 ma) at burial depths around 2000 m for temperature close to 120°C. Before 203 ma, for temperatures <145°C, burial depth <3300 m, and TR <50%, phase behaviour of generated black oil was defined by primary product evolution. Secondary cracking of oil to gas predominated with increasing burial depth and temperature in Middle-Late Jurassic times. Kerogen conversion was completed in the Early Jurassic (187 ma) at depths close to 4000 m and temperatures around 165°C.

In the Lower Cambrian shale reservoir, bubble point pressure was much lower than the reservoir pressure during the whole maturation process. Unconventional shale resources can therefore only be present as a single phase, and were dominated by a single liquid phase (black oil and volatile oil) during the primary generation process and a single vapor phase (wet gas and dry gas) during secondary cracking processes.

7.1.4. Methane Sorption Capacity

The high-pressure (up to 25 MPa) methane sorption isotherms were measured for shale samples from the Lower Silurian and Lower Cambrian formations in the UYP. The results indicate that the excess methane sorption capacity of the Lower Silurian shale is between 0.045 and 0.064 mmol/g rock and that of the Lower Cambrian shale is between 0.036 and 0.210 mmol/g rock. The measured isotherms can be well fitted by the corrected Langmuir function. The Langmuir sorption capacity is between 0.096 and 0.115 mmol/g rock for the Lower Silurian shale, whereas it ranges from 0.077 to 0.310 mmol/g rock for the Lower Cambrian shale. The shape of the sorption isotherms and sorption capacity vary from sample to sample and might be affected by the TOC content, thermal maturity, clay minerals, moisture content, particle size, pore properties, as well as the measured temperature and pressure conditions.

Under the measured pressure range, the sorption capacity of selected immature AU Cambrian samples increases monotonously with increasing pressure, whereas that of UYP

Chapter 7 Summary and Outlook

overmature samples shows a maxima during a pressure range of 8.8-14.2 MPa. The TOC content shows a significant effect on methane sorption capacity. With a TOC content increase, the sorption capacity increases positively, exhibiting a distinct linear correlation. The TOC-normalised sorption values increase positively with thermal maturity. In contrast, the corresponding pressure of the maximum excess sorption and Langmuir pressure clearly decrease with thermal maturity. The effect of clay minerals is clearly revealed by the TOC-normalised sorption values; however, it showed relatively less of an effect compared to the TOC content. The measured samples have a moisture content between 0.43 and 2.28%, which reduces the impact of clay minerals on the sorption capacity. The measured high TOC content sample shows a high total cumulative pore volume, surface area, total porosity, and thus higher sorption capacity compared to the similar mature sample that has less TOC. In addition, the particle size has a slight effect on the sorption capacity.

The T_{vap}-GC measured gas hydrocarbons are characterised by extremely low detectable quantities between 9.8 and 29.0 µg/g rock (0.5-1.4 mg/g TOC) of the Lower Silurian core samples and between 2.5 and 20.8 µg/g rock (0.02-0.34 mg/g TOC) of the Lower Cambrian and Ediacaran outcrop samples. Contrary to the sorption isotherms, the TOC content is negatively correlated with the measured gas, which most likely was impacted by weathering processes. Nevertheless, clay minerals show a strong effect on the T_{vap}-GC results.

7.1.5. Mineralogy and Lithofacies

Investigations of mineralogical composition and lithofacies on selected samples from the Ediacaran, Lower Cambrian, and Lower Silurian intervals at the UYP indicate the following:

Minerals typical of siliciclastic sediments (quartz, feldspar, and pyrite) dominate in the analyzed formations. Clay minerals occur in moderate concentrations, whereas carbonates are generally rare or absent. Furthermore, the Ediacaran and Lower Cambrian shales generally possess more siliceous minerals and less clay mineral than the Lower Silurian shales.

Lithofacies analysis revealed that laminated and non-laminated siliceous mudstones predominate, and there are minor contributions from calcareous shale-mudstone and others. The Ediacaran and Lower Cambrian shales were deposited in restricted deep-water marine platform to marine basin environments, whereas the Lower Silurian shales were deposited in a

more restricted marine basin environment. Nevertheless, the high TOC content in all formations are a consequence of bottom water anoxia devoid of significant bioturbation.

7.1.6. Petrophysical and Rock Mechanical Properties

Most investigated samples show an extremely tight matrix characterised by nm to μm scale pores, Hg-porosity lower than 1%, and He-porosity ranging from 1% to 4%, with only a few samples having a porosity value in excess of 10%. The porosity and the pore volume is significantly dependent on the occurrence of pores with a diameter lower than 100 nm. Numerous small pores are within the organic matter; therefore, the porosity correlates positively with TOC content and not with mineral content. The intrinsic matrix permeability coefficients measured on four plugs at 30 MPa confining pressure are less than 20.2 nD ($2 \times 10^{-20} \text{m}^2$). Compared to the production of shale gas plays in the U.S., the matrix permeability is rather low.

The rock mechanical measurements are characterised by high compressive strength, Young's modulus, tensile strength, and mode I fracture toughness but low Poisson's ratio. Consistent with mineral properties, the Lower Cambrian shale is commonly more brittle than the Lower Silurian shale. Nevertheless, the rock mechanical properties of the measured samples depend on the overall compositions and physical features.

7.2. Outlook

Shale gas in China is still in its infancy. The measurements conducted and results achieved in this research thus could contribute to the understanding on these hot black shale formations in south China and greatly add to what is known from other published data. Nevertheless, more detailed investigations are necessary, and the issues listed in the following paragraphs should be addressed in the future research.

First of all, more detailed geological investigation is needed. Compared to the successful shale gas plays in the United States (e.g., the Barnett and Marcellus shale), these marine shale formations are characterised by their old geological age, from Ediacaran to Early Paleozoic, and complicated geological evolution history, successively impacted by the Caledonian, Indosinian, Yanshanian, and Himalayan tectonic movements. These geological events should have significantly altered the geological distribution of shale formations in the UYP, and hence black shales can be found from surface to more than 5000 m deep. Tectonic

Chapter 7 Summary and Outlook

movements also produce faults and structural highs and lows, which may significantly impact the hydrocarbon generation, migration, and storage capability of reservoir and source rocks. In addition, in essentially all organic rich shales, the basic building blocks conform to well understood sedimentary geology, stratigraphic controls, and architectures (Passey et al., 2010). The rigorous characterisation of these geological packages allows for the understanding and exploration of the best intervals.

Secondary, the heterogeneity of shale reservoirs must be taken into account. Although the thickness of these organic rich intervals in the UYP can be higher than a hundred meters, vertical variability in TOC is generally high. Concerning the investigation of petrophysical and rock mechanical properties of rocks that have such low porosity and permeability, a much larger dataset is required to account for the heterogeneity of rocks and variation of rock physical properties at the reservoir scale. In addition, fluid transport processes in these types of rocks are still poorly understood, and such measurements are technically difficult and sensitive to experimental conditions and sample quality.

Moreover, the investigation of original type and composition of the organic matter is fraught with difficulty because of the high thermal maturity. Methods like stable isotope ratio and biomarker may provide more information to clarify these questions. The reconstruction of the original TOC content needs a more rigorous model, while limitations of the applied model of hydrocarbon generation exist with respect to petroleum expulsion since generated hydrocarbons were regarded as retained petroleum.

References

- Abouelresh, M.O. and Slatt, R.M., 2012. Lithofacies and sequence stratigraphy of the Barnett Shale in east-central Fort Worth Basin, Texas. *AAPG Bulletin*, 96(1): 1-22.
- Abousleiman, Y., Tran, M., Hoang, S., Bobko, C., Ortega, A. and Ulm, F.-J., 2007. Geomechanics field and laboratory characterization of the Woodford Shale: The next gas play, SPE Annual Technical Conference and Exhibition.
- Amann-Hildenbrand, A., Ghanizadeh, A. and Krooss, B.M., 2012. Transport properties of unconventional gas systems. *Marine and Petroleum Geology*, 31(1): 90-99.
- Ambrose, G.J., Kruse, P.D. and Putnam, P.E., 2001. Geology and hydrocarbon potential of the southern Georgina Basin, Australia. *APPEA Journal*, 41(1): 139-163.
- Ambrose, G.J. and Putnam, P.E., 2005. Carbonate ramp facies and oil plays in the Middle–Late Cambrian, southern Georgina Basin, Australia. In: T.J. Munson and G.J. Ambrose (Editors), *Proceedings of the Central Australian Basins Symposium (CABS)*. Northern Territory Geological Survey, Alice Springs, Northern Territory, Australia, pp. 236-253.
- Ambrose, G.J. and Putnam, P.E., 2007. Carbonate ramp facies and oil plays in the Middle–Late Cambrian, southern Georgina Basin, Australia. In: T.J. Munson and G.J. Ambrose (Editors), *Proceedings of the Central Australian Basins Symposium (CABS)*. Northern Territory Geological Survey, Alice Springs, Northern Territory, Australia, pp. 236-253.
- Ambrose, R., Hartman, R., Diaz-Campos, M., Akkutlu, I.Y. and Sondergeld, C., 2012. Shale gas-in-place calculations part I: New pore-scale considerations. *SPE Journal*, 17(1): 219-229.
- Ambrose, R., Hartman, R., diaz campos, m., Akkutlu, I.Y. and Sondergeld, C., 2010. New pore-scale considerations for shale gas in place calculations, SPE Unconventional Gas Conference.
- Aringhieri, R., 2004. Nanoporosity characteristics of some natural clay minerals and soils. *Clays and clay minerals*, 52(6): 700-704.
- Beamish, B. and Crosdale, P., 1995. The influence of maceral content on the sorption of gases by coal and the association with outbursting, International symposium-cum-workshop on management and control of high gas emissions and outbursts in underground coal mines: Wollongong, Australia, National Organising Committee of the Symposium, pp. 353-361.
- Behar, F., Beaumont, V. and De B. Penteado, H.L., 2001. Technologie Rock-Eval 6 : performances et développements. *Oil & Gas Science and Technology - Rev. IFP*, 56(2): 111-134.
- Behar, F., Vandenbroucke, M., Tang, Y., Marquis, F. and Espitalie, J., 1997. Thermal cracking of kerogen in open and closed systems: determination of kinetic parameters and stoichiometric coefficients for oil and gas generation. *Organic Geochemistry*, 26(5–6): 321-339.
- Bennett, P.J., Philipchuk, P. and Freeman, A., 2010. Arthur Creek “hot shale”: A Bakken unconventional oil analogy in the Georgina Basin of Northern Territory, Australia, AAPG International Conference and Exhibition, Calgary, Canada.
- Bertrand, R., 1993. Standardization of solid bitumen reflectance to vitrinite in some Paleozoic sequences of Canada. *Energy Sources*, 15(2): 269-287.
- Bhullar, A.G., di Primio, R., Karlsen, D.A. and Gustin, D.-P., 2003. Determination of the timing of petroleum system events using petroleum geochemical, fluid inclusion, and PVT data: An example from the Rind Discovery and Frøy Field, Norwegian North Sea. In: S. Düppenbecker and R. Marzi (eds.), *Multidimensional basin modeling*, AAPG/Datapages Discovery Series No. 7, p. 123-135.
- Bieniawski, Z. and Hawkes, I., 1978. Suggested methods for determining tensile strength of rock materials. *International Journal of Rock Mechanics and Mining Sciences & Geomechanics Abstracts*, 15(3): 99-103.
- Boreham, C.J. and Ambrose, G.J., 2007. Cambrian petroleum systems in the southern Georgina Basin, Northern Territory, Australia. In: T.J. Munson and G.J. Ambrose (Editors), *Proceedings of the Central Australian Basins Symposium (CABS)*. Northern Territory Geological Survey, Alice Springs, Northern Territory, Australia, pp. 254-281.
- Boreham, C.J., Edwards, D.S., Hall, L., Bernecker, T., Carr, L.K., Chen, J., Smith, T.E., Laurie, J., Stacey, A., Tan, J. and Horsfield, B., 2013. Unconventional Middle Cambrian petroleum systems in the Georgina Basin, Australia, *Fundamental Controls on Petroleum Systems in Lower Paleozoic and Older Strata*. AAPG Hedberg Conference, Beijing, China.
- Bowker, K.A., 2007. Barnett Shale gas production, Fort Worth Basin: Issues and discussion. *AAPG Bulletin*, 91(4): 523-533.

References

- Bratovich, M. and Sommer, D., 2009. Application of an integrated petrophysical evaluation approach to North American shale gas reservoirs, SPWLA 2nd India Regional Symposium SPWLA, India, pp. 1-14.
- Braun, R.L. and Burnham, A.K., 1992. PMOD: a flexible model of oil and gas generation, cracking, and expulsion. *Organic Geochemistry*, 19(1-3): 161-172.
- Britt, L. and Schoeffler, J., 2009. The geomechanics of a shale play: What makes a shale prospective, SPE Eastern Regional Meeting.
- Buchardt, B. and Lewan, M., 1990. Reflectance of vitrinite-like macerals as a thermal maturity index for Cambrian-Ordovician Alum shale, southern Scandinavia (1). *AAPG Bulletin*, 74(4): 394-406.
- Buller, D., Hughes, S., Market, J., Petre, J., Spain, D. and Odumosu, T., 2010. Petrophysical evaluation for enhancing hydraulic stimulation in horizontal shale gas wells, SPE Annual Technical Conference and Exhibition.
- Burnham, A.K., Braun, R.L., Gregg, H.R. and Samoun, A.M., 1987. Comparison of methods for measuring kerogen pyrolysis rates and fitting kinetic parameters. *Energy & Fuels*, 1(6): 452-458.
- Bustin, R.M., Bustin, A., Ross, D., Chalmers, G., Murthy, V., Laxmi, C. and Cui, X., 2009. Shale gas opportunities and challenges. *Search and Discovery Articles*, 40382: 20-23.
- Bustin, R.M. and Clarkson, C.R., 1998. Geological controls on coalbed methane reservoir capacity and gas content. *International Journal of Coal Geology*, 38(1-2): 3-26.
- Carles, P., Egermann, P., Lenormand, R. and Lombard, J., 2007. Low permeability measurements using steady-state and transient methods, International symposium of the SCA.
- Carter, K.M., Harper, J.A., Schmid, K.W. and Kostelnik, J., 2011. Unconventional natural gas resources in Pennsylvania: The backstory of the modern Marcellus Shale play. *Environmental Geosciences*, 18(4): 217-257.
- Chalmers, G.R. and Bustin, R.M., 2007a. On the effects of petrographic composition on coalbed methane sorption. *International Journal of Coal Geology*, 69(4): 288-304.
- Chalmers, G.R. and Bustin, R.M., 2007b. The organic matter distribution and methane capacity of the Lower Cretaceous strata of northeastern British Columbia, Canada. *International Journal of Coal Geology*, 70(1): 223-239.
- Chalmers, G.R., Bustin, R.M. and Power, I.M., 2012. Characterization of gas shale pore systems by porosimetry, pycnometry, surface area, and field emission scanning electron microscopy/transmission electron microscopy image analyses: Examples from the Barnett, Woodford, Haynesville, Marcellus, and Doig units. *AAPG Bulletin*, 96(6): 1099-1119.
- Chalmers, G.R.L. and Bustin, R.M., 2008. Lower Cretaceous gas shales in northeastern British Columbia, Part I: geological controls on methane sorption capacity. *Bulletin of Canadian Petroleum Geology*, 56(1): 1-21.
- Chen, M. and Jin, Y., 2012. Shale gas fracturing technology parameters optimization based on core analysis. *Petroleum Drilling Techniques*, 40(4): 7-12.
- Chen, S., Zhu, Y., Wang, H., Liu, H., Wei, W. and Fang, J., 2011. Characteristics and significance of mineral compositions of Lower Silurian Longmaxi Formation shale gas reservoir in the southern margin of Sichuan Basin. *Acta Petrolei Sinica*, 32(5): 775-782.
- Chen, W., Zhou, W., Luo, P., Deng, H., Li, Q., Shan, R. and Qi, M., 2013. Analysis of the shale gas reservoir in the Lower Silurian Longmaxi Formation, Changxin1 well, southeast Sichuan Basin, China. *Acta Petrological Sinica*, 29(3): 1073-1086.
- Chen, X., Xiao, C. and Chen, H., 1987. Wufengian (Ashgillian) graptolite faunal differentiation and anoxic environment in south China. *Acta Palaeontologica Sinica*, 26: 338-352.
- Chen, Z., 2011. Exploration for shale gas of Longtan Member in Permian Leping Formation, Sichuan Basin. *Natural Gas Technology and Economy*, 5(2): 21-27.
- Cheng, A.-L. and Huang, W.-L., 2004. Selective adsorption of hydrocarbon gases on clays and organic matter. *Organic Geochemistry*, 35(4): 413-423.
- Cheng, K., Wang, S., Dong, D., Huang, J. and Li, X., 2009. Accumulation conditions of shale gas reservoirs in the Lower Cambrian Qiongzhusi Formation, the Upper Yangtze Region. *Natural Gas Industry*, 29(5): 40-44.
- Chung, H.M., Gormly, J.R. and Squires, R.M., 1988. Origin of gaseous hydrocarbons in subsurface environments: Theoretical considerations of carbon isotope distribution. *Chemical Geology*, 71(1-3): 97-104.
- Clarkson, C. and Bustin, R., 1999a. The effect of pore structure and gas pressure upon the transport properties of coal: a laboratory and modeling study. 1. Isotherms and pore volume distributions. *Fuel*, 78(11): 1333-1344.
- Clarkson, C. and Bustin, R., 1999b. The effect of pore structure and gas pressure upon the transport properties of coal: a laboratory and modeling study. 2. Adsorption rate modeling. *Fuel*, 78(11): 1345-1362.
- Clarkson, C., Jensen, J. and Blasingame, T., 2011. Reservoir engineering for unconventional reservoirs: What do we have to consider?, North American Unconventional Gas Conference and Exhibition.

References

- Clarkson, C.R. and Bustin, R.M., 2000. Binary gas adsorption/desorption isotherms: effect of moisture and coal composition upon carbon dioxide selectivity over methane. *International Journal of Coal Geology*, 42(4): 241-271.
- Clayton, C., 1991. Carbon isotope fractionation during natural gas generation from kerogen. *Marine and Petroleum Geology*, 8(2): 232-240.
- Clayton, J. and King, J., 1987. Effects of weathering on biological marker and aromatic hydrocarbon composition of organic matter in Phosphoria shale outcrop. *Geochimica et Cosmochimica Acta*, 51(8): 2153-2157.
- Clayton, J.L. and Swetland, P.J., 1978. Subaerial weathering of sedimentary organic matter. *Geochimica et Cosmochimica Acta*, 42(3): 305-312.
- Cooles, G., Mackenzie, A. and Quigley, T., 1986. Calculation of petroleum masses generated and expelled from source rocks. *Organic Geochemistry*, 10(1): 235-245.
- Crosdale, P.J., Beamish, B. and Valix, M., 1998. Coalbed methane sorption related to coal composition. *International Journal of Coal Geology*, 35(1): 147-158.
- Curtis, J.B., 2002. Fractured Shale-Gas Systems. *AAPG Bulletin*, 86(11): 1921-1938.
- Curtis, M.E., Sondergeld, C.H., Ambrose, R.J. and Rai, C.S., 2012. Microstructural investigation of gas shales in two and three dimensions using nanometer-scale resolution imaging. *AAPG Bulletin*, 96(4): 665-677.
- Dai, J., 2003. Pool forming periods and gas sources of Weiyuan gas field. *Petroleum Geology & Experiment*(05): 473-480.
- Dai, J., Liu, D. and Gao, G., 2003. Discovery of marine muddy hydrocarbon source rocks in the southern margin of the North China Block and its significance for gas exploration. *Geological Review*, 49(3): 322-329.
- Dai, J., Ni, Y., Zou, C., Tao, S., Hu, G., Hu, A., Yang, C. and Tao, X., 2009. Stable carbon isotopes of alkane gases from the Xujiache coal measures and implication for gas-source correlation in the Sichuan Basin, SW China. *Organic Geochemistry*, pp. 638-646.
- Dai, J., Pei, X. and Qi, H., 1992. *China Natural Gas Geology*. Petroleum Industry Press, 298 pp.
- Dai, J., Xia, X., Qin, S. and Zhao, J., 2004. Origins of partially reversed alkane $\delta^{13}\text{C}$ values for biogenic gases in China. *Organic Geochemistry*, 35(4): 405-411.
- Day, S., Sakurovs, R. and Weir, S., 2008. Supercritical gas sorption on moist coals. *International Journal of Coal Geology*, 74(3-4): 203-214.
- Demaison, G. and Moore, G., 1980. Anoxic environments and oil source bed genesis. *Organic Geochemistry*, 2(1): 9-31.
- di Primio, R., Dieckmann, V. and Mills, N., 1998. PVT and phase behaviour analysis in petroleum exploration. *Organic Geochemistry*, 29(1-3): 207-222.
- di Primio, R. and Horsfield, B., 2006. From petroleum-type organofacies to hydrocarbon phase prediction. *AAPG Bulletin*, 90(7): 1031-1058.
- di Primio, R. and Neumann, V., 2008. HPHT reservoir evolution: a case study from Jade and Judy fields, Central Graben, UK North Sea. *International Journal of Earth Sciences*, 97(5): 1101-1114.
- di Primio, R. and Skeie, J.E., 2004. Development of a compositional kinetic model for hydrocarbon generation and phase equilibria modelling: a case study from Snorre Field, Norwegian North Sea. *Geological Society, London, Special Publications*, 237(1): 157-174.
- Diaz, H.G., Miller, C. and Lewis, R., 2012. sCore: A classification scheme for organic mudstones based on bulk mineralogy, Search and Discovery Article. AAPG, Ft. Worth, Texas.
- Diaz, H.G., Miller, C., Lewis, R. and Fuentes, C.C., 2013. Evaluating the impact of mineralogy on reservoir quality and completion quality of organic shale plays, Search and Discovery Article. AAPG, Salt Lake City, Utah.
- Dieckmann, V., Schenk, H.J., Horsfield, B. and Welte, D.H., 1998. Kinetics of petroleum generation and cracking by programmed-temperature closed-system pyrolysis of Toarcian Shales. *Fuel*, 77(1-2): 23-31.
- Dong, D., Cheng, K., Wang, Y., Li, X., Wang, S. and Huang, J., 2010. Forming condition and characteristics of shale gas in the Lower Paleozoic of the Upper Yangtze Region, China. *Oil & Gas Geology*, 31(3): 288-299.
- Dubinin, M., 1975. Physical adsorption of gases and vapors in micropores. *Progress in surface and membrane science*, 9: 1-70.
- Editorial Committee of the Sichuan Oil & Gas field, 1989. *The Sichuan Oil & Gas field*. Petroleum Geology of China, 10. Petroleum Industry Press, Beijing 516 pp.
- EIA, 2011a. Review of Emerging Resources: U.S. Shale Gas and Shale Oil Plays U.S. Department of Energy, Washington. DC.
- EIA, 2011b. World Shale Gas Resources: An Initial Assessment of 14 Regions Outside the United States. U.S. Department of Energy Washington. DC.
- EIA, 2013a. Annual Energy Outlook. U.S. Department of Energy Washington, DC.
- EIA, 2013b. Technically Recoverable Shale Oil and Shale Gas Resources: An Assessment of 137 Shale Formations in 41 Countries Outside the United States. U.S. Department of Energy Washington. DC.

References

- Eisma, E. and Jurg, J.W., 1967. Fundamental aspects of the diagenesis of organic matter and the formation of hydrocarbons, 7th World Petroleum Congress.
- Espitalié, J., Laporte, J., L., Madec, M., Marquis, F., Leplat, P., Paulet, J. and Boutefeu, A., 1977. Méthode rapide de caractérisation des roches mères, de leur potentiel pétrolier et de leur degré d'évolution. *Oil & Gas Science and Technology - Rev. IFP*, 32(1): 23-42.
- Espitalié, J., Madec, M. and Tissot, B., 1980. Role of mineral matrix in kerogen pyrolysis: influence on petroleum generation and migration. *AAPG Bulletin*, 64(1): 59-66.
- Espitalié, J., Marquis, F. and Barsony, I., 1984. Geochemical logging. In: K.T. Voorheers (eds.), *Analytical pyrolysis techniques and applications*. Butterworth, London, 276-304.
- Feng, G. and Chen, S., 1988. Relationship between the reflectance of bitumen and vitrinite rock. *Natural Gas Industry*, 8(8): 20-26.
- Ferworm, K., Zumberge, J., Reed, J. and Brown, S., 2008. Gas character anomalies found in highly productive shale gas wells, Technical presentation, GeoMark Research, Houston.
- Fischer, C., Schmidt, C., Bauer, A., Gaupp, R. and Heide, K., 2009. Mineralogical and geochemical alteration of low-grade metamorphic black slates due to oxidative weathering. *Chemie der Erde-Geochemistry*, 69(2): 127-142.
- Gan, H., Nandi, S. and Walker Jr, P., 1972. Nature of the porosity in American coals. *Fuel*, 51(4): 272-277.
- Gasparik, M., Bertier, P., Gensterblum, Y., Ghanizadeh, A., Krooss, B. and Littke, R., 2013. Geological Controls on the Methane Storage Capacity in Organic-Rich Shales. *International Journal of Coal Geology*.
- Gasparik, M., Ghanizadeh, A., Bertier, P., Gensterblum, Y., Bouw, S. and Krooss, B.M., 2012. High-pressure methane sorption isotherms of black shales from the Netherlands. *Energy & Fuels*, 26: 4995-5004.
- Ghanizadeh, A., Amann-Hildenbrand, A., Gasparik, M., Gensterblum, Y., Krooss, B.M. and Littke, R., 2013a. Experimental study of fluid transport processes in the matrix system of the European organic-rich shales: II. Posidonia Shale (Lower Toarcian, northern Germany) *International Journal of Coal Geology*(in press).
- Ghanizadeh, A., Gasparik, M., Amann-Hildenbrand, A., Gensterblum, Y. and Krooss, B.M., 2013b. Lithological Controls on Matrix Permeability of Organic-rich Shales: An Experimental Study. *Energy Procedia*, 40: 127-136.
- Glorioso, J.C. and Rattia, A., 2012. Unconventional reservoirs: Basic petrophysical concepts for shale gas, SPE/EAGE European Unconventional Resources Conference & Exhibition - From Potential to Production.
- Goldberg, T., Strauss, H., Guo, Q. and Liu, C., 2007. Reconstructing marine redox conditions for the Early Cambrian Yangtze Platform: Evidence from biogenic sulphur and organic carbon isotopes. *Palaeogeography, Palaeoclimatology, Palaeoecology*, 254(1-2): 175-193.
- Grieser, W. and Bray, J., 2007. Identification of production potential in unconventional reservoirs, Production and Operations Symposium.
- Guo, H., Aziz, N. and Schmidt, L., 1993. Rock fracture-toughness determination by the Brazilian test. *Engineering Geology*, 33(3): 177-188.
- Guo, L., Jiang, Z., Zhang, J. and Li, Y., 2011a. Paleoenvironment of Lower Silurian black shale and its significance to the potential of shale gas, southeast of Chongqing, China. *Energy, Exploration & Exploitation*, 29(5): 597-616.
- Guo, T., Li, Y. and Wei, Z., 2011b. Reservoir-forming Condition of Shale Gas in Ziliujing Formation of Yuanba Area in Sichuan Basin. *Natural Gas Geoscience*, 22(2): 1-7.
- Guo, Z., 1996. *The Formation and Development of Sichuan Basin*. Geological press, Beijing, 200 pp.
- Hackley, P.C., 2012. Geological and geochemical characterization of the Lower Cretaceous Pearsall Formation, Maverick Basin, south Texas: A future shale gas resource? *AAPG Bulletin*, 96(8): 1449-1482.
- Haines, P.W., Hand, M. and Sandiford, M., 2001. Palaeozoic synorogenic sedimentation in central and northern Australia: A review of distribution and timing with implications for the evolution of intracontinental orogens. *Australian Journal of Earth Sciences*, 48(6): 911-928.
- Hamblin, A., 2006. The "Shale Gas" concept in Canada: a preliminary inventory of possibilities. *Geological Survey of Canada, Open File*, 5384: 108.
- Hammes, U., Hamlin, H.S. and Ewing, T.E., 2011. Geologic analysis of the Upper Jurassic Haynesville Shale in east Texas and west Louisiana. *AAPG Bulletin*, 95(10): 1643-1666.
- Han, S., Zhang, J., Li, Y., Horsfield, B., Tang, X., Jiang, W. and Chen, Q., 2013. Evaluation of Lower Cambrian shale in northern Guizhou Province, south China: Implications for shale gas potential. *Energy & Fuels*, 27(6): 2933-2941.
- Han, Y. and Wu, C., 1993. Geothermal gradient and heat flow values of some deep wells in Sichuan Basin. *Oil & Gas Geology*, 14(1): 80-84.
- Hao, F., Guo, T., Zhu, Y., Cai, X., Zou, H. and Li, P., 2008. Evidence for multiple stages of oil cracking and thermochemical sulfate reduction in the Puguang gas field, Sichuan Basin, China. *AAPG Bulletin*, 92(5): 611-637.

References

- Harris, N.B., Miskimins, J.L. and Mnich, C.A., 2011. Mechanical anisotropy in the Woodford Shale, Permian Basin: Origin, magnitude, and scale. *The Leading Edge*, 30(3): 284-291.
- Hartgers, W.A., Damsté, J.S.S. and de Leeuw, J.W., 1994. Geochemical significance of alkylbenzene distributions in flash pyrolysates of kerogens, coals, and asphaltenes. *Geochimica et Cosmochimica Acta*, 58(7): 1759-1775.
- He, F. and Zhu, T., 2012. Favorable targets of breakthrough and built-up of shale gas in continental facies in Lower Jurassic, Sichuan Basin. *Petroleum Geology & Experiment*, 34(3): 246-251.
- Hickey, J.J. and Henk, B., 2007. Lithofacies summary of the Mississippian Barnett Shale, Mitchell 2 T.P. Sims well, Wise County, Texas. *AAPG Bulletin*, 91(4): 437-443.
- Hildenbrand, A., Krooss, B., Busch, A. and Gaschnitz, R., 2006. Evolution of methane sorption capacity of coal seams as a function of burial history - a case study from the Campine Basin, NE Belgium. *International Journal of Coal Geology*, 66(3): 179-203.
- Horsfield, B., 1989. Practical criteria for classifying kerogens: Some observations from pyrolysis-gas chromatography. *Geochimica et Cosmochimica Acta*, 53(4): 891-901.
- Horsfield, B., Disko, U. and Leistner, F., 1989. The micro-scale simulation of maturation: outline of a new technique and its potential applications. *Geologische Rundschau*, 78(1): 361-373.
- Horsfield, B. and Douglas, A., 1980. The influence of minerals on the pyrolysis of kerogens. *Geochimica et Cosmochimica Acta*, 44(8): 1119-1131.
- Horsfield, B. and Dueppenbecker, S.J., 1991. The decomposition of posidonia shale and green river shale kerogens using microscale sealed vessel (MSSV) pyrolysis. *Journal of Analytical and Applied Pyrolysis*, 20(0): 107-123.
- Horsfield, B. and Rullkötter, J., 1994. Diagenesis, catagenesis, and metagenesis of organic matter. *Memoirs-American Association of Petroleum Geologists*: 189-189.
- Huang, J., 1986. Thermal evolution gas in Lower Paleozoic to Proterozoic of Sichuan Basin and its exploration prospects. *Natural Gas Industry*, 6(4): 8-14.
- Huang, J., Chen, S., Song, J., Wang, L., Gou, X., Wang, T. and Dai, H., 1997. Hydrocarbon source systems and formation of gas fields in Sichuan Basin. *Science in China Series D: Earth Sciences*, 40(1): 32-42.
- Huang, J., Zou, C., Li, J., Dong, D., Wang, S., Wang, S. and Cheng, K., 2012a. Shale gas generation and potential of the Lower Cambrian Qiongzhusi Formation in Southern Sichuan Basin, China. *Petroleum Exploration and Development*, 39(1): 69-75.
- Huang, J., Zou, C., Li, J., Dong, D., Wang, S., Wang, S., Wang, Y. and Li, D., 2012b. Shale gas accumulation conditions and favorable zones of Silurian Longmaxi Formation in south Sichuan Basin, China. *Journal of China Coal Society*, 37(5): 782-787.
- Hunt, J.M., 1995. *Petroleum Geochemistry and Geology*. W. H. Freeman 743 pp.
- Jacob, H., 1967. Petrologie von asphaltiten und asphaltischen pyrobitumina. *Erdöl und Kohle*, 20: 393-400.
- Jacob, H., 1985. Disperse solid bitumens as an indicator for migration and maturity in prospecting for oil and gas. *Erdöl und Kohle-Erdgas-Petrochemie*, 38(8): 365.
- Jacobi, D., Breig, J., LeCompte, B., Kopal, M., Hursan, G., Mendez, F., Bliven, S. and Longo, J., 2009. Effective geochemical and geomechanical characterization of shale gas reservoirs from the wellbore environment: Caney and the Woodford shale, SPE Annual Technical Conference and Exhibition.
- James, A.T., 1983. Correlation of natural gas by use of carbon isotopic distribution between hydrocarbon components. *AAPG Bulletin*, 67(7): 1176-1191.
- Jarvie, D. and Lundell, L., 1991. Hydrocarbon generation modeling of naturally and artificially matured Barnett Shale, Fort Worth Basin, Texas, Southwest Regional Geochemistry Meeting, The Woodlands, Texas.
- Jarvie, D.M., 2008. Unconventional Shale resource plays: shale-gas and shale-oil opportunities, Fort Worth Business Press meeting.
- Jarvie, D.M., Claxton, B., Henk, F. and Breyer, J., 2001. Oil and shale gas from the Barnett Shale, Fort Worth Basin, Texas, AAPG Annual Meeting Program, Denver, CO.
- Jarvie, D.M., Hill, R.J., Ruble, T.E. and Pollastro, R.M., 2007. Unconventional shale-gas systems: The Mississippian Barnett Shale of north-central Texas as one model for thermogenic shale-gas assessment. *AAPG Bulletin*, 91(4): 475-499.
- Jenden, P.D., Drazan, D.J. and Kaplan, I.R., 1993. Mixing of thermogenic natural gases in northern Appalachian Basin. *AAPG Bulletin*, 77(6): 980-998.
- Ji, L., Zhang, T., Milliken, K.L., Qu, J. and Zhang, X., 2012. Experimental investigation of main controls to methane adsorption in clay-rich rocks. *Applied Geochemistry*, 27(12): 2533-2545.
- Jia, D., Wei, G., Chen, Z., Li, B., Zeng, Q. and Yang, G., 2006. Longmen Shan fold-thrust belt and its relation to the western Sichuan Basin in central China: New insights from hydrocarbon exploration. *AAPG Bulletin*, 90(9): 1425-1447.
- Jia, W., Peng, P.a., Yu, C. and Xiao, Z., 2007. Source of 1,2,3,4-tetramethylbenzene in asphaltenes from the Tarim Basin. *Journal of Asian Earth Sciences*, 30(5-6): 591-598.

References

- Jian, C., Wang, X., Zhang, L., Wan, Y., Lei, Y., Sun, J. and Guo, C., 2013. Geological characteristics of shale and exploration potential of continental shale gas in 7th member of Yanchang Formation, southeast Ordos Basin. *Geology in China*, 40(6): 1880-1888.
- Jiang, Y., Dong, D., Qi, L., Shen, Y., Jiang, C. and He, F., 2010. Basic features and evaluation of shale gas reservoirs. *Natural Gas Industry*, 30(10): 7-12.
- Joubert, J.I., Grein, C.T. and Bienstock, D., 1974. Effect of moisture on the methane capacity of American coals. *Fuel*, 53(3): 186-191.
- Jüntgen, H. and Schwuger, M., 1966. Aussagekraft der Quecksilber-Porosimetrie bei der Charakterisierung poröser Stoffe. *Chemie Ingenieur Technik*, 38(12): 1271-1278.
- Kinley, T.J., Cook, L.W., Breyer, J.A., Jarvie, D.M. and Busbey, A.B., 2008. Hydrocarbon potential of the Barnett Shale (Mississippian), Delaware Basin, west Texas and southeastern New Mexico. *AAPG Bulletin*, 92(8): 967-991.
- Klinkenberg, L., 1941. The permeability of porous media to liquids and gases, *Drilling and Production Practice*. American Petroleum Institute, pp. 200-213.
- Korsch, R.J., Huazhao, M., Zhaocai, S. and Gorter, J.D., 1991. The Sichuan basin, southwest China: a late proterozoic (Sinian) petroleum province. *Precambrian Research*, 54(1): 45-63.
- Krooss, B., Van Bergen, F., Gensterblum, Y., Siemons, N., Pagnier, H. and David, P., 2002. High-pressure methane and carbon dioxide adsorption on dry and moisture-equilibrated Pennsylvanian coals. *International Journal of Coal Geology*, 51(2): 69-92.
- Kuhn, P., Primio, R.D. and Horsfield, B., 2010. Bulk composition and phase behaviour of petroleum sourced by the Bakken Formation of the Williston Basin. *Geological Society, London, Petroleum Geology Conference series*, 7: 1065-1077.
- Lafargue, E., Marquis, F. and Pillot, D., 1998. Rock-Eval 6 applications in hydrocarbon exploration, production, and soil contamination studies. *Oil & Gas Science and Technology*, 53(4): 421-437.
- Lamberson, M.N. and Bustin, R.M., 1993. Coalbed methane characteristics of Gates Formation coals, northeastern British Columbia: effect of maceral composition. *AAPG Bulletin*, 77(12): 2062-2076.
- Lash, G.G. and Engelder, T., 2011. Thickness trends and sequence stratigraphy of the Middle Devonian Marcellus Formation, Appalachian Basin: Implications for Acadian foreland basin evolution. *AAPG Bulletin*, 95(1): 61-103.
- Laughrey, C.D. and Baldassare, F.J., 1998. Geochemistry and origin of some natural gases in the Plateau Province, central Appalachian Basin, Pennsylvania and Ohio. *AAPG Bulletin*, 82(2): 317-335.
- Laxminarayana, C. and Crosdale, P.J., 1999. Role of coal type and rank on methane sorption characteristics of Bowen Basin, Australia coals. *International Journal of Coal Geology*, 40(4): 309-325.
- Levy, J.H., Day, S.J. and Killingley, J.S., 1997. Methane capacities of Bowen Basin coals related to coal properties. *Fuel*, 76(9): 813-819.
- Lewan, M.D., Comer, J., Hamilton-Smith, T., Hasenmueller, N., Guthrie, J., Hatch, J., Gautier, D. and Frankie, W., 1995. Feasibility study of material-balance assessment of petroleum from the New Albany shale in the Illinois Basin. US Government Printing Office.
- Leythaeuser, D., 1973. Effects of weathering on organic matter in shales. *Geochimica et Cosmochimica Acta*, 37(1): 113-120.
- Li, J., Yu, B., Liu, C. and Sun, M., 2012a. Clay minerals of black shale and their effects on physical properties of shale gas reservoirs in the southeast of Chongqing: a case study from Lujiao outcrop section in Pengshui, Chongqing. *Geoscience*, 26(4): 732-740.
- Li, J., Yu, B., Zhang, J., Li, Y. and Wu, J., 2012b. Reservoir characteristics and their influence factors of the Lower Cambrian dark shale in northern Guizhou. *Oil & Gas Geology*, 33(3): 364-374.
- Li, Q., Chen, M., Jin, Y., Hou, B. and Zhang, J., 2012c. Rock mechanical properties and brittleness evaluation of shale gas reservoir. *Petroleum Drilling Techniques*, 40(4): 17-22.
- Li, X., Zhao, P., Sun, J., Fu, T., Lai, S., Tian, X., Ma, S. and Wang, F., 2013. Study on the accumulation conditions of shale gas from the Lower Paleozoic in the south region of Sichuan Basin. *Journal of China Coal Society*, 38(5): 864-890.
- Li, Z.-X., Zhang, L. and Powell, C.M., 1995. South China in Rodinia: Part of the missing link between Australia-East Antarctica and Laurentia? *Geology*, 23(5): 407-410.
- Li, Z.X., Li, X.H., Kenny, P.D., Wang, J., Zhang, S. and Zhou, H., 2003. Geochronology of Neoproterozoic syn-rift magmatism in the Yangtze Craton, South China and correlations with their continents: evidence for a mantle superplume hat broke up Rodinia. *Precambrian Research*, 122: 85-109.
- Liang, D. and Chen, J., 2005. Oil-source correlations for high and over matured marine source rocks in south China. *Petroleum Exploration and Development*, 32(3): 8-14.
- Liang, D., Guo, T., Bian, L., Chen, J. and Zhao, Z., 2009a. Some progresses on studies of hydrocarbon generation and accumulation in marine sedimentary regions, southern China (Part 3): Controlling factors on the sedimentary facies and development of palaeozoic marine source rocks. *Marine Origin Petroleum Geology*, 14(2): 1-19.

References

- Liang, D., Guo, T., Chen, J., Bian, L. and Zhao, Z., 2008. Some progresses on studies of hydrocarbon generation and accumulation in marine sedimentary region, southern China (Part 1): Distribution of four suits of regional marine source rocks. *Marine Origin Petroleum Geology*, 13(3): 1-16.
- Liang, D., Guo, T., Chen, J., Bian, L. and Zhao, Z., 2009b. Some progresses on studies of hydrocarbon generation and accumulation in marine sedimentary region, southern China (Part 2): geochemical characteristics of four suits of regional marine source rocks, south China. *Marine Origin Petroleum Geology*, 14(1): 1-15.
- Littke, R., Klusmann, U., Krooss, B. and Leythaeuser, D., 1991. Quantification of loss of calcite, pyrite, and organic matter due to weathering of Toarcian black shales and effects on kerogen and bitumen characteristics. *Geochimica et Cosmochimica Acta*, 55(11): 3369-3378.
- Liu, D., Song, Y., Xue, A., Li, Y., Luo, Z., Shen, X., Yang, X., Zhang, Z. and Tao, S., 2000. Structural and Natural Gas Accumulation Belt of the Sichuan Basin. Petroleum Industry Press, Beijing, 107 pp.
- Liu, H., Wang, H., Liu, R., Zhao, Q. and Lin, Y., 2010. China Shale Gas Resources and Prospect Potential. *Acta Geologica Sinica*, 84(9): 1374-1378.
- Liu, S., Ma, W., Luba, J., Huang, W., Zeng, X. and Zhang, C., 2011. Characteristics of the shale gas reservoir rocks in the Lower Silurian Longmaxi Formation, East Sichuan Basin, China. *Acta Petrologica Sinica*, 27(8): 2239-2252.
- Long, P., Zhang, J., Li, Y., Nie, H., Tang, Y., Zhang, Q. and Liu, Z., 2009. Potential of the Lower Paleozoic Shale Gas Resources in Chongqing and Its Adjacent Areas. *Natural Gas Industry*, 29(12): 125-129.
- Long, P., Zhang, J., Li, Y., Tang, X., Cheng, L., Liu, Z. and Han, S., 2012. Reservoir-forming conditions and strategic select favorable area of shale gas in the Lower Paleozoic of Chongqing and its adjacent area. *Earth Science Frontiers*, 19(2): 221-233.
- Loucks, R.G., Reed, R.M., Ruppel, S.C. and Hammes, U., 2012. Spectrum of pore types and networks in mudrocks and a descriptive classification for matrix-related mudrock pores. *AAPG Bulletin*, 96(6): 1071-1098.
- Loucks, R.G., Reed, R.M., Ruppel, S.C. and Jarvie, D.M., 2009. Morphology, genesis, and distribution of nanometer-scale pores in siliceous mudstones of the Mississippian Barnett Shale. *Journal of Sedimentary Research*, 79(12): 848-861.
- Loucks, R.G. and Ruppel, S.C., 2007. Mississippian Barnett Shale: Lithofacies and depositional setting of a deep-water shale-gas succession in the Fort Worth Basin, Texas. *AAPG Bulletin*, 91(4): 579-601.
- Lu, X.-C., Li, F.-C. and Watson, A.T., 1995. Adsorption measurements in Devonian shales. *Fuel*, 74(4): 599-603.
- Lüders, V., Plessen, B. and di Primio, R., 2012. Stable carbon isotopic ratios of CH₄-CO₂-bearing fluid inclusions in fracture-fill mineralization from the Lower Saxony Basin (Germany) - A tool for tracing gas sources and maturity. *Marine and Petroleum Geology*, 30(1): 174-183.
- Ma, Y., Cai, X., Zhao, P., Luo, Y. and Zhang, X., 2010. Distribution and further exploration of the large-medium sized gas fields in Sichuan Basin. *Acta Petrol Sinica*, 31(3): 347-354.
- Ma, Y., Guo, X., Guo, T., Huang, R., Cai, X. and Li, G., 2007. The Puguang gas field: New giant discovery in the mature Sichuan Basin, southwest China *AAPG Bulletin*, 91: 627-643.
- Ma, Y.S., Mu, C.L., Guo, X.S., Tan, Q.Y. and Yu, Q., 2006. Characteristic and framework of the Changxingian sedimentation in the northeastern Sichuan Basin (in Chinese with English abstract). *Geological Review*, 52(1): 25-39.
- Mahlstedt, N., 2012. Evaluating the late gas potential of source rocks stemming from different sedimentary environments, Berlin, Technische Universität Berlin, Diss., .
- Martineau, D.F., 2007. History of the Newark East field and the Barnett Shale as a gas reservoir. *AAPG Bulletin*, 91(4): 399-403.
- Martini, A., Walter, L., Budai, J., Ku, T., Kaiser, C. and Schoell, M., 1998. Genetic and temporal relations between formation waters and biogenic methane: Upper Devonian Antrim Shale, Michigan Basin, USA. *Geochimica et Cosmochimica Acta*, 62(10): 1699-1720.
- Martini, A.M., Walter, L.M., Ku, T.C.W., Budai, J.M., McIntosh, J.C. and Schoell, M., 2003. Microbial production and modification of gases in sedimentary basins: A geochemical case study from a Devonian shale gas play, Michigan basin. *AAPG Bulletin*, 87(8): 1355-1375.
- Martini, A.M., Walter, L.M. and McIntosh, J.C., 2008. Identification of microbial and thermogenic gas components from Upper Devonian black shale cores, Illinois and Michigan basins. *AAPG Bulletin*, 92(3): 327-339.
- Marynowski, L., Kurkiewicz, S., Rakociński, M. and Simoneit, B.R., 2011. Effects of weathering on organic matter: I. Changes in molecular composition of extractable organic compounds caused by paleoweathering of a Lower Carboniferous (Tournaisian) marine black shale. *Chemical Geology*, 285(1): 144-156.
- Mastalerz, M., Gluskoter, H. and Rupp, J., 2004. Carbon dioxide and methane sorption in high volatile bituminous coals from Indiana, USA. *International Journal of Coal Geology*, 60(1): 43-55.

References

- Meng, Q., Wang, E. and Hu, J., 2005. Mesozoic sedimentary evolution of the northwest Sichuan basin: Implication for continued clockwise rotation of the South China block. *Geological Society of America Bulletin*, 117(3-4): 396-410.
- Miceli Romero, A. and Philp, R.P., 2012. Organic geochemistry of the Woodford Shale, southeastern Oklahoma: How variable can shales be? *AAPG Bulletin*, 96(3): 493-517.
- Michels, A. and Wouters, H., 1941. Isotherms of helium between 0° and 150°C up to 200 Amagat. *Physica*, 8(8): 923-932.
- Milliken, K.L., Rudnicki, M., Awwiller, D.N. and Zhang, T., 2013. Organic matter-hosted pore system, Marcellus Formation (Devonian), Pennsylvania. *AAPG Bulletin*, 97(2): 177-200.
- Montgomery, S.L., Jarvie, D.M., Bowker, K.A. and Pollastro, R.M., 2005. Mississippian Barnett Shale, Fort Worth basin, north-central Texas: Gas-shale play with multi-trillion cubic foot potential. *AAPG Bulletin*, 89(2): 155-175.
- Mu, E., Li, J., Ge, M., Chen, X., Ni, Y. and Lin, Y., 1981. Late Ordovician paleogeography of south China. *Acta Stratigraphica Sinica*, 5: 165-170.
- Muscio, G.P. and Horsfield, B., 1996. Neof ormation of inert carbon during the natural maturation of a marine source rock: Bakken Shale, Williston Basin. *Energy & Fuels*, 10(1): 10-18.
- Muscio, G.P.A., Horsfield, B. and Welte, D.H., 1994. Occurrence of thermogenic gas in the immature zone - implications from the Bakken in-source reservoir system. *Organic Geochemistry*, 22(3-5): 461-476.
- National Bureau of Statistics, P. and Energy Bureau, P. (Editors), 1991-2010. *China Energy Statistical Yearbook*. China Statistics Press, Beijing.
- National Energy Administration, 2011. *Shale Gas Developing Plan*, Beijing, pp. 1-15.
- Nie, H., Zhang, J. and Li, Y., 2011. Accumation conditions of the Lower Cambrian shale gas in the Sichuan Basin and its periphery. *Acta Petrolei Sinica*, 32(6): 959-967.
- Nie, Y., Leng, J., Han, J., Sun, L. and Shen, C., 2013. Exploration potential of shale gas in Cengong block, southeastern Guizhou province. *Oil & Gas Geology*, 34(2): 274-280.
- Passey, Q., Bohacs, K., Esch, W., Klimentidis, R. and Sinha, S., 2010. From oil-prone source rock to gas-producing shale reservoir-geologic and petrophysical characterization of unconventional shale gas reservoirs, International Oil and Gas Conference and Exhibition in China.
- Pawlewicz, M.J. and King, J., 1992. Vitrinite and solid bitumen reflectance: some correlations and applications. *USGS bulletin*(2007): 58-60.
- Pelet, R., 1985. Evaluation quantitative des produits formés lors de l'évolution géochimique de la matière organique. *Revue de l'Institut français du pétrole*, 40: 551-562.
- Peters, K.E. and Cassa, M.R., 1994. Applied source rock geochemistry. *Memoirs-American Association of Petroleum Geologists*: 93-93.
- Peters, K.E., Walters, C. and Moldowan, J., 2005. *The Biomarker Guide, Volume 1: Biomarkers and Isotopes in the Environment and Human History*. Cambridge University Press, New York, 471 pp.
- Petsch, S., Berner, R. and Eglinton, T., 2000. A field study of the chemical weathering of ancient sedimentary organic matter. *Organic Geochemistry*, 31(5): 475-487.
- Plesch, A., Shaw, J.H. and Kronman, D., 2007. Mechanics of low-relief detachment folding in the Bajiaochang field, Sichuan Basin, China. *AAPG Bulletin*, 91(11): 1559-1575.
- Pollastro, R.M., Jarvie, D.M., Hill, R.J. and Adams, C.W., 2007. Geologic framework of the Mississippian barnett shale, barnett-paleozoic total petroleum system, Bend arch-Fort Worth Basin, Texas. *AAPG Bulletin*, 91(4): 405-436.
- Prinz, D. and Littke, R., 2005. Development of the micro-and ultramicroporous structure of coals with rank as deduced from the accessibility to water. *Fuel*, 84(12): 1645-1652.
- Prinz, D., Pyckhout-Hintzen, W. and Littke, R., 2004. Development of the meso-and macroporous structure of coals with rank as analysed with small angle neutron scattering and adsorption experiments. *Fuel*, 83(4): 547-556.
- Prinzhofer, A., Mello, M.R. and Takaki, T., 2000. Geochemical characterization of natural gas: A physical multivariable approach and its applications in maturity and migration estimates. *AAPG Bulletin*, 84(8): 1152-1172.
- Reading, H.G., 2009. *Sedimentary environments: processes, facies and stratigraphy*. Wiley. com, 688 pp.
- Rice, D.D. and Claypool, G.E., 1981. Generation, accumulation, and resource potential of biogenic gas. *AAPG Bulletin*, 65(1): 5-25.
- Rickman, R., Mullen, M., Petre, J., Grieser, W. and Kundert, D., 2008. A practical use of shale petrophysics for stimulation design optimization: All shale plays are not clones of the Barnett Shale, SPE Annual Technical Conference and Exhibition.
- Rodriguez, N.D. and Philp, R.P., 2010. Geochemical characterization of gases from the Mississippian Barnett Shale, Fort Worth Basin, Texas. *AAPG Bulletin*, 94(11): 1641-1656.
- Ross, D.J. and Bustin, R.M., 2007. Impact of mass balance calculations on adsorption capacities in microporous shale gas reservoirs. *Fuel*, 86(17): 2696-2706.

References

- Ross, D.J.K. and Bustin, R.M., 2008. Characterizing the shale gas resource potential of Devonian–Mississippian strata in the Western Canada sedimentary basin: Application of an integrated formation evaluation. *AAPG Bulletin*, 92(1): 87-125.
- Ross, D.J.K. and Bustin, R.M., 2009. The importance of shale composition and pore structure upon gas storage potential of shale gas reservoirs. *Marine and Petroleum Geology*, 26(6): 916-927.
- Santamaria, O. and Horsfield, B., 2004. Gas generation potential of Upper Jurassic (Tithonian) source rocks in the Sonda de Campeche, Mexico. The circum-Gulf of Mexico and the Caribbean: Hydrocarbon habitats, basin formation, and plate tectonics: *AAPG Memoir*, 79: 349-363.
- Schenk, H. and Horsfield, B., 1998. Using natural maturation series to evaluate the utility of parallel reaction kinetics models: an investigation of Toarcian shales and Carboniferous coals, Germany. *Organic Geochemistry*, 29(1): 137-154.
- Schenk, H.J., Di Primio, R. and Horsfield, B., 1997. The conversion of oil into gas in petroleum reservoirs. Part 1: Comparative kinetic investigation of gas generation from crude oils of lacustrine, marine and fluviodeltaic origin by programmed-temperature closed-system pyrolysis. *Organic Geochemistry*, 26(7–8): 467-481.
- Schettler, P. and Parmoly, C., 1990. The measurement of gas desorption isotherms for Devonian shale. *GRI Devonian Gas Shale Technology Review*, 7(1): 4-9.
- Schlumberger, 2012. Successes in shale plays, Schlumberger, www.slb.com/shale.
- Schoell, M., 1980. The hydrogen and carbon isotopic composition of methane from natural gases of various origins. *Geochimica et Cosmochimica Acta*, 44(5): 649-661.
- Schoell, M., 1983. Genetic characterization of natural gases. *AAPG Bulletin*, 67(12): 2225-2238.
- Scotese, C.R., 2009. Late Proterozoic plate tectonics and palaeogeography: a tale of two supercontinents, Rodinia and Pannotia. *Geological Society, London, Special Publications*, 326(1): 67-83.
- Scotese, C.R. and McKerrow, W.S., 1990. Revised World maps and introduction. *Geological Society, London, Memoirs*, 12(1): 1-21.
- Seewald, J. and Whelan, J., 2005. Isotopic and chemical composition of natural gas from the Potato Hills Field, Southeastern Oklahoma: Evidence for an Abiogenic Origin?, *AAPG Research Conference, Origin of Petroleum*.
- Setzmann, U. and Wagner, W., 1991. A new equation of state and tables of thermodynamic properties for methane covering the range from the melting line to 625 K at pressures up to 1000 MPa. *J. Phys. Chem. Ref. Data*, 20(6): 1061-1155.
- Sierra, R., Tran, M., Abousleiman, Y. and Slatt, R., 2010. Woodford Shale mechanical properties and the impacts of lithofacies, *Proceedings symposium on the 44th US rock mechanics symposium and 5th US–Canada rock mechanics symposium, Salt Lake City, Utah*, pp. 1-10.
- Slatt, R.M. and Abousleiman, Y., 2011. Merging sequence stratigraphy and geomechanics for unconventional gas shales. *The Leading Edge*, 30(3): 274-282.
- Slatt, R.M. and O'Brien, N.R., 2011. Pore types in the Barnett and Woodford gas shales: Contribution to understanding gas storage and migration pathways in fine-grained rocks. *AAPG Bulletin*, 95(12): 2017-2030.
- Sondergeld, C.H. and Rai, C.S., 2011. Elastic anisotropy of shales. *The Leading Edge*, 30(3): 324-331.
- Stahl, W., 1974. Carbon isotope fractionations in natural gases. *Nature*, 251(5471): 134-135.
- Stahl, W.J. and Carey Jr, B.D., 1975. Source-rock identification by isotope analyses of natural gases from fields in the Val Verde and Delaware basins, west Texas. *Chemical Geology*, 16(4): 257-267.
- Steiner, M., Li, G., Qian, Y., Zhu, M. and Erdtmann, B.-D., 2007. Neoproterozoic to Early Cambrian small shelly fossil assemblages and a revised biostratigraphic correlation of the Yangtze Platform (China). *Palaeogeography, Palaeoclimatology, Palaeoecology*, 254(1–2): 67-99.
- Steiner, M., Wallis, E., Erdtmann, B.-D., Zhao, Y. and Yang, R., 2001. Submarine-hydrothermal exhalative ore layers in black shales from South China and associated fossils — insights into a Lower Cambrian facies and bio-evolution. *Palaeogeography, Palaeoclimatology, Palaeoecology*, 169(3–4): 165-191.
- Strapoć, D., Mastalerz, M., Schimmelmann, A., Drobniak, A. and Hasenmueller, N.R., 2010. Geochemical constraints on the origin and volume of gas in the New Albany Shale (Devonian–Mississippian), eastern Illinois Basin. *AAPG Bulletin*, 94(11): 1713-1740.
- Tan, J., Horsfield, B., Fink, R., Krooss, B., Schulz, H.-M., Rybacki, E., Zhang, J., Boreham, C.J., van Graas, G. and Tocher, B.A., 2014a. Shale gas potential of the major marine shale formations in the Upper Yangtze Platform, south China, Part III: Mineralogical, lithofacial, petrophysical, and rock mechanical properties. *Energy & Fuels* (in press).
- Tan, J., Horsfield, B., Mahlstedt, N., Zhang, J., Boreham, C.J., Hippler, D., van Graas, G. and Tocher, B.A., 2014b. Shale gas potential of the major marine shale formations in the Upper Yangtze Platform, south China, Part I: Geological and geochemical characterisation. *Organic Geochemistry* (In Review).
- Tan, J., Horsfield, B., Mahlstedt, N., Zhang, J., di Primio, R., Vu, T.A.T., Boreham, C.J., van Graas, G. and Tocher, B.A., 2013. Physical properties of petroleum formed during maturation of Lower Cambrian

References

- shale in the upper Yangtze Platform, South China, as inferred from Phase Kinetics modelling. *Marine and Petroleum Geology*, 48: 47-56.
- Tang, Y., Perry, J.K., Jenden, P.D. and Schoell, M., 2000. Mathematical modeling of stable carbon isotope ratios in natural gases. *Geochimica et Cosmochimica Acta*, 64(15): 2673-2687.
- Tegelaar, E.W. and Noble, R.A., 1994. Kinetics of hydrocarbon generation as a function of the molecular structure of kerogen as revealed by pyrolysis-gas chromatography. *Organic Geochemistry*, 22(3-5): 543-574.
- Tian, H., Pan, L., Xiao, X., Wilkins, R.W.T., Meng, Z. and Huang, B., 2013. A preliminary study on the pore characterization of Lower Silurian black shales in the Chuandong Thrust Fold Belt, southwestern China using low pressure N₂ adsorption and FE-SEM methods. *Marine and Petroleum Geology*, 48(0): 8-19.
- Tilley, B., McLellan, S., Hiebert, S., Quartero, B., Veilleux, B. and Muehlenbachs, K., 2011. Gas isotope reversals in fractured gas reservoirs of the western Canadian Foothills: Mature shale gases in disguise. *AAPG Bulletin*, 95(8): 1399-1422.
- Tissot, B. and Welte, D., 1984. *Petroleum Formation and Occurrence*, 2nd ed. Springer-Verlag, New York, 699 pp.
- Ulusay, R. and Hudson, J.A., 2007. The complete ISRM suggested methods for rock characterization, testing and monitoring: 1974-2006. International Society for Rock Mechanics, Commission on Testing Methods.
- van Krevelen, D., 1961. *Coal: Typology, Chemistry, Physics, Constitution*. Elsevier Publishing Company.
- Vandenbroucke, M. and Largeau, C., 2007. Kerogen origin, evolution and structure. *Organic Geochemistry*, 38(5): 719-833.
- Volk, H., George, S.C., Kempton, R.H., Liu, K., Ahmed, M. and Ambrose, G.J., 2007. Petroleum migration in the Georgina Basin: Evidence from the geochemistry of oil inclusions and bitumens. In: T.J. Munson and G.J. Ambrose (Editors), *Proceedings of the Central Australian Basins Symposium (CABS)*. Northern Territory Geological Survey, Alice Springs, Northern Territory, Australia, pp. 282-303.
- Vu, T.A.T., 2008. *Origin and Maturation of organic Matter in New Zealand's Coals*, Universitätsbibliothek, Diss.,.
- Wang, C., Juang, L., Lee, C., Hsu, T., Lee, J. and Chao, H., 2004. Effects of exchanged surfactant cations on the pore structure and adsorption characteristics of montmorillonite. *Journal of colloid and interface science*, 280(1): 27-35.
- Wang, G. and Carr, Timothy R., 2013. Organic-rich Marcellus Shale lithofacies modeling and distribution pattern analysis in the Appalachian Basin. *AAPG Bulletin*, 97(12): 2173-2205.
- Wang, K., Chatterton, B.D.E. and Wang, Y., 1997. An organic carbon isotope record of Late Ordovician to Early Silurian marine sedimentary rocks, Yangtze Sea, South China: Implications for CO₂ changes during the Hirnantian glaciation. *Palaeogeography, Palaeoclimatology, Palaeoecology*, 132(1-4): 147-158.
- Wang, L., Zou, C., Deng, P., Chen, S., Zhang, Q., Xu, B. and Li, H., 2009a. Geochemical evidence of shale gas existed in the Lower Paleozoic Sichuan Basin. *Natural Gas Industry*, 29(5): 59-62.
- Wang, S., Chen, G., Dong, D., Yang, G., Lu, Z., Xu, Y. and Huang, Y., 2009b. Accumulation conditions and exploitation prospect of shale gas in the Lower Paleozoic Sichuan Basin. *Natural Gas Industry*, 29(5): 51-58.
- Wang, S., Li, D., Li, J., Dong, D., Zhang, W. and Ma, J., 2011. Exploration potential of shale gas in the Ordos Basin. *Natural Gas Industry*, 31(12): 40-46.
- Wang, S., Song, Z., Cao, T. and Song, X., 2013a. The methane sorption capacity of Paleozoic shales from the Sichuan Basin, China. *Marine and Petroleum Geology*, 44(0): 112-119.
- Wang, S., Wang, L., Huang, J., Li, X. and Li, D., 2009c. Accumulation conditions of shale gas reservoirs in Silurian of the Upper Yangtze Region. *Natural Gas Industry*, 29(5): 45-50.
- Wang, Y., Zhu, Y., Chen, S., Zhang, X. and Zhang, J., 2013b. Formation conditions of shale gas in Lower Cambrian Niutitang Formation, northwestern Hunan. *Journal of China University of Mining & Technology*, 42(4): 586-594.
- Washburn, E.W., 1921. The dynamics of capillary flow. *Physical review*, 17(3): 273.
- Wei, K., Morrow, N. and Brower, K., 1986. Effect of fluid, confining pressure, and temperature on absolute permeabilities of low-permeability sandstones. *SPE Formation Evaluation*, 1(4): 413-423.
- Weniger, P., Franců, J., Hemza, P. and Krooss, B.M., 2012. Investigations on the methane and carbon dioxide sorption capacity of coals from the SW Upper Silesian Coal Basin, Czech Republic. *International Journal of Coal Geology*, 93: 23-39.
- Weniger, P., Kalkreuth, W., Busch, A. and Krooss, B.M., 2010. High-pressure methane and carbon dioxide sorption on coal and shale samples from the Paraná Basin, Brazil. *International Journal of Coal Geology*, 84(3): 190-205.
- Werne, J.P., Sageman, B.B., Lyons, T.W. and Hollander, D.J., 2002. An integrated assessment of a "type euxinic" deposit: Evidence for multiple controls on black shale deposition in the middle Devonian Oatka Creek Formation. *American Journal of Science*, 302(2): 110-143.

References

- Wildman, R.A., Berner, R.A., Petsch, S.T., Bolton, E.W., Eckert, J.O., Mok, U. and Evans, J.B., 2004. The weathering of sedimentary organic matter as a control on atmospheric O₂: I. Analysis of a black shale. *American Journal of Science*, 304(3): 234-249.
- Wirth, R., 2004. Focused Ion Beam (FIB) A novel technology for advanced application of micro-and nanoanalysis in geosciences and applied mineralogy. *European Journal of Mineralogy*, 16(6): 863-876.
- Wirth, R., 2009. Focused Ion Beam (FIB) combined with SEM and TEM: Advanced analytical tools for studies of chemical composition, microstructure and crystal structure in geomaterials on a nanometre scale. *Chemical Geology*, 261(3): 217-229.
- Wu, J., Yu, B., Zhang, J. and Li, Y., 2013. Pore characteristics and controlling factors in the organic-rich shale of the Lower Silurian Longmaxi Formation revealed by samples from a well in southeastern Chongqing. *Earth Science Frontiers*, 20(3): 260-269.
- Wu, Q., Li, X., Liu, H. and Xia, C., 2011. Log interpretations and the application of core testing technology in the shale-gas: Taking the exploration and development of the Sichuan Basin as an example. *Acta Petrologica Sinica*, 32(3): 484-488.
- Xia, X., Litvinov, S. and Muhler, M., 2006. Consistent approach to adsorption thermodynamics on heterogeneous surfaces using different empirical energy distribution models. *Langmuir*, 22(19): 8063-8070.
- Xia, X. and Tang, Y., 2012. Isotope fractionation of methane during natural gas flow with coupled diffusion and adsorption/desorption. *Geochimica et Cosmochimica Acta*, 77(0): 489-503.
- Xu, M., Zhu, C., Tian, Y., Rao, S. and Hu, S., 2011. Borehole temperature logging and characteristics of subsurface temperature in the Sichuan Basin. *Chinese Journal Geophysics*, 54(4): 1052-1060.
- Xu, Y., Shen, P. and Li, Y., 1989. The oldest gas pool of China - Weiyuan Sinian gas pool, Sichuan Province. *Acta Sedimentologica Sinica*(04): 3-13.
- Ye, J. and Zeng, H., 2008. Pooling conditions and exploration prospect of shale gas in Xujiahe Formation in western Sichuan depression. *Natural Gas Industry*, 28(12): 18-25.
- Yee, D., Seidle, J.P. and Hanson, W.B., 1993. Gas sorption on coal and measurement of gas content. *Hydrocarbons from coal: AAPG Studies in Geology*, 38: 203-218.
- Yin, C., Wang, T., Wang, S. and Lin, F., 2001. Differences between Kerogen and oil cracked gases in Sinian reservoir of Weiyuan and Ziyang area. *Acta Sedimentologica Sinica*, 19(1): 156-164.
- Yu, C., Bao, S., Qin, Q., Nie, H., Zhu, H. and Shao, X., 2012. Analysis of reservoir-forming conditions of shale gas in Lower Silurian of southeast Sichuan area. *Journal of Oil and Gas Technology*, 34(2): 41-46.
- Zhang, B., Zhao, Z., Zhang, S. and Chen, J., 2007a. Discussion on marine source rocks thermal evolution patterns in the Tarim Basin and Sichuan Basin, west China. *Chinese Science Bulletin*, 52(zk1): 141-149.
- Zhang, D., Li, Y., Zhang, J., Qiao, D., Pan, J., Jiang, W., Zhang, J. and Ren, S., 2012a. Shale gas potential assessment and selection of favorite exploration areas in China, *China Land and Resources News*. Ministry of Land and Resources of China, Beijing, pp. 4.
- Zhang, J., Jiang, S., Tang, X., Zhang, P., Tang, Y. and Jin, T., 2009. Accumulation types and resources characteristics of shale gas in China. *Natural Gas Industry*, 29(12): 109-114.
- Zhang, J., Nie, H., Xu, B., Jiang, S., Zhang, P. and Wang, Z., 2008a. Geological condition of shale gas accumulation in Sichuan Basin. *Natural Gas Industry*, 28(2): 151-156.
- Zhang, L., Wei, G., Han, L., Wang, L. and Wang, D., 2008b. Evaluation of the high and over matured Sinian-Lower Cambrian Paleozoic source rocks in the Sichuan Basin. *Petroleum Geology & Experiment*, 30(3): 286-290.
- Zhang, L., Wei, G., Li, X., Wang, Z. and Xiao, X., 2007b. The thermal history of Sinian-Lower Paleozoic high/over mature source rock in Sichuan Basin. *Natural Gas Geoscience*, 18(5): 726-731.
- Zhang, T., Ellis, G.S., Ruppel, S.C., Milliken, K. and Yang, R., 2012b. Effect of organic-matter type and thermal maturity on methane adsorption in shale-gas systems. *Organic Geochemistry*, 47(0): 120-131.
- Zhang, Z., Shen, J., Gong, X., Zhao, Y., Mao, J. and Yan, C., 1996. A preliminary discussion on preservation condition of Kaili Fauna, Middle Cambrian, Taijiang, Guizhou. *Acta Palaeontologica Sinica*, 35: 607-622.
- Zhang, Z., Yang, L., Teng, J. and Badal, J., 2011. An overview of the earth crust under China. *Earth-Science Reviews*, 104(1-3): 143-166.
- Zhao, H., Givens, N.B. and Curtis, B., 2007. Thermal maturity of the Barnett Shale determined from well-log analysis. *AAPG Bulletin*, 91(4): 535-549.
- Zheng, R., He, L., Liang, X. and Xu, W., 2013. Forming conditions of shale gas (oil) plays in the Lower Jurassic Da'anzhai member in the eastern Sichuan Basin. *Natural Gas Industry*, 33(12): 30-40.
- Zhu, C., Xu, M., Yuan, Y., Zhao, Y., Shan, J., He, Z., Tian, Y. and Hu, S., 2010. Palaeo-geothermal response and record of the effusing of Emeishan basalts in Sichuan basin. *Chinese Sci Bull*, 55(6): 474-482.
- Zhu, G., Zhang, S., Liang, Y., Ma, Y., Dai, J., Li, J. and Zhou, G., 2006. The characteristics of natural gas in Sichuan basin and its sources. *Earth Science Frontiers*, 13(2): 243-248.

References

- Zhu, Y., Liu, E., Martinez, A., Payne, M.A. and Harris, C.E., 2011. Understanding geophysical responses of shale-gas plays. *The Leading Edge*, 30(3): 332-338.
- Zou, C., Dong, D., Wang, S., Li, J., Li, X., Wang, Y., Li, D. and Cheng, K., 2010. Geological characteristics and resource potential of shale gas in China. *Petroleum Exploration and Development*, 37(6): 641-653.
- Zou, C., Dong, D., Yang, H., Wang, Y., Huang, J., Wang, S. and Fu, C., 2011. Conditions of shale gas accumulation and exploration practices in China. *Natural Gas Industry*, 31(12): 26-39.
- Zumberge, J., Ferworn, K. and Curtis, J., 2009. Gas character anomalies found in highly productive shale gas wells. *Geochimica et Cosmochimica Acta Supplement*, 73: 1539.

Appendix

Table A1 Bulk kinetics data of Figure 4.7

Frequency factor		A= 8.4292E+14
Ea (kcal/mol)	Fraction of total potential (%)	
44	0.25	
45	0.15	
46	0.41	
47	0.33	
48	0.64	
49	0.62	
50	1.18	
51	1.15	
52	2.53	
53	3.67	
54	12.01	
55	9.59	
56	36.50	
57	14.05	
58	7.46	
59	4.91	
60	1.07	
61	2.03	
62	0.09	
63	0.87	
64	0.00	
65	0.00	
66	0.00	
67	0.49	

Table A2 Compositional kinetics data of Figure 4.7

Ea kcal/mol	Potential of hydrocarbons (%)													
	n-C1	n-C2	n-C3	i-C4	n-C4	i-C5	n-C5	n-C6	C7-15	C16-25	C26-35	C36-45	C46-55	C56-80
44	0.008	0.005	0.006	0.002	0.002	0.001	0.002	0.011	0.093	0.079	0.043	0.021	0.010	0.007
45	0.005	0.003	0.004	0.001	0.001	0.000	0.001	0.006	0.055	0.046	0.025	0.012	0.006	0.004
46	0.014	0.008	0.010	0.003	0.004	0.001	0.003	0.017	0.155	0.130	0.072	0.035	0.016	0.011
47	0.011	0.007	0.008	0.002	0.003	0.001	0.003	0.014	0.126	0.106	0.058	0.029	0.013	0.009
48	0.021	0.013	0.016	0.004	0.006	0.002	0.005	0.027	0.239	0.201	0.111	0.054	0.025	0.017
49	0.021	0.013	0.015	0.004	0.006	0.002	0.005	0.026	0.232	0.196	0.108	0.053	0.024	0.016
50	0.040	0.024	0.029	0.008	0.011	0.003	0.009	0.050	0.445	0.375	0.207	0.101	0.046	0.031
51	0.039	0.024	0.028	0.008	0.011	0.003	0.009	0.049	0.432	0.364	0.201	0.098	0.045	0.030
52	0.085	0.052	0.063	0.017	0.024	0.006	0.020	0.107	0.951	0.801	0.442	0.216	0.099	0.067
53	0.123	0.075	0.090	0.024	0.035	0.009	0.029	0.155	1.376	1.160	0.640	0.313	0.144	0.096
54	0.485	0.294	0.323	0.064	0.143	0.026	0.115	0.454	3.486	3.213	1.950	1.051	0.530	0.405
55	0.460	0.270	0.287	0.052	0.131	0.022	0.103	0.372	2.575	2.360	1.423	0.762	0.382	0.290
56	1.974	1.114	1.184	0.178	0.588	0.073	0.460	1.539	9.674	8.704	5.149	2.704	1.328	0.981
57	0.999	0.516	0.552	0.065	0.287	0.028	0.215	0.703	3.946	3.159	1.649	0.764	0.331	0.206
58	0.531	0.274	0.293	0.035	0.152	0.015	0.114	0.374	2.096	1.678	0.876	0.406	0.176	0.109
59	0.349	0.181	0.193	0.023	0.100	0.010	0.075	0.246	1.379	1.104	0.576	0.267	0.116	0.072
60	0.076	0.039	0.042	0.005	0.022	0.002	0.016	0.053	0.300	0.240	0.125	0.058	0.025	0.016
61	0.144	0.075	0.080	0.009	0.041	0.004	0.031	0.102	0.570	0.457	0.238	0.110	0.048	0.030
62	0.007	0.003	0.004	0.000	0.002	0.000	0.001	0.005	0.026	0.021	0.011	0.005	0.002	0.001
63	0.062	0.032	0.034	0.004	0.018	0.002	0.013	0.043	0.244	0.195	0.102	0.047	0.020	0.013
64	0.000	0.000	0.000	0.000	0.000	0.000	0.000	0.000	0.000	0.000	0.000	0.000	0.000	0.000
65	0.000	0.000	0.000	0.000	0.000	0.000	0.000	0.000	0.000	0.000	0.000	0.000	0.000	0.000
66	0.000	0.000	0.000	0.000	0.000	0.000	0.000	0.000	0.000	0.000	0.000	0.000	0.000	0.000
67	0.035	0.018	0.019	0.002	0.010	0.001	0.008	0.025	0.138	0.111	0.058	0.027	0.012	0.007
68	0.000	0.000	0.000	0.000	0.000	0.000	0.000	0.000	0.000	0.000	0.000	0.000	0.000	0.000

Appendix

Table A3 TR evolution with a function of temperature of Figure 4.8

Temperature(°C)	TR (%)						
1	0.00	51	0.00	101	0.04	151	0.69
2	0.00	52	0.00	102	0.04	152	0.71
3	0.00	53	0.00	103	0.04	153	0.74
4	0.00	54	0.00	104	0.04	154	0.76
5	0.00	55	0.00	105	0.05	155	0.78
6	0.00	56	0.00	106	0.05	156	0.80
7	0.00	57	0.00	107	0.05	157	0.82
8	0.00	58	0.00	108	0.05	158	0.83
9	0.00	59	0.00	109	0.06	159	0.85
10	0.00	60	0.00	110	0.06	160	0.86
11	0.00	61	0.00	111	0.06	161	0.87
12	0.00	62	0.00	112	0.07	162	0.88
13	0.00	63	0.00	113	0.07	163	0.89
14	0.00	64	0.00	114	0.07	164	0.90
15	0.00	65	0.00	115	0.08	165	0.91
16	0.00	66	0.00	116	0.08	166	0.91
17	0.00	67	0.01	117	0.09	167	0.92
18	0.00	68	0.01	118	0.09	168	0.93
19	0.00	69	0.01	119	0.10	169	0.93
20	0.00	70	0.01	120	0.10	170	0.94
21	0.00	71	0.01	121	0.11	171	0.94
22	0.00	72	0.01	122	0.12	172	0.95
23	0.00	73	0.01	123	0.13	173	0.95
24	0.00	74	0.01	124	0.14	174	0.95
25	0.00	75	0.01	125	0.15	175	0.96
26	0.00	76	0.01	126	0.16	176	0.96
27	0.00	77	0.01	127	0.17	177	0.96
28	0.00	78	0.01	128	0.18	178	0.97
29	0.00	79	0.01	129	0.19	179	0.97
30	0.00	80	0.01	130	0.20	180	0.97
31	0.00	81	0.01	131	0.22	181	0.97
32	0.00	82	0.01	132	0.23	182	0.97
33	0.00	83	0.02	133	0.25	183	0.98
34	0.00	84	0.02	134	0.27	184	0.98
35	0.00	85	0.02	135	0.29	185	0.98
36	0.00	86	0.02	136	0.31	186	0.98
37	0.00	87	0.02	137	0.33	187	0.98
38	0.00	88	0.02	138	0.35	188	0.98
39	0.00	89	0.02	139	0.37	189	0.98
40	0.00	90	0.02	140	0.39	190	0.99
41	0.00	91	0.02	141	0.41	191	0.99
42	0.00	92	0.02	142	0.44	192	0.99
43	0.00	93	0.03	143	0.46	193	0.99
44	0.00	94	0.03	144	0.49	194	0.99
45	0.00	95	0.03	145	0.51	195	0.99
46	0.00	96	0.03	146	0.54	196	0.99
47	0.00	97	0.03	147	0.57	197	0.99
48	0.00	98	0.03	148	0.60	198	0.99
49	0.00	99	0.03	149	0.63	199	0.99
50	0.00	100	0.04	150	0.66	200	0.99

Table A4 Calculated GOR, P_{sat} , B_o evolution with a function of TR in Figure 4.9

TR	10	30	50	70	90
GOR (Sm ³ /Sm ³)	62.9	88.6	113.2	130.1	176.2
B_o (Sm ³ /Sm ³)	1.25	1.32	1.39	1.45	1.61
P_{sat} (bar)	100.56	138.77	162.23	173.8	188.52
100× B_o (m ³ /Sm ³)	124.9	131.8	139.3	144.8	161.2

Appendix

Table A5 High-pressure (up to 25 MPa) methane sorption capacity

G009507	
Pressure [MPa]	Excess Sorption [mmol/g rock]
0.0000	0.0000
1.4698	0.0275
2.7071	0.0386
3.7141	0.0450
4.5318	0.0492
5.1960	0.0520
5.7362	0.0540
8.6309	0.0589
10.9438	0.0598
12.8294	0.0591
14.3889	0.0576
15.6842	0.0564
16.7684	0.0545
17.6710	0.0533
18.4240	0.0523
19.0502	0.0513
19.5723	0.0500
20.3326	0.0487
20.9669	0.0478

G009509	
Pressure [MPa]	Excess Sorption [mmol/g rock]
0.0000	0.0000
1.7562	0.0206
3.9752	0.0318
5.9486	0.0380
7.6976	0.0415
9.3554	0.0437
10.8502	0.0448
12.2057	0.0452
13.4433	0.0452
14.5786	0.0448
15.6232	0.0444
16.5791	0.0437
17.4586	0.0430
18.2595	0.0424
18.9895	0.0417
19.6537	0.0410
20.2530	0.0403
20.7935	0.0398
21.2699	0.0393
21.6876962	0.03893319
22.0452305	0.03844121
22.3519184	0.03815302
22.6111643	0.03785048
22.8278146	0.03761727
23.0005574	0.03739083
23.1382476	0.03720559
23.2404082	0.03710512

Appendix

G011298	
Pressure [MPa]	Excess Sorption [mmol/g rock]
0.0000	0.0000
2.0220	0.0330
4.1720	0.0469
6.0833	0.0542
7.7949	0.0586
9.3221	0.0612
10.7103	0.0627
11.9718	0.0635
13.1260	0.0638
14.1903	0.0637
15.1592	0.0635
16.0489	0.0631
16.8609	0.0627
17.6013	0.0621
18.2761	0.0616
18.8823	0.0611
19.4350	0.0605
19.9300	0.0601
20.3702	0.0598
20.7572869	0.05937571
21.0929594	0.05913234
21.3821195	0.05883581
21.6288196	0.05859083
21.8331246	0.05846428
21.9977806	0.05839103
22.1273125	0.0583587
22.2260389	0.05832152
22.2914259	0.05830082
22.3367567	0.05831004
22.3596489	0.058412

G009517	
Pressure [MPa]	Excess Sorption [mmol/g rock]
0.0000	0.0000
1.3745	0.0396
2.6973	0.0546
3.9208	0.0628
5.0528	0.0672
6.1062	0.0701
7.0832	0.0716
7.9930	0.0724
8.8417	0.0726
9.6377	0.0724
10.3875	0.0719
11.0904	0.0712
11.7548	0.0704
12.3795	0.0695
12.9684	0.0686
13.5232	0.0678
14.4718	0.0650
15.2005	0.0634
15.8788	0.0618
16.5052946	0.06018923
17.0858762	0.05903799
17.6230645	0.05795611
18.116079	0.05678717
18.5689629	0.05608352
18.9772591	0.05536518
19.3480258	0.05482198
19.8218931	0.05355006
20.1064639	0.0531493
20.3595848	0.05269836

Appendix

G009518	
Pressure [MPa]	Excess Sorption [mmol/g rock]
0.0000	0.0000
1.7130	0.0507
3.5344	0.0724
5.2196	0.0845
6.7555	0.0920
8.1590	0.0969
9.4489	0.1001
10.6286	0.1018
11.7210	0.1028
12.7308	0.1032
13.6690	0.1032
14.5476	0.1028
15.3607	0.1024
16.1175	0.1018
16.8228	0.1010
17.4759	0.1003
18.0805	0.0993
18.6408	0.0982
19.1636	0.0973
19.6423722	0.09654129
20.0794027	0.09569359
20.4777283	0.09492031
20.8363317	0.09445083
21.1546636	0.09386326
21.4371903	0.09338397
21.6849142	0.09298306
21.8979549	0.09266145
22.0806239	0.0924679
22.2317312	0.09216384
22.3545416	0.09216008

G009520	
Pressure [MPa]	Excess Sorption [mmol/g rock]
0.0000	0.0000
1.3916	0.0550
2.6759	0.0769
3.7340	0.0890
4.5892	0.0969
5.2760	0.1024
7.2379	0.1117
9.3500	0.1173
11.0274	0.1203
12.3762	0.1213
14.6380	0.1187
16.4938	0.1155
13.2931	0.1206
15.6025	0.1171
17.5154	0.1133
19.1092	0.1108
20.4368	0.1089

Appendix

G009521	
Pressure [MPa]	Excess Sorption [mmol/g rock]
0.0000	0.0000
1.9850	0.0114
3.4600	0.0190
4.5725	0.0230
5.4100	0.0262
6.0450	0.0281
8.1675	0.0323
9.7750	0.0348
11.6550	0.0360
13.1000	0.0363
14.2175	0.0364
16.4675	0.0353
18.2625	0.0343
19.7025	0.0327
21.1325	0.0325
22.2825	0.0321
23.1850	0.0322
23.9100	0.0318
24.4825	0.0316
24.9275	0.03156899
25.275	0.03136426

G011313 (0.5-1.0mm)	
Pressure [MPa]	Excess Sorption [mmol/g rock]
0.0000	0.0000
1.6392	0.0175
3.3010	0.0249
4.8559	0.0295
6.2759	0.0322
7.5839	0.0340
8.7865	0.0350
9.9012	0.0356
10.9340	0.0360
11.8844	0.0359
12.7814	0.0355
13.6206	0.0354
14.4027	0.0348
15.1320	0.0348
16.1946	0.0335
16.8133	0.0329
17.3930	0.0322
17.9276	0.0319
18.4300	0.0310
18.8989554	0.03059827
19.331168	0.02977077
19.7311597	0.02953887
20.0988404	0.02896857
20.4380991	0.02842885
20.7478745	0.02833871
21.0308237	0.02786009
21.2897785	0.02736075

Appendix

G011313 (<0.5mm)	
Pressure [MPa]	Excess Sorption [mmol/g rock]
0.0000	0.0000
1.7681	0.0191
3.4006	0.0264
4.8835	0.0306
6.2274	0.0333
7.4459	0.0350
8.5601	0.0362
9.5803	0.0368
10.5247	0.0372
11.3909	0.0372
12.1936	0.0371
12.9338	0.0370
13.6198	0.0367
14.2529	0.0362
14.8370	0.0358
15.5794	0.0351
16.2640	0.0346
16.8991	0.0337
17.4889	0.0332
18.0322025	0.03243911
18.5316938	0.03172686
18.9885425	0.03115192
19.4077805	0.03054301
19.7869172	0.03003389
20.1258436	0.02956765
20.4297538	0.02926456
20.6974058	0.02888484
20.9370493	0.02838908
21.1455463	0.02811476
21.3216422	0.02807402
21.4674473	0.02774958
21.5912498	0.02759688
21.6894669	0.02740799
21.765843	0.02740097
21.8225999	0.02725468

G011319	
Pressure [MPa]	Excess Sorption [mmol/g rock]
0.0000	0.0000
1.4150	0.1143
2.7850	0.1542
3.9125	0.1739
4.8075	0.1858
5.5175	0.1925
6.0725	0.1982
9.6800	0.2098
12.1525	0.2098
14.1225	0.2071
15.7000	0.2034
16.9675	0.1999
17.9925	0.1961
18.8100	0.1937
19.4650	0.1915
19.9925	0.1892
20.4100	0.1876
20.7375	0.1870
21.0000	0.1860
21.2075	0.18492059
21.7775	0.18278272
22.2325	0.18136145
22.5975	0.17961601

Appendix

G006491	
Pressure [MPa]	Excess Sorption [mmol/g rock]
0.0000	0.0000
1.7212	0.0301
3.4065	0.0490
5.1331	0.0636
6.7471	0.0744
8.2086	0.0825
9.5432	0.0883
10.7679	0.0927
11.8926	0.0959
12.9336	0.0983
13.8962	0.1001
14.7883	0.1013
15.6136	0.1023
16.3789	0.1028
17.0868	0.1033
17.7395	0.1036
18.3406	0.1037
18.8914	0.1038
19.3931	0.1039
19.8458312	0.10390652
20.2571965	0.10390998
20.6238102	0.10391497
20.9507074	0.10394215
21.2389022	0.10392805
21.4897735	0.10403675
21.7070912	0.10413615
21.8870579	0.10424524
22.0384541	0.10423605
22.1606826	0.10437467
22.2558796	0.10441602
22.3257008	0.10446908
22.3732441	0.10470779

G006492	
Pressure [MPa]	Excess Sorption [mmol/g rock]
0.0000	0.0000
1.7550	0.0465
3.1400	0.0706
4.6725	0.0903
6.5175	0.1095
7.9450	0.1208
9.4725	0.1295
10.6675	0.1356
12.5875	0.1422
14.1050	0.1475
15.3200	0.1500
16.2875	0.1528
17.0625	0.1543
17.6775	0.1565
18.1700	0.1574
19.3350	0.1585
20.2775	0.1595
21.0350	0.1610
21.6475	0.1610
22.135	0.1616266
22.5225	0.16217736

Appendix

Table A6 Porosity and bulk density results of Figure 6. 8

Unit	ID	Depth	TOC (%)	Bulk density (g/cm ³)	Hg-porosity (%)	He-porosity (%)
Lower Silurian shale	G009524	136	1.96	2.67	0.58	
	G009525	207	1.47	2.63	0.34	14.62
	G009526	267	2.31	2.60	0.69	
	G009527	276	1.69	2.60	0.61	
	G009528	285	1.68	2.63	0.81	
	G009529	321	2.21	2.63	0.42	
	G009509	0	1.68	2.627	0.709	2.4
Lower Cambrian shale	G009519	0	8.15	2.557	0.667	1.2
	G011312	53.09	1.55	2.66	0.31	13.26
	G011313	109.4	1.38	2.69	0.26	2.02
	G011314	166.47	1.76	2.71	0.33	10.79
	G011315	200.3	1.21	2.76	0.21	
	G011316	243.84	1.85	2.59	0.28	
	G011317	22.5	5.69	2.55	0.68	14.88
	G011318	32.02	3.15	2.62	0.51	0.72
	G011319	47.48	13.20	2.33	0.78	9.31
	G011320	65.08	1.09	2.66	0.53	
	G011321	77.68	2.12	2.63	0.36	0.43
Ediacaran shale	G011322	86.14	14.50	2.43	1.06	6.11
	G011323	162.86	1.28	2.65	0.31	0.60
	G011324	271.73	0.37	2.75	0.30	
	G011325	326	0.33	2.71	0.61	2.63
	G011326	351.5	0.52	2.71	0.36	3.29
AU Cambrian shale	G012284	345.5	10.7	2.4035	0.93	0.8
	G012285	790.81	2.14	2.557	3.29	1.3
	G012286	107.69	1.01	2.134	1.77	2.3

Table A7 Helium permeability results of Figure 6.10

Sample ID	Test No.	P _{conf} [MPa]	T [°C]	P _{up} [bar]	P _{down} [bar]	P _{mean} [MPa]	1/P _{mean} [MPa ⁻¹]	k _{gas} [nD]	k _∞ [nD]	b [1/MPa]
25	1	30	46	21.4	0.1	1.1	0.9	33.4	9.1	0.34
	2			31.0	10.2	2.1	0.5	21.1		
	3			40.6	20.1	3.1	0.3	18.0		
	4			50.7	29.8	4.1	0.2	16.1		
	5	30	45	20.1	0.4	1.1	0.9	30.7	8.1	0.33
	6			29.8	10.2	2.1	0.5	20.0		
	7			39.4	19.9	3.0	0.3	16.3		
	8			51.4	29.7	4.1	0.2	14.0		
28	1	30	46	22.4	0.9	1.2	0.8	50.2	18.6	0.49
	2			32.1	11.8	2.2	0.5	35.9		
	3			41.2	20.5	3.1	0.3	31.5		
	4			54.2	30.8	4.2	0.2	26.7		
	5	30	46	0.9	21.9	1.1	0.9	52.7	20.2	0.55
	6			11.4	31.1	2.1	0.5	37.9		
	7			20.7	41.4	3.1	0.3	32.3		
	8			30.4	52.4	4.1	0.2	29.3		
43	1	30	52	1.1	20.5	1.1	0.9	27.7	7.5	0.35
	2			10.9	31.3	2.1	0.5	17.9		
	3			20.8	42.0	3.1	0.3	14.1		
	4			31.7	51.3	4.1	0.2	13.1		
	5			24.7	22.1	2.3	0.4	18.4		
	6	26.4	23.2	2.5	0.4	17.8	7.9	0.32		
	7	28.6	24.5	2.6	0.4	17.2				
	8	31.1	26.4	2.9	0.3	16.5				
	9	31.8	28.5	3.0	0.3	16.0				
58	1	30	46	1.03	124.30	6.24	0.16	0.06		

P_{conf.} is confining pressure; P_{up} is the initial pressure at the upstream side; P_{down} is the initial pressure at the downstream side; P_{mean} is the mean pressure between upstream and downstream side during each test; k_{gas} is the apparent gas permeability coefficient; k_∞ is the intrinsic or Klinkenberg corrected permeability coefficient; and b is the klinkenberg flip factor.

Appendix

Table A8 Mineralogy, UCS, and E results of Figure 6.12

ID	TOC (%)	Quartz+Carbonate+Feldspar+Pyrite (%)	Clay+Mica+TOC (%)	Carbonate + Feldspar (%)	Porosity (%)	UCS (Mpa)	E(Gpa)
G009507	3.3	63.09	40.21	16.21		140.89	20.01
G009509	1.7	59.83	41.88	16.77	2.5	129.51	13.88
G009511-1	0.9	67.01	33.88	36.34		169.18	18.31
G009511-2	0.9	67.01	33.88	36.34		152.29	16.44
G009512	3.9	65.48	38.41	10.82		94.29	15.44
G009519-1	8.15	77.095	31.06	34.71	1	196.79	22.65
G009519-4	8.15	77.095	31.06	34.71	1.7	167.19	14.25
G012284	10.7	87.57	23.14	39.81	1.2	234.66	22.06
G012285	2.1	81.85	20.24	42.67	0.8	221.04	24.61

Table A9 TCS results of Figure 6.13

Sample ID	G009509	G009519-1	G009519-2	G012284	G012285-1	G012285-2	G012286-1	G012286-2
S3 (Mpa)	S1 (Mpa)							
0	129.5	196.8	167.2	234.7	221			
12	199.3	295.4		327.7	268.9	273.2	133.1	177.8
18	218.9	289.2		334	301.3	301.9	155.7	200.1
24	210.1	307.3		338	325.6	326	176.2	220.4
30	241.4	345.7		375.7	344.3	344.4	200	240.1
36				381.8				

Table A10 Rock mechanical results of Figures 6.14-6.15

Sample ID	UCS (Mpa)	E(Gpa)	E* (Gpa)	E12*(Gpa)	TCS12	TCS18	TCS24	TCS30	TCS36	μ	St(Mpa)	KIC(MN/m1.5)	Vp(km/s)
G009507	140.89	20.01									12.95668	1.06322336	
G009509	129.51	13.88	15	18	199.3	218.9	210.1	241.4		0.63	13.40962	1.03455437	3.14
G009511-1	169.18	18.31									12.36959	1.179174555	
G009511-2	152.29	16.44											
G009512	94.29	15.44									10.43245	1.092541419	
G009519-1	196.79	22.65	27	23	295.4	289.2	307.3	345.7		0.85	17.13993	1.701604448	3.7
G009519-4	167.19	14.25	16										3.79
G012284	234.66	22.06	27	22	327.1	334	338	375.7	381.8	0.69	11.41578	1.125072225	3.62
G012285-1	221.04	24.61	31	24	268.9	301.3	325.6	344.3		0.78	19.31267	1.734465513	3.85
G012285-2				26	273.2	301.9	326	344.4		0.74			3.91
G012286-1				12	133.1	155.7	176.2	200		0.7			3.05
G012286-2				18	177.8	200.1	220.4	240.1		0.66			3.05

*denotes data measured by Geomecon;

Mineralogy and TOC data can be found in Table 6.2.